

# **Microwave enhanced chemical vapour infiltration of silicon carbide fibre preforms**

**Andrea D'Angio'**

Thesis submitted to the University of Birmingham  
for the degree of Doctor of Philosophy

School of Metallurgy and Materials  
College of Engineering and Physical Sciences  
University of Birmingham  
January 2018

UNIVERSITY OF  
BIRMINGHAM

**University of Birmingham Research Archive**

**e-theses repository**

This unpublished thesis/dissertation is copyright of the author and/or third parties. The intellectual property rights of the author or third parties in respect of this work are as defined by The Copyright Designs and Patents Act 1988 or as modified by any successor legislation.

Any use made of information contained in this thesis/dissertation must be in accordance with that legislation and must be properly acknowledged. Further distribution or reproduction in any format is prohibited without the permission of the copyright holder.

# Abstract

An investigation into the fundamentals of the deposition of silicon carbide within porous silicon carbide fibre preforms using microwave-enhanced chemical vapour infiltration has been carried out.

The study of the kinetics of deposition revealed an Arrhenius behaviour of the matrix growth rate against the temperature in the range 800-1000°C and a linear dependence on the pressure in the range 20 - 70 kPa. This is typical of a surface-reaction limited regime.

The morphology of the SiC deposited changed with both temperature and pressure. Increases in both lead to a transition from a smooth, globular deposit morphology to something that was rougher and more angular; this corresponded to the transition from a nucleation to a growth regime. Stoichiometric SiC was predominantly found in the central region of the samples infiltrated at 1000°C, but the deposit became more silicon-rich (up to 2.6 at %) the farther from the initial deposit.

Dielectric properties showed that ZMI Tyranno silicon carbide fibres readily absorbed microwave energy. In specific conditions of temperatures and pressures, 900-950°C and 50 kPa, an inside-out deposition pattern was observed indicating a temperature gradient across the preform. Deposition of silicon carbide and silicon caused the gradual flattening of the temperature gradient.

# Acknowledgment

I am profoundly indebted to Prof. J.G.P. Binner for the supervision, discussions, advice and trust during the entire research programme. Above all, I say thank you for the invaluable teaching.

I personally thank my colleague Matthew Porter. His contribution in this work has been fundamental, in particular he helped on the dielectric property measurements, Raman spectroscopy analysis and he constantly offered support throughout the whole project.

Many thanks are also extended to:

- Dr. A. Paul who contributed to the set up of the MECVI equipment
- Dr. Ji Zou for the enjoyable discussions about ceramics
- Dr. V. Rubio and all the members of the Ceramic Research Group of the University of Birmingham
- Dr. W. Fahrenholtz and G. Hilmas for giving me the opportunity to spend three months in their research group at Missouri University and Technology.

A personal thank you goes to all my family and friends who supported me during these years. A special thank for Lorenza, my fiancée who had always encouraged and backed me up during these years.

I would finally like to acknowledge the University of Birmingham for the financial support.

*“Science means constantly walking a tightrope between blind faith and curiosity; between expertise and creativity; between bias and openness; between experience and epiphany; between ambition and passion; and between arrogance and conviction - in short, between an old today and a new tomorrow”*

(Heinrich Rohrer)

---

# Table of Contents

<b>1</b>	<b>Introduction .....</b>	<b>1</b>
<b>2</b>	<b>Literature survey .....</b>	<b>4</b>
2.1	Advanced structural ceramics .....	4
2.2	Ceramic Matrix Composites (CMCs) .....	5
2.3	Fibre-reinforced ceramic matrix composites (FRCMCs) .....	9
2.3.1	Interest in and properties of FRCMCs .....	9
2.3.2	SiC <sub>f</sub> /SiC system.....	14
2.3.2.1	Introduction to silicon carbide .....	14
2.3.2.2	Silicon carbide fibres.....	16
2.3.2.2.1	Effect of the microstructure on the mechanical and environmental performance of silicon carbide fibres.....	18
2.3.2.2.2	SiC fibres from CVD .....	20
2.3.2.2.3	SiC fibres from polymeric precursor .....	21
2.3.2.3	Properties of SiC <sub>f</sub> /SiC composites .....	32
2.3.2.4	Properties of preforms .....	33
2.3.2.5	Fibre/matrix interface .....	35
2.3.2.6	Applications of the SiC <sub>f</sub> /SiC system.....	37

---

2.4	Fabrication of FRCMCs .....	37
2.4.1	Introduction .....	37
2.4.2	Matrix formation and available techniques .....	38
2.4.2.1	Powder processing .....	38
2.4.2.1.1	Slurry infiltration.....	39
2.4.2.2	Liquid metal infiltration .....	40
2.4.2.3	Polymer impregnation and pyrolysis (PIP).....	42
2.5	Chemical vapour infiltration .....	46
2.5.1	Introduction .....	46
2.5.2	CVI variants.....	49
2.5.2.1	Thermal gradient heated, isobaric .....	50
2.5.2.2	Forced flow, isothermal (IFCVI) and thermal gradient (TFCVI) 51	
2.5.2.3	Pulsed-pressure (PCVI).....	52
2.5.2.4	Microwave enhanced chemical vapour infiltration (MECVI) ....	52
2.5.2.5	Consideration of the residual porosity and multi-stage approach	
	<b>Error! Bookmark not defined.</b>	
2.6	Chemistry of the CVI process in SiC <sub>f</sub> /SiC composites .....	57
2.7	Transport phenomena .....	62
2.8	Microwave enhanced chemical vapour infiltration (MECVI)	64
2.8.1	Nature of microwaves.....	64

---

2.8.2	Microwave radiation and applications in ceramics .....	70
2.8.3	Generators and applicators of microwaves .....	71
2.8.3.1	Microwave generator .....	71
2.8.3.2	Waveguides .....	72
2.8.3.3	Microwave applicator .....	73
2.8.3.4	Temperature measurements.....	74
2.8.4	Silicon carbide and microwaves .....	76
2.8.5	Volumetric heating.....	79
2.8.6	Focus on microwave-enhanced chemical vapour infiltration .....	82
2.8.6.1	Process variables .....	83
2.8.6.2	Benefits and disadvantages of MECVI .....	84
2.8.6.3	Experimental results .....	85

### **3 Experimental procedure ..... 87**

3.1	MECVI equipment .....	87
3.1.1	Microwave unit .....	89
3.1.2	Gas cleaning and exhaust system.....	91
3.1.3	Gas delivery system .....	93
3.2	CVI of SiC fibrous materials .....	96
3.2.1	Starting materials .....	96
3.2.1.1	Fibre fabric.....	96

---

3.2.1.2	Methyltrichlorosilane (MTS) .....	97
3.2.2	Experimental procedure .....	98
3.2.2.1	Loading.....	98
3.2.2.2	Purge and setpoint temperature .....	99
3.2.2.3	Infiltration .....	100
3.2.2.4	Cooling at the end of the run .....	103
3.2.2.5	Experimental problems encountered during MECVI experiments 104	
3.3	Characterisation .....	108
3.3.1	Microscopy .....	108
3.3.1.1	Optical microscopy .....	108
3.3.1.2	Scanning electron microscopy .....	109
3.3.1.3	Energy-dispersive X-ray analysis (EDS).....	110
3.3.1.4	Wavelength-dispersive X-ray analysis (WDS) .....	111
3.3.1.5	Transmission electron microscopy.....	111
3.3.2	Raman Spectroscopy .....	112
3.3.3	Dielectric permittivity measurements.....	112
3.3.3.1	Introduction .....	112
3.3.3.2	Equipment.....	113
3.3.3.3	Calculations .....	115
<b>4</b>	<b>Results and discussion .....</b>	<b>117</b>

---

4.1	Preliminary results.....	117
4.1.1	Thermodynamics of the Si-C-H-Cl system .....	117
4.1.2	The presence of oxygen in the Si-C-H-Cl system.....	122
4.2	Kinetics .....	125
4.2.1	Matrix growth rate.....	125
4.2.1.1	Influence of temperature .....	125
4.2.1.2	Influence of pressure .....	127
4.2.2	Activation energy.....	130
4.2.3	Mass transport and chemical reactivity .....	132
4.3	Morphology and stoichiometry.....	136
4.3.1	Morphology of the deposit .....	136
4.3.1.1	Influence of the temperature .....	136
4.3.1.2	Influence of the pressure .....	143
4.3.1.3	Influence of arcing on the morphology of the matrix .....	146
4.3.1.4	CVD experiments.....	148
4.3.2	Composition of the deposit.....	151
4.3.2.1	Dispersive X-ray spectroscopy .....	151
4.3.2.2	Raman spectroscopy .....	158
4.3.3	TEM analysis.....	164
4.4	Deposition pattern .....	173
4.4.1	Influence of temperature .....	173

---

4.4.2	Influence of the pressure .....	181
4.4.3	Thermal conductivity influence .....	188
4.4.4	The role of the powder .....	189
4.5	Dielectric properties.....	191
4.5.1	Permittivity effect.....	200
<b>5</b>	<b>Conclusions and future work.....</b>	<b>203</b>
5.1	Conclusions .....	203
5.1.1	Thermodynamics study .....	203
5.1.2	Kinetics study .....	204
5.1.3	Physiochemical properties of the SiC deposit .....	204
5.1.4	Deposition pattern .....	206
5.1.5	Dielectric permittivity .....	207
5.2	Future Work .....	207
<b>6</b>	<b>Appendix I.....</b>	<b>212</b>
<b>7</b>	<b>Appendix II.....</b>	<b>214</b>
<b>8</b>	<b>References.....</b>	<b>215</b>

---

## Table of figures

Figure 2-1. Stress-strain curves for a ceramic matrix composites and a related monolithic ceramic [5]. .....	6
Figure 2-2. Crack deflection and crack bridging in ZrB <sub>2</sub> -SiC composite. Adapted from [37]. .....	7
Figure 2-3. Transformation toughening of tetragonal zirconia to monoclinic system [39]. .....	8
Figure 2-4. Comparison of a fracture surface of a SiC <sub>f</sub> -SiC composite with (a) and without (b) fibre pull-out. Adapted from [45]. .....	9
Figure 2-5. Ashby diagram of the specific strength against the maximum service temperature of materials for aerospace applications. ....	11
Figure 2-6. Drawing of the LEAP engine with the CMC inserts and their functions. Adapted from [69]. .....	12
Figure 2-7. Manufacturing steps of the ceramic fibres from polymeric precursor route [73]. .....	18
Figure 2-8. Microstructure of the CVD SiC fibres [73]. .....	21
Figure 2-9. Microstructural of the three generations of SiC fibres. Adapted from [88]. .....	23
Figure 2-10. Comparison of the creep strain and rupture strength at 1400°C between Super-Sylramic fibres and SiC fibres of the third generation. Adapted from [86, 116]. .....	29
Figure 2-11. Variation of the tensile strength against temperature of commercially available SiC fibres after annealing in inert atmosphere (a) and in air (b). Adapted from [73]. .....	29
Figure 2-12. Several types of weaving. Adapted from [130]. ....	33

---

Figure 2-13. Stacking of plies for a composite material; the final properties depends on the number of plies and orientation [130]. .....	34
Figure 2-14. The number of fibres determines the dimension of the bundle. Adapted from [131]. .....	34
Figure 2-15. Fibre architectures. Adapted from [133]......	35
Figure 2-16. Schematic of the liquid silicon infiltration (LSI) process [166]. .....	42
Figure 2-17. Schematic of fabrication of SiC based composites by PIP [166] ..	43
Figure 2-18. Flow chart of polymer infiltration and pyrolysis of SiC <sub>f</sub> /SiC composite .....	44
Figure 2-19. Schematic of an isothermal chemical vapour infiltration [166]. .....	46
Figure 2-20. Void filling during CVI .....	47
Figure 2-21. Macroporosity (on the left) and microporosity (on the right) [155, 220]......	55
Figure 2-22. Thermodynamic yields for the solid deposition of SiC as function of hydrogen-methyltrichlorosilane ratio [193]. Temperature is in K. ....	60
Figure 2-23. Mass transfer mechanism in chemical vapour infiltration. Steps (i), (ii), (iv) and (v): mass transfer by diffusion. Steps (iii): chemical reaction [193].	62
Figure 2-24. Electromagnetic spectrum and microwave radiation [251]......	65
Figure 2-25. Schematic of a magnetron [275]. .....	72
Figure 2-26. Temperature difference versus characteristic heating time for microwave and conventional heating [261]. .....	81
Figure 2-27. Heating method in a conventional CVI and in a Microwave enhanced CVI process. ....	83
Figure 2-28. Microstructure of a SiC <sub>f</sub> /SiC composite fabricated by MECVI. Adapted from [16]. .....	83

---

Figure 3-1. Photograph of the MECVI equipment .....	88
Figure 3-2. Schematic diagram of the MECVI apparatus - MFC= mass flow controller, MW= microwave radiation and P = pressure transducer.....	88
Figure 3-3. Photograph of the microwave-heated CVI unit .....	89
Figure 3-4. Magnetron for the microwave generation .....	90
Figure 3-5. Manual and autotuner systems to minimise the reflected power for a more efficient heating.....	91
Figure 3-6. 3D rendering of the microwave cavity and reactor.....	92
Figure 3-7. Photograph of the turntable and the configuration of the inlet and outlet .....	92
Figure 3-8. Photograph of the gas cleaning and exhaust system .....	93
Figure 3-9. Schematic (side view) of the configuration for the detection of the sample temperature .....	95
Figure 3-10. Fibre preform fabrication route .....	97
Figure 3-11. Partial pressure of MTS. Adapted from [316].....	98
Figure 3-12. Photograph of the sample arrangement. ....	99
Figure 3-13. Temperature difference of the reading of the 2-colour pyrometers at the top (black solid line) and at the bottom of the cavity (red solid line). ....	105
Figure 3-14. Temperature (black solid line) drop due to the formation of silica in the first stage of MECVI. Power (blue solid line) was increased from 890 to 970 W. Blue dotted line represents the reflected power.....	106
Figure 3-15. Breakdown voltage as function of partial pressure of hydrogen at different distance between two electrodes. ....	107
Figure 3-16. Dual mode microwave cavity at ITACA, Spain. ....	113

---

Figure 3-17. Schematic of the dual mode cavity for the measurements of the dielectric properties at high temperature. Adapted from [324].	114
Figure 4-1. Variation of the carbon species generated by the decomposition of MTS as function of the temperature. The plot was generated by the software HSC Chemistry 7.0.	119
Figure 4-2. Variation of the silicon species generated by the decomposition of MTS as function of the temperature. The plot was generated by the software HSC Chemistry 7.0.	120
Figure 4-3. Variation of the carbon species generated by the decomposition of MTS as function of the pressure. The plot was generated by the software HSC Chemistry 7.0.	120
Figure 4-4. Variation of the silicon species generated by the decomposition of MTS as function of the pressure. The plot was generated by the software HSC Chemistry 7.0.	121
Figure 4-5. Composition of the solid deposit generated from the decomposition of MTS as function of the temperature. The plot was generated by the software HSC Chemistry 7.0.	121
Figure 4-6. Composition of the solid deposit generated from the decomposition of MTS as function of the pressure. The plot was generated by the software HSC Chemistry 7.0.	122
Figure 4-7. Variation of the composition of the deposit and species containing oxygen as a function of increasing oxygen content during the decomposition of MTS at a) 900°C, b) 950°C and c) 1000°C. The plot was generated by the software HSC Chemistry 7.0.	123
Figure 4-8. Natural logarithm of the matrix growth rate $G_{SiC}$ against the reciprocal temperature at $P = 30$ kPa, $Q_{H_2} = 300$ ml min <sup>-1</sup> .	126

---

Figure 4-9. SiC matrix growth rate, relative densification rate and yield of the decomposition of MTS as function of the pressure for infiltration temperature of 900, 950 and 1000°C, $Q_{H_2} = 300 \text{ ml min}^{-1}$ .....	128
Figure 4-10. Average pore residence time as a function of the infiltration temperature ranging from 700 to 1200°C.....	129
Figure 4-11. Average pore residence time as a function of the total pressure for various hydrogen flow rates. ....	129
Figure 4-12. Average pore residence time as a function of the flow rate for various total gas pressures.....	130
Figure 4-13. Matrix growth rate against the reciprocal of the temperature at different pressures. $Q_{H_2} = 300 \text{ ml min}^{-1}$ and $\alpha = 10$ .....	132
Figure 4-14. SEM-SEI images of the morphology of the deposit at: (a) and (b) 900°C, (c) and (d) 950°C and (e) and (f) 1000°C. Total pressure was 30 kPa, total flow rate $300 \text{ cm}^3 \text{ min}^{-1}$ and gas ratio $\sim 10$ .....	138
Figure 4-15. SEM-SEI image of the fracture surface showing columnar growth .....	139
Figure 4-16. SEM-SEI images of the morphology of the SiC deposited at 900°C in different location within the preform: (a) and (b) centre, (c) and (d) 5 mm and (e) and (f) 10 mm from the centre. Total pressure was 30 kPa, total flow rate $300 \text{ cm}^3 \text{ min}^{-1}$ and gas ratio $\sim 10$ . ....	141
Figure 4-17. SEM-SEI images of the morphology of the SiC deposited at 1000°C in different location within the preform: (a) and (b) centre, (c) and (d) 10 mm and (e) and (f) 20 mm from the centre. Total pressure was 30 kPa, total flow rate $300 \text{ cm}^3 \text{ min}^{-1}$ and gas ratio $\sim 10$ . ....	142
Figure 4-18. SEM-SEI images of the difference between the deposit morphology in the inner (a) and on the outer (b) part of the tow. Sample infiltrated at 950°C, 30 kPa, total flow rate of $300 \text{ ml min}^{-1}$ and gas ratio $\sim 10$ . ....	143

---

Figure 4-19. SEM-SEI images of the morphology of the SiC deposited at 900°C at different pressure: (a) and (b) 30 kPa, (c) and (d) 50 kPa and (e) and (f) 70 kPa. Total flow rate 300 cm <sup>3</sup> min <sup>-1</sup> and gas ratio ~10.....	145
Figure 4-20. SEM-SEI images at different magnification of the formation of SiC deposit with elongated structure at 1000°C, 70 kPa, flow rate 300 cm <sup>3</sup> min <sup>-1</sup> and gas ratio ~10.....	146
Figure 4-21. SEM-SEI images at different magnification of the formation of SiC filaments following arcing events; infiltration conditions were 1000°C, 20 kPa, α~10.....	147
Figure 4-22. SEM-SEI images of the formation of spherical agglomerate of SiC whiskers due to the arcing; infiltration conditions were 1000°C, 15 kPa, α~10. ....	147
Figure 4-23. SEM-SEI images of the deposit grown on a single layer of fabric made of Tyranno- ZMI silicon carbide fibre at: (a) and (b) 1100°C, (c) and (d) 1000°C, (e) and (f) 900°C. Hydrogen flow rate was 300 ml min <sup>-1</sup> and gas ratio ~10.....	150
Figure 4-24. Schematic of the deposit growth modes (a) Volmer-Weber (or island formation), (b) Frank–van der Mer (layer-by-layer) and (c) Stranski–Krastanov (layer-plus-island) .....	151
Figure 4-25. Contour map of the composition of the deposit growth at different temperatures. ΔSi/C indicates the deviation of the Si/C ratio from stoichiometric silicon carbide. Negative values represent regions with carbon excess whilst positive values indicate excess of silicon. ....	153
Figure 4-26. SEM-BSE images of the co-deposition of silicon within the fibre tow at different magnification (a) and (b); (c) comparison of the EDS spectra in two different locations within the tow. ....	154
Figure 4-27. Silicon inclusions counted in the SiC matrix grown at 900°C, 30 kPa, α~10 and Q <sub>H2</sub> = 300 ml min <sup>-1</sup> .....	155

---

Figure 4-28. Contour map of the silicon inclusions counted in the SiC matrix grown at 950°C, 30 kPa, $\alpha \sim 10$ and $Q_{H_2} = 300 \text{ ml min}^{-1}$ .....	155
Figure 4-29. Silicon inclusions counted in the matrix growth at 1000°C, 30 kPa, $\alpha \sim 10$ and $Q_{H_2} = 300 \text{ ml min}^{-1}$ .....	156
Figure 4-30. Oxygen content (atomic percentage) in the matrix growth at 900°C, 30 kPa, $\alpha \sim 10$ and $Q_{H_2} = 300 \text{ ml min}^{-1}$ . ....	157
Figure 4-31. Oxygen content (atomic percentage) in the matrix growth at 950°C, 30 kPa, $\alpha \sim 10$ and $Q_{H_2} = 300 \text{ ml min}^{-1}$ . ....	157
Figure 4-32. Oxygen content (atomic percentage) in the matrix growth at 1000°C, 30 kPa, $\alpha \sim 10$ and $Q_{H_2} = 300 \text{ ml min}^{-1}$ . ....	158
Figure 4-33. Raman spectra of high purity SiC (in red) and cubic silicon carbide (in black) grown by CVD. The inset shows in detail the range of shift in which the LO and TO bands of SiC are typically located. ....	161
Figure 4-34. Raman spectra of Tyranno ZMI SiC fibres.....	161
Figure 4-35. Raman spectra of the SiC matrix growth at 900°C, 30 kPa and $\alpha$ ratio $\sim 10$ . The inset shows the shift range $650\text{-}1000 \text{ cm}^{-1}$ in which the TO and LO bands of SiC are typically located. ....	162
Figure 4-36. Raman spectra of the SiC matrix growth at 950°C, 30 kPa and $\alpha$ ratio $\sim 10$ . The inset shows the shift range $650\text{-}1000 \text{ cm}^{-1}$ in which the TO and LO bands of SiC are typically located.....	162
Figure 4-37. Raman spectra of the SiC matrix growth at 1000°C, 30 kPa and $\alpha$ ratio $\sim 10$ . The inset shows the shift range $650\text{-}1000 \text{ cm}^{-1}$ in which the TO and LO bands of SiC are typically located.....	163
Figure 4-38. Comparison of the Raman spectra of the SiC matrix growth at different temperatures, 30 kPa and $\alpha$ ratio $\sim 10$ .....	163
Figure 4-39. Bright field of the matrix growth between two SiC fibres at 900°C, 30 kPa, $\alpha \sim 10$ and $Q_{H_2} = 300 \text{ ml min}^{-1}$ . ....	165

---

Figure 4-40. Dark field of the matrix growth between two SiC fibres at 900°C, 30 kPa, $\alpha \sim 10$ and $Q_{H_2} = 300 \text{ ml min}^{-1}$ . .....	165
Figure 4-41. Details of the inclusions within the matrix at different magnification, (a), (c) and (e). Striations perpendicular to the growth directions indicated the presence of stacking faults which produced the streaking of the diffraction pattern (b), (d) and (f).....	166
Figure 4-42. (a) Bright field of the matrix growth between two SiC fibres at 950°C, 30 kPa, $\alpha \sim 10$ and $Q_{H_2} = 300 \text{ ml min}^{-1}$ ; (b) colour map reconstruction of the crystalline orientation; the main direction of growth is $[111]$ .....	167
Figure 4-43. (a) Bright field of the matrix growth between two SiC fibres at 1000°C, 30 kPa, $\alpha \sim 10$ and $Q_{H_2} = 300 \text{ ml min}^{-1}$ ; (b) colour map reconstruction of the crystalline orientation. ....	168
Figure 4-44. (a) Bright field image of the matrix growth between two fibres; (b) the different coloured arrows indicate typical discontinuities observed in the SiC deposit; 1000°C, 30 kPa, $\alpha \sim 10$ and $Q_{H_2} = 300 \text{ ml min}^{-1}$ . ....	169
Figure 4-45. Layer of Si-O was formed between the fibre and the matrix. Very fine and acicular crystallites growth was observed on the Si-O layer during the first stage of the CVI. ....	170
Figure 4-46. Layers of Si-O were formed on the growing SiC matrix each time the CVI process was stopped to allow the mass gain to be measured. The zig-zag morphology observed was due the angular termination of SiC crystallites. ....	170
Figure 4-47. (a) Residual nanoporosity due to the imperfect merging of the matrix growing in opposite directions from two adjacent fibres; (b) the nanoporosity has a typical size of $\sim 70 \text{ nm}$ . ....	171
Figure 4-48. Growth model of the SiC matrix on ZMI Tyranno SiC fibres. ....	172
Figure 4-49. Schematic of the (a) different morphology as function of temperature and pressure, (b) stoichiometry, (c) crystallite orientation and (d) size in the temperature interval 900-1000°C.....	173

---

Figure 4-50. Optical microscopy images of the deposition pattern of SiC preforms infiltrated for 8 hours (stopped at interval of 2, 4 and 8 hours) at different temperatures, (a) 900°C, (b) 950°C and (c) 1000°C; 30 kPa, $\alpha \sim 10$ and $Q_{H_2} = 300 \text{ ml min}^{-1}$ . .....	174
Figure 4-51. SEM-BSE images of the state of the intratow infiltration at different location in preform infiltrated for 8 hours at 900°C, 30 kPa, $\alpha \sim 10$ and $Q_{H_2} = 300 \text{ ml min}^{-1}$ . .....	175
Figure 4-52. SEM-BSE images of the state of the intratow infiltration at different location in preform infiltrated for 8 hours at 950°C, 30 kPa, $\alpha \sim 10$ and $Q_{H_2} = 300 \text{ ml min}^{-1}$ . .....	176
Figure 4-53. SEM-BSE images of the state of the intratow over the thickness at 0 mm from the centre in preform infiltrated for 8 hours at 950°C, 30 kPa, $\alpha \sim 10$ and $Q_{H_2} = 300 \text{ ml min}^{-1}$ . .....	177
Figure 4-54. SEM-BSE images of the state of the intratow infiltration at different location in preform infiltrated for 8 hours at 1000°C, 30 kPa, $\alpha \sim 10$ and $Q_{H_2} = 300 \text{ ml min}^{-1}$ . .....	178
Figure 4-55. SEM-BSE images of the state of the infiltration in the preforms infiltrated at 950 and 1000°C at 20 mm from the centre and at different locations over the thickness. ....	179
Figure 4-56. SEM-BSE images of the side of the preform showing an infiltrated layer of powder adjacent to the SiC fibres. ....	180
Figure 4-57. SEM-SEI image showing the initiation of the tows merging in a preform infiltrated for 8 hours at 1000°C, 30 kPa, $\alpha \sim 10$ and $Q_{H_2} = 300 \text{ ml min}^{-1}$ . .....	181
Figure 4-58. Optical microscopy imaged of the deposition pattern of SiC preforms infiltrated for 8 hours (stopped at intervals of 2, 2 and 4 hours) at different pressure; 900°C, $\alpha \sim 10$ and $Q_{H_2} = 300 \text{ ml min}^{-1}$ . .....	182

---

Figure 4-59. SEM-BSE images showing the details of the state of the intratow infiltration at different locations in the range 0-10 mm from the centre; preform infiltrated for 8 hours at 900°C, 50 kPa, $\alpha \sim 10$ and $Q_{H_2} = 300 \text{ ml min}^{-1}$ .....	183
Figure 4-60. SEM-BSE images showing the details of the state of the intratow infiltration at different locations in the range 15-25 mm from the centre; preform infiltrated for 8 hours at 900°C, 50 kPa, $\alpha \sim 10$ and $Q_{H_2} = 300 \text{ ml min}^{-1}$ .....	184
Figure 4-61. Reconstruction of different locations from the centre of the entire thickness of the preform infiltrated for 8 hours at 900°C, 50 kPa, $\alpha \sim 10$ and $Q_{H_2} = 300 \text{ ml min}^{-1}$ .....	185
Figure 4-62. Optical microscopy image of the SiC preform infiltrated for 4 hours at 950°C and 50 kPa.....	186
Figure 4-63. Optical microscopy image of the SiC preform infiltrated for 4 hours at 950°C and 70 kPa.....	186
Figure 4-64. SEM-BSE images showing the details of the state of the infiltration at different location of a preform infiltrated for 8 hours at 1000°C, 70 kPa, $\alpha \sim 10$ and $Q_{H_2} = 300 \text{ ml min}^{-1}$ .....	188
Figure 4-65. SEM images of the infiltration of a powder layer between the tow (a) and (b); (c) microporosity due to the incomplete merging of the matrix growth on the SiC powder; (d) and (e) penetration of the powder within the tow and incomplete infiltration; (f) some SiC particles were not coated by CVI. Micrograph (a) was obtained in backscattered electron mode whilst micrographs from (b) to (f) in secondary electron mode.....	190
Figure 4-66. SEM-BSE imaged showing the reduction of intertow spacing because of the powder layer.....	191
Figure 4-67. Dielectric permittivity of silicon carbide fibres Tyranno ZMI as function of the temperature; (a) is the real part and (b) the imaginary part. ....	193

---

Figure 4-68. Dielectric permittivity of three commercial available silicon carbide powders with different particle size (D50); (a) is the real part and (b) is the imaginary part. ....	194
Figure 4-69. Comparison of the dielectric permittivity of the single constituents of a SiCf/SiC preform; (a) and (b) the real and imaginary parts. ....	195
Figure 4-70. Variations of the half-power penetration depth as a function of the temperature for the single constituents of a SiCf/SiC preform. ....	196
Figure 4-71. Microwave power required to heat a SiCf/SiC preform up to the setpoint temperature. Preform consisted of a stack of twenty 51 mm-diameter discs; the hydrogen flow rate was 300 ml min <sup>-1</sup> . ....	197
Figure 4-72. (a) Heating behaviour and (b) microwave power variation for a standard 20-layer sample during a MECVI process. The fluctuations of forward power are due to the control unit when the setpoint temperature was reached. ....	198
Figure 4-73. Microwave power increase as the infiltration process proceeds for 8 hours. ....	199
Figure 4-74. Variation of the temperature difference $\Delta T_{CE}$ between the centre of the surface of the preform and the side surface distant 25 mm from the centre. ....	200

---

## List of tables

Table 1. Some properties of advanced ceramics and comparison with stainless steel [26-28] .....	5
Table 2. Physical, mechanical and thermal properties of SiC [25]. .....	16
Table 3. Physical, mechanical and thermal properties of the commercially available SiC fibres [73, 85, 86]. .....	30
Table 4. Properties of SiC <sub>f</sub> /SiC composites. ....	32
Table 5. Benefits and drawbacks of several methods for fabrication of FRCMCs .....	44
Table 6. Fabrication of SiC <sub>f</sub> /SiC composites by different techniques.....	45
Table 7. Precursor gases and temperature for the deposition of some ceramic matrices. ....	48
Table 8. Chemical vapour infiltration variants. Adapted from [11]. .....	50
Table 9. SiC deposition by several CVI routes.....	53
Table 10. Combination of PIP and CVI for SiC <sub>f</sub> /SiC fabrication .....	56
Table 11. Resistivity and skin depth of some silicon-based materials. Adapted from [11] and [296]. .....	78
Table 12. Experimental achievements of MECVI.....	86
Table 13. List of the preforms infiltrated with MTS/H <sub>2</sub> including the dimensions and the parameters of infiltration.....	102
Table 14. Parameters and dimensionless numbers describing transport phenomena in CVD/CVI.....	133
Table 15. Estimation of the Peclet number for intratow and intertow porosities in different conditions of temperature and pressure (Q <sub>H<sub>2</sub></sub> = 300 ml min <sup>-1</sup> ). .....	134

---

Table 16. Estimation of Damkohler numbers under different conditions of temperature and pressure.....	136
Table 17. Raman frequencies of the principal cubic and hexagonal polytypes of silicon carbide. Adapted from [352] and [353]......	159
Table 18. Molecular diffusivity $D_m$ and $D_{eff}$ of the mixture MTS/H <sub>2</sub> as function of pressure and temperature.....	212

---

# List of symbols

$\alpha$ gas flow ratio ( $Q_{H_2}/Q_{MTS}$ )	$\varepsilon'$ real part of the dielectric permittivity
$\alpha_s$ thermal diffusivity ( $m^2 s^{-1}$ )	$\varepsilon''$ imaginary part of the dielectric permittivity
$A_d$ available deposition area ( $m^2$ )	$\varepsilon_0$ vacuum electric permittivity ( $8.8542 \times 10^{-12} F m^{-1}$ )
$A_t$ cross sectional area ( $m^2$ )	$\varepsilon_r$ relative permittivity
$\beta$ thermal runaway factor	$\varepsilon_p$ porosity fraction (%)
$c$ speed of light ( $299792458 m s^{-1}$ )	$\eta_g$ relative volume sample/cavity
$c_p$ thermal capacity ( $J kg^{-1} K^{-1}$ )	$\eta$ MTS-SiC yield (%)
$D_{eff}$ effective diffusivity ( $m^2 s^{-1}$ )	$f$ frequency ( $s^{-1}$ )
$D_m$ Fick's diffusivity ( $m^2 s^{-1}$ )	$f_{ut}$ frequency of the sample holder ( $s^{-1}$ )
$D_K$ Knudsen's diffusivity ( $m^2 s^{-1}$ )	$f_{uts}$ frequency of the specimen in the sample holder ( $s^{-1}$ )
$D$ penetration depth (mm)	$f_{u0}$ frequency of the empty cavity ( $s^{-1}$ )
$Da_I$ Damkohler number I	$\Delta f$ shift of frequency ( $s^{-1}$ )
$Da_{II}$ Damkohler number II	$\Phi$ diameter (mm)
$d_p$ pore diameter ( $\mu m$ )	$G_{SiC}$ matrix growth rate ( $mol m^2 s^{-1}$ )
$E$ Young's modulus (GPa)	$G_{SiC(0)}$ initial matrix growth rate ( $mol m^2 s^{-1}$ )
$\mathbf{E}$ electric field vector	$\mathbf{H}$ magnetic field vector
$E_a$ activation energy ( $J mol^{-1}$ )	$\mathbf{J}$ electric current density vector
$E_0$ acceleration voltage (kV)	
$E_c$ critical excitation voltage (kV)	
$\varepsilon$ complex electric permeability ( $F m^{-1}$ )	

---

$j$ irradiance	$n_{O_2}^{res}$ residual amount of oxygen (mol)
$k_s$ thermal conductivity ( $W m^{-1} K^{-1}$ )	$\omega$ angular frequency ( $rad s^{-1}$ )
$k_r$ reaction rate ( $m s^{-1}$ )	$P$ pressure
$k_{ins}$ thermal conductivity insulation ( $W m^{-1} K^{-1}$ )	$P_0$ atmospheric pressure (101 kPa)
$K_{IC}$ fracture toughness ( $MPa m^{-1/2}$ )	$Pe$ peclet number
$\Delta m_m$ mass gain (mg)	$Q_{MTS}$ methyltrichlorosilane flow rate ( $ml min^{-1}$ )
$\Delta m_{MTS}$ mass of MTS consumed	$Q_{H_2}$ hydrogen flow rate ( $ml min^{-1}$ )
$L$ thickness (mm)	$Q_t$ total flow rate ( $ml min^{-1}$ )
$L_{O_2}$ leak rate ( $mol min^{-1}$ )	$Q$ Q factor
$\Lambda_s$ length scale of the sample (mm)	$Q_{ut}$ Q factor sample holder
$M_{SiC}$ molar mass of SiC ( $g mol^{-1}$ )	$Q_{uts}$ Q factor of the specimen in the sample holder
$M_{MTS}$ molar mass of MTS ( $g mol^{-1}$ )	$Q_{u0}$ Q factor empty cavity
$m_f$ mass fibrous preform (g)	$R_s$ spatial resolution ( $\mu m$ )
$\mu$ magnetic permeability	$Re$ Reynolds number
$\mu'$ real part pf magnetic permeability	$r_H$ hydraulic radius (m)
$\mu''$ imaginary part of magnetic permeability	$\rho$ electric resistivity ( $\Omega m$ )
$\mu_0$ vacuum magnetic permeability ( $4\pi \times 10^{-7} H m^{-1}$ )	$\rho_s$ sample density ( $g cm^{-3}$ )
$\mu_v$ viscosity (Pa s)	$\rho_r$ relative density (%)
$N$ depolarisation factor	$\Psi$ effectiveness of the active species (%)
$n_{MTS}$ MTS feed (mol)	$\mathbf{S}$ Poynting's vector
$n_{O_2}^i$ initial amount of oxygen	$S_A$ specific surface area ( $m^2 g^{-1}$ )

---

$\sigma_e$ electric conductivity (S m <sup>-1</sup> )	$\tau_{ins}$ equalisation time of insulation (s)
$\sigma_{eff}$ dielectric conductivity (S m <sup>-1</sup> )	$\tau_T$ characteristic heating time (s)
$\sigma_u$ rupture stress (MPa)	$\tan\delta$ loss tangent
$\sigma_{elastic}$ elastic limit stress (MPa)	$\theta$ Thiele number
$\sigma_B$ Boltzmann constant	$v$ gas velocity (m s <sup>-1</sup> )
$t_i$ infiltration time (min)	$v_p$ gas pore velocity (m s <sup>-1</sup> )
$t_0$ backfill time (s)	$V_f$ volume fraction (%)
$T$ temperature (°C)	$V_B$ breakdown voltage (V)
$T_0$ room temperature (25°C)	$\xi$ tortuosity factor
$\Delta T_{CE}$ temperature difference centre-edge of the prform (°C)	$X$ x-ray penetration depth (μm)
$\tau$ pore residence time (s)	$\chi_s$ thermal diffusivity (m <sup>2</sup> s <sup>-1</sup> )
$\tau_s$ equalisation time of sample(s)	$\chi_{ins}$ thermal diffusivity insulation (m <sup>2</sup> s <sup>-1</sup> )
	$w$ absorbed microwave energy (J)

---

# Glossary

<b>Tow</b>	Bundle of untwisted continuous fibres
<b>Fabric</b>	Cloth produced by weaving fibres
<b>Preform</b>	Three-dimensional fabric forms. They can be designed to have a specific shape for structural and/or functional requirements.
<b>Intratow porosity</b>	Porosity between the fibres within the tow
<b>Intertow porosity</b>	Porosity between tows of fibres
<b>Precursor</b>	A substance that participates in a chemical reaction that produces another compound
<b>Deposition</b>	Process in which a gaseous precursor(s) react/decompose on the substrate surface yielding a solid material
<b>Infiltration</b>	Deposition of material within a porous preform using chemical vapour infiltration

# 1 Introduction

Continuous fibre reinforced ceramic matrix composites (FRCMCs) offer excellent high temperature mechanical properties and overcome the limitations associated with technical conventional ceramics, such as brittle failure and low flaw tolerance [1-4].

In the last decades, their needs have resulted in the development of numerous fabrication processes [5, 6]. Low temperature and pressure processes are required to preserve the physical integrity of the fibres and to avoid thermal damages which could result in reduced performance and reliability of the reinforcement. In this direction, although other manufacturing processes are available, chemical vapour infiltration (CVI) has enormous potential for the processing of FRCMCs [7-13] It also benefits from its near-net shape capability and microstructural control. However, long processing time, up to several months, and hence increased cost, represent a major drawback. Isothermal isobaric CVI can result in non-uniform densified composites since the deposition of the matrix material occurs preferentially at the outer surfaces [7]. This generates the premature blockage of the surface channels which prevents the gaseous reagents from penetrating to the centre of the preform. Consequently, a high residual porosity is located in the centre of the preform, deleteriously affecting the final mechanical properties [7].

The use of temperature and pressure gradients can address this issue, but to only a certain extent and leading to several inconveniences. For example, thermal gradient forced-flow CVI can achieve higher density than isothermal isobaric CVI,

but the setup is more complex and some non-uniform densification patterns can still occur [7, 11, 14].

The search for efficient variants of CVI to yield rapid and complete densification is still ongoing and the use of microwave heating has been considered as promising [12, 15-17].

Microwave radiation can be used to generate a controllable inverse temperature profile during the heating of the fibrous ceramic preform [16, 18]. This permits the CVI to occur from the inside out with consequently more homogeneous and complete densification. Microwave enhanced CVI (MECVI) avoids pore closure and reduces the deposition time potentially from months to 48-72 hours [19-21].

This thesis reports the investigation of the basics of the deposition mechanism occurring in a MECVI process depositing SiC matrix within a silicon carbide Tyranno ZMI-based fibre preform. The objectives of the research programme were:

- to setup equipment capable of conducting MECVI experiments;
- to evaluate the kinetics of the SiC infiltration when using methyltrichlorosilane (MTS) and hydrogen, in parallel with the characterisation of the microstructure, morphology and stoichiometry of the deposited material on SiC fibres;
- to draw a state diagram of the morphology of the deposited SiC as function of the temperature and pressure;

- to evaluate the SiC matrix deposition pattern when varying the thermodynamic variables.

The thesis is divided into six chapters. Chapter 2 is dedicated to a review of the literature which is relevant to this work. This includes the interest in FRCMCs, the range of techniques available for the production of SiC<sub>r</sub>-SiC and the description of the different CVI processes with a specific focus on the use of the microwave heating. The experimental procedure is presented in Chapter 3. It is divided into three sections: the details of the MECVI system, the materials used and the procedure of infiltration and the characterisation techniques. The results and the discussion of the results of this project are presented in Chapter 4. The chapter begins by presenting some preliminary results on the thermodynamics of the thermal decomposition of MTS and role of the oxygen in the reaction. Then, a detailed study of the kinetics, microstructure and morphology of the deposited matrix as function of the main thermodynamic variables follows. Characterisation includes cross-section scanning electron microscopy (SEM), energy and wavelength dispersive spectroscopy (EDS and WDS), transmission electron microscopy (TEM), Raman spectroscopy, and measurements of the dielectric permittivity. Subsequently, the analysis of the deposition patterns for different conditions of temperature and pressure and the role of the dielectric properties are presented. Conclusions from the work are drawn in Chapter 5 in parallel with an outline of the areas where further research can be carried out in order to prove the effectiveness of the MECVI on a pre-pilot line.

## 2 Literature survey

### 2.1 Advanced structural ceramics

The most widely accepted definition of ceramics is that they are inorganic, non-metallic materials made from compounds consisting of metals and non-metal. Ceramics can be divided into two groups: traditional ceramics including clay, silicate glasses and cements and advanced ceramics such as carbides, borides, nitrides, pure oxides ( $\text{Al}_2\text{O}_3$ ,  $\text{ZrO}_2$ ,  $\text{Y}_2\text{O}_3$  and  $\text{ThO}_2$ ) and many other non-silicates.

Advanced structural ceramics offer a wide range of desirable properties which means that they are extensively used for a diverse range of applications, for example:

- Aerospace: thermal protection systems in rocket exhaust cones, thermal barrier coatings, insulating tiles for the space shuttle, engine components, combustion liners, shrouds, windshield glass.
- Automotive: spark and glow plugs, catalytic converters, ceramic filters, fuel injection systems, valves, airbag sensors, knocking and parking distance sensors, thermistors, vibration sensors, oxygen sensors, glass windshields, piston rings, brake pads, PTC heaters.
- Medical (bio-ceramics): orthopaedic joint replacement, prosthesis, dental restoration, bone implants.
- Military: ballistic vests, armour, heat shield and thermal barriers, leading edges, nozzle throats, nose cones.
- Energy: nuclear fuel cladding, nuclear fuel, neutron absorbers, SOFCs, vortex hydrocyclones, metering valves.

## Chapter 2. Literature survey

Overall, it can be said that advanced ceramics exhibit high refractoriness, hardness and wear resistance, good chemical inertness and high temperature mechanical performance. In Table 1 are displayed some mechanical and thermal properties of advanced ceramics [1, 22-25]. It should be noted that whilst many of these properties are extremely useful, monolithic ceramics suffer from relatively low fracture toughness.

Table 1. Some properties of advanced ceramics and comparison with stainless steel [26-28] .

	Density /g cm <sup>-3</sup>	Melting / °C	Young modulus / GPa	Strength / MPa	Hardness / GPa	Toughness / MPa m <sup>1/2</sup>	Thermal conductivity / W m <sup>-1</sup> K <sup>-1</sup>
Al <sub>2</sub> O <sub>3</sub>	3.95 - 4.1	2072	300	330-550	12-14	3.5 - 4.5	30
ZrO <sub>2</sub>	5.5 - 5.68	2725	210	400 - 900 (TZP- TTZ)	12-13	10.0-13.0	1-4
Si <sub>3</sub> N <sub>4</sub>	3.2	1900 (sublimation)	310	370-500	16	6.1	10-30
B <sub>4</sub> C	2.52	3036	460	250	35	<3	20-50
TiC	4.94	~3000	451	258	30	2-4	110
SiC	3.21	~2700 (sublimation)	415	359-500	32	4.0	26.3
HfC	12.76	3900	510	333	23	1.8	30
WC	15.63	2827	550	345	17-24	28	84
TaC	14.5	~3850	560	340	25	4-5	180
ZrB <sub>2</sub>	6.09	3245	490-500	380	21-28	3.7	45-130
TiB <sub>2</sub>	4.52	3225	551	370	33	5	60-120
HfB <sub>2</sub>	11.19	3380	450-530	480	21-28	3.5-4.5	70
Diamond	3.5	Not at atm pressure	> 1 GPa	--	115	--	600-2000
Stainless Steel 304	8.00	1400-1500	200	505 (ultimate)	1.3	Up to 50	16.2

## 2.2 Ceramic Matrix Composites (CMCs)

When monolithic ceramics fail under mechanical or thermo-mechanical constraints, they tend to fracture catastrophically, because of cracks promoted by

defects and voids. This brittleness and lack of plasticity before failure, unlike in metals and alloys, partially limits their use as structural materials.

Better mechanical performance can be achieved if a second phase (particles, whiskers\*, platelets, chopped or continuous fibres) is embedded into the matrix material [3]. These materials are called composites and if the matrix is a ceramic then they are called ceramic matrix composites (CMCs). For polymer and metal matrix composites, the primary goal is to increase the elastic modulus compared to the matrix material, for CMCs the goal is to enhance the fracture toughness.

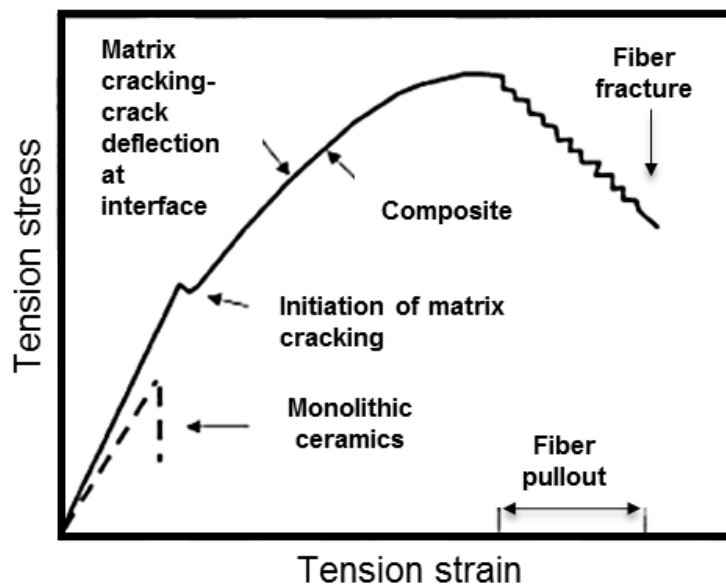


Figure 2-1. Stress-strain curves for a ceramic matrix composites and a related monolithic ceramic [5].

According to the theory of fracture mechanics, a secondary phase dissipates the energy associated with crack propagation, resulting in a tougher material. Some of the main energy-dissipating mechanisms are listed and illustrated below

---

\* SiC whiskers seem to constitute a major airborne health hazard [29, 30].

### Crack bowing

Dispersed particles and voids can pin the crack front and impede the crack motion, this is known as crack bowing [31].

### Crack bridging

An existing initial flaw in the brittle matrix would propagate and, because of stress concentration around the inclusions, would encircle the unbroken inclusions. The inclusions would act as bridges between the opposing faces of the crack. This prevents a further crack opening until the inclusion stretch reaches a critical value [32, 33].

### 2<sup>nd</sup> phase – matrix thermal expansion mismatch toughening

Local residual stresses in the vicinity of the secondary phases, due to the mismatch between the linear thermal coefficients during cooling after fabrication, can provoke crack deflection. Systems such as TiC-SiC and ZrB<sub>2</sub>-SiC (see Figure 2-2) have been widely explored in this context [34-36].

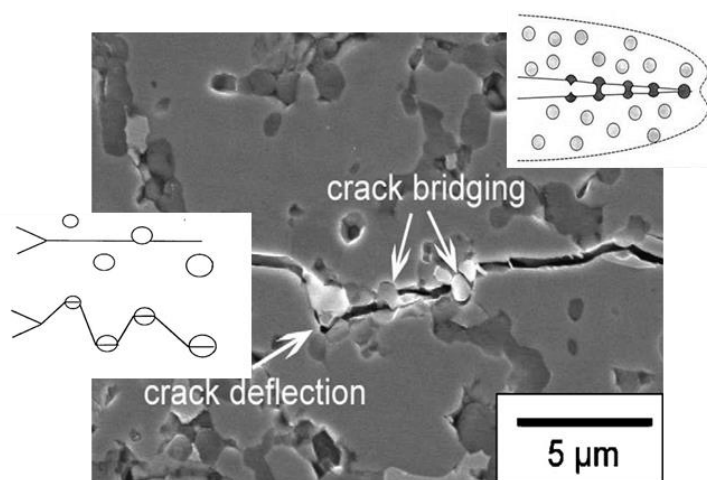


Figure 2-2. Crack deflection and crack bridging in ZrB<sub>2</sub>-SiC composite. Adapted from [37].

### Phase transformation toughening

In zirconia-stabilised systems [38], if sufficient quantities of the metastable tetragonal phase is present, then an applied stress, magnified by the stress concentration at a crack tip, can cause the tetragonal phase to transform into monoclinic, with the associated volume expansion. This phase transformation can then put the crack into compression, retarding its growth, and enhancing the fracture toughness [27], as shown in Figure 2-3.

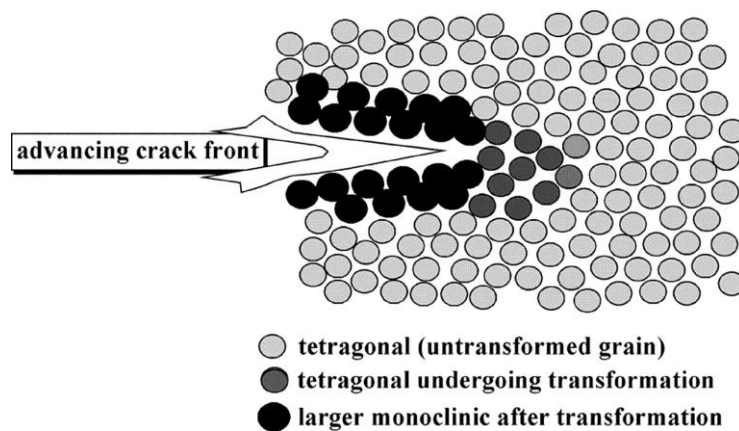


Figure 2-3. Transformation toughening of tetragonal zirconia to monoclinic system [39].

### Interface delamination and fibre pull-out

High fracture energy is achieved by introducing a weak interface between the matrix and the reinforcing phase [4, 40-42]. The main energy-absorbing mechanism is the pulling out of the fibre from their sockets in the matrix during crack advance. For instance, pyrolytic carbon (PyC) and boron nitride (BN) have both been successfully used to achieve weak interfaces in SiC fibres – SiC matrix composites [42-44].

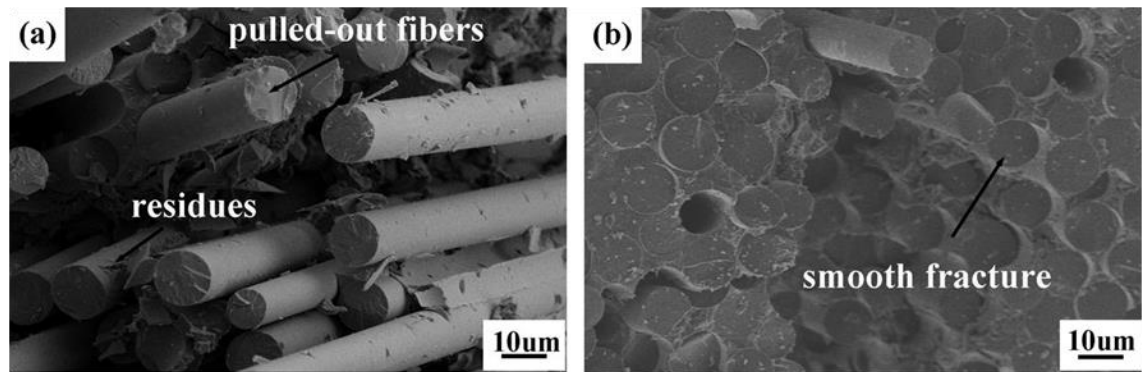


Figure 2-4. Comparison of a fracture surface of a SiC<sub>f</sub>-SiC composite with (a) and without (b) fibre pull-out. Adapted from [45].

## 2.3 Fibre-reinforced ceramic matrix composites (FRCMCs)

### 2.3.1 Interest in and properties of FRCMCs

CMCs with a fibrous reinforcing phase are defined as fibre-reinforced ceramic matrix composites (FRCMCs). Whilst the mechanical improvements due to the integration of whiskers and chopped fibres in ceramic matrices are somewhat limited, the incorporation of long multi-strand fibres has resulted so far in [46-51]:

- Elongation to rupture above 0.5%
- Fracture toughness values as high as  $\sim 40 \text{ MPa m}^{1/2}$
- Strength retention up to the service temperature
- Dynamical load capability

The commercially available FRCMCs are made with carbon, silicon carbide, alumina or mullite fibres [6, 12, 52-58]. The matrices deposited are commonly carbon (for C<sub>f</sub>/C), silicon carbide (for C<sub>f</sub>/SiC and SiC<sub>f</sub>/SiC) and alumina (for oxide-fibrous composites).

Components made of CMCs instead of metal alloys allow the turbine engines of aircraft and power plants to operate more efficiently at higher temperatures,

combusting fuel more completely and reducing pollutant quantities [6, 55, 56]. Figure 2-5 shows the selection of materials on the basis of the maximum temperature service for aerospace applications. C<sub>f</sub>/C composites provide excellent performance due to their thermo-mechanical characteristics; they are produced mainly by pyrolysis of an organic matrix or by chemical vapour infiltration C<sub>f</sub>/C [12]. In terms of performance, they offer a 60% weight saving compared to the traditional steel [59] and for this reason they found applications in lightweight brakes. In 1973, Dunlop, using chemical vapour infiltration, manufactured the brakes of the VC10 aircraft followed, a year later, by Concorde [12, 59]. Brembo, historically the leader in brake manufacture for Formula One, produced carbo-ceramic brakes, whilst Meggit Aircraft Braking System and HITCO supplies carbon-carbon brakes for military aircraft. Snecma Propulsion Solide with the Sepcarb™ and Honeywell Friction Materials with the Carbenix™ materials were also involved in the development of C<sub>f</sub>/C [12].

In order to improve the oxidation resistance and thus the application lifetime, research focused on using ceramics instead of the carbon as matrix [7, 58, 60].

For instance, silicon carbide is suitable as a matrix due to its high oxidation resistance and superior temperature stability [61]. The C<sub>f</sub>/SiC system has been widely explored [58, 60] and revealed also as having outstanding mechanical properties such as a value of fracture toughness of 22 MPa m<sup>1/2</sup>, an elongation to rupture of 0.75% and a tensile strength of 475 MPa [58, 62].

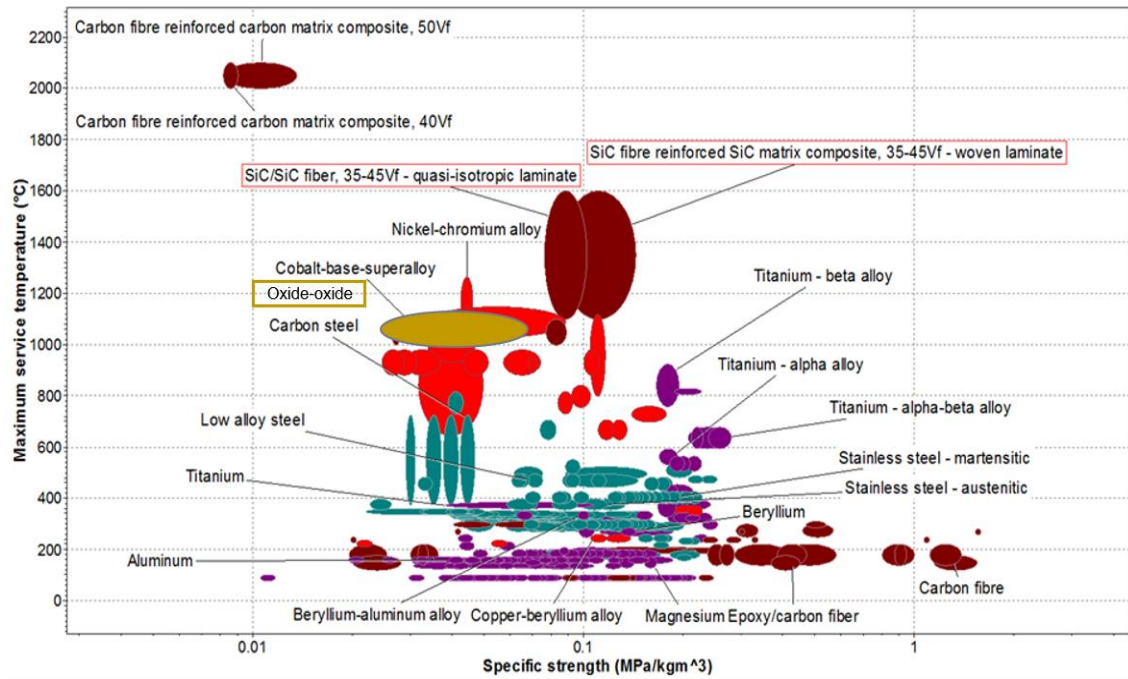


Figure 2-5. Ashby diagram of the specific strength against the maximum service temperature of materials for aerospace applications<sup>†</sup>.

The appealing performance of the C<sub>f</sub>/SiC attracted the attention of NASA; the nose cap of the hot structures of the NASA X-38, which was planned to serve as the technology carrier for a new Crew Return Vehicle (CRV) for the International Space Station [63], is made of C/C-SiC composites derived from fabric preregs laid-up and cured using an autoclave technique

In oxygen-rich environments however, C<sub>f</sub> cannot withstand elevated temperature for long duration applications. Continuous silicon carbide fibre-reinforced ceramic matrix composites overcome the issue of the oxidation and the retention of the mechanical properties up to ~1300°C [6, 49, 64, 65]. Snecma Propulsion Solide for example [66] has developed a SiC<sub>f</sub>/SiC composite, called CeraSep. It was intended for nuclear applications, for instance the fuel cladding, and aeronautical applications such as aircraft brakes and nozzle flaps. The Societe Europeenne

<sup>†</sup> Data were extrapolated from the database of the software for material selection CES Selector, Granta design Ltd, Cambridge, UK.

de Propulsion (SEP) has produced a SiC<sub>f</sub>/SiC composite by chemical vapour infiltration [67, 68]. These 2D SiC fibre-reinforced laminates had a 10% of porosity and a flexural strength of 300 MPa, which decreased above 1300°C; no degradation was observed after 500 h at 1100°C in air and it displayed a toughness of 25 MPa m<sup>1/2</sup> [67, 68].

More recently, prompted by a pluridecennial US Department Of Energy programme, CFM International, a joint company of Safran Aircraft Engines and GE, has begun manufacturing the LEAP engine, which is the first widely deployed CMC-containing product [55, 56]. The SiC-SiC turbine shroud lining of the LEAP engine is able to withstand temperatures of 1315°C (2400°F) resulting in 15% savings of fuel. In August 2017, LEAP started being equipped on Airbus A320neo. Other LEAP engines will fly on Boeing 737Max. Figure 2-6 shows the LEAP engine with the CMC inserts.

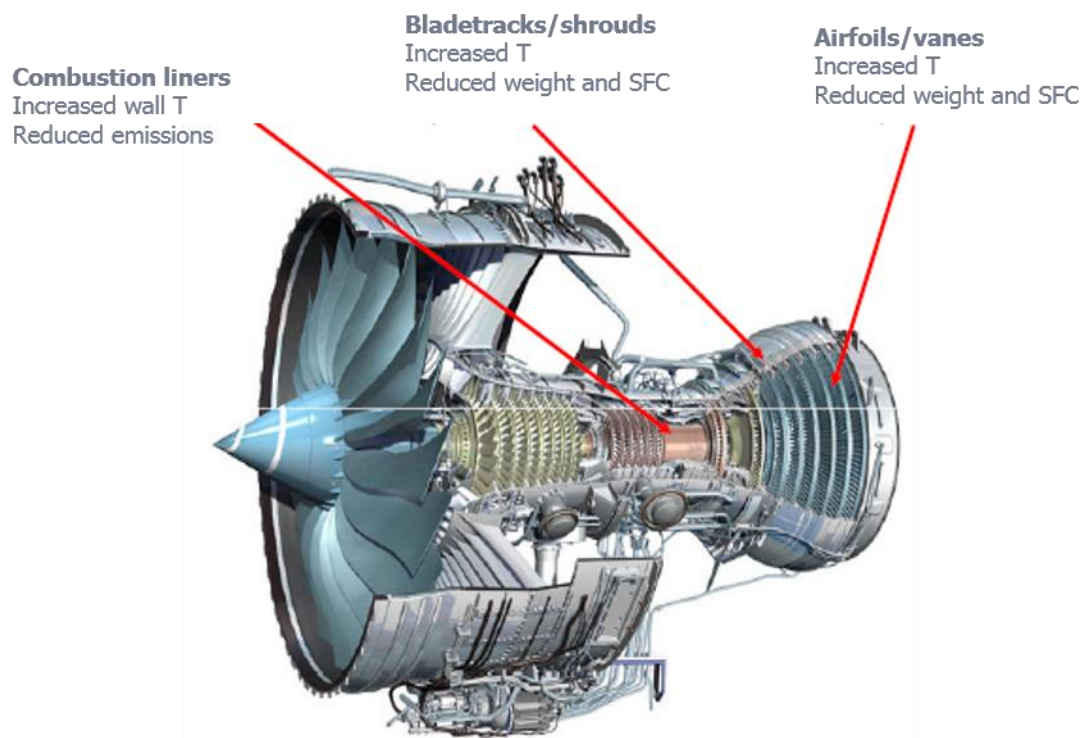


Figure 2-6. Drawing of the LEAP engine with the CMC inserts and their functions. Adapted from [69].

In 2019 GE will produce the series engine GE9X with 5 CMC parts- two combustion liners, two nozzles and one shroud [6, 70]. It appears clearly that the interest in FRCMCs application is still growing because of the new road map for cutting the emissions of internal combustion engines [71].

According to some cost analysis predictions [70], CMC inserts reduce the fuel cost per hour of flight from \$3,326 to \$2,827.

This technological interest also reflects the trend of the global market: according to a recent report [57] *“the ceramic matrix composites market is projected to reach USD 7.51 Billion by 2026, growing at a CAGR of 9.65%, from 2016 to 2026. The demand for light weight and high-performance ceramic matrix composites in automotive and aerospace & defence applications is propelled by the regulatory norms emphasizing on the use of light weight and fuel efficient materials”*.

It is also worth mentioning that oxide fibres including glass, mullite, zirconia and alumina are also used in CMCs.  $\alpha$ -Al<sub>2</sub>O<sub>3</sub> fibres were manufactured by Du Pont as early as 1979. Subsequently, 3M Co. in the USA produced Nextel 610 fibres, with a tensile strength of 2.4 GPa and a Young's modulus of 330 GPa [72, 73] With Nextel 720 consisting of  $\alpha$ -Al<sub>2</sub>O<sub>3</sub> and mullite [74], the high temperature performance and creep resistance improved. COI Ceramics Inc. (San Diego, USA) manufactures combustor and exhaust systems on Boeing 787 aircraft [6, 75] and Axiom Materials Inc. (Santa Ana, USA) supplies prepregs of Nextel 610 and 720 fibres and an aluminosilicate matrix [76]. Composites Horizons (Covina, USA) manufactures mixer and centre body assemblies for civil jets [55]. Nevertheless, oxide CMCs generally display inferior creep resistance compared to non-oxide CMCs, which could limit their use as structural components [43].

The fabrication methods of a composite structure are generally based on the densification of a porous, fibrous body, varying from 10 to 80% of theoretical density, known as a *preform*. They can be fabricated by the weaving of continuous fibres, needle-punching of fibrous mats, or by embedding chopped fibres in resins.

### 2.3.2 SiC<sub>f</sub>/SiC system

#### 2.3.2.1 Introduction to silicon carbide

Silicon carbide, SiC, also known as carborundum, is the most widely used non-oxide ceramic. It occurs in nature as moissanite, but this is extremely rare so all available commercially SiC is synthetic. Several manufacturing processes can be used to synthesise SiC [77]; the Acheson process (1896) combines silica and carbon in a graphite electric resistance furnace between 1600 and 2500°C. High-quality SiC can be produced by the sublimation of SiC powder in an argon furnace at 2500-2700°C and redeposition of flake-like single crystals (Lely process, 1955). Seeded sublimation growth (1978), otherwise known as the physical vapour transport method (PVT), can be also used [78]. This method uses a high quality seed crystal surface to begin the growth process, whereas in the Lely process, growth begins on a graphite membrane. Other vapour phase growth method of SiC production includes high-temperature chemical vapour deposition (HT-CVD) which consists of the deposition of SiC from the reaction of silane (e.g. SiH<sub>4</sub>) with a carbon source such as methane or propane. In halide-CVD (HCVD), the SiC is grown from the decomposition of a carborosilane such as methyltrichlorosilane or from the reaction of chlorinated Si precursor (e.g. SiCl<sub>4</sub>, H<sub>2</sub>SiCl<sub>2</sub>, HSiCl<sub>3</sub>) with a carbon precursor (methane or propane) [25, 79]. Silicon

carbide can be grown by liquid phase epitaxy (LPE) [80]. On a substrate surface, a film of melt of silicon reacts with a carbon source and generates a thin film of silicon carbide. The thermal decomposition of polymers such as poly(methylsilyne) in inert atmospheres and at relatively low temperature [81] can also be used.

SiC exhibits polytypism, which is a special type of polymorphism occurring in layered materials when the geometry of a repeating structural layer is maintained but the layer stacking sequence of the overall crystal structure varies. According to Cheung [82], more than 250 different crystalline structures of SiC have been identified. Two main families of crystalline arrangement of SiC can be identified:  $\alpha$ -SiC and  $\beta$ -SiC.  $\alpha$ -SiC is formed at temperatures greater than 1700°C and has a hexagonal crystal structure similar to wurtzite [25]. It is the most commonly encountered form of SiC; some of the most common hexagonal polytypes are 2H, 4H, 6H and 8H-SiC.  $\beta$ -SiC has a cubic structure similar to the zinc blende and is formed at temperatures below 1700°C [25]. There is only one cubic SiC polytypes, known as 3C-SiC. It is also worth mentioning the rhombohedral crystalline structures, labelled with R, e.g. 15R. Silicon carbide does not melt at any known pressure rather it sublimates at 2700°C at atmospheric pressure. The ceramic has a low coefficient of thermal expansion ranging from 4.0 to  $4.8 \times 10^{-6}$  K<sup>-1</sup>. Table 2 reports some typical physical, mechanical and thermal properties of SiC.

Table 2. Physical, mechanical and thermal properties of SiC [25].

Property	Value
Density / g cm <sup>-3</sup>	3.21
Molar mass / g mol <sup>-1</sup>	40.1
Lattice	3C, (zinc blend crystalline structure) 2H, 4H, 6H (hexagonal crystalline structure)
Lattice constant / Å	$\beta$ -SiC 3C: 4.3596  $\alpha$ -SiC 2H: 3.073, 5.048 4H: 3.073, 10.053 6H: 3.073, 15.110
Electron mobility / cm <sup>2</sup> V <sup>-1</sup> s <sup>-1</sup>	900
Band gap /eV	2.36 (cubic) 3.05 (hexagonal)
Temperature of melting / °C	Decompose at ~2700
Thermal conductivity / W m <sup>-1</sup> K <sup>-1</sup>	26.3
Specific heat capacity (at 0°C) / J kg <sup>-1</sup> K <sup>-1</sup>	820
Young Modulus / GPa	415
Strength / MPa	Up to 550
Hardness / GPa	32
Fracture toughness / MPa m <sup>1/2</sup>	4.0

### 2.3.2.2 Silicon carbide fibres

The early development of SiC fibres occurred in the 1970s [83]. Since then, they have been continuously developed and improved [84]. The method of fabrication greatly affects the chemical composition and final microstructure of the fibres and hence their thermo-mechanical performance.

Two different approaches are available commercially to prepare SiC fibres [73]:

- Chemical vapour deposition (CVD). A layer of SiC from a gaseous precursor such as methyltrichlorosilane is deposited on a continuous core filament. The family of SCS fibres made by Speciality Materials consist of  $\beta$ -SiC on 33  $\mu\text{m}$  carbon filaments, whereas Sigma™ by Tisics uses tungsten wires. The external diameter of the CVD SiC fibres is typically 75-140  $\mu\text{m}$ . As a consequence they have low flexibility and cannot be woven.
- Preceramic polymer. This manufacturing process is similar to that of carbon fibres and is based on the melt or dry spinning of organic polymers. Today, many commercially available SiC fibres such as Nicalon™, Tyranno™ and Sylramic™ are obtained with this route using poly(organo)silanes and poly(organo)silazanes. A polymer with a high molecular weight, adequate viscoelasticity and thermal stability enables a stable melt spinning process to be used without breaking the filament [73, 85-88]. Subsequently, the green fibres are cured thermally or by electron beam irradiation. The last step involves the conversion of the spun polymer to ceramic fibres by pyrolysis [73, 85-88]. The diagram in Figure 2-7 shows the main step of the manufacturing process of SiC fibres from preceramic polymeric route. The microstructural, mechanical and thermal properties are dependent on the precise production conditions [86].

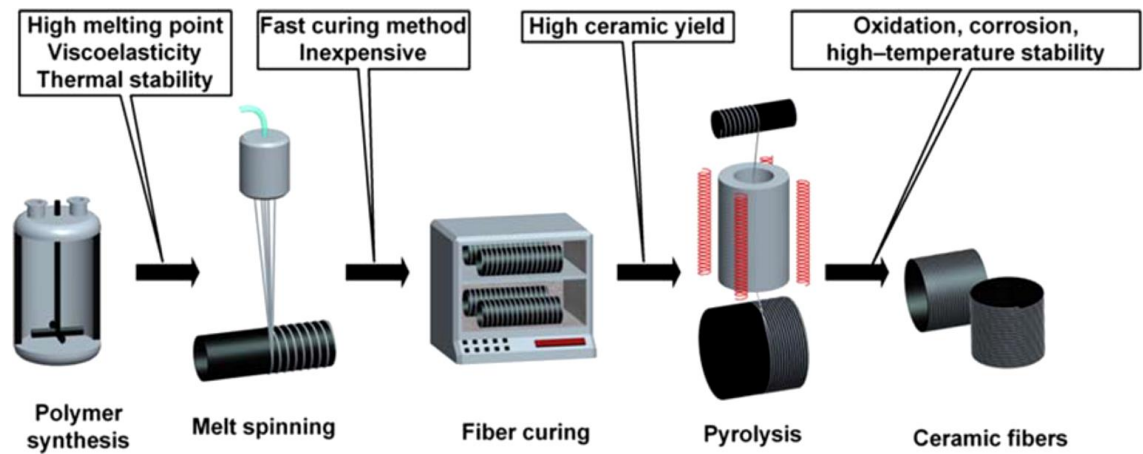


Figure 2-7. Manufacturing steps of the ceramic fibres from polymeric precursor route [73].

### 2.3.2.2.1 Effect of the microstructure on the mechanical and environmental performance of silicon carbide fibres

Oxygen is the key factor in controlling the microstructure, the mechanical performance and the environmental performance. In silicon carbide fibres the oxygen is present as intergranular amorphous (“glassy”) oxycarbide phase, Si-O-C. The amorphous phase is subject to viscous flow and, as the temperature increase, the viscosity falls [27, 89, 90]. For this reason, the Young’s modulus and creep resistance are greatly affected from the oxygen content. The main creep mechanism associated with the presence of the Si-O-C, involves the grain boundary sliding [27, 89, 90]. The amorphous phase is also responsible for the low thermal conductivity if compared to stoichiometric SiC.

Particle size is a major influencing factor on the creep resistance. In this case the mechanism is due to the diffusion, under the combined effect of temperature and applied load, of vacancies through grains (Nabarro-Herring creep) and along grain boundaries (Coble creep) [27, 89, 90]. The dependence of the creep rate

from the grain size is inverse-square for the Nabarro-Herring creep and inverse-cubic for the Coble creep. Diffusional flow can be also coupled with grain boundary sliding and this has been observed in SiC fibres [89]. It must be noted that the finer microstructure provides higher tensile strength (at room temperature) and reduces the thermal conductivity [25, 86].

Free carbon decreases the density and the oxidation resistance as it vaporises at temperature as low as 450°C [27, 91]. The effect of the carbon on creep is more complex. If it is in excess, and not totally dissolved in the Si-O-C network, the creep resistance increases [92].

The effect of impurities and dopants depends specifically on their nature. For instance, aluminium can be used as sintering aids and it increases the thermal conductivity and the creep rate [88, 93].

Depending on the amount of the amorphous phase, silicon carbide fibres have different performance in oxygen-rich and inert atmosphere. Regardless from the atmosphere, above 1200°C the Si-O-C phase suffers transformations such as SiC crystallisation and concomitant release of gases [88].

In inert atmospheres the amorphous Si-O-C phase decomposes and crystallizes to  $\beta$ -SiC. Alongside this, SiO and CO gases are also evolved and this is combined with an accelerated SiC crystal growth [73, 88, 94]. As a consequence, a steep drop in tensile strength and Young's modulus occurs [73].

In an oxidative environment, at high temperature a passivating layer of silica is observed on the surface of the fibres. This layer impedes the outgassing of SiO and CO and slow down the strength loss [73, 88]. It must be noted that if the heat

treatment in oxygen-rich atmosphere continues, the glassy phase decomposes and the oxidation becomes active with consequent degradation of the fibre.

### 2.3.2.2.2 SiC fibres from CVD

#### **Tisics Sigma™ fibres**

Tisics Sigma™ is a monofilament of tungsten (diameter of ~14 µm) coated with β-SiC and a final overcoat of carbon (~5 µm). The outer diameter ranges from 100 to 140 µm [95, 96]. These fibres are generally used for titanium matrix composites as a creep-retardant and stiffener [97]. Tisics produces also fibres with a duplex coating of titanium diboride (~1 µm) and pyrolytic graphite (~1 µm) [96].

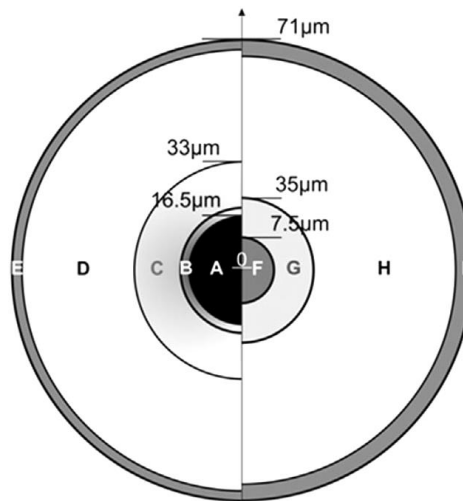
#### **SCS-6™ and SCS-Ultra™ fibres**

SCS fibre core is a ~33 µm carbon filament coated with a 1.5 µm layer of pyrolytic carbon. A second layer is made of a non-uniform silicon carbide with two regions: an inner carbon-rich silicon carbide (~16 µm thick) whilst the SiC is near-stoichiometric in the outer region. The fibre is then coated with an additional protective layer of duplex C-SiC coating (1.5-3.0 µm). The total diameter is between 140 - 150 µm and the tensile strength of 4 GPa is retained in inert atmosphere up to 1400°C [73]. They are designed for use in metal-matrix composites because they resist liquid-phase aluminium and titanium bonding processes. A further improvement of SCS fibre is SCS-Ultra [98]. The difference is in the distribution of the carbon excess, more localized around the core of the fibre, and in the much finer grain size of the stoichiometric silicon carbide (200 nm) [99]. The result is an improved tensile strength up to 5.0 GPa with an

excellent creep-rupture resistance; Materials Division at NASA Glenn Research Center [100] reported that SCS-Ultra is the most creep-rupture resistant fibre. A comparison between the microstructure of the SCS-6 fibres and the sigma fibres is shown in Figure 2-8.

### SCS-6 fibers

- A: Carbon core
- B: pyrolytic graphite coating
- C: carbon rich  $\beta$ -SiC grains
- D: near stoichiometric  $\beta$ -SiC grains
- E: carbon+SiC surface coating



### Sigma fibers

- F: Tungsten core
- G: carbon rich  $\beta$ -SiC grains
- H: near stoichiometric  $\beta$ -SiC grains
- I: turbostratic carbon surface coating

Figure 2-8. Microstructure of the CVD SiC fibres [73].

Despite their high performance, the large diameter of the CVD-SiC fibres limits their use because it is almost impossible to weave them and make complex parts; they are mainly used as unidirectional reinforcement.

### **2.3.2.2.3 SiC fibres from polymeric precursor**

Research and development have led to the commercialization of three generations of SiC fibres from polymeric precursor

Oxygen reduction was the guideline for the development of the second generation of SiC fibres (Hi-Nicalon and Tyranno ZMI). New precursor [85, 101] for Tyranno ZMI and electron beam curing [102] for Hi-Nicalon allowed having oxygen content respectively below 10 [101] and 1 wt% [103, 104]. Higher

production temperature was possible with formation of larger grains and hence, reduced creep rate (although lower tensile strength). Further improvement led to the third generation of SiC fibres (Hi-Nicalon Type S, Tyranno SA3, Sylramic, Sylramic i-BN). They are characterised by a low oxygen content and near-stoichiometric composition [73, 85, 86, 88, 105, 106]. Creep rate has been drastically reduced with  $\beta$ -SiC crystals of 200 nm (possible due to the higher temperature production above 1700°C). In this generation of fibres, sintering aids like aluminium for Tyranno SA3 [93] and boron for Sylramic [106] are incorporated in the fibre structure to form a dense fibre and/or to provide interfacial coating. The schematic in Figure 2-9 outlines the microstructure evolution of the three SiC fibre generations and Table 3 reports the properties of the commercially available SiC fibres from polymeric precursor and CVD.

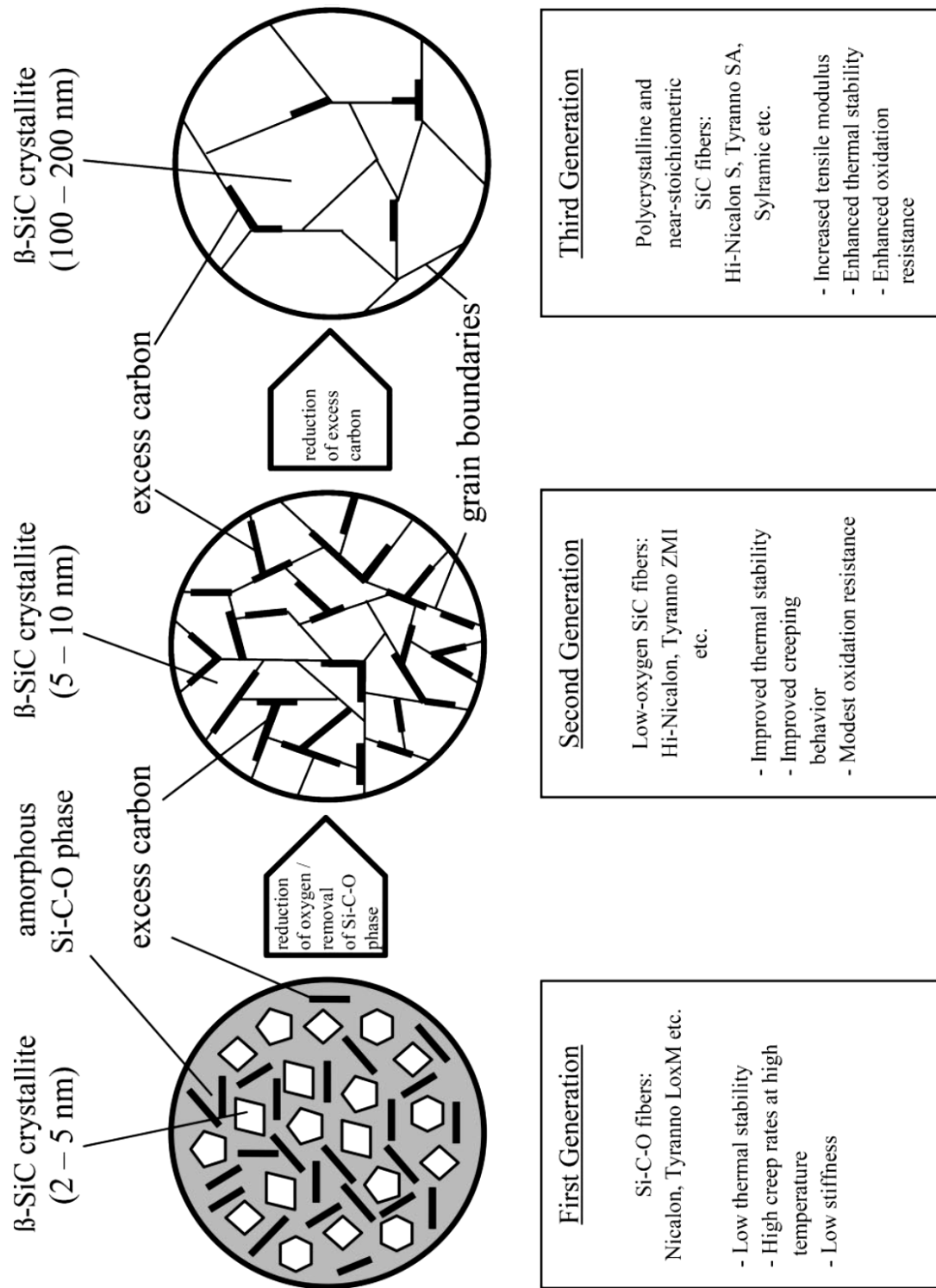


Figure 2-9. Microstructural of the three generations of SiC fibres. Adapted from [88].

### **Nicalon™ (NGS Advanced Fibres Toyama, Japan)**

The research at Nippon Carbon Company (Nippon Carbon Co., Japan) in the 70's led to the commercialization of Nicalon fibres [83, 85, 86, 91].

#### 1) First generation: *Nicalon*

The fibres are cured in air at 200°C and pyrolysed at 1200°C in inert gas. The microstructure is characterized by  $\beta$ -SiC nanocrystallites of 2-5 nm size embedded in an amorphous Si-C-O phase with ~12 wt % oxygen [94, 107]

The thermal and mechanical stability of these fibres is limited to 1200°C [73]. In fact, at higher temperatures and in inert atmospheres the amorphous Si-C-O phase decomposes and crystallizes to  $\beta$ -SiC with the evolution of SiO and CO gases combined with an accelerated SiC crystal growth [73, 94].

#### 2) Second generation: *Hi-Nicalon*

The development of these fibres was due to achieving a reduction in the oxygen content to <1 wt% [73, 86, 94, 103, 104, 108]; the crystallite size is around 5-10 nm [109]. They are manufactured the same as for the classic Nicalon fibres, except for the curing method, which is performed using electron beam irradiation in an inert environment to avoid oxygen contamination [73, 85, 102, 110]. The reduction in oxygen also allowed the use of higher manufacturing temperature (1300°C in inert gas), The reduction of oxygen content, with the consequent avoidance of the Si-C-O phase, permits the extension of the working temperature up to 1500°C. The passive oxidation behaviour is similar to Nicalon fibres but the layer of protective silica is thinner [103].

### 3) Third generation: *Hi-Nicalon™ Type S*

Hi-Nicalon Type S fibre has the highest Young's modulus, about 420 GPa, and improved thermal properties in comparison to the other fibres from the Nicalon family [73, 85, 91, 105, 107]. The enhanced properties of these third generation of SiC fibres were achieved by controlling the pyrolysis at 1600°C using hydrogen with the objective to reduce the carbon content of the fibres and hence to achieve a near stoichiometric C/Si ratio [73]. To remove silicon due to the carbonisation, the fibres were treated in HCl-containing atmosphere [88]. Crystallite size is typically 50–100 nm [73, 85, 86, 91]. As a result, Hi-Nicalon Type S fibres have improved creep and oxidation resistance up to 1400°C [73, 85, 86, 91, 105].

### **Tyranno™ (UBE Industries Inc., Japan)**

Silicon carbide fibres have been developed also by UBE Industries in Japan. They explored the grafting of a metal into a poly-carbosilane chemical chain [93, 101, 111]. The reaction of polycarbosilane (PCS) with metal (Ti, Zr, Al) at 250°C in a stream of nitrogen produces a complex compound polymetalcarbosilane. (PMCS). The polymer is melt-spun into a continuous filament and cured in air. The pyrolysis occurs in a firing furnace at 1500°C in nitrogen atmosphere [101]. Three generations of Tyranno™ SiC fibres have been commercialised.

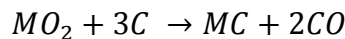
### 1) First generation: *Tyranno S* and *Tyranno LOX-M*

The composition of Tyranno S and LOX-M is based on the quaternary system Si-Ti-C-O. The fibre consisted of 3-5 nm  $\beta$ -SiC crystals in an amorphous oxygen-rich Si-Ti-C-O matrix (up to about 20 wt% O). Similarly to Nicalon 200, they cannot be used in CMCs for long-term performance at high temperature [88]. In

particular, in an inert atmosphere the crystallization of  $\beta$ -SiC, TiC and outgassing of CO and SiO degrade the fibre.

### 2) Second Generation: *Tyranno ZMI*

The titanium is replaced by zirconium resulting in a precursor with lower oxygen content [112]. The fibres contain 9 wt% of oxygen and offer a better thermo-mechanical performance than the previous generation [88, 101, 112]. The crystallite size is larger than the previous generation at around 5-10 nm embedded in an amorphous Si-Zr-C-O matrix (up to 1 wt% of zirconium). The higher thermal stability than the previous generation is due to the lower reactivity of ZrO<sub>2</sub> than that of TiO<sub>2</sub> with an excess of carbon [112], which is responsible of the following deleterious reaction



where M is the metallic element of the polymetalcarbosilane of the fibre precursor.

### 3) Third generation: *Tyranno SA3*

These Si-Al-C-O fibres-based are obtained from polycarboaluminosilane fibres cured in air and pyrolysed [88, 93, 101]. At this stage, the oxygen content and the excess carbon is around 12%. The last step is sintering at 1800°C, which is aided by the aluminium. The final oxygen content is less than 1% and Tyranno SA3 fibres are near-stoichiometric with a crystallites size of 200 nm [73, 85].

### Sylramic

Boron has been used since 1970s as sintering aid for silicon carbide [113]. Sylramic SiC fibres were initially developed by Dow Corning (Dow Corning Corporation, MI) [114] implanting boron in the polycarbosilane chain. A high temperature pyrolysis run performed at 1800°C under argon for 1 hour, preceded by a burn-out run, removes oxygen and excess carbon as volatile species. However, gaseous boron implantation was substituted by addition of boron powder to a polytitanocarbosilane. The final result was a near stoichiometric SiC fibres with small grains of B<sub>4</sub>C and TiB<sub>2</sub> [85, 91, 106, 108].

### Sylramic-iBN

Sylramic-iBN silicon carbide fibres are an exclusive product developed by NASA Glenn Research Center (Ohio, USA). The vendor is COI Ceramics Inc. (San Diego, California, USA), an ATK Group (Arlington, VA, USA) affiliate. These fibres are coated with boron nitride, which enhances fibre *pull-out*, the main energy-absorbing mechanism in FRCMCs. This improves the toughness of CMCs made from the fibres [73, 85, 86]. The oxygen content is well below 1% and the β-SiC crystallite size is 100-200 nm [73].

### Super Sylramic

Sylramic-iBN fibres are the best performing fibres because they show the highest creep resistance and thermal stability. However, further study at NASA Glenn Research Centre [65, 115-117] is oriented in the development of fibres, Super Sylramic-iBN and -iC with higher creep resistance and higher rupture strength and stress-rupture time. The creep rate decreases if i) larger grain size

(up to 500 nm) are formed and the grain size is homogeneous in the entire fibre  
ii) the microstructure is free from pores and impurity. Recent tests [86, 116] reported the improvement in terms of creep resistance of the Super Sylramic iBN and Super Sylramic-iC, respectively BN and carbon coated. At 1400°C in air Super Sylramic-iBN have the lowest creep strain whilst Hi-Nicalon (2<sup>nd</sup> generation) fibres have a strain of almost 2.5%. In terms of endurance, the rupture strength of Super Sylramic-iBN is almost 400 MPa after 1000 hours of exposure to air at 1400°C. In the same conditions Hi-Nicalon S have a rupture strength below 300 MPa and value even below 200 MPa for Tyranno SA which have a limited life of 100 hours.

Figure 2-11 shows the mechanical performance under tensile testing of the SiC fibres against the temperature after annealing in argon and air. After annealing in argon, Tyranno SA3 have been tested at 2000°C with a residual tensile strength of 2 GPa. Sylramic-iBN are potentially the most performing fibres as they retain the strength at high temperature. Amongst the fibres of the second generation, Tyranno ZMI performed better up to 1500°C. The fibres of the first generation have a noticeable drop of the tensile strength at temperature as low as 1300°C.

In air, the fibres of the Nicalon family generally performed better, but the Nicalon NL202 (first generation) lose their structural integrity at 1400°C after only 10 hours of exposure.

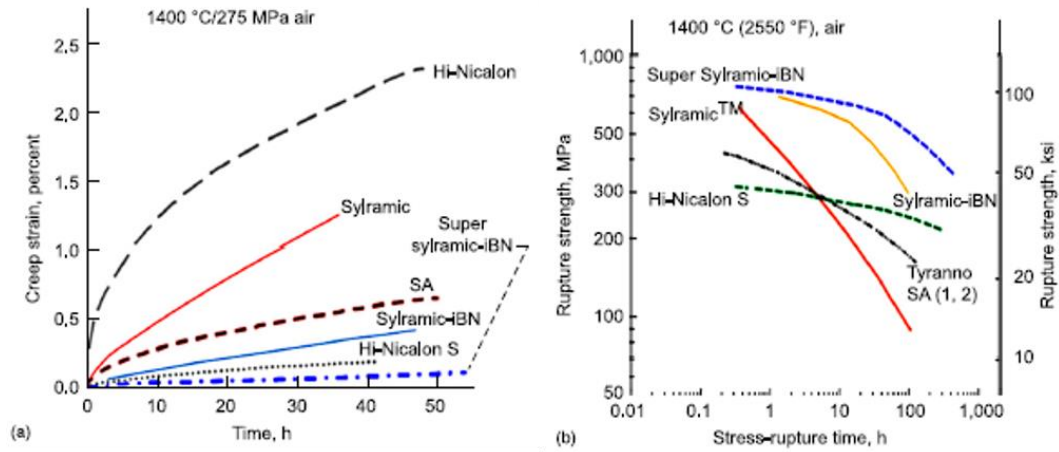


Figure 2-10. Comparison of the creep strain and rupture strength at 1400°C between Super-Sylramic fibres and SiC fibres of the third generation. Adapted from [86, 116].

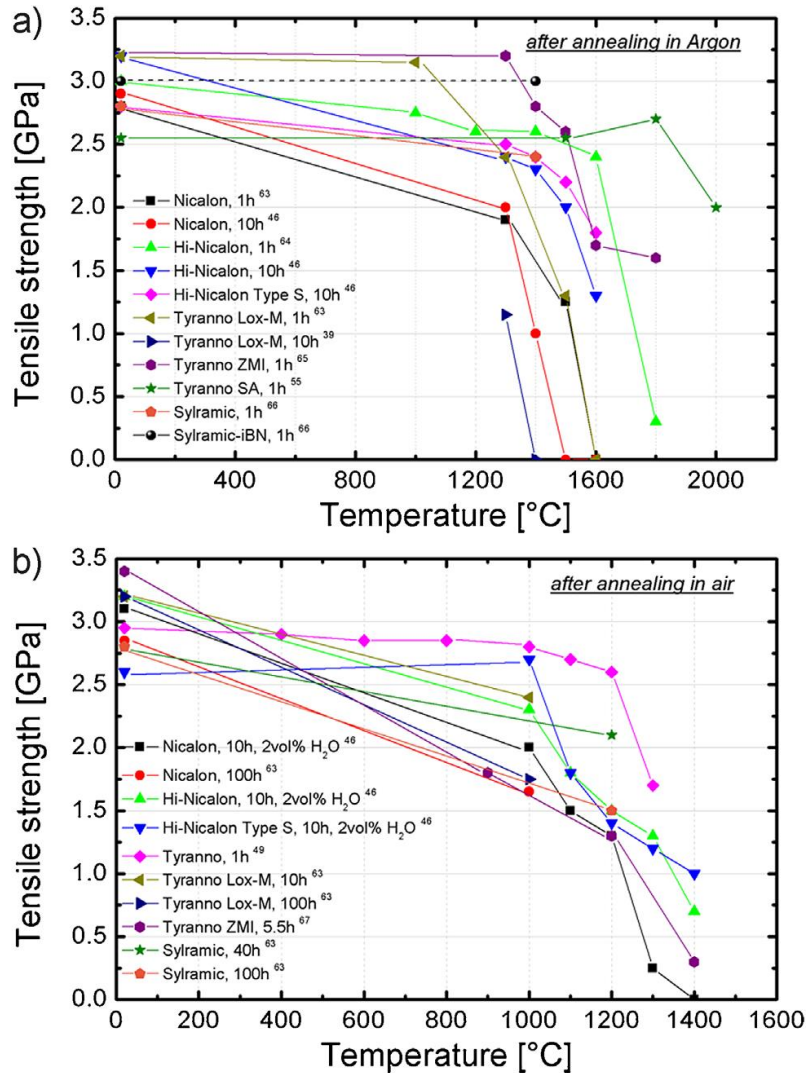


Figure 2-11. Variation of the tensile strength against temperature of commercially available SiC fibres after annealing in inert atmosphere (a) and in air (b). Adapted from [73].

Table 3. Physical, mechanical and thermal properties of the commercially available SiC fibres [73, 85, 86].

Trade name (manufacturer)	Production method	Temperature production / °C	Composition / wt%	Structure	Diameter / μm	Density / g cm <sup>-3</sup>	Tensile strength / GPa	Tensile modulus / GPa	Thermal conductivity / W m <sup>-1</sup> K <sup>-1</sup>	Cost € per kg
Nicalon NL200 (Nippon Carbon)	Polymeric precursor	1200	56.6Si + 37.1C + 11.7 O	2 nm crystallites Amorphous Si-C-O phase	14	2.55	3.0	220	3	1000
Tyranno Lox-M (Ube Industries)	Polymeric precursor	1200	55.4Si + 32.4C + 10.2 O + 2 Ti	1 nm crystallites Amorphous Si-C-O phase	11	2.35	3.3	186	1.4	1200
Hi-Nicalon (Nippon Carbon)	Polymeric precursor	1300	62.4Si + 37.1C + 0.5 O	5-10 nm crystallites with residual amorphous Si-C-O phase	14	2.74	2.8	270	8	3250
Tyranno ZMI (Ube Industries)	Polymeric precursor	1300	56.1Si + 37.1C + 8.7 O + 1 Zr	5-10 nm crystallites Amorphous Si-C-O phase	11	2.48	3.4	193	2.5	1400
Hi-Nicalon Type S (Nippon Carbon)	Polymeric precursor	1600	68.9 Si + 30.9 C + 0.2 O	100 nm crustallites near-stoichiometric	12	3.1	2.6	420	18	7000
Tyranno SA3 (Ube Industries)	Polymeric precursor	1600	55.4 Si+32.4 C + 10.2 + 2Al	200 nm crystallites near-stoichiometric	7-10	3.1	2.8	380	64.5	6500
Sylramic (IATK-COI)	Polymeric precursor	>1700	67 Si + 29 C + 0.8 O + 2.3 B + 0.4 N + 2.1 Ti	100 nm crustallites near-stoichiometric	10	2.95	2.8	310	40-45	8000
Sylramic iBN	Polymeric precursor	>1700	SiC/BN	100 nm crystallites near-stoichiometric BN coating	10	3.05	3.2	400	>46	10500
SCS6 and Ultra (Specialty Materials)	CVD	1300	70 Si + 30 C + carbon filament	100 nm columnar SiC on 33 μm C filament SiC/C coating	140	3.0	5.9	415	70	8300
Sigma (Tisits)	CVD	--	11 W + 86 SiC 1.3 C + 1.7 TiB <sub>2</sub>	14 μm W filament 80 μm SiC layer and duplex C/TiB <sub>2</sub> layer	100	3.5	4.0	400	--	7600

### Other SiC-based fibres

#### *SiCN(O) fibres*

At the beginning of 1970s, Bayer (Bayer AG, Leverkusen, Germany) announced the production of shaped articles of homogeneous mixtures of silicon carbide and nitride through the synthesis of a polycarbosilazane (PCSZ) [73, 118-120].

Heat treatment studies [121] have shown that SiCN(O) fibres have a higher thermal stability than Si-O-C because nitrogen delays crystal nucleation by hindering the structural rearrangements.. At 1400°C, the Si-C-N-(O) fibres have a maximum Young's modulus and an ultimate strength higher than Si-O-C fibres [73]. SiCN fibres with less than 2 wt% of oxygen are currently produced by Matech GSM (Westlake, CA, USA) [122].

#### *SiBCN fibre*

Borosilicon carbonitride fibres can be synthesised by pyrolysis of a preceramic polyborosilazane [123, 124]. In comparison to SiCN and Si-O-C systems, SiBCN fibres retain thermal stability up to 1800°C in inert atmosphere [73] because of the preservation of an amorphous state rather than the typical crystallization of SiC in SiC(O) fibres and SiC/Si<sub>3</sub>N<sub>4</sub> in SiCN filaments. The oxidation resistance is fulfilled by the formation of a double layer SiO<sub>2</sub>/BN that prevents the oxygen diffusion into the core of the material.

2.3.2.3 Properties of SiC<sub>f</sub>/SiC composites

Considerable effort has been devoted to the development of SiC<sub>f</sub>/SiC composites and Table 4 reports some physical, thermal and mechanical properties at room temperature for a two-dimensional reinforced SiC matrix composites.

Table 4. Properties of SiC<sub>f</sub>/SiC composites.

Properties	I generation [125]	II generation [126, 127]	III generation [10, 46-48, 50, 126, 128, 129]	Sylramic iBN [46]
Flexural strength /GPa	0.35-0.45	0.35	0.48-0.65	--
Tensile strength / GPa	0.15-0.30	0.2-0.5	0.27-0.55	0.31-0.45
Compressive strength / GPa	0.3-0.6	--	0.42-0.43	--
Shear strength / GPa	0.03-0.06	--	0.03-0.04	--
Young's modulus / GPa	170-200	170-200	200-280	200-300
Fracture toughness / MPa m <sup>1/2</sup>	5-25	5-16	11-46	--
Elongation at fracture %	0.2-0.3	0.5	0.2-0.85	0.3-0.55
Weibull modulus	10-15	--	--	--
Max temperature in inert atmosphere / °C Max temperature service in air / °C	1200 1100	1450 1200	1650-1900 1350	1800-1850 >1350
Thermal conductivity / W m <sup>-1</sup> K <sup>-1</sup>	15-20	15-50	15-50	25-40
Coefficient of thermal expansion / 10 <sup>-6</sup> K <sup>-1</sup>	4.0	5	4.6-4.8	--
Open porosity vol. %	10-15	5-15	2-20	2-14
Absolute density / g cm <sup>-3</sup>	2.3-2.5	2.5-2.7	2.3-2.9	2.5-2.9

The main properties that make SiC<sub>f</sub>/SiC so attractive for industry are:

- Low density
- Good chemical resistance

- Excellent thermo-mechanical properties
- Good thermal shock resistance
- Relatively high toughness
- Good oxidation resistance (compared to carbon fibre)
- Low activation for nuclear applications
- Good wear resistance

### 2.3.2.4 Properties of preforms

The fibre preform is an arrangement of fibres that constitutes a porous body with a complex architecture; these can be achieved via weaving twisting, interlacing stitching and interloping of the fibres. The volume of fibres and how they are arranged in the preform affect the mechanical properties of the composite and also the ease of manufacturing it.

The major variables that influence the preform properties are:

- Type of weaves (e.g. plain, satin, twill, panama etc.)

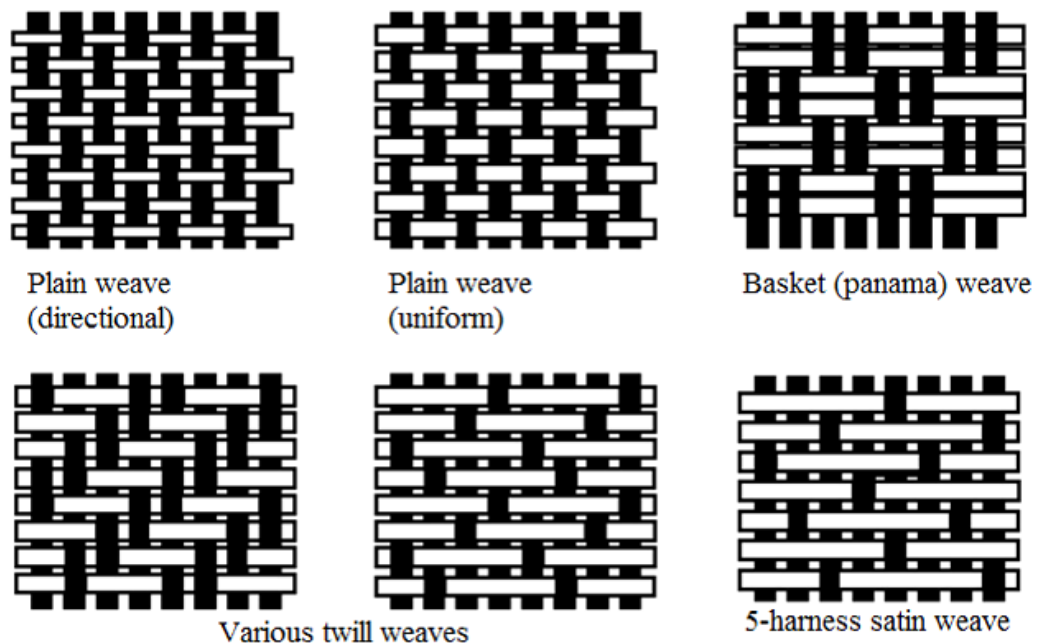


Figure 2-12. Several types of weaving. Adapted from [130].

- Number and orientation of plies.

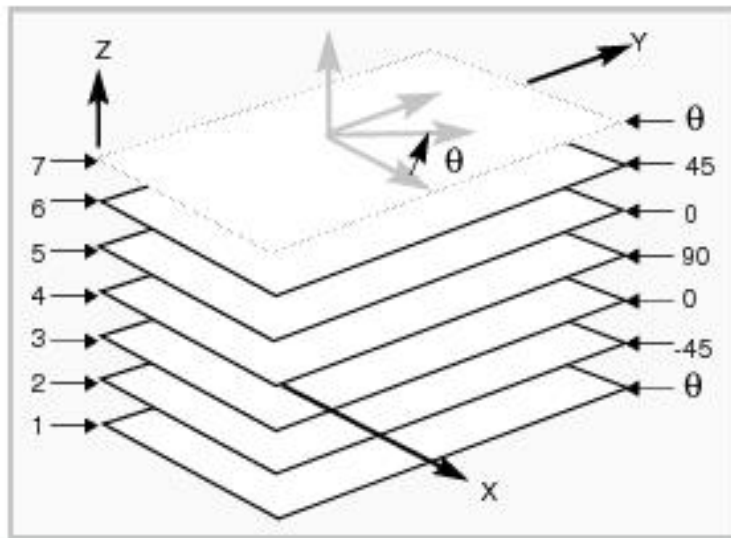


Figure 2-13. Stacking of plies for a composite material; the final properties depends on the number of plies and orientation [130].

- Fibre diameter; weavability when diameter is  $<20\ \mu\text{m}$  (e.g. SCS fibres cannot be woven because their diameter is above  $\sim 80\ \mu\text{m}$ ).
- Number of fibres per bundle.

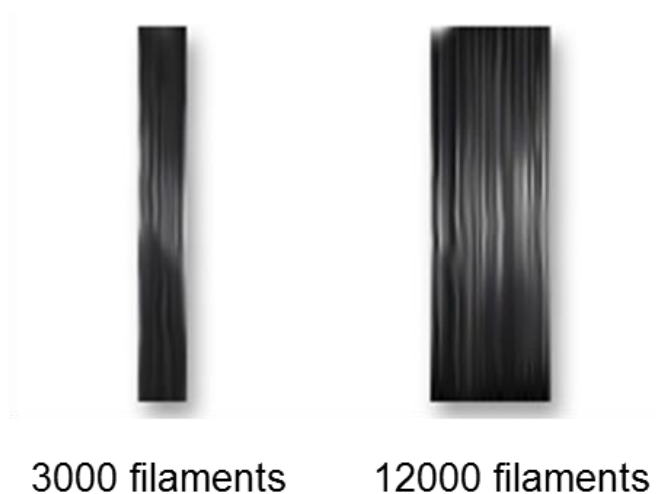


Figure 2-14. The number of fibres determines the dimension of the bundle. Adapted from [131].

- Architecture: two-dimensional, three-dimensional preforms, four-dimensional and five-dimensional preforms [132].

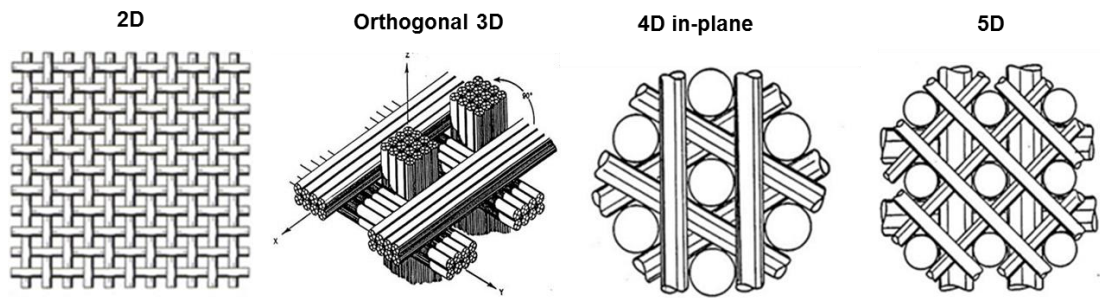


Figure 2-15. Fibre architectures. Adapted from [133].

- Volume fibre fraction: the initial density of a preform can vary from 10 to 80% of the theoretical value. Generally, the higher the volume, the greater the tensile strength and elastic moduli. If the fibres are coated, the toughness is enhanced because of pull-out. The fibre content also determines the initial porosity, due to the interlacing of tows and lay-up of the plies, which is called intratow porosity (see section 0). The pore size is typically in the range 100-500  $\mu\text{m}$ .
- A factor that identifies how the structure of the pores restricts the flow of the gases is known as the tortuosity, or arch-cord ratio of a pore channel.
- The fibre-matrix interface plays a pivotal role in the mechanical performance of the FRCMCs as will be discussed in the next paragraph since it increases the toughness and protects the fibre from potential damage during processing and use.

### 2.3.2.5 Fibre/matrix interface

The fibre-matrix interface exerts key role in the mechanical performance of SiCf/SiC because the load transfer from the matrix to the fibre and vice versa occurs through the interface and hence is related to the characteristics of the interface [4, 40, 42-44, 51, 134-136]. Moreover, the interface must retain high

temperature properties in hostile environments such as irradiation in nuclear reactors, oxidation and corrosion in hot parts of engines [127].

If the interfacial bond of the SiC fibres and SiC matrix is too strong, there will not be any impediment to the crack propagation, resulting in a smooth and flat fracture surface similarly to the brittle monolithic ceramics. Conversely, if the fibres are coated with a thin layer of a material acting as solid lubricant [42] such as boron nitride (BN) [135, 136] or pyrolytic graphite (PyC) [7, 10, 44, 127] the composites show an evident pull-out resulting in an improved toughness [127]; the optimal thickness is in the range 0.1-1  $\mu\text{m}$  [7] otherwise the soft nature of the coating prevails and the strength decreases. PyC interface noticeably improved the fracture toughness and the maximum strain rate [44]. However, it oxidizes at temperatures as low as 400°C, which is well below the service temperature of SiC<sub>f</sub>/SiC [43]. BN coatings provide a better resistance to oxidation because of the formation of a borosilicate glass layer that is impervious to O<sub>2</sub> diffusion at high temperature [43]. BN is the material of choice in the CMC inserts of LEAP Engine [69].

However, also BN shows some limits. If the oxidation of BN into B<sub>2</sub>O<sub>3</sub> is faster than the formation of the borosilicate glass, the interface layer will be eroded with consequent vanishing of the pull-out as energy-dissipating mechanism [43]. For this reason, Si-doped BN coating [46], multilayer coating PyC/SiC [126], BN/PyC [45], BN/SiC [43] and BN/Si<sub>3</sub>N<sub>4</sub> [137] have been objects of study to further enhance the protection of the fibres.

The interface coating has also the function to heal defects on the surface of the fibres [138], reduce the roughness and protect the fibres during the manufacturing process [135].

### 2.3.2.6 Applications of the SiCf/SiC system

SiCf/SiC is very attractive material for applications requiring a life of several thousands of hours in relatively demanding environments such as:

- Nuclear fusion reactors and nuclear fuel cladding [48, 53, 66, 126, 139].
- Aerospace applications including aircraft brakes, gas turbine blades, nozzle flaps, shrouds and combustion liners of aircraft engines [6, 55, 56, 66, 69, 70, 140, 141].
- Automotive applications including exhaust gas, combustors and wear parts [142-144].
- Heat exchangers, burners and incinerators [144].

## 2.4 Fabrication of FRCMCs

### 2.4.1 Introduction

The manufacturing process usually consists of the following three steps:

1. Shaping, lay-up and fixation of the fibres.
2. Matrix formation
3. Further treatments like machining, polishing, joining and coating

In the first step, the fibres are assembled in a unidirectional, two-dimensional or three-dimensional assembly using techniques such as lay-up of fabrics, filament winding, braiding and knotting. The result of this procedure is the *fibre-preform*.

## 2.4.2 Matrix formation and available techniques

Matrix formation for SiC<sub>r</sub>-SiC has been explored via numerous routes including [145]:

- Powder processing
- Melt infiltration (MI), e.g. silicon, infiltration (LSI)
- Polymer impregnation and pyrolysis (PIP)
- Chemical vapour infiltration (CVI)

Each of these will be briefly reviewed in turn.

### 2.4.2.1 Powder processing

The powder processing route used for monolithic ceramics can be adapted to the fabrication of CMCs, with the reinforcements being whiskers, particulates or chopped fibres. The use of long continuous fibres has generally been avoided because of potential damage to the fibres during the mixing and consolidation process, although some studies have been undertaken [139, 146].

A typical powder processing route involves the following steps [5]:

- Mixing of matrix and reinforcement phase, e.g. via ball milling
- Green body fabrication, e.g. cold pressing, injection moulding, tape casting, etc.
- Machining if required
- Binder removal if required

- Consolidation and densification e.g. hot pressing, hot isostatic pressing (HIP)

As one example, short fibres or whiskers can be mixed with a ceramic slurry, dried and hot-pressed [5, 147]. During hot-pressing the fibres can undergo some orienting in the plane perpendicular to the hot-press axis. The main goal is to obtain homogeneous composite and as the reinforcement material tends to agglomerate, so the preparation of the slurry with respect to mixing technique, dispersant, pH control and viscosity is very important [3]. Moreover, the presence of the reinforcement can hinder the densification during sintering [148].

### 2.4.2.1.1 Slurry infiltration

For FRCMCs, fibre tows or preforms are impregnated in a tank containing the liquid slurry made of the matrix powder, liquid carrier (typically water, acetone, or alcohol), binder and, if required, an additional wetting agent. The slurry stability and composition, e.g. solid loading, carrier fluid and percentage of binder, are crucial to achieve adequate infiltration. The impregnation step is often vacuum assisted [139, 149].

After the evaporation of the solvent and burning out of the organic binder, the lay-up can be consolidated via a heat treatment such as hot-pressing [146] or undergo a further, different manufacturing process, e.g. CVI, PIP, MI [46, 150].

### NITE process

In the NITE (Nano-Infiltration and Transient Eutectoid) process [128, 146, 151] the matrix is formed through the transient liquid-phase sintering of SiC powder mixed sintering aids [128]. The fibrous preform or a single layer of fabric is infiltrated with a mixture of nanosized SiC powder with sintering additives such as  $\text{Al}_2\text{O}_3$  and  $\text{Y}_2\text{O}_3$  [128].

Polycarbosilane (PCS) can be added to promote the densification of the matrix inside the tows [128, 146, 151]. The material is then densified by hot-pressing at high temperatures (1750–1800°C) under pressures ranging from 15 to 20 MPa [47, 146, 151]. The SiC<sub>f</sub>/SiC composites fabricated by the NITE process exhibit near-full density (99%) and high strengths in excess of 400 MPa.

### **Electrophoretic deposition (EPD)**

Electrophoretic deposition (EPD) is a process in which electrically charged particles, dispersed in a polar fluid, are transported into the preform by an electric field [152, 153]; in practice, two electrodes are immersed into a well dispersed suspension (including a surfactant) [154]. A potential difference is then applied. The movement of ceramic particles in a suspension within an electric field is governed mainly by factors such as the field strength, the pH of the suspension and its ionic strength [155]. In one approach [152], silicon carbide mats have been infiltrated with SiC particles by EPD. In another study, in the SiC<sub>f</sub>/SiC system, a reduction in porosity above 25% was achieved in only 2 minutes [155]. The process needs subsequent stages like CVI [156], PIP [93] or LSI [157].

#### **2.4.2.2 Liquid metal infiltration**

The vast majority of work has involved silicon [58, 157-165], since it has a melting point of only 1410°C. When used to infiltrate a porous carbon preform, e.g. made of felt, charcoal, etc., a silicon carbide body can be formed.

The process is usually performed in a BN-coated tank placed in a graphite element furnace at a temperature between the melting point of silicon and 1900°C, in a vacuum that is below 1 bar, and for a couple of hours. As the liquid

silicon travels through the channels of the preform due to capillary forces, the carbon is converted to silicon carbide [58]. The final composite still contains carbon and unreacted silicon, which could limit the long-term use temperature [160].

The preform is infiltrated with carbon black slurry, or any other source of carbon such as a phenolic resin or crystalline cellulose, and the carbon fibres are typically protected with a duplex layer of BN, to weaken the fibre/matrix interface, and SiC to isolate the fibre from attack by the melt [58, 158].

The amount of silicon needed for the conversion can be calculated, but it is almost inevitable some residual silicon remains. Although it is counterproductive for the performance at higher temperatures, the silicon bonds the silicon carbide particulates together and forms a matrix that is somewhat denser, hence stronger, than that obtained by CVI [5, 46].

The liquid metal infiltration processes have several advantages [5]: (1) they produce a fairly dense matrix with a minimum of porosity; (2) the processing time is shorter than for most ceramic matrix composite fabrication processes and is relatively cheap; and (3) the closed porosity at the surface can often eliminate the need for a final oxidation resistant coating; (4) a reaction bonded SiC matrix is effectively produced. The major disadvantage for SiC<sub>f</sub>/SiC composites is the high temperatures required for liquid silicon infiltration, which exposes the fibres to possible degradation due to the high temperatures and the corrosive nature of liquid silicon [5]. The exothermic nature of the reaction between Si and C can further increase the temperature [159]. Figure 2-16 displays the key steps of the liquid silicon infiltration process.

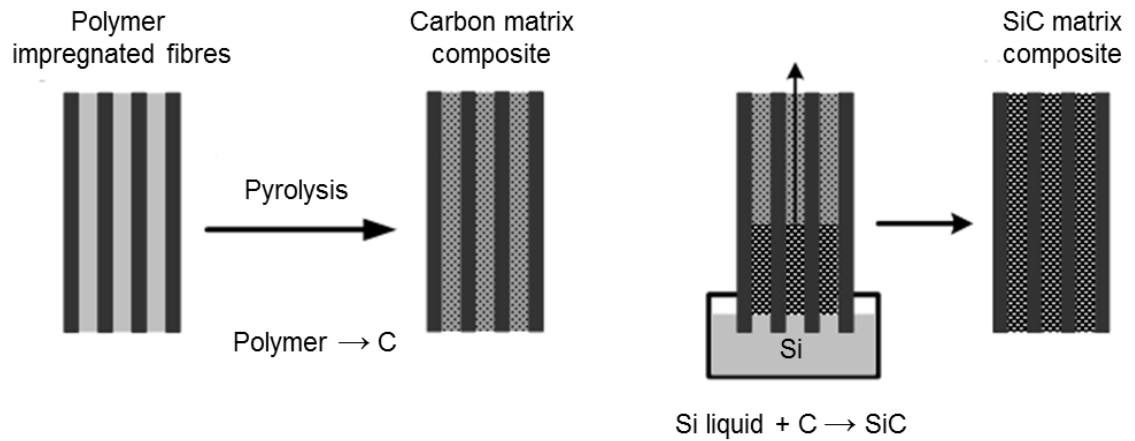


Figure 2-16. Schematic of the liquid silicon infiltration (LSI) process [166].

### 2.4.2.3 Polymer impregnation and pyrolysis (PIP)

Due to the development of low-viscosity, high-yield polymer precursors for stoichiometric SiC, the use of PIP has become an attractive alternative for fabricating the matrices of C<sub>i</sub>/SiC and SiC<sub>i</sub>/SiC composites [167-174]. The polymer precursor is infiltrated into the woven fibre preforms at ambient temperature and then heated to temperatures above 1000°C, whereupon the polymer pyrolysis into amorphous or crystalline SiC [175]. Multiple infiltration and pyrolysis cycles are necessary to achieve high density [5], because of the mass loss and volume shrinkage of the polymer during heat treatment [176].

As shown in Figure 2-17, the process consists of [5]:

- Infiltration of the preform with the polymer,
- Consolidation of the impregnated preform,
- Curing of the polymer matrix to prevent melting during subsequent processing,
- Pyrolysis of the cured polymer to convert it to a ceramic matrix,

- Repeating the infiltration and pyrolysis process multiple times to produce the desired density.

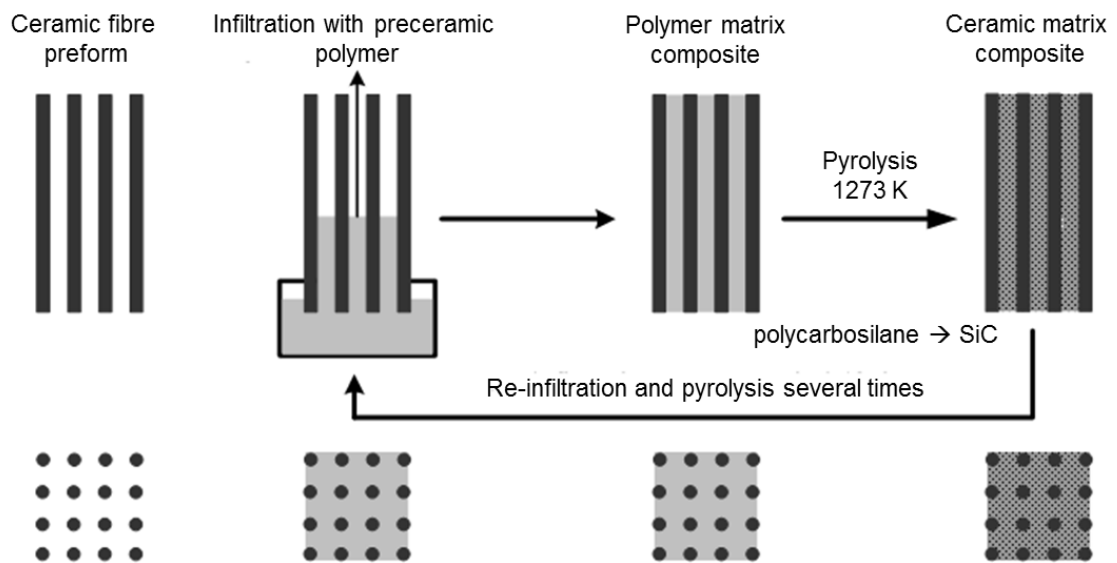


Figure 2-17. Schematic of fabrication of SiC based composites by PIP [166]

Figure 2-18 shows the fabrication of Nicaloceram™ SiC<sub>f</sub>/SiC composite by PIP, adapted from [177, 178].

SiC or Si<sub>3</sub>N<sub>4</sub> powders can be added to the polymer to reduce the number of infiltration cycles [179], or hybrid techniques (slurry infiltration + PIP) [150] are also common to reduce the number of impregnations

Table 5 summarizes the benefits and drawbacks of the techniques currently available for the fabrication of FRCMCs.

Table 6 focuses on some experiments for the fabrication of SiC<sub>f</sub>/SiC composites by the routes summarised in Table 5. The experimental conditions used and resulting properties are summarized.

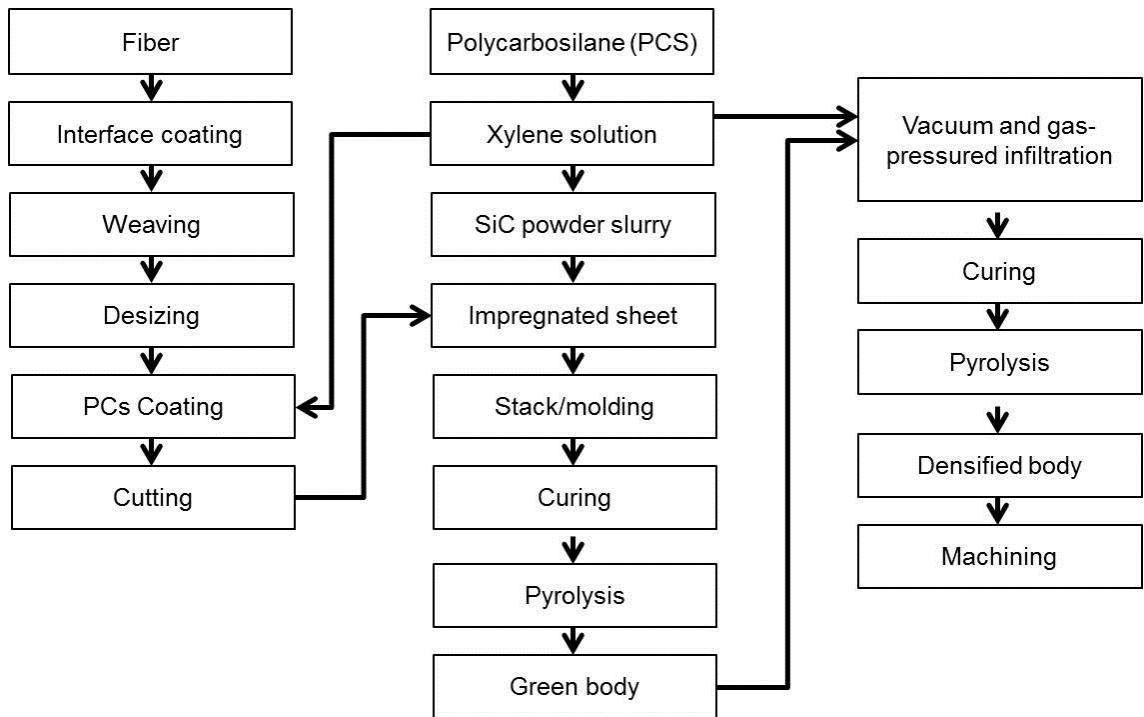


Figure 2-18. Flow chart of polymer infiltration and pyrolysis of SiC<sub>f</sub>/SiC composite

Table 5. Benefits and drawbacks of several methods for fabrication of FRCMCs

Matrix formation process	Processing temperatures / °C	Advantages	Disadvantages
Hot-pressing	Up to 1800	Simple, stacked lay-ups Standard set up	Multiple heating steps Simple geometries
Melt infiltration	Up to 2000	Dense matrix formation Near net shape processing	High molten matrix temperatures Restrictions on matrix choices Reduced creep resistance at high temperature
Polymer impregnation and pyrolysis	1000-1400	Similar to resin transfer moulding in polymers. Simple tooling Moulding techniques similar to polymer moulding	Multiple impregnations and pyrolysis Residual porosity Crystallinity of the matrix
Slurry infiltration	1000-1800	Low cost manufacturing Moulding techniques similar to polymer moulding	Critical fibre architecture Slurry composition Additional manufacturing step

Table 6. Fabrication of SiCf/SiC composites by different techniques

Type of process	Material used	Initial stage	Process conditions	Achievable density	Mechanical properties	Limitations
Slurry casting + Melt infiltration [144]	BN-coated Hi-Nicalon fibres Slurry of SiC and C powders water-based Melted silicon	Slip impregnation and casting of a matrix slurry	T ~1400°C Atm.= vac t= 5 h	~97%	$\sigma_u$ =460 MPa Non-brittle failure	15-20 vol.% of Si in the matrix Possible oxidation of the Si in oxidising atmosphere
PIP [176]	Nicalon fibres PCS-hexane	Impregnation with PCS under vacuum	1100°C Atm= Ar Several impregnations P = 7 kPa	70.0%	$\sigma_u$ = 240 MPa	Insufficient polymer-to-ceramic conversion during pyrolysis
PIP [175]	SiC fibres 3D architecture, PyC coating PCS	Impregnation with PCS by vacuum infiltration	1100°C Atm= Ar Several impregnations	n/a	$\sigma_u$ = 230-514 MPa $K_{IC}$ = 15.6-31.9 MPa m <sup>1/2</sup>	Heat treatment needed to transform the matrix from amorphous to crystalline
PIP [169]	PyC coated Nicalon fibres PCS-hexane MTS+H <sub>2</sub>	Impregnation with boiling PCS for 20 min	PIP T=1000°C Atm.= Ar 6 cycles	71%	$\sigma_u$ = 224 MPa $K_{IC}$ =6.2 MPa m <sup>1/2</sup>	Low density Vulnerability to oxidation Large pores in the range 100-150 $\mu$ m
Hot pressing [139]	Hi- Nicalon cloth SiC sheet (=3:1)	Vacuum impregnation of slurry through cloth. Stacking with SiC sheet	T= 1750°C P= 40 MPa t= 2 h	95.6% (7.5 wt.% aids)	$\sigma_u$ = 240-260 MPa	Damage on fibres (too high T) Non-uniform distribution of the matrix Non-stoichiometry(sintering aids)
NITE [47]	PyC coated Tyranno SA3 fibres V <sub>f</sub> = 31 – 33% 30 nm SiC powder with sintering aids	Slurry dipping and PCS	Hot pressing at 1720-1780°C, 15-20 MPa, 2 hours	86.1-90.9 %	$\sigma_u$ = 268-331 MPa E= 110-130 GPa	Limited pullout when temperature and pressure increased. Low pressure and temperature increased the crack deflection but lower strength and stiffness. Sintering aids altered the composition of the matrix
NITE [151]	Tyranno SA3 fibres, PyC coating 0.5 $\mu$ m SiC powder with sintering aids	Slurry impregnation	Hot pressing at 1900°C, 20 MPa, 1 h	96 - 99 %	$\sigma_u$ = 356-408 MPa E= 300-358 GPa $\sigma_u$ = 140-167 MPa E= 230-288 GPa	Brittleness at high temperature
Slurry infiltration + and MI [157]	Tyranno SA3 fibres $\beta$ -SiC and carbon black slurry Melt silicon	Electrophoretic deposition of the powder on the fabric	T ~1550°C Atm.= vac. 10 <sup>-3</sup> kPa t= 0.5 h	n/a	$\sigma_u$ = 192 MPa	Residual C and formation of silica

## 2.5 Chemical vapour infiltration

### 2.5.1 Introduction

Vapour phase routes are promising since they involve relatively low processing temperatures and pressures, and the purity of the solid deposit can meet the requirements for long-term performance in a demanding environment.

Chemical vapour infiltration (CVI) involves the thermal decomposition of a gas phase to yield a solid matrix within a heated porous preform such as a carbon or silicon carbide textile [11-13, 156, 180-186].

CVI is essentially a variant of the chemical vapour deposition (CVD) process [187] often used in the semiconductor industry [188]. The differences are that: i) the amount of material to be deposited is larger than in CVD and ii) in CVI, the coating occurs throughout the interior of a porous body rather than on a bulk substrate.

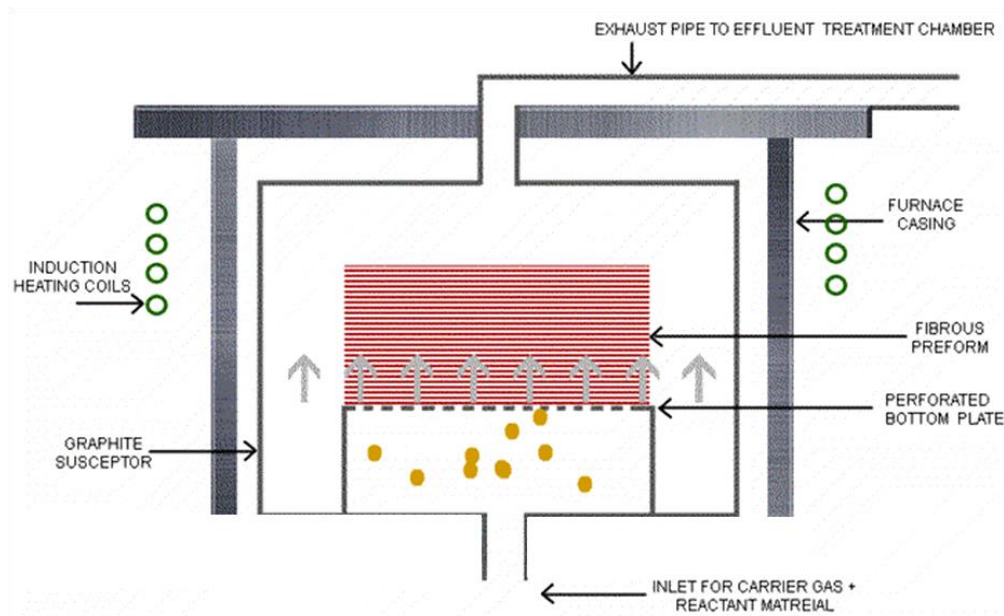


Figure 2-19. Schematic of an isothermal chemical vapour infiltration [166].

In the isothermal and isobaric CVI process (ICVI) [183, 189-191], the preform is placed in a furnace and heated until it achieves a uniform temperature. It is then infiltrated by a gaseous species that decomposes, depositing the desired solid phase. As the deposition process continues, the thickness of the material deposited around the fibres increases until it eventually fills the free space. Hence, the porosity decreases until the pores are completely obstructed or filled, as shown in Figure 2-20 .

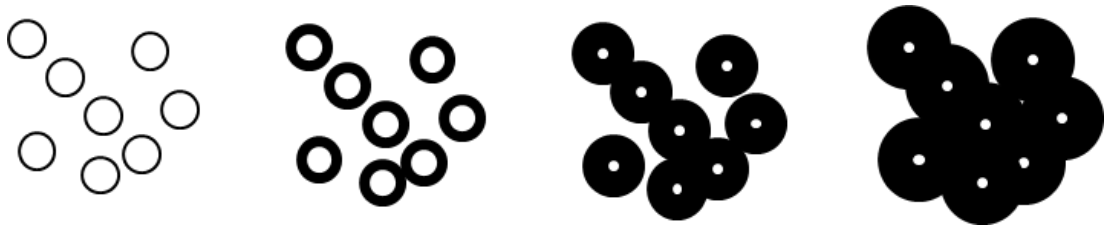


Figure 2-20. Void filling during CVI

The process of pore closure is crucial for the final properties of the FRCMC; excessive trapped porosity reduces many properties, including strength and chemical oxidation / oxidation resistance.

CVI has been extensively investigated [9, 11, 192, 193] because it offers some distinctive advantages compared to other routes to FRCMCs

- Production of materials at low processing temperature and pressure. As a consequence it avoids fibre stress or damage;
- Manufacturing of near-net-shape components
- The matrix is pure and fine grained;
- Deposition of interfacial layers can be achieved *in-situ* to enhance fibre pull-out as discussed in section 2.3.2.5;

## Chapter 2. Literature survey

---

- A wide range of compositions is possible, as shown in Table 7;
- No sintering aids that can affect the composition of the matrix are required;
- Can be used as initial/final densification step of materials fabricated by other process such as PIP and melt infiltration, as discussed in section 0
- With one run it is possible to densify more than one preform, even with complex shapes.

Table 7. Precursor gases and temperature for the deposition of some ceramic matrices.

Matrix deposit	Reactant gases	Temperature / °C
C	CH <sub>4</sub> -H <sub>2</sub>	1000-1200
TiC	TiCl <sub>4</sub> -CH <sub>4</sub> -H <sub>2</sub>	900-1000
SiC	CH <sub>3</sub> SiCl <sub>3</sub> -H <sub>2</sub>	1000-1400
B <sub>4</sub> C	BCl <sub>3</sub> -CH <sub>4</sub> -H <sub>2</sub>	1200-1400
TiN	TiCl <sub>4</sub> - NH <sub>3</sub> -H <sub>2</sub>	900-1000
Si <sub>3</sub> N <sub>4</sub>	SiCl <sub>4</sub> (or SiH <sub>4</sub> )-NH <sub>3</sub> -H <sub>2</sub>	1000-1400
BN	BCl <sub>3</sub> -NH <sub>3</sub> -H <sub>2</sub>	1000-1400
AlN	AlCl <sub>3</sub> -NH <sub>3</sub> -H <sub>2</sub>	800-1200
Al <sub>2</sub> O <sub>3</sub>	AlCl <sub>3</sub> -CO <sub>2</sub> -H <sub>2</sub>	900-1000
SiO <sub>2</sub>	SiH <sub>4</sub> - CO <sub>2</sub> -H <sub>2</sub>	200-600
TiO <sub>2</sub>	TiCl <sub>3</sub> -H <sub>2</sub> O	800-1000
ZrO <sub>2</sub>	ZrCl <sub>4</sub> - CO <sub>2</sub> -H <sub>2</sub>	900-1200
TiB <sub>2</sub>	TiCl <sub>4</sub> - BCl <sub>3</sub> -H <sub>2</sub>	800-1000

ICVI is the most well-known and commercially used process for the production of the carbon brakes and some aeronautical components.

Although the benefits are evident, ICVI suffers from a main drawback. The deposition occurs preferentially near the outer surface where the concentration of reactants, and often the temperature, is highest [193]. As a result, “crusting” occurs and seals the porosity at the surface of the preform. Therefore, the infiltration has to be stopped and it is necessary reopen the porosity through machining. In order to reduce the extent of crusting, possibilities are to: i) decrease the process temperature, though this decreases the deposition rate and hence increases the process time or ii) work at reduced pressure improving the gas diffusion in the preform. Nevertheless, as result of crusting, the processing time can be up to 2000 hours and hence the process is not cheap [11, 189, 194].

Overall, the process is complex because it requires detailed awareness of the reaction chemistry, kinetics, temperature distribution, heat source, pressure and preform geometry [180, 193]. The final microstructure depends on all these variables and hence the thermo-mechanical properties. On this basis, a variety of CVI processes have been developed.

### 2.5.2 CVI variants

CVI can be divided into several categories depending on [12]:

- The presence or absence of thermal gradients,
- The pressure conditions: isobaric, forced flow or pressure pulse and whether atmospheric or vacuum,
- The heating method: radiation, induction, microwave

Table 8 shows how temperature, pressure and heating method vary for several CVI processes.

Table 8. Chemical vapour infiltration variants. Adapted from [11].

CVI process	Temperature		Heating		Pressure			
	Uniform	Gradient	Radiative	Inductive	Uniform	Gradient	Atmospheric	Low
Plasma enhanced low pressure								
Thermal gradient, radiantly heated, isobaric								
Thermal gradient, inductively heated, isobaric								
Liquid immersion, thermal gradient, inductively heated isobaric, atm. pressure								
Isothermal, forced flow								
Isothermal, pulsed pressure								
Thermal gradient, forced flow								
Microwave-heated, isobaric or forced-flow								
Catalyst-enhanced, isothermal, isobaric								
Particle-transport enhanced, isothermal, isobaric								

Some of the main variants of CVI are described below and the benefits and drawbacks of each technique are reported.

**2.5.2.1 Thermal gradient heated, isobaric**

A thermal gradient is applied, radiantly or inductively, to the preform. The gradient is created by one part of the preform being closer to the hot wall of the furnace [11, 195]. This temperature gradient allows the deposition to occur preferentially in the hot zone and the densification front proceeds from the hotter zone toward the cooler region. The gas phase flows into the cooler side of the preform so that the gas does not encounter a sealed region.

The advantage is a shorter infiltration time compared to isothermal CVI, typically 120 hours. For instance, the centre of a 3 cm-thick carbon tubular preform was densified with carbon up to 93% after 50 hours with a conversion methyltrichlorosilane (MTS) to SiC of 20-30% [196].

One preform can be densified per run and controlling the deposition is difficult without a sophisticated and hence expensive temperature control system [11].

### **2.5.2.2 Forced flow, isothermal (IFCVI) and thermal gradient (TFCVI)**

In the IFCVI process [197-199], the temperature is constant but a pressure gradient is imposed across the thickness of the preform. The most explored sub-variant is the thermal-gradient forced-flow CVI (TFCVI) [14, 84, 195, 200-205] which combines the benefits of thermal gradient and pressure gradient CVI. The reactants flow over the cooler surface both axially and radially from the cooler side to the hotter side. The deposition is led by the thermal front moving toward the cooler region, preventing the entrance side from sealing. The process is terminated when the pressure gradient becomes too large: it means that the flow passages are closed and the porosity is largely filled. The result is homogeneous density in a relatively short processing time of 10-40 hours [9], with a density above 90% [201] and a deposition rate of up to 1 mm h<sup>-1</sup>.

The gas flow and temperature controls are very complex, especially when processing multiple and/or complex-shaped components.

### 2.5.2.3 Pulsed-pressure (PCVI)

In this alternative method, the flow is pulsed inside the chamber. A pump evacuates the chamber and then the reactants are injected very quickly, this procedure is repeated several times. The result is that reagents flow into and out the preform cyclically [11, 206, 207]. The freshness of the gas feed ensures a uniformity of the gas composition throughout the volume of the chamber and removes all by-products which may become trapped in the preform. In addition, if the preform is fed periodically with different composition of reactants, it is possible to prepare multi-layered ceramics [208]. Another variation is to combine the PCVI with the thermal-gradient CVI (PTCVI) which has been demonstrated to be capable to generate an inverse density gradient and hence overcome the formation of the crust [200].

Although this variant of CVI is theoretically attractive, the high cost of the equipment reduces its usefulness.

### 2.5.2.4 Microwave enhanced chemical vapour infiltration (MECVI)

The heating of the preform is performed by microwaves and as a result of the nature of the volumetric heating, coupled with surface losses due to radiation and conduction, an inverse temperature profile is generated. This concept is explained in section 2.8.5. As a result of the inverse temperature profile, deposition starts preferentially in the centre and moves toward the surface of the preform. Premature pore closure due to crusting is avoided and the densification can occur as little as in 48 -72 hours. This technique can only be used if the sample absorbs microwaves; however, this will also be discussed in some detail,

in Section 2.8. A variation, patented by Honeywell [209], of the microwave CVI technique exploits the use of radio-frequencies [209]. Golecki et al. [210] reported the densification up to 76% of C-C disk (10.8 cm o.d. x 4.4 cm i.d. x 3.0 cm thick) in 50 hours using RF heating at frequencies of 4.9 to 8.6 kHz and power in the range 8.8 to 13.2 kW. A model [211] has shown that a carbon preform can be infiltrated with carbon using methane as the precursor at  $\sim 1100^{\circ}\text{C}$  in 60 hours with a reduction in porosity of 91%. In the conventional CVI model the same result is achieved in 300 hours. Experimental work has also been undertaken and subsequently exploited by Dunlop Aviation [19]. Table 9 below focuses on some experiments for the fabrication of  $\text{SiC}_f/\text{SiC}$  composites by the CVI route

Table 9. SiC deposition by several CVI routes

CVI variation	SiC fibre preform	Optimum parameters	Results achieved	Authors
ICVI	Nicalon cloth 200 mm long	T = 980°C P = 2-13 kPa $P_{\text{tot}}/P_{\text{MTS}} = 6.3-14$ $Q_t = 170-450 \text{ ml min}^{-1}$	N/A	[212]
	Carbon disc $\Phi = 14.0 \text{ mm}$ , L = 23 mm 2D weaves	N/A	$\rho_r = 90 \pm 2\%$ Machining	[38]
	Hi-Nicalon (PyC coated) 3D braided	T = 1100°C P = 2-3 kPa $\text{H}_2/\text{MTS mol} = 10$ Argon as diluent gas	$\sigma_{s(\text{RT})} = 920 \text{ MPa}$ $\sigma_{s(1000^{\circ}\text{C})} = 1010 \text{ MPa}$ $K_{\text{IC}} = 41.5 \text{ MPa m}^{1/2}$ brittle fracture at high temperature	[49]
	Tyranno ZMI fibres 100 nm BN coating	T = 1000°C P = 5 kPa 720 hours. 2 hours post treatment	5.2% open porosity $\sigma_u = 134 - 377 \text{ MPa}$ $K_{\text{IC}} = 5.2 - 15.2 \text{ MPa m}^{1/2}$	[194]
	Ni-Nicalon Types S and Tyranno SA3, PyC coating	N/A	$\sigma_u = 266-288 \text{ MPa}$ E = 218-230 GPa	[48]
IFCVI	Nicalon fibres $V_f = 46 \text{ vol}\%$	T = 1098°C P = 6.65 kPa $\text{H}_2/\text{MTS molar ratio}=6$ $Q_{\text{tot}} = 2400 \text{ ml min}^{-1}$	$\rho_r = 75\%$ t = N/A	[199]
	Tyranno-SA/ Hi-Nicalon $\Phi = 75 \text{ mm}$ L=12.5 mm	T= 1200°C P inlet = 100 kPa P outlet=70 kPa $Q_{\text{H}_2} = 750 \text{ ml min}^{-1}$ $Q_{\text{MTS}} = 0.5 \text{ g min}^{-1}$	$\rho_r = 72-89\%$ $\sigma_{\text{elastic}}$ of Tyranno SA composites = 93-110 MPa $\sigma_{\text{elastic}}$ of Hi-Nicalon composites = 140-152 MPa	[213, 214]
	Tyranno SA3 Disc $\Phi = 40 \text{ mm}$ , L=20mm $V_f = 43\%$ 100 nm PyC/SiC multilayer	T = 1000°C, P =15kPa 15 hours	$\rho_r = 78.2 - 90.4 \%$ $\sigma_u = 281 - 606 \text{ MPa}$ E = 135 - 156 GPa	[50]

Table 9. (continued)

CVI variation	SiC fibre preform	Optimum parameters	Results achieved	Authors
IFCVI	Tyranno SA3 $V_f = 35.2\text{-}39.9\text{ vol\%}$ PyC coated	$T = 1050^\circ\text{C}$ P outlet = 5 kPa P inlet=100 kPa $Q_{H_2} = 450\text{ ml min}^{-1}$ $Q_{MTS} = 0.3\text{ g min}^{-1}$ $\alpha \sim 10$	$\rho_r = 85.6 - 86.6\%$ $\sigma_u = 201 - 304\text{ MPa}$ $E = 192 - 252\text{ GPa}$	[215]
TFCVI	C Disc $\Phi = 44.5\text{ mm}$ , $L = 12.7\text{ mm}$ Two step process	Top $T = 1200^\circ\text{C}$ Bottom $T = 950^\circ\text{C}$ $Q_{H_2} = 500\text{ ml min}^{-1}$ $Q_{MTS} = 45\text{ ml min}^{-1}$	$\rho_r = 90 \pm 2\%$ $t = 10\text{ h}$	[201]
	C Disc $\Phi = 246\text{ mm}$ , $L = 12.7\text{ mm}$ $V_f = 33\text{ vol\%}$	Top $T = 1100^\circ\text{C}$ P = 6.6 Pa $Q_{H_2} = 5000\text{ ml min}^{-1}$ $Q_{MTS} = 5\text{ g min}^{-1}$	$\rho_r = 85\text{-}90\%$ $t = 40\text{ h}$ uniform deposition	[204]
	C Disc $\Phi = 51.0\text{ mm}$ $V_f = 39\text{ vol\%}$	Top $T = 1200^\circ\text{C}$ Bottom $T = 650\text{-}1010^\circ\text{C}$	$\rho_r = 82\%$ $t = 20\text{ h}$	[198]
	tubular Nextel 312 $\Phi$ (outer) = 66.4 mm $\Phi$ (inner) = 50.8 mm $V_f = 34.4\text{ vol\%}$	Top $T = 1203^\circ\text{C}$ Bottom $T = 1087^\circ\text{C}$ P = n/a $Q_i = 6\text{ l min}^{-1}$ $\alpha \sim 5$	$\rho_r = 80\%$ $t = 32\text{ hours}$	[14]
	Nicalon NL200 $V_f = 37\text{ vol\%}$ $\Phi = 50.8\text{ mm}$ , $L = 45\text{ mm}$	Top $T = 1200^\circ\text{C}$ Bottom $T = 750^\circ\text{C}$ P outlet = 101 kPa P inlet = 113-170 kPa $\alpha \sim 12$	Centre $\rho_r = 85\%$ $t = 36\text{ hours}$	[203]
PCVI	C plate Hollow disk Initial density 71%	$\text{SiCl}_4\text{-CH}_4\text{-H}_2$ system $T = 900\text{-}1100^\circ\text{C}$ Hold time = 1.5 s Cycle = $10^4\text{-}10^5$	$\rho_r = 93.4\%$ $t = 8.4\text{ h}$	[216]

### 2.5.2.5 Consideration of the residual porosity and multi-stage approach

Any of the composites made by any of the CVI techniques typically still contain a porosity of 10-20% [198, 201]. Two types of porosity [16, 217-219] can be identified in an infiltrated 2-dimensional fibrous preform:

- Intertow. Large macropores between the bundles (tows) with a typical size of 100-500  $\mu\text{m}$ .
- Intratow. Micropores of 10-20  $\mu\text{m}$  between the fibres.

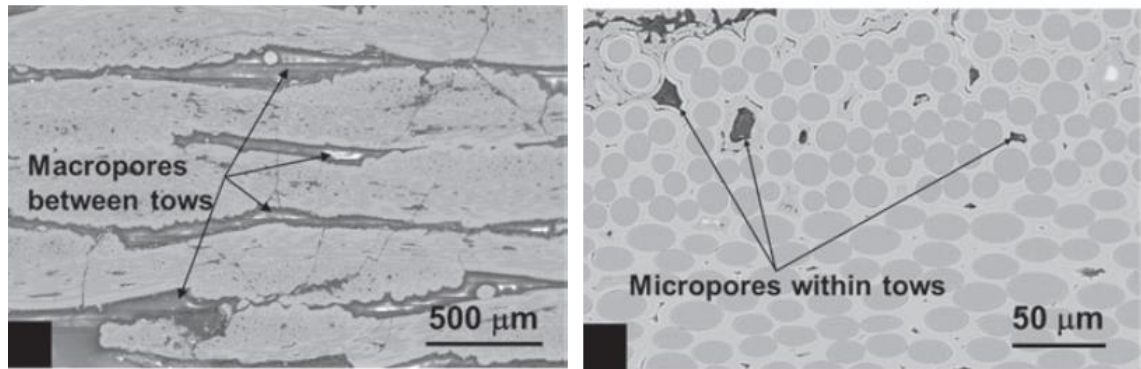


Figure 2-21. Macroporosity (on the left) and microporosity (on the right) [155, 220].

Firstly, when the minimum percolation threshold for transport through the pore structure is reached [155], infiltration become more difficult and, secondly, the infiltration of macropores (up to 500  $\mu\text{m}$  in size) can simply take too much time. Unfortunately, such macropores are the main cause of the loss of mechanical performance. They are difficult to eliminate because they result from the lay-up of the fibre sheets. When the composite reaches 70% of theoretical density, the remaining porosity is mainly due to the macropores. This is the reason why densification up to 80-90% is time and costly consuming [221].

To reduce these infiltration limitations, multi-stage processes have been investigated. [222]. A possible approach is the preinfiltration of the macropores. For instance, a reduction of the porosity to 15% has been reached through a preinfiltration with SiC slurry and then repeated PIP [150, 169, 179]. Other experiments combined CVI, PIP and MI as reported in Table 10.

In general, CVI is a very versatile technique and it is suitable for a wide variety of hybrid processes. A further example is the fabrication of SiC<sub>f</sub>/SiC by vapour silicon infiltration (VSI): a SiC<sub>f</sub> 3D preform has been infiltrated with carbon by CVI using propylene as precursor and then converted to SiC with Si vapour. The

properties achieved were an open porosity of 5-7%, a flexural strength of 250-280 MPa and a fracture toughness of 16 MPa m<sup>1/2</sup> [223].

Table 10. Combination of PIP and CVI for SiC<sub>f</sub>/SiC fabrication

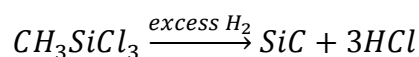
Type of process	Material used	Initial stage	Process conditions	$\rho_r$ (%)	Mechanical properties	Limitations
CVI+PIP [224]	PyC coated Nicalon fibres PCS with nanosized SiC powder - xylene	ICVI	PIP: P = 5 bar T = 30 min 5 to 7 cycles Atm.= Ar/N <sub>2</sub>  CVI: T=1100°C P=2.7 kPa MTS/H <sub>2</sub> = 0.02 t=24h	85%	E = 51.5 GPa $\sigma_r$ = 360 MPa	Residual porosity still high
PIP+CVI [169]	PyC coated Nicalon fibres PCS - hexane MTS/H <sub>2</sub>	Impregnation with boiling PCS for 20 min	CVI: T=1200°C P=10 kPa, Q <sub>MTS</sub> =100 ml min <sup>-1</sup>  PIP: T=1000°C Atm.= Ar 6 cycles	82% (71% without CVI)	$\sigma_u$ = 296 MPa K <sub>1c</sub> =10.9 MPa m <sup>1/2</sup> (without CVI) $\sigma_u$ = 224 MPa K <sub>1c</sub> =6.2 MPa m <sup>1/2</sup> )	Low density Vulnerability to oxidation Pores in the range 100-150 $\mu$ m
CVI+PIP [2]	PyC coated Nicalon fibres and PCS	IFCVI	H <sub>2</sub> /MTS molar ratio = 10 T = 1100-1200°C Atm = N <sub>2</sub>	71%	$\sigma_u$ = 175-200 MPa (RT) $\sigma_u$ = 100 MPa (1000°C)	High porosity Brittleness at high T
CVI+PIP [225]	PyC coated Ni-Nicalon and PCS	ICVI	CVI : T = 950°C P = 0.1 kPa, 30 hours PIP: 7 cycles of infiltration, curing and pyrolysis	83-87 %	$\sigma_u$ = 555-627 MPa K <sub>1c</sub> =12-38 MPa m <sup>1/2</sup>	Microstructure discontinuity and porosity still high although 7 cycles of PIP
CVI+ (slurry infiltration) + MI [46]	Si-doped BN coating iBN Syramic fibres	ICVI	n/a	98%	E = 210-250 GPa $\sigma_u$ = 310-450 MPa	~20% silicon 4 steps involved in the manufacturing process
CVI+PIP [46]	Si-doped BN coating iBN Syramic fibres	ICVI	n/a	84%	E = 200 GPa $\sigma_u$ = 330 MPa	Residual porosity
CVI+PIP [168]	NL 207 Nippon Carbon 100 nm PyC coated	ICVI	CVI: T=950°C P= 0.1 kPa, 20 hours PIP: 7 cycles of infiltration, curing and pyrolysis	72%	$\sigma_u$ = 247 MPa	Residual porosity

## 2.6 Chemistry of the CVI process in SiC<sub>f</sub>/SiC composites

The chemistry, transport phenomena and thermodynamics of a chemical vapour infiltration process depend on a large number of parameters such as the gas composition of the gaseous mixture, temperature, partial pressure of the gases, nature of the substrate or the architecture of the preform [193, 226]. Heterogeneous reaction, intermediates, by-products, gaseous species and co-deposit are commonly formed in CVI/CVD processes, reducing the yield. It must be taken into account that the thermodynamic studies are based on the assumption of the system at equilibrium and the kinetics are not taken into account. CVD and CVI are processes far from equilibrium, which implies the potential for disagreement between predictions and actual experimental results.

SiC can be formed by the reaction of silane with a carbon source ( $\text{SiH}_x + \text{C}_y\text{H}_z$ ), chlorosilane with a carbon source ( $\text{SiCl}_x + \text{C}_y\text{H}_z$ ) or (chloro)carbosilane such as methyltrichlorosilane ( $\text{CH}_3\text{SiCl}_3$  or MTS), dimethyldichlorosilane ( $(\text{CH}_3)_2\text{SiCl}_2$ ), or trimethylchlorosilane ( $(\text{CH}_3)_3\text{SiCl}$ ) in the presence of  $\text{H}_2$  and a hot surface (for CVD) or porous network (CVI) [227].

Amongst these, MTS is the preferred precursor because of the presence of one atom of silicon and one of carbon in the molecule. The deposited solid is stoichiometric  $\beta$ -SiC [228]. The reaction can be expressed by:



To obtain a fine and pure solid, the deposition has to be managed in a reductive atmosphere. It is common to use a carrier gas such as Ar,  $\text{N}_2$  or  $\text{H}_2$ . These are

not only diluent gases, but they have an effect on the mechanism of deposition and on the physiochemical properties of the deposit [229, 230].

Equation **Error! Reference source not found.** is the overall reaction; it consists of multiple heterogeneous and homogeneous steps. Several reaction mechanisms have been proposed from thermodynamic and kinetics considerations [231-235] and/or from experiments of gas chromatography [236] infrared [237] and ab-initio calculations [238]. As a general belief, there is the breakage of the MTS molecule into radicals ( $\text{SiCl}_3$  and  $\text{CH}_3$ ) because Si-C bond has the lowest dissociation enthalpy in the MTS molecule and for this reason it will break more easily than Si-Cl and Si-H. Then, the process proceeds with separate pathways for silicon and carbon and only at the final stage, on the substrate, there is the combination of Si and C and the desorption of HCl. Equations 2-2 to 2-15 show a model [203] of the chemical formation of SiC from MTS.

In the gas phase:

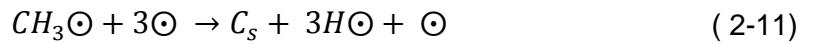
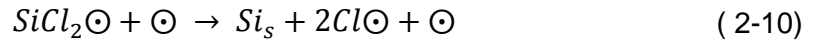


At the substrate surface ( $\odot$  is a free surface site):

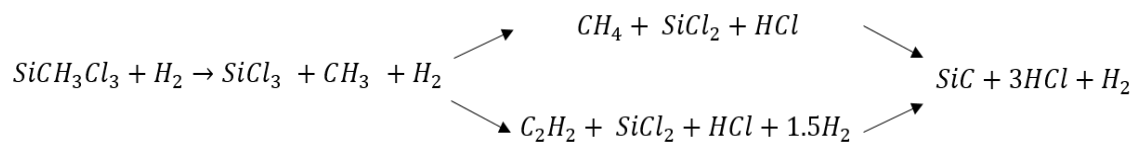




Surface reaction and desorption:



Langlais [239] proposed a dependence of the deposition mechanism from temperature. Below ~875°C MTS decomposes to a little extent and it is directly adsorbed onto the substrate following first-order kinetics. At higher temperature, MTS decomposes to fragmented groups, which subsequently adsorb on the substrate and react to form SiC. In the range ~875-1025°C the main carbon-bearing species is methane which is substituted from acetylene at higher temperatures [228]. The role of C<sub>2</sub>H<sub>2</sub> has been confirmed from kinetics studies [228, 233, 235, 240] and found in the gas phase by Ivanova et al. as reported in [203].



Other studies proposed the formation of complex cyclic-hydrocarbons containing more than three atoms of silicon [241] and carbochlorosilanes [238].

The purity and the stoichiometry of the SiC deposit depends on some process parameters, in particular the temperature and the gas phase composition. The main codeposits experimentally observed are free silicon and carbon. Silicon is deposited at low temperatures below 1000-1050°C [236] [227]. and according to some authors, only above 1400°C, is the SiC totally pure [242]. Low  $\alpha$  (high fraction of MTS in the gaseous mixture) reduces the amount of silicon because of an etching action of the HCl [243], but a very high fraction of MTS, combined with high temperature, can promote the codeposition of carbon. Phase diagrams shown in Figure 2-22 reports the thermodynamic yields of Si, SiC and C from MTS decomposition as function of  $\alpha$  at different temperatures.

The deposition of silicon carbide rather than secondary phases like free carbon and silicon is promoted when the ratio  $\alpha = \frac{P_{H_2}}{P_{MTS}}$  is in the range 10-1000 [193, 233, 234, 244] as shown in the Figure 2-22.

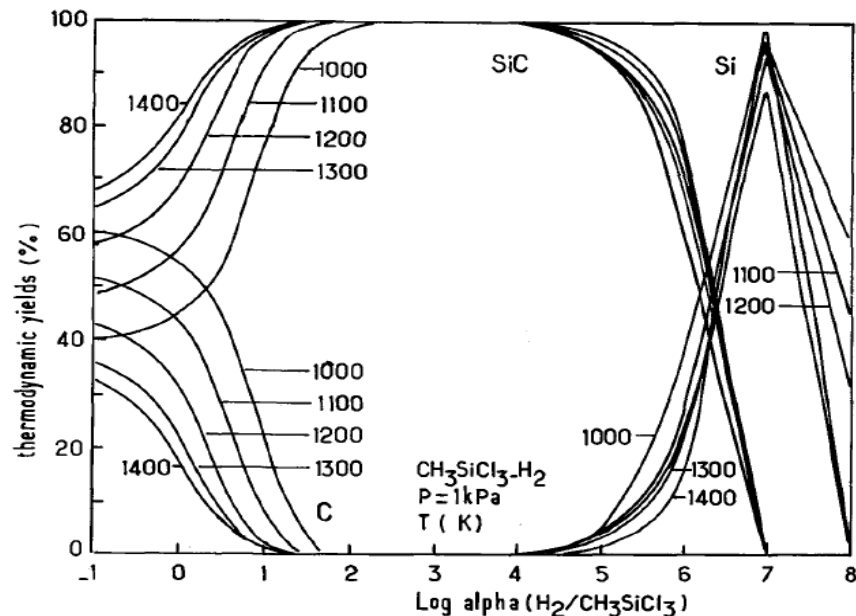
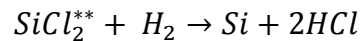


Figure 2-22. Thermodynamic yields for the solid deposition of SiC as function of hydrogen-methyltrichlorosilane ratio [193]. Temperature is in K.

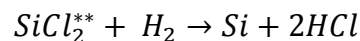
As observed by Zhang et al. [236], an additional factor that needs to be taken into account is the ratio of the available area for the deposition,  $A_s$ , and the volume in which the reactants are confined,  $V_R$ . Stoichiometric SiC is generally favoured above 1050°C and/or at high  $A_s/V_R$  ratio. This is of particular interest for CVI where the specific surface deposition area is much larger than the substrate area for process CVD.

As mentioned earlier,  $H_2$  is not only a carrier gas. In the same conditions of pressure and temperature, the morphology of the deposit changes and the roughness of the surface increases [229, 230]. In a surface reaction mechanism proposed from Loumagne et al. [234], hydrogen is essential in the collision with the  $SiCl_2^{**\ddagger}$  adsorbed on the substrate, according to the reaction



A change in the amount of  $H_2$  affects the amount of codeposited silicon.

Lee et al. [229] observed that the use of argon or nitrogen led to the codeposition of carbon, In their model the methane is adsorbed on the surface and would react with the chlorine ( $Cl_2$ ) formed in the gas phase according to the reaction:



Reduced  $H_2$  content may result in the increase of relative amount of  $Cl_2$  in the gas phase. Consequently,  $N_2$  or Ar addition could lead to the lack of reactive  $H_2$  gas and to the excess carbon deposition.

---

<sup>‡</sup> The symbol \*\* indicates the adsorption of  $SiCl_2$  on the hollow bridge sites of the growing  $\beta$ -SiC in the direction [111] [234]

Note that MTS has to be handled carefully because it reacts with water, moist air, or steam to produce heat and toxic, corrosive fumes of hydrogen chloride, potentially dangerous for the users and detrimental for the equipment. A less toxic process would be preferable, but the stoichiometric SiC deposited makes MTS the favourite gaseous precursor of SiC.

### 2.7 Transport phenomena

The complex mechanism of the deposition of a solid within a substrate or preform has five distinctive steps [12, 193, 245, 246] as shown in Figure 2-23:

- i. Diffusion of the fresh gas precursor through a boundary layer wetting the substrate.
- ii. Diffusion of the reactants into the inner surface of the pore.
- iii. Surface reaction of the gaseous precursor on the heated substrate. The by-products are formed.
- iv. Desorption of by-products out of the pore.
- v. Release of the by-products through the boundary layer.

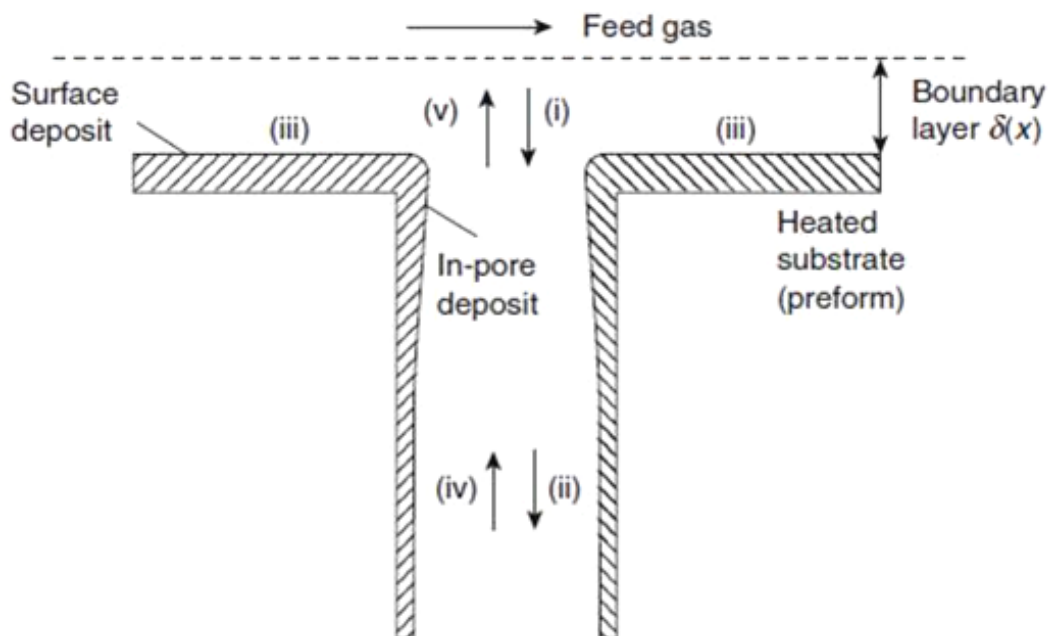


Figure 2-23. Mass transfer mechanism in chemical vapour infiltration. Steps (i), (ii), (iv) and (v): mass transfer by diffusion. Steps (iii): chemical reaction [193].

Diffusion phenomena control the rate of the deposition in stages (i), (ii), (iv) and (v); in stage (iii) the deposition on the surface of the pore is controlled by the surface reaction. The slowest step determines the deposition rate [12]. Temperature, pressure and gas flow rate govern the process and their variation is responsible for the transition from a regime of surface kinetics to a domain where the deposition is controlled by mass transfer [12, 193].

From this discussion, the CVI should be performed under conditions where the deposition is limited by surface kinetics [247] (step iii) and not by mass transfer of the reactants/products in the vapour phase. If this requirement is not met, the deposition near the entrance of the pore will be favoured with respect to the interior of the pore, resulting in a premature pore sealing and, hence, high residual porosity. This behaviour is typical of isothermal and isobaric chemical vapour infiltration [183, 205, 248].

On this basis, CVI has to be performed at low temperatures (chemical vapour processes are thermally activated) and low pressure (enhanced diffusion along the length of the pore). Unfortunately, such conditions typically lead to reduced thermodynamic yield and low matrix growth rate [193]. Since there are two competing mechanisms: diffusion along the pores in steps ii and iv and surface reaction in step iii, in which reactants are adsorbed and by-product released, some dimensionless parameters can be used to assess the prevalent mechanism: for instance the Thiele modulus  $\theta$  [249] may estimate the prevalent mechanism in the deposition of a solid matrix in a porous preform. It is defined as:

$$\theta = \left( \frac{2k_s L^2}{D_{eff} d_p} \right)^{0.5} \quad (2-15)$$

where  $k_s$  is the first-order reaction rate,  $L$  is the length of a cylindrical pore,  $d_p$  the diameter and  $D_{eff}$  the gas diffusivity, which includes both the Fickian and the Knudsen diffusion. The latter can be neglected for pores of larger dimensions (> 5  $\mu\text{m}$ ). The mass transfer equation of a species in the pore shows that the smaller  $\theta$  is, the more uniform the deposition rate.

If the diffusion is Fickian,  $\theta$  decreases at lower pressure [192] and the infiltration is more uniform. In other words, the concentration gradient along the pore channel is lower and hence the pore closure is avoided or delayed. Fitzer et al. [227] showed that a pore of 10 micrometres in radius has a maximum infiltration depth  $L_{max}$  of 7 mm at 800°C, whilst only 1 mm at 1000°C. Note however, that this is a simplified model which does not take into account the change of entities during the infiltration.

## **2.8 Microwave enhanced chemical vapour infiltration (MECVI)**

### **2.8.1 Nature of microwaves**

Microwaves are a form of electromagnetic radiation with wavelengths ranging from as long as one meter to as short as one millimetre, equivalent to 300 MHz – 300 GHz in the frequency domain [250]. The range for microwave heating is narrower, mainly between 0.4-40 GHz, see Figure 2-24.

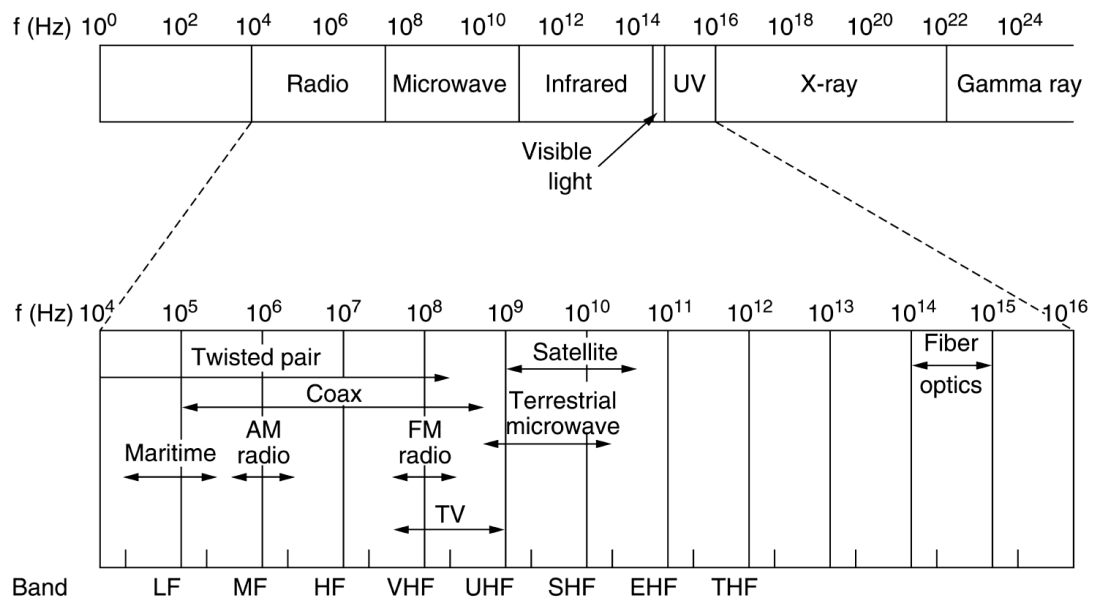


Figure 2-24. Electromagnetic spectrum and microwave radiation [251].

Microwaves are coherent and polarised waves. They are known as transverse electromagnetic waves (TEM) since the electric field and the magnetic field are perpendicular to each other and are both perpendicular to the axis of propagation.

An electric field applied to a dielectric material, results in the formation of dipoles. The dipoles can move and become aligned to the direction of the electric field. This phenomenon is called polarization of which there are four different types [252, 253]:

- i. Electric polarization: a temporary distortion of the electronic arrangement of the atoms.
- ii. Ionic polarization: the applied electric field unbalances the charge distribution of a molecule. Ionic bonds are deformed, which results in a redistribution of the charge in the material due to the movement of cations and anions.

iii. Dipole (orientation) polarization: permanent dipoles are oriented under an applied field.

iv. Maxwell-Wagner polarization affects the interface between the components of an heterogeneous system

Microwave fields tend to interact most with dipole polarization. When an electric field is applied the dipole tends to follow the reversals of the applied field. However there is a characteristic lag time between the polarization and the reversal of the electric field, known as the relaxation time. This time is due to the dissipation of energy as heat within the material [252]. This mechanism is responsible for microwave heating.

The energy conversion and power absorbed as heating rate can be derived from the Maxwell equations in differential form [254-256]:

$$\nabla \times \mathbf{H} = \mathbf{J} + \varepsilon \frac{\partial \mathbf{E}}{\partial t} \quad (2-16)$$

$$\nabla \times \mathbf{E} = -\mu \frac{\partial \mathbf{H}}{\partial t} \quad (2-17)$$

where  $\mathbf{E}$  is the electric field vector,  $\mathbf{H}$  the magnetic field,  $\mu$  the complex magnetic permeability and  $\varepsilon$  the complex dielectric permittivity.

The time periodic sinusoidal electromagnetic field and can be written as [254, 255]:

$$\mathbf{E} = E_c e^{-i\omega t} \quad (2-18)$$

$$\mathbf{H} = H_c e^{-i\omega t} \quad (2-19)$$

$$\mathbf{J} = J_c e^{-i\omega t} \quad (2-20)$$

The Poynting vector is defined [254, 255] as:

$$\mathbf{S} = \mathbf{E} \times \mathbf{H} \quad (2-21)$$

It appears in the Poynting theorem as an electromagnetic field energy-conservation law [255]:

$$-\frac{\partial w}{\partial t} = \mathbf{J} \cdot \mathbf{E} + \nabla \cdot \mathbf{S} \quad (2-22)$$

The rate of energy stored in the electromagnetic field within the volume  $V$  of the media is equal to the sum of power loss due to heating and the net power supplied to the enclosed surface,  $A$ .

It can be demonstrated that the time-averaged power transmitted,  $\langle w \rangle$ , across the surface  $A$  of a volume  $V$  is given by the real part of the integral of the equation [256, 257] :

$$\langle w \rangle = \text{Re} \left( \frac{1}{2} \oint_A \mathbf{E} \times \mathbf{H}^* d\mathbf{A} \right) \quad (2-23)$$

Where the symbol \* denotes the complex conjugate.

The complex dielectric and magnetic properties of the material are [256, 257] :

$$\varepsilon = \varepsilon' - i\varepsilon'' \quad (2-24)$$

$$\mu = \mu' - i\mu'' \quad (2-25)$$

It can be derived [256, 257] that:

$$\langle w \rangle = Re \left( \frac{1}{2} \int_V (\mathbf{J} \cdot \mathbf{E}^* - \omega \varepsilon'' \mathbf{E} \cdot \mathbf{E}^* - \omega \mu'' \mathbf{H} \cdot \mathbf{H}^*) dV \right) \quad (2-26)$$

The heat loss due to the Joule effect can be defined [256] as:

$$\mathbf{J} = \sigma_e \cdot \mathbf{E} \quad (2-27)$$

where  $\sigma_e$  is the conductivity. For a dielectric the magnetic permeability is very small and the last term can be neglected. Hence:

$$\langle w \rangle = Re \frac{1}{2} \int_V (\sigma_e - \omega \varepsilon'') \mathbf{E} \cdot \mathbf{E}^* dV \quad (2-28)$$

Finally:

$$\langle w \rangle = \frac{1}{2} (\sigma_e - \omega \varepsilon'') |\mathbf{E}|^2 \quad (2-29)$$

The permittivity can also be expressed in the form:

$$\varepsilon_r = \frac{\varepsilon}{\varepsilon_0} = \varepsilon_r' - i \varepsilon_r'' \quad (2-30)$$

where  $\varepsilon_0$  is the vacuum permittivity and the subscript  $r$  indicates the relative permittivity of the medium.

The dielectric loss can be represented by the dielectric conductivity  $\sigma_{eff}$  [256, 258] :

$$\varepsilon_r''(\omega) = \frac{\sigma_{eff}}{\omega\varepsilon_0} \quad (2-31)$$

The power of heating per unit of volume which equals the absorbed microwave power is [257]:

$$\langle w \rangle = \sigma_{eff} |\mathbf{E}|^2 \quad (2-32)$$

Not all materials can be heated by the application of a microwave field because the heating depends on the ability of the dipoles to follow the electromagnetic field [257, 259].

The interaction and absorption of energy from microwave radiation is determined by the complex permittivity. The real part  $\varepsilon'$  is the dielectric permittivity and it is a measure of the electrical polarization of the material, which indicates the attitude of the dipoles to respond to the dielectric field; the imaginary  $\varepsilon''$  part represents the dielectric loss factor, in other words the ability of the dipoles to absorb energy from the electromagnetic field and dissipate it as heat [252]. Because of the absorption, the electromagnetic field decreases as the wave penetrates into the material. The dissipation is characterized with the loss tangent [256, 257]:

$$\tan\delta = \frac{\varepsilon''}{\varepsilon'} = \frac{\varepsilon_r''}{\varepsilon_r'} = \frac{\sigma_{eff}}{2\pi f \varepsilon_0 \varepsilon_r'} \quad (2-33)$$

For  $\tan\delta$  values above 0.1, the material strongly reflects the radiation and inhibits the heating. For very low values such as in pure boron nitride alumina and silicon nitride,  $10^{-3}$ - $10^{-4}$ , the material is regarded as microwave transparent [260]. Therefore, the materials able to be heated by microwave have an intermediate value. From equations 2-33 and 2-34, the following equation can be derived:

$$\langle w \rangle = |E|^2 \sigma_{eff} = 2\pi f \varepsilon_0 \varepsilon_r' \tan \delta |E|^2 \quad (2-34)$$

The equation is valid only for very thin materials [261]. In fact, as the electromagnetic wave transverses the medium, the energy penetrates into it and the power absorbed is a function of the distance  $x$  from the surface [256]:

$$w(x) = P_0 e^{-\frac{2x}{d}} \quad (2-35)$$

where  $P_0$  is the power transmitted at the surface and  $d$  is the skin depth: it is the distance from the surface at which the power drops to  $1/e$  of its surface value.

It can be demonstrated that the skin depth [261] is:

$$d = \frac{c}{\omega} \sqrt{\frac{2 \left[ 1 + \sqrt{1 + (\tan \delta)^2} \right]}{\varepsilon' (\tan \delta)^2}} \quad (2-36)$$

Thus, a detailed awareness of the dielectric properties of the material is required.

### **2.8.2 Microwave radiation and applications in ceramics**

Microwave processing is a well-established process in the food, polymer, rubber and wood industries [262, 263]. The kitchen microwave oven is now ubiquitous throughout the world. In the last four decades, microwave processing has been investigated for a range of ceramic forming routes including drying, sol-gel processing, slip casting, calcining, joining, sintering and chemical vapour infiltration [34, 252, 255, 257, 259-261, 264-272], amongst others.

Most microwave applications utilize the conversion of the microwave energy into a thermal form, i.e. the achievement of microwave heating. One important advantage of microwave heating is the volumetric nature of the energy absorption

in many materials. In contrast to conventional furnaces, in which the heat is generated by conduction or radiation, microwave energy is directly absorbed into the material. Consequently the heating rate can be much higher with a resulting reduction in processing time. Improvements in quality, such as less defective microstructures have also been claimed [273]. It is known that, in general higher heating rates can lead to finer microstructures, as shown by other processes such as spark plasma sintering [274].

### 2.8.3 Generators and applicators of microwaves

Microwave systems consist of three main components:

- source;
- transmission line;
- applicator.

#### 2.8.3.1 Microwave generator

Microwave sources include magnetrons, travelling wave tubes and klystrons. Amongst these sources, the magnetron is the most common and lowest cost available.

A magnetron consists of a metallic vacuum tube with a filament running down through the centre acting as cathode. The metal block of the tube acts itself as anode. The space within the tube is called cavity resonator or interaction space. Around the tube there are some circular cavities connected to the interaction space through some openings. In Figure 2-25 a schematic of a magnetron is shown. The configuration of a magnetron resembles a *revolver*.

The electrons emitted from the cathode through thermionic emission spiral outward in a cycloid as consequence of the Lorentz Force. As electrons sweep past these openings, they induce a resonant radio field in the cavity. A portion of the field is extracted with a short antenna that is connected to a waveguide.

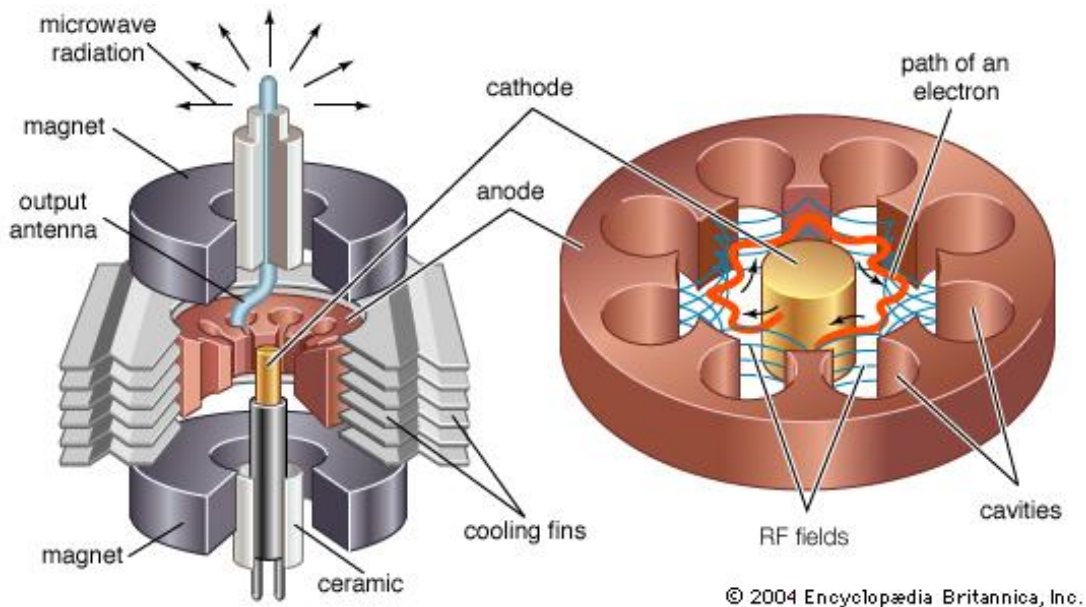


Figure 2-25. Schematic of a magnetron [275].

### 2.8.3.2 Waveguides

The portion of the field is extracted with a short antenna, which is connected to a waveguide, often a rectangular cross-section, metallic hollow tube. The waves can propagate along the waveguide as linear combination of transverse electric modes (TE) or transverse magnetic modes (TM) and transmitted to the applicator.

Transverse modes of electromagnetic waves are electromagnetic field patterns that occur because of boundary conditions imposed on the wave by the waveguide [257]. Modes in waveguides can be distinguished as transverse electromagnetic (TEM), transverse electric (TE) and transverse magnetic (TM) modes; hybrid modes of TE and TM are also possible [257].

In TE modes there is no electric field in the direction of propagation, whilst in TM modes the magnetic field is zero along the direction of propagation.

### 2.8.3.3 Microwave applicator

Commonly, microwave applicators are closed chambers with metal walls. The electromagnetic waves confined in the cavity reflect multiple times, forming standing wave patterns (modes) [257]. Such constructive interference leads to an amplification of the field strength when the round-trip distance is equal to a positive integer of the wavelength.

Applicators commercially available include single-mode and multi-mode versions amongst others.

#### Single-mode applicator [257]

A single mode applicator can support only one resonant mode. This implies that the size of a single mode applicator is approximately that of the wavelength. In a single-mode applicator there are regions with high and low field strengths and, hence, the heating pattern is not homogeneous. In general a single mode cavity has a high energy field corresponding to the location of high field strength. The possibility of focusing the microwave field at a given location has been widely explored for the joining of ceramics [276, 277] and the studying of the curing kinetics of thermosetting resins [278].

Although single mode applicators have some applications and can reach high field strength, they require a fine tuning and suffer from geometrical limitations and non-uniform heating that does not adapt well to the industrial heating applications.

### Multi-mode applicator [257]

In multimode applicators a number of modes are excited simultaneously. The size of the cavity is larger since there are resonant modes [261], as can be deduced from the equation for the resonant frequencies in a rectangular cavity:

$$f_{nml} = c \left[ \left( \frac{l}{2d} \right)^2 + \left( \frac{m}{2b} \right)^2 + \left( \frac{n}{2a} \right)^2 \right]^{1/2} \quad (2-37)$$

Where  $a$ ,  $b$ ,  $d$  are the dimension of the cavity;  $c$  the speed light;  $n$ ,  $m$ ,  $l$  the integer of half-sinusoids variations of the standing wave pattern.

The advantage of this regime is the more homogeneous heating pattern due to the presence of multiple hot spots in the cavity. Further improvements of the microwave power uniformity can be achieved by introducing reflector fans (mode stirrers) which mix the modes and redistribute the field uninterruptedly or positioning the sample (also called charge or load) onto a turntable that rotates during the microwave processing. Mode stirrers and turntables create a time-averaged uniformity of the electromagnetic field [257].

#### **2.8.3.4 Temperature measurements**

Temperature measurement inside a microwave cavity is not trivial [279, 280]. This is mainly due to the possible interference of the microwave radiation with the measurement device. In several works, the interaction of the thermocouple metal sheath with microwaves has been reported, i.e. creation of discharge which locally affect the temperature [156]. An alternative to conventional temperature

measurements via a thermocouple is the use of an infrared (radiation from 0.7 to 14  $\mu\text{m}$ ) pyrometer [279]. This is based on non-contact measurements of the energy radiated from the sample with respect to irradiance and wavelength.

An optical head focuses the thermal radiation onto the detector and through the Stefan-Boltzmann law measures the temperature [281]:

$$j = \sigma_B \varepsilon^* T^4 \quad (2-38)$$

$j$  is the irradiance,  $\varepsilon^*$  the emissivity,  $\sigma_B$  the Stefan-Boltzmann constant and  $T$  the temperature.

Emissivity has a central significance to temperature determination by pyrometry [282]. The emissivity is the ratio of the power of the thermal radiation from a surface to the radiation from an ideal black surface at the same temperature. For the latter the emissivity is 1 [282]. Bodies that emit less thermal radiation than a perfect blackbody are called grey bodies and emissivity is lower than one.

The emissivity in IR-measurements is an input parameter and it is usually determined from a table (for silicon carbide, emissivity is in the range 0.83-0.96) [283]. The emitted radiation is a function of wavelength and can greatly vary with it. The so-called one-colour pyrometer is set on a single narrow spectral band. Due to Wien's law the peak frequency of the emitted radiation shifts with temperature and this shift is enhanced at high temperature. Thus, at high temperature, a single colour pyrometer can provide a value very far from the actual temperature [284].

In contrast, a two-colour pyrometer adopts an emissivity-free scheme that measures the radiance within two or more narrow spectral bands and tries to

determine the object temperature from the signal ratio, hence eliminating the influence of the emissivity [284].

### 2.8.4 Silicon carbide and microwaves

Silicon carbide has intermediate value of loss factor and hence will readily absorb microwaves at 2.45 GHz. At higher temperature the  $\tan\delta$  is mainly affected by ohmic type losses and the dielectric losses can be neglected [264]. Silicon carbide has been also used for processing materials that are microwave transparent. In fact, silicon carbide cylinders have been used as passive heating elements for MW-assisted organic synthesis [285, 286] and as susceptors for microwave hybrid heating systems [287]. Since SiC exists in a plurality of forms and crystalline arrangements, the absorption of microwaves of each system is very different. The main factors are affecting the dielectric properties of SiC are:

- form (e.g. wires, tubes, flakes, platelets, powder, whiskers and fibres)
- polytype (e.g. hexagonal or cubic)
- particle size or crystal size
- porosity
- dopants, defects and impurities
- heat treatment (e.g. annealing)

In addition, a great effect on the microwave absorption is due to temperature and frequency. The increase of dielectric loss with temperature is a general characteristic of ceramics and lower frequencies, generally, provide greater penetration depth.

Zhang et al. [288] investigated  $\beta$ -SiC nanowires with different stacking fault populations and stacking planes which was fabricated by simply varying the heating temperature. SiC nanowires with a higher stacking fault content leads to a greater population of dipoles and hence more energy dissipation. Similarly, from a comparison between microcrystalline powders and nanofibres [289], the enhanced microwave response of nanofibres was attributed to the high specific surface and the defect concentration.

Sugawara et al. [290] observed that in the range of frequency 0.8-11.2 GHz both for  $\alpha$  and  $\beta$ -SiC powders the relative permittivity and the dielectric loss increase with temperature and that this effect is enhanced at lower frequency. For the cubic phase  $\tan \delta$  was 0.5 at 1200°C whilst the hexagonal phase reached a maximum value of 0.2, indicating that the cubic silicon carbide is a better MW absorber [287, 290]. The work of Sugawara et al. [290] also focused on dependence of the MW heating from the particle size: the heating rates of the SiC particles increased with their radii. Special structures of SiC materials such as porous and hollow structures were proposed to improve absorption capacity [291]. The special structure increases specific inner surface areas which results in subsequent multi-reflection of the incident EM waves. Sun et al. [292] focused their work on the effect of dopants and impurities. A comparison of high-purity SiC nanopowder and powder doped with aluminium showed a decrease of  $\tan \delta$  from 0.7 to 0.1. Opposite results were obtained by nitrogen [293] and nickel doping [294]. Thermal treatments can also induce a change of dielectric properties [295]; the annealing above 1500°C of SiC nanopowders obtained by pyrolysis of polycarbosilane or laser pyrolysis substantially reduced the dielectric loss of SiC. Devlin et al. [17] observed that Si-C-O Nicalon fibre increased its

## Chapter 2. Literature survey

electrical resistivity by one order of magnitude when the  $\beta$ -SiC crystallite size increased from 1.8 to 2.0 nm following annealing in inert atmosphere at 1200-1300°C

SiC fibres (first generation) with significant Si-C-O amorphous phase result in different resistivity from crystalline  $\beta$ -SiC. Of Tyranno ZMI fibres Table 11 shows the skin depth and resistivity values of SiC based materials.

Table 11. Resistivity and skin depth of some silicon-based materials. Adapted from [11] and [296].

Material	Resistivity / $\Omega$ cm	Skin depth /cm (at 2.45 GHz)	Note
Nicalon fibre Low resistivity	0.5-5	0.07-0.23	Heated to > 1000°C
Nicalon fibre Ceramic grade	1000	3.2	Heated to > 1000°C
Nicalon fibre High resistivity	>10 <sup>6</sup>	>100	No significant heating
SiCf/SiC with Lox-M low resistivity	0.65	0.04	--
SiCf/SiC with Tyranno Lox-M high resistivity	45	200	--
Bulk $\beta$ -SiC	0.01-100	0.01-1	Appears to reflect microwaves at 1000°C
Silicon	10 <sup>5</sup>	32	Apparently increases matrix resistivity in Si-rich SiC

Microwave absorbing properties of Tyranno ZMI fibres (second generation) have been measured in the range 8.2-10.4 GHz. The loss factor was 0.93 at room temperature and increase to 1.02 at 1200°C [297]. When the 2 mm-thick ZMI/epoxy composites could absorb 80% microwave energy in the range of 2.65 GHz span, indicating the ZMI fibres are a favourable microwave absorber [297].

### 2.8.5 Volumetric heating

As mentioned in section 2.8.4, absorptive materials can be heated volumetrically. For conventional heating, the heat transfer mechanism is substantially conduction [261]. The temperature inside the sample is equal to temperature of the surface only when the heating time of the process  $\tau_T$  is very long [261]. In a conventional furnace, the energy is transferred by infrared thermal radiation with a frequency on the order of the terahertz, corresponding to a skin depth of hundreds of micrometres. In the volumetric microwave heating, the surrounding atmosphere is, however, not directly affected by the microwaves, and hence it is colder than the dielectric. The surface of the dielectric will therefore lose heat to its surroundings by conduction and/or radiation. This leads to the interior of microwave heated body often becoming hotter than the surface, generating an inverse temperature profile across the sample [298-301]. The temperature gradient,  $\Delta T$ , depends on several variables, such as the dielectric properties of the material, the nature and temperature of the surrounding environment and the presence or absence of any insulation. This creation of an inverse temperature profile is a fundamental concept for microwave heated chemical vapour infiltration as described in section 2.8.6.

The difference in the microwave and conventional heating mechanism can be described by considering with a simple model based on the thermal conduction [261].

For the conventional heating, the density of heat is confined in a thin layer near the surface. There is a characteristic time of temperature equalisation,  $\tau_s$ , which depends i) on the dimensions and ii) the thermal diffusivity,  $\chi_s$ , or equivalently the

thermal conductivity,  $k_s$ , of the sample. The temperature gradient can be reduced only when the heating time of the process  $\tau_T$  is much larger than  $\tau_s$  [261]:

$$\Delta T \sim T \frac{\tau_s}{\tau_T} \quad (2-39)$$

Only for  $\tau_T \gg \tau_s$  a constant temperature is maintained.

Conversely, in microwave heating the temperature difference in the sample is never zero and the inner part of the sample is hotter than the surface. In some microwave processing applications, the sample is often insulated using an insulating material with a low thermal diffusivity and conductivity,  $\chi_{ins} \ll \chi_s$  and  $k_{ins} \ll k_s$ , to reduce this temperature gradient [261]. Hence, the thermal properties of the insulation play a crucial role. Assuming that the insulation is not a microwave-absorptive material, it can be demonstrated that the microwaves can heat the sample faster and improve the temperature uniformity [261]. However, if the heating time is too slow the temperature gradient will be larger in microwave than in conventional heating. This phenomenon is shown in Figure 2-26.

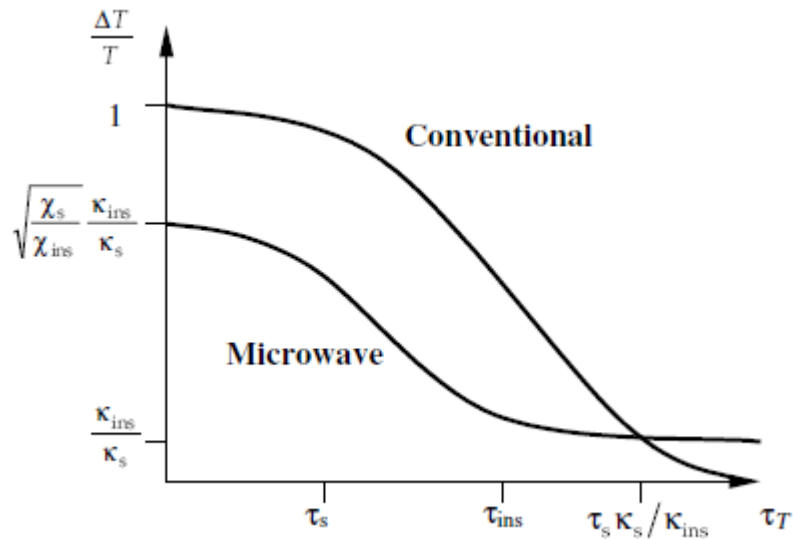


Figure 2-26. Temperature difference versus characteristic heating time for microwave and conventional heating [261].

Microwave heating can also lead to a variety of thermal phenomena. One of the most problematic is the thermal instability, commonly called “thermal runaway” [259, 261, 302]. It results from a non-uniform temperature distribution combined with the dependence of the microwave absorptivity on temperature. The effect tends to occur in materials in which the dielectric loss factor increases steeply with temperature. If one local region of a body starts to become hotter than elsewhere, its dielectric loss increases leading to more microwave energy absorption and in turn more heating. This has been demonstrated in a range of ceramics [303]. At an extreme level, thermal runaway can even lead to local melting of a material [259, 304].

The thermal runaway has been described mathematically by a parameter  $\beta$  [261]:

$$\beta = \frac{T}{w} \frac{\partial w}{\partial T} \quad (2-40)$$

where  $w$  is the adsorbed microwave power (per unit of volume).

An empirical estimation suggests that a thermal runaway is likely when  $\beta$  reaches a critical value  $\beta_c$  [261], defined as:

$$\beta_c \approx \left( \frac{\tau_s}{\tau_T} + \frac{k_{ins}}{k_s} \right)^{-1} \quad (2-41)$$

### 2.8.6 Focus on microwave-enhanced chemical vapour infiltration

The aim of microwave-enhanced chemical vapour infiltration (MECVI) [16-21, 265, 298, 300, 305-313] is to overcome the preferential deposition that occurs in the outer region of preforms with ICVI and which results in a premature sealing of the porosity. As previously mentioned in section 2.5, the crusting requires the process to be stopped, to allow the pores to be re-opened by machining. This leads to a consequent increase in the costs and process time. In MECVI the preforms are heated by microwaves, which create an inverse temperature profile [156, 298-300] as described in section 2.8.5, see Figure 2-27). This leads to the deposition occurring from inside out, with the consequent avoidance of crusting, see Figure 2-28.

The densification is much faster, e.g. 48-72 hours, compared to conventional CVI. Greater efficiency could be achieved if the process were combined with forced-flow and pressure pulsed techniques [182].

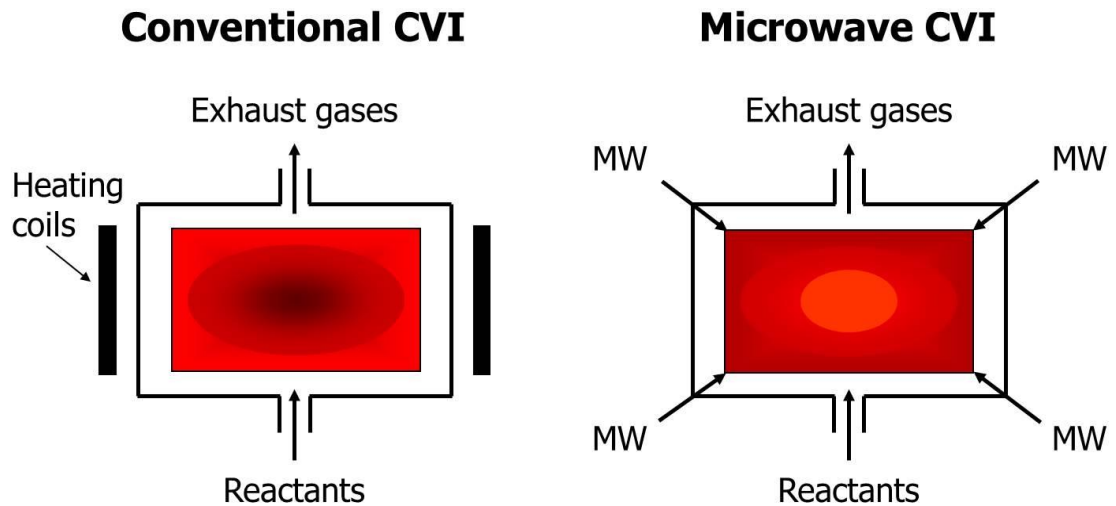


Figure 2-27. Heating method in a conventional CVI and in a Microwave enhanced CVI process.

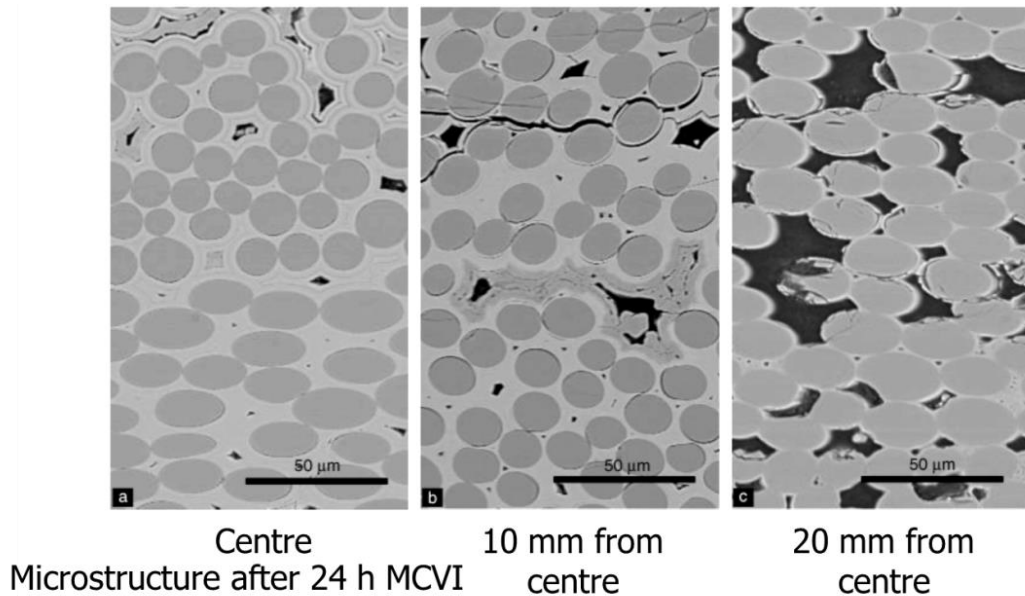


Figure 2-28. Microstructure of a SiC<sub>t</sub>/SiC composite fabricated by MECVI. Adapted from [16].

### 2.8.6.1 Process variables

In addition to parameters such as temperature, gas flow rates, pressure and preform geometry, MECVI requires an understanding of the dielectric properties of the ceramic preform and matrix [314]. The dielectric properties affect the

kinetics and the conversion rate and are themselves dependent on numerous parameters like temperature and electric field. In addition  $\epsilon'_r$ ,  $\tan \delta$ ,  $E$  are all interdependent and  $E$  depends on the location of the sample in the cavity, on the geometry and density of the preform. Hence, as the infiltration proceeds, the substrate changes its ability to absorb energy from microwave field. Thus, density and compositions gradients can locally change the microwave heating and the densification evolves with a complex pattern.

Overall, the preform microstructure changes in time as the matrix is deposited with different dielectric properties. Some theoretical models [18, 298] and finite element method simulation [309] have been developed showing the inverse profile supported by experimental results [305].

### 2.8.6.2 Benefits and disadvantages of MECVI

The main advantages of MECVI are:

- Potentially short processing times (48-72 hours)
- No machining operation required to remove the crusting
- Low processing temperatures (1000°C) and low pressure ( $10^0$ - $10^2$  mbar), which prevents the fibres from damages and reduces potential residual stresses.

However, some drawbacks associated with MECVI include:

- Thermal runaway due to the local variability in the electromagnetic field. It would results in an inhomogeneous temperature distribution with potential hot spot and consequent damage to the composite.

- No work has yet been undertaken on preforms that have a complex shape; this could lead to difficulties in controlling the temperature profile
- Gas plasma can form limiting the minimum pressure that can be used.

### 2.8.6.3 Experimental results

Table 12 reports the experimental work carried out to date on the infiltration by MECVI for different ceramic systems, in particular SiC, Si<sub>3</sub>N<sub>4</sub>, Al<sub>2</sub>O<sub>3</sub> and ZrO<sub>2</sub>. So far, for SiC<sub>f</sub>-based preforms, Nicalon fibres have been widely investigated because, even if they offer lower mechanical performance than Hi-Nicalon, they display excellent microwave absorption (and a lower price). Nicalon preforms (diameter of 50 mm, 1 cm thick) have been densified to near-theoretical density in the centre with an overall density of 70% in only 19 hours [125]. Oxide fibre CMCs achieved a density of 85%, which is competitive with the commercial oxide FRCMCs fabricated by conventional CVI [15]. Also C<sub>f</sub>/C composites have been produced by MECVI [315], even though carbon fibres are not good microwave absorbers.

Table 12. Experimental achievements of MECVI

Pressure Approach	Preform	Process conditions	Microwave features	Achieved density	Deposition rate	Ref.
Isobaric	SiC Nicalon cloth $\Phi = 70$ mm	$P_t = 40-80$ kPa $Q_{H_2} = 500-4000$ ml $\text{min}^{-1}$ $P_{MTS} = 0.1-2.5$ kPa	2.45 GHz, 0.7 kW	Weight gain = 11.5% $t = 3$ h	0.03-0.42 g $\text{h}^{-1}$	[265]
Isobaric	SiC/Nicalon fibres $L = 0.5-1.0$ mm	$P_t = 73$ kPa	2.45 GHz, 0.7 kW Single-mode cavity	N/A	SiC matrix surface composites	[311]
Isobaric	$\text{Si}_3\text{N}_4$ /Nicalon fibres $\Phi = 50$ mm	$T = 950^\circ\text{C}$ $P_t = 46.7$ kPa	2.45 GHz, 0.7-1.3 kW Single-mode cavity	$t = 17.5$ h	Deposition at the centre: 0.4 g $\text{h}^{-1}$	[17]
Forced-flow	SiC/Nicalon $V_f = 42-46$ vol%	$T = 975^\circ\text{C}$ $P_{\text{outlet}} < 100$ kPa $Q_t = 140$ ml $\text{min}^{-1}$ (50 ml $\text{min}^{-1}$ of $\text{N}_2$ ) $\alpha = 10$	2.45 GHz	$t = 35$ h $\rho_r = 57.8\%$	Matrix growth rate: 11.4 $\mu\text{g cm}^{-2} \text{h}^{-1}$	[21]
Forced-flow	Nicalon cloth $\Phi = 50$ mm $L = 7-10$ mm	$T = 1000^\circ\text{C}$ $P_t = 95-97$ kPa $Q_{H_2} = 250$ ml $\text{min}^{-1}$ $Q_{MTS} = 0.575$ g $\text{min}^{-1}$	2.45 GHz, 5 kW Multi-mode cavity	$\rho_r = 70\%$ Centre density= 100% $t = 19$ h	Centre reaching near full density	[19]
Forced-flow	10 layers Nicalon cloth $V_f = 11$ vol% $\text{Si}_3\text{N}_4$	$T = 950^\circ\text{C}$ $P_t = 46.7$ kPa	2.45 GHz, 0.7-1.3 kW Single-mode cavity	$\rho_r = 60\%$ $t = 29.5$ h	0.69 g $\text{h}^{-1}$	[313]
Forced-flow	$\text{Al}_2\text{O}_3$ fibres / $\text{Al}_2\text{O}_3$ $V_f = 37-42$ vol%	$T = 885^\circ\text{C}$ $P_{\text{inlet}} = 15-81$ kPa $P_{\text{outlet}} = 3.2$ kPa $Q_t = 80$ ml $\text{min}^{-1}$	2.45 GHz, 3 kW Single-mode cavity	$\rho_r = 52\%$ $t = 14$ h	0.68 g $\text{h}^{-1}$	[310]
† Forced-flow	$\text{Al}_2\text{O}_3$ fibres / $\text{Al}_2\text{O}_3$ $V_f = 40$ vol% $\Phi = 50$ mm $L = 7-10$ mm	$T = 1000-1100^\circ\text{C}$ $P = 6.7-13.3$ kPa $Q_t = 150-250$ ml $\text{min}^{-1}$	Hybrid heating: 2.45 GHz cavity with LSC susceptor	$\rho_r = 76\%$ centre $t = 20.5$ h	0.42 g $\text{h}^{-1}$	[15]
Forced-flow	$\text{ZrO}_2$ fibre board $\text{ZrCl}_4 + \text{CO}_2$	$T = 750-1000^\circ\text{C}$ $P_t = 17-85$ kPa	2.45 GHz, 5 kW Multi-mode cavity	N/A	N/A	[19]
Isobaric	30 layers Nicalon cloth, $\Phi = 48$ mm $L = 10$ mm	$T = 800-1050^\circ\text{C}$ $P_t = 70$ kPa $Q_{H_2} = 300$ ml $\text{min}^{-1}$ MTS fraction at inlet (vol%)= 1.3	2.45 GHz, 0.5-5 kW Multi-mode cavity	$\rho_r = 55\%$ Centre density= 73% $t = 24$ h (10 h if pre-infiltrated with SiC slurry)	2.3-22.1 mg $\text{min}^{-1}$	[16, 305]
Isobaric	15 layers of Nicalon NL202 Preform shape: bricks 20x40x80 mm	$T = 1000-1100^\circ\text{C}$ $P_t = 101$ kPa $Q_{H_2} = 180$ ml $\text{hr}^{-1}$ $\text{H}_2/\text{MTS} = 500-1000$ MTS fraction= 0.15-0.30	2.45 GHz, 6 kW Multi-mode cavity	Weight gain = 70% $t = 18$ hr	N/A	[20]
Isobaric	30 layers Nicalon NL202 Preform shape: disc $\Phi = 48$ mm $L = 10$ mm	$T = 1000^\circ\text{C}$ $P_t = 70$ kPa $Q_{H_2} = 300$ ml $\text{min}^{-1}$ $\text{H}_2/\text{MTS} \sim 10-30$	2.45 GHz, 3kW Multi-mode cavity	Centre density= 75% $t = 24$ h	N/A	[156]

† LSC= lanthanum-strontium (15 mol%)-chromite

## 3 Experimental procedure

This chapter describes the experimental work carried out in the course of the research project. It is divided into three main sections: section 3.1 outlines the MECVI equipment; whilst the raw materials and experimental protocol are reported in section 3.2, and finally in section 3.3, the material characterisation is outlined.

### 3.1 MECVI equipment

Figure 3-1 shows a photograph of the forced-flow MECVI equipment which consists of three distinctive subsystems:

- the microwave unit (also referred to as the microwave CVI) and the chamber/reactor where the CVI occurs;
- the gas delivery system;
- the gas cleaning system (also referred to as the "scrubber" system) and the exhaust line.

A schematic diagram of the apparatus is presented in Figure 3-2.

All the units are electronically interconnected in order to carry out the chemical vapour infiltration process automatically, following a cycle pre-set by the users. A multi-level alarm system was developed by the manufacturers, SAIREM, Neyron, France and Archer Technicoat Ltd (High Wycombe, UK), to address all the health and safety issues related to the use of electromagnetic radiation, hazardous chemicals and explosive gases.

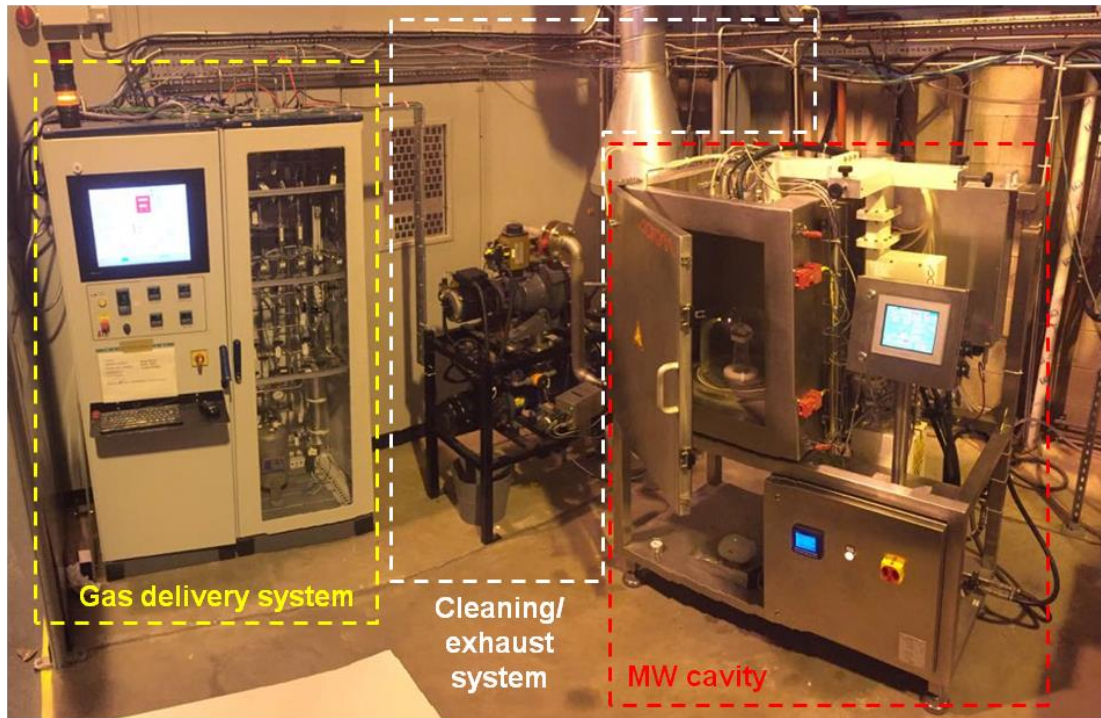


Figure 3-1. Photograph of the MECVI equipment

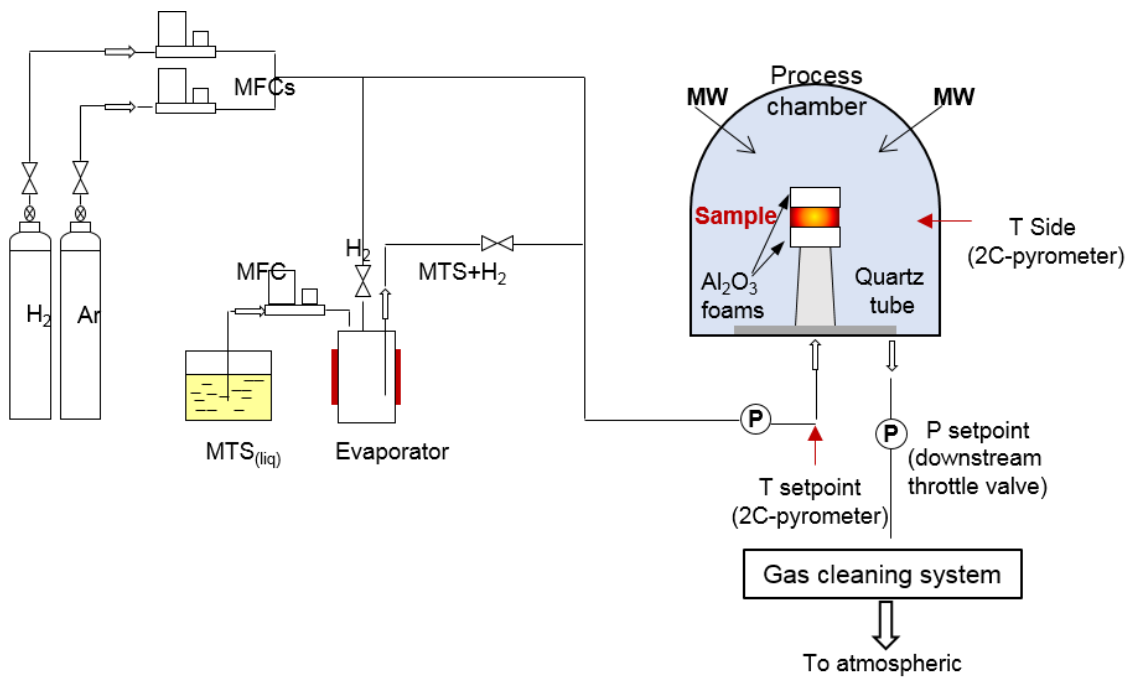


Figure 3-2. Schematic diagram of the MECVI apparatus - MFC= mass flow controller, MW= microwave radiation and P = pressure transducer.

### 3.1.1 Microwave unit

The microwave-assisted CVI unit (Labotron HTE M30KB CL PRO, Sairem, Neyron, France) system includes the magnetron, the control unit and the cavity (Figure 3-3)

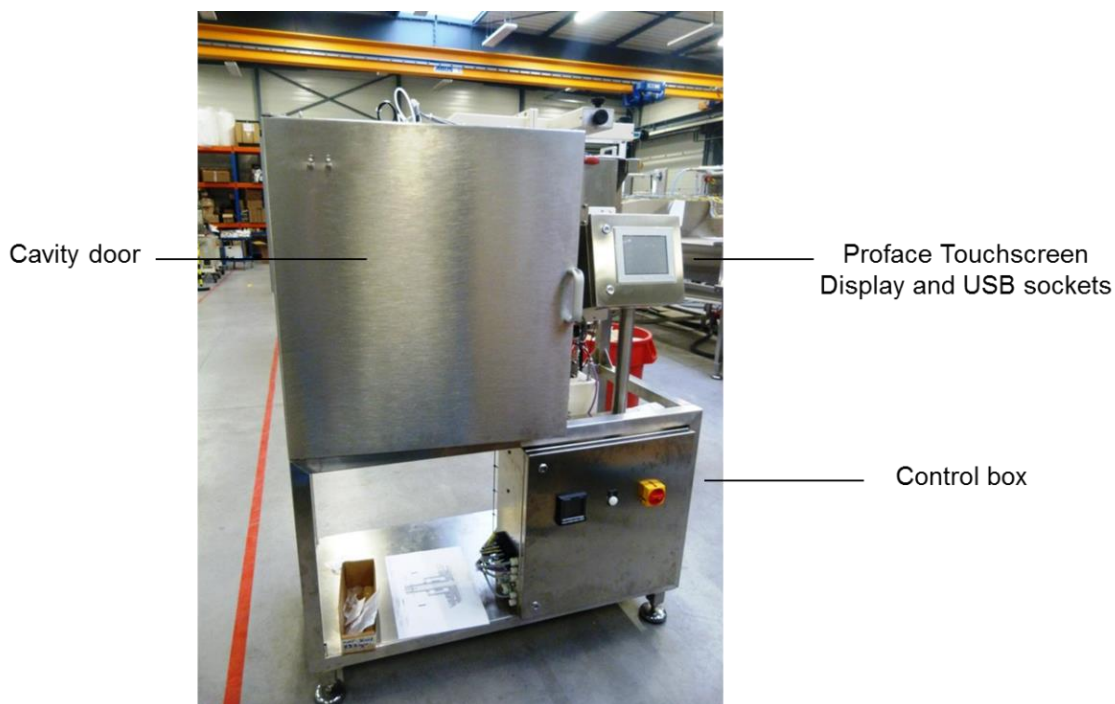


Figure 3-3. Photograph of the microwave-heated CVI unit

The microwave energy was generated at the fixed frequency of 2.45 GHz by the continuous-wave magnetron (Magnetron 2M265-M12WJ, Muegge Electronics, GmbH, Germany) shown in Figure 3-4. Controlled-pulse and ramp regimes were also possible. The output power was adjustable in the range 0.02 - 3.00 kW. The magnetron was water-cooled with a once-through water flow of 20 l min<sup>-1</sup> at ambient temperature. The microwaves were transmitted to the reactor through a rectangular cross-section metallic waveguide located on the top side of the cavity.

Figure 3-4. Magnetron for the microwave generation



The cavity was built in stainless steel 316L. A once-through water cooling system maintained the temperature of the cavity and of the waveguide below 60°C to avoid any excessive heating of the cavity walls. Thermal expansion of the waveguide could affect the frequency behaviour and propagation of the modes. A turntable, with adjustable rotation speed, was used to continuously perturb the electromagnetic field and hence generates homogeneous heating; during the run the sample rotated and, from preliminary experiments, the rotation speed did not affect the heating of the preform.

An E/H impedance tuner (Sairem, Neyron, France) and a 4-stub autotuner (AI4S, Sairem, Neyron, France), Figure 3-5, were used to minimise reflected power and hence ensure an effective coupling of the microwaves with the impedance of the sample. Moreover, the autotuner was also designed to protect the magnetron from excessive reflected power, which could cause overheating and hence reduced efficiency.

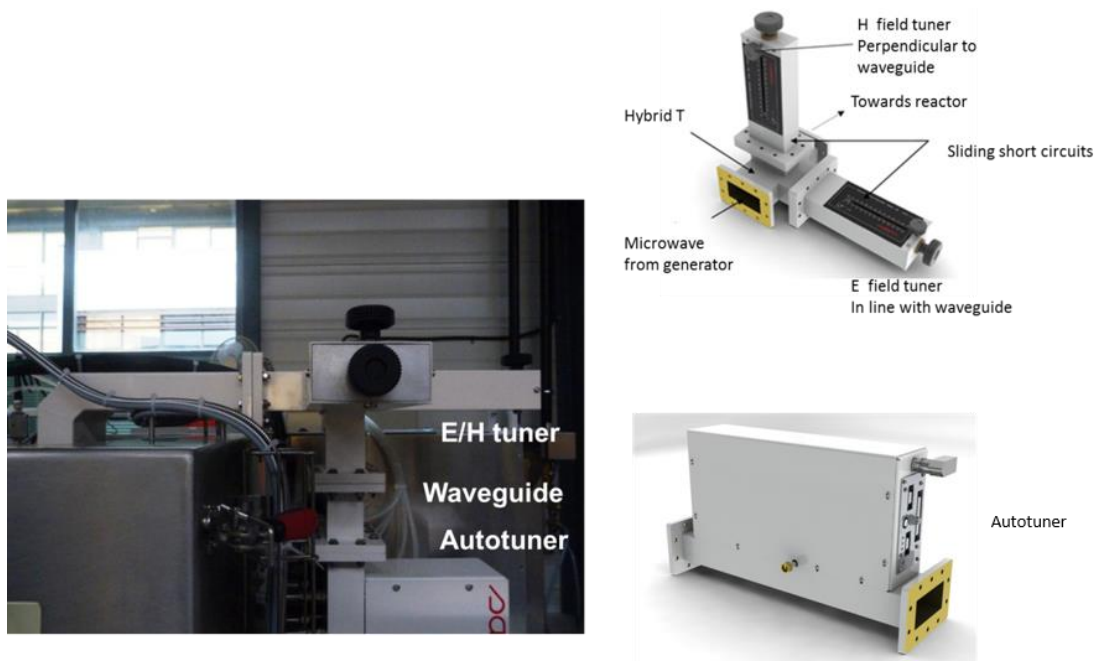


Figure 3-5. Manual and autotuner systems to minimise the reflected power for a more efficient heating

The microwave cavity was equipped with a microwave surveymeter (DFM M24DC, Sairem, Neyron, France) capable of detecting any microwave leaks; the safety threshold was set at  $5 \times 10^{-3} \text{ W cm}^{-2}$ . The cavity door had two safety-interlock switches (Trojan Guardmaster, Allen-Bradley, Rockwell Automation Inc., WI, USA) and a fibre optic arcing detector was installed and interlocked with the MW generator.

### 3.1.2 Gas cleaning and exhaust system

The CVI process was carried out under a MW-transparent quartz bell jar (Quartz Scientific, High Wycombe, UK) placed inside the cavity, Figure 3-6. The bell jar, diameter of 35 cm, height of 50 cm and wall thickness of 0.75 cm, had a wide flange that was fitted on an "O" ring, keeping a sealed environment inside, Figure 3-7. The mixed gases was introduced through the bottom of the turntable by a

central inlet, the outlet allowed the gases to evacuate the reactor after they had passed through the sample,

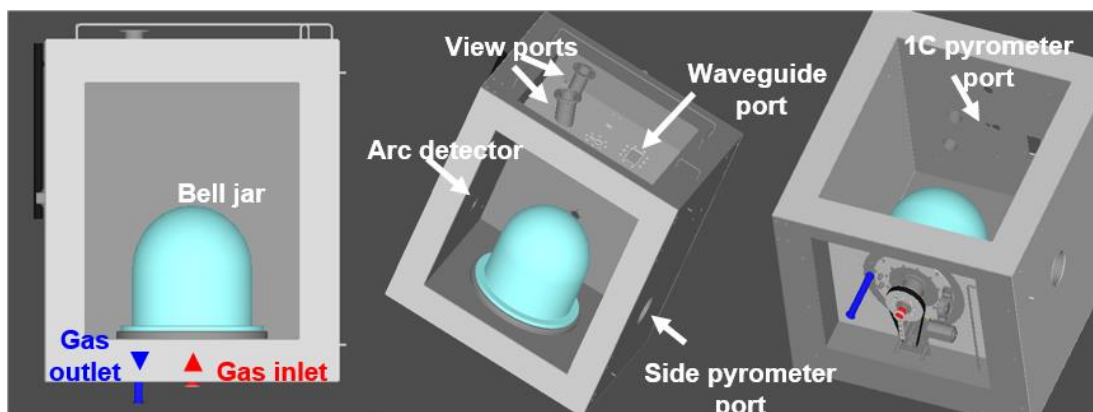


Figure 3-6. 3D rendering of the microwave cavity and reactor

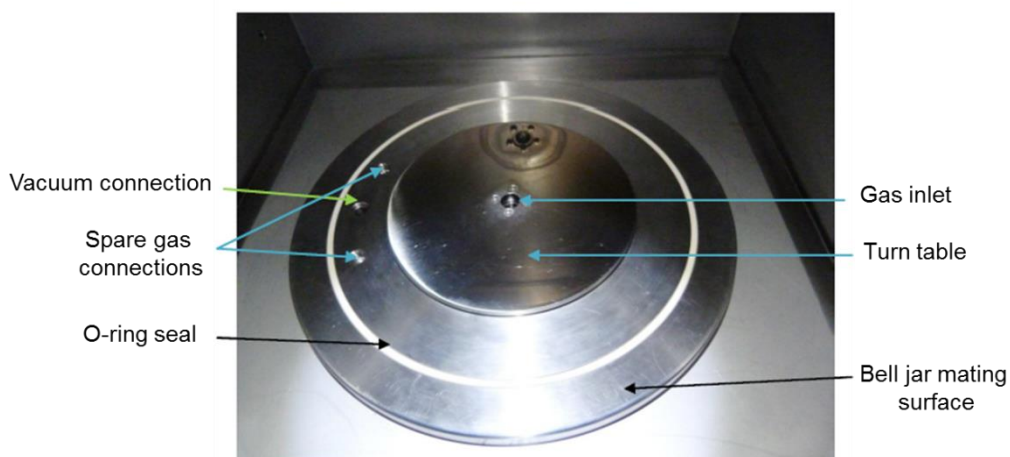


Figure 3-7. Photograph of the turntable and the configuration of the inlet and outlet

The thermal decomposition of MTS into SiC, described in Chapter 2, is dependent on the temperature. The exhaust gases are therefore a mixture of unreacted MTS, H<sub>2</sub> and by-products generated from the decomposition such as HCl and other chlorine-based species. These were neutralised by a scrubber system, Figure 3-8, consisting of a 5cm-thick PVC tank containing 250 litres of water. The solution was kept in the pH range 7-9 by sucking in a 0.3 M solution of NaOH contained in an external reservoir. A liquid ring pump (TRHE 32-60/C-M/A3,

Pompe Travaini srl, Italy) backed by a roots booster pump (RUVAC WAU 251 FP, Oerlikon Leybold Vacuum, Germany) had the functions of evacuating the gases from the reactor and removing all the air in the first stage of the CVI process. The efficiency of the liquid ring pump was determined by the temperature of the liquid so that a chiller was used to maintain the temperature between 11-13°C.

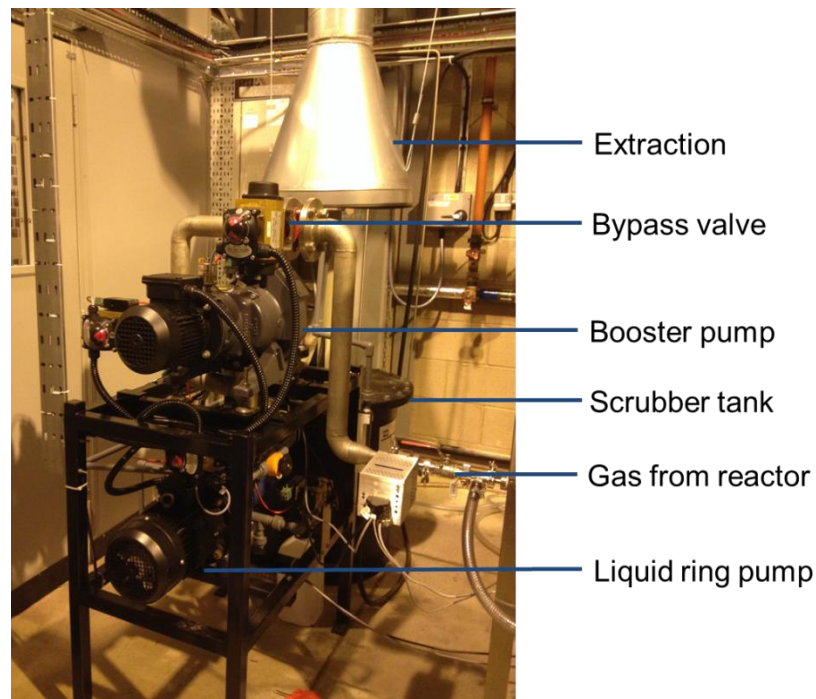


Figure 3-8. Photograph of the gas cleaning and exhaust system

### 3.1.3 Gas delivery system

Since the CVI process necessitates a controlled atmosphere within the reactor under the bell jar, an accurate control of the pressure, gas composition and temperature and a completely leak-free assembly, were all required.

#### *Gas flow control*

99.995%-purity hydrogen and argon (The BOC group plc, Manchester, UK) were metered by calibrated mass flow controllers (MFCs) (Coriflow, Bronkhorst Ltd,

Newmarket, UK) with an accuracy of 0.05% of the full scale (2.000 l min<sup>-1</sup>). MTS was contained in a stainless steel vessel with maximum capacity of 6 litres. A pressure relief valve (connected to the scrubber tank) set at 6 atm was fitted in case of pressure build-up inside the vessel. The flow of liquid MTS was controlled by a MFC with an accuracy of 1 g h<sup>-1</sup> (Coriflow, Bronkhorst Ltd, Newmarket, UK). The minimum usable amount was 10 g h<sup>-1</sup> and the maximum 200 g h<sup>-1</sup>. The MTS was metered and passed through an evaporator set at 65°C, which was close to the boiling point of MTS (66°C).

#### *Pressure control*

Process pressure was monitored by a pressure transducer (Baratron 747B, MKS Instruments Ltd, Crewe, UK with an accuracy of measurement of 100 Pa) with an Inconel all-welded sensor to maximise the resistance to corrosive process gases. The transducer was heated up to 45°C to prevent MTS condensing onto it. The pressure transducer was placed downstream of the chamber and another digital pressure transducer with data logger was placed upstream. The pressure was controlled with a self-tuning control algorithm and high speed operation throttle valve (T3Bi High Speed Exhaust Throttle Valve, MKS Instruments Ltd, Crewe, UK) connected to the transducer. Pressure control was possible within  $\pm 5\%$  of the set point value.

#### *Temperature control*

The temperature was measured at multiple points with three pyrometers integrated with the MW control unit. A 1-colour pyrometer (thermoMETER CTM3, Micro-epsilon, NC, USA with a response time of 5 ms and an accuracy of 0.3% of the measured temperature) was placed at the top of the cavity and used to

control temperature up to 750°C; an emissivity value of 0.85 was set for SiC. Two 2-colour pyrometers (thermoMETER CTratio M1, Micro-epsilon, NC, USA with a response time of 5 ms and an accuracy of 0.5% of the measured temperature) were placed i) at the bottom of the turntable and ii) focused on the side of the sample. The working range of the 2C-pyrometers was 700-1800°C. A feedback control system between the temperature output and the microwave unit tuned the forward microwave power and kept, with the help of PID (proportional, integral and derivative) control, the temperature close to the set-point. An upper limit on the maximum temperature was always set to prevent the sample from undergoing any thermal runaway. The pyrometer was not in direct contact with the gas stream as shown in Figure 3-9.

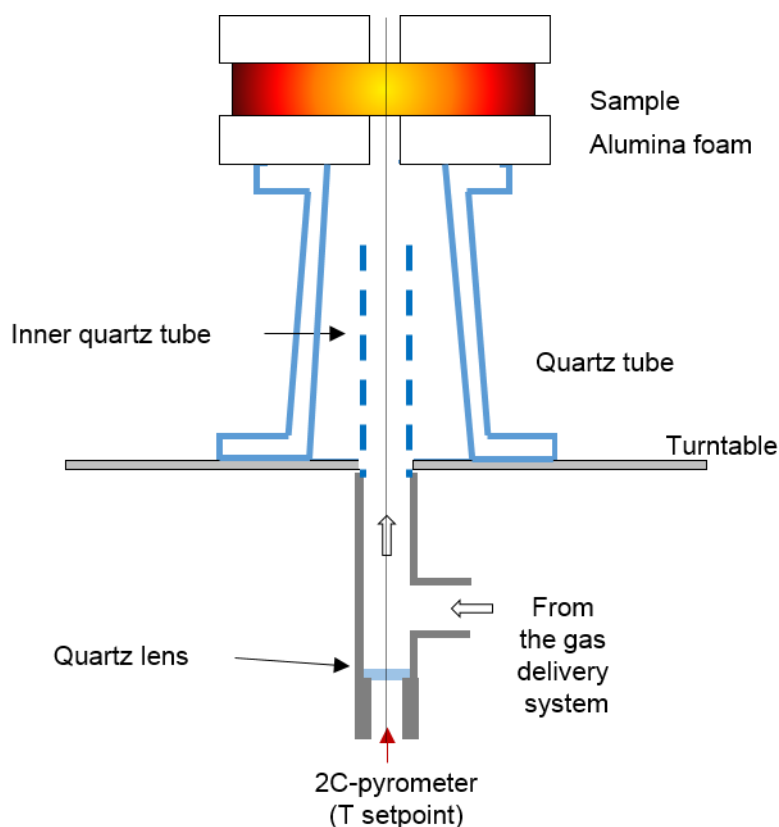


Figure 3-9. Schematic (side view) of the configuration for the detection of the sample temperature

No thermocouples were used to avoid the interaction between the essential metal sheath and the microwaves (the creation of discharges can affect the local temperature) and the lack of resistance of the sheath material to the very corrosive environment. However, pyrometry is best suited to measure the surface of samples, hence limiting the accuracy of temperature measurement in case of volumetric heating. For this purpose, as a preliminary experiment, a thermal imaging camera (FLIR A8000sc-Series MWIR, FLIR Systems, West Malling, UK) was also used to check the temperature distribution on the top surface of the sample.

### 3.2 CVI of SiC fibrous materials

#### 3.2.1 Starting materials

##### 3.2.1.1 Fibre fabric

Tyranno ZMI fibres manufactured by UBE Industries were used in this research project. The fibres were woven into two-dimensional cloth with 800 filaments per yarn. The average diameter of the fibre was  $11 \pm 3 \mu\text{m}$ . The fabric was produced as a plain weave cloth that provided a high porosity and an architecture that was easy to handle compared to satin or other weaves. The areal weight of the fabric was  $0.25 \pm 0.02 \text{ kg m}^{-2}$  for a thickness of  $0.27 \pm 0.01 \text{ mm}$  and a specific surface area of  $106 \text{ m}^2 \text{ kg}^{-1}$ . The density of the Tyranno ZMI fibre was given as  $2.48 \text{ g cm}^{-3}$ . The chemical composition of the fibres is 56, 1 Si, 34.2 C, 8.7 O and 1 Zr wt%.

Each fibrous preform for the MECVI process was prepared by stacking multiple layers of fabric arranged together in a random orientation. Ten to thirty discs with

a 51.0 mm diameter were cut out from the cloth used a heat-treated steel wad punch (nominal diameter 50.8 mm), aligned, stacked and stitched (by hand) with pure cotton yarn. The stitching held the preform firmly, reducing the risk of delamination during transport between laboratories and loading the preform into the reactor. The role of the stitching was crucial as the interlayer gap was determined by the stitching tightness. The stitching pattern was the same for all the preforms: six stitches at 20 mm from the centre and four at 10 mm. Prior to stitching, the fabric was washed in boiling water for 10 minutes to remove the seizing of polyethylene oxide covering the fibres. The mass loss of the fabric after the deseizing was  $1.2 \pm 0.1\%$  which is consistent with the data provided by the supplier.

The average thickness for a 20-layer preform was  $7.2 \pm 0.5$  mm (measured with a digital calliper before CVI and also using the microscope with reticule after the process). A schematic of the preform fabrication process is shown in Figure 3-10.

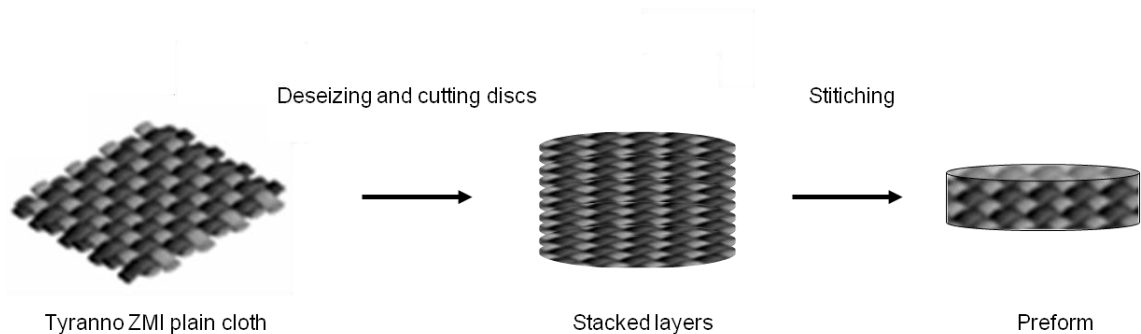


Figure 3-10. Fibre preform fabrication route

#### 3.2.1.2 Methyltrichlorosilane (MTS)

Methyltrichlorosilane (MTS) was used as the precursor for silicon carbide in the MECVI process. MTS has a boiling point of  $66.4^{\circ}\text{C}$  and is readily vaporised and diluted with hydrogen. The molecular weight is  $149.98 \text{ g mol}^{-1}$  and the density of

the liquid is  $1.273 \text{ kg m}^{-3}$ . MTS was sourced from Sigma Aldrich Corporation, St. Louis, MO, USA.

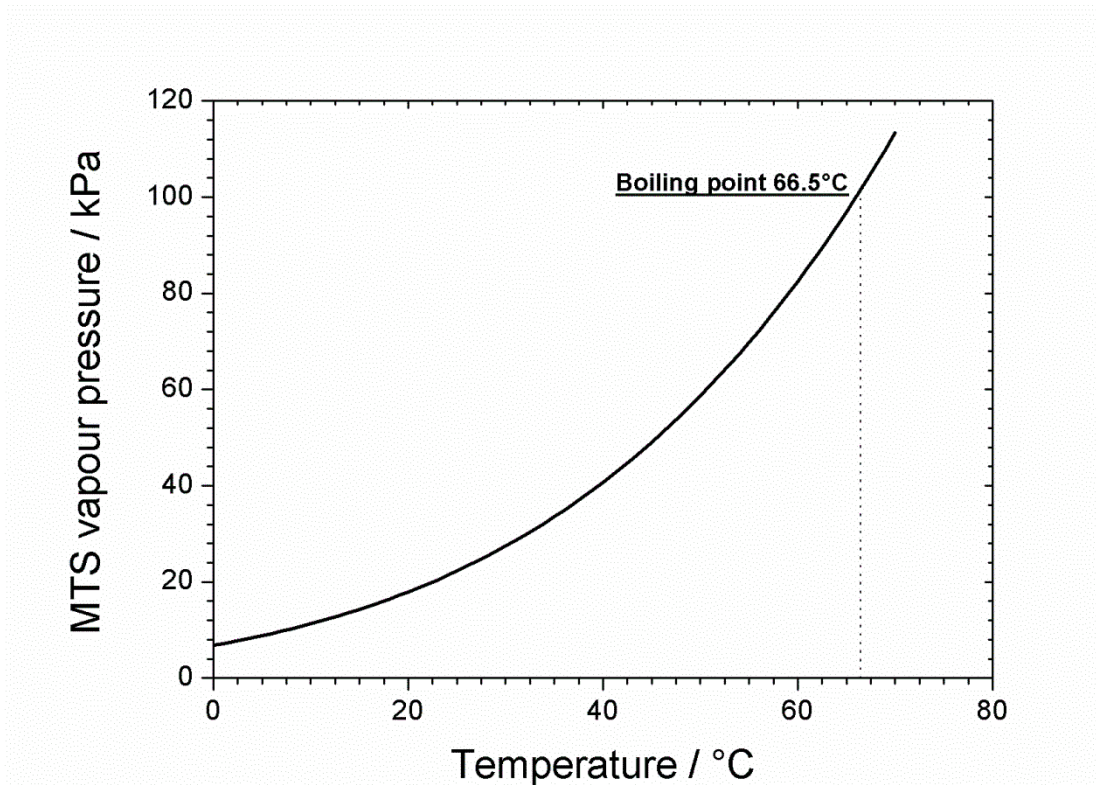


Figure 3-11. Partial pressure of MTS. Adapted from [316].

### 3.2.2 Experimental procedure

#### 3.2.2.1 Loading

Alumina foams (Selee Corp., Hendersonville, NC, USA) with a nominal porosity of 30 pores per inch) were used as insulators and were placed above and below the preforms, see Figure 3-12. The foams prevented excessive heat loss from the surfaces. To allow the pyrometers to read the temperature, the alumina foam had a hole in the centre. The assembly was placed on the top of a tapered quartz tube with flanges on the extremities to both support the sample in a stable manner and to increase the surface contact with the turntable and alumina foam. An inner

quartz tube was fitted to direct the gas flow toward the centre of the sample as shown in Figure 3-9.

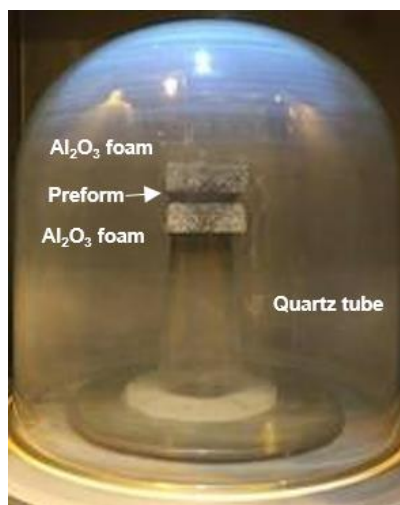


Figure 3-12. Photograph of the sample arrangement.

The samples insulation discs were loaded into a similar location for each new MECVI run in the microwave cavity, aligning the centre of the preform with the pyrometer laser spot.

### 3.2.2.2 Purge and setpoint temperature

The reactor was evacuated with the liquid ring pump backed by the booster pump as mentioned in section 3.1.2. An additional two-stage rotary vane pump (Edwards RV9, Clevedon, United Kingdom) was used to further decrease the vacuum level. The minimum value reached was 100 Pa. The vacuum integrity was maintained at better than a leak rate of 10 Pa min<sup>-1</sup>, which preliminary tests proved to be acceptable. Argon was flushed through the system for 5 minutes at a rate of 2.0 l min<sup>-1</sup>. This procedure was repeated three times and then repeated with H<sub>2</sub>. The pressure was set to the required value and the reactor back-filled with hydrogen. Once the required pressure was reached, the gas flow was set to the desired value and the microwave generator turned on. The sample was slowly

brought to required temperature by gradually increasing the microwave power level in order to avoid thermal runaway. The cavity was tuned using the E/H impedance tuner to minimise the reflected power.

### 3.2.2.3 Infiltration

Once the temperature was stable at the setpoint, MTS was mixed in the evaporator with hydrogen and the mixture allowed to enter the reactor. It was observed that the introduction of MTS in the gas stream cooled the sample at the start of the infiltration. By increasing the microwave power, the temperature was adjusted and kept stable at the setpoint value. Experiments were carried out for a maximum of 8 hours because of the Health and Safety regulations regarding overnight experiments. However, depending on the requirements of the experiments, the infiltrations were conducted intermittently for 2, 4, 8-hours period of time.

#### *Infiltration rate*

A study of the kinetics on 20-layer preforms was performed to determine the influence of pressure, temperature, hydrogen flow rates and gas ratio on the infiltration rate. The temperature was varied from a minimum of 800 to a maximum of 1100°C, pressure from 16 to 70 kPa, whilst the hydrogen flow rate was fixed to 300 ml min<sup>-1</sup>. The parameters were varied during runs of 8 hours.

The infiltration rate,  $\dot{m}$ , was expressed in mg min<sup>-1</sup>, the matrix growth rate,  $G_{SiC}$ , (mol m<sup>2</sup> s<sup>-1</sup>) was determined by

$$G_{SiC} = \frac{\Delta m_m}{M_{SiC} t_i A_d} \quad (3-1)$$

where  $M_{SiC}$  is the SiC molar mass (40.11 g mol<sup>-1</sup>),  $t_i$  is the infiltration time (s) and  $A_d$  is the total available surface for the deposition (m<sup>2</sup>).

$A_d$  is defined as:

$$A_d = S_A m_f \quad (3-2)$$

where  $S_A$  is the specific surface area of the porous preform (m<sup>2</sup> g<sup>-1</sup>) and  $m_f$  is the initial fibre mass (g). The kinetics was further investigated using the Arrhenius law to determine the activation energy for the decomposition of MTS.

$$G_{SiC} = G_{SiC(0)} \exp\left(\frac{E_a}{RT}\right) \quad (3-3)$$

where  $G_{SiC(0)}$  is a pre-exponential factor (mol m<sup>-2</sup> s<sup>-1</sup>),  $E_a$  is the activation energy (J mol<sup>-1</sup>), R is the universal gas constant (J K<sup>-1</sup> mol<sup>-1</sup>) and T is the temperature (K).  $E_a$  and  $G_{SiC(0)}$  can be determined by the fitting of  $\ln(G_{SiC})$  vs  $1/T$ .

#### *Conversion rate*

The percentage conversion rate or yield of the reaction MTS to SiC,  $\eta$ , was calculated as:

$$\eta = \left( \frac{M_{SiC}}{M_{MTS}} \cdot \frac{\Delta m_m}{\Delta m_{MTS}} \right) \times 100 \quad (3-4)$$

$M_{MTS}$  is the molecular mass of MTS in g mol<sup>-1</sup> and  $\Delta m_{MTS}$  is the mass of consumed MTS in g.

### Chapter 3. Experimental procedure

Table 13 reports the preforms infiltrated by MECVI in this experimental work with the conditions of the infiltration.

Table 13. List of the preforms infiltrated with MTS/H<sub>2</sub> including the dimensions and the parameters of infiltration.

Sample ID	Temperature / °C	Pressure / kPa	$\alpha$	Q <sub>H<sub>2</sub></sub> / ml min <sup>-1</sup>	Dimensions Diameter / mm (Number of layers)	Infiltration time / h
S_900_20	900	20	10	300	50.8 (20)	8
S_900_30	900	30	"	"	"	8
S_900_50	900	50	"	"	"	8
S_900_70	900	70	"	"	"	8
S_950_20 §	950	20	"	"	"	8
S_950_30	950	30	"	"	"	8
S_950_50	950	50	"	"	"	4
S_950_70	950	70	"	"	"	4
S_1000_20 †	1000	20	"	"	"	8
S_1000_30	1000	30	"	"	"	8
S_1000_50*	1000	50	"	"	"	2
S_1000_70 ‡	1000	70	"	"	"	3.5
CVD_1100†	1100	30	"	300	50.8 (1)	4
CVD_1000	1000	30	"	"	"	4
CVD_1000_15†	1000	15	"	"	"	4
CVD_900	900	30	"	"	"	4

§Initial mass of the preform was higher because of a different amount of slurry applied on the side of the preform

† Arcing observed for some preforms.

‡ Formation of a thick layer on the layer of fabric facing the gas inlet.

\* Implosion of the bell jar did not allow the completion of the experiments

#### *Gas velocities and residence time*

The velocity  $v$  (ms<sup>-1</sup>) of the feeding gas inside the quartz tube was calculated from

$$v = \frac{Q_{H_2} T P_0}{A_t T_0 P} \quad (3-5)$$

where  $P_0$  and  $T_0$  are respectively the standard pressure (101 kPa) and standard temperature (298 K),  $A_t$  is the cross sectional area of the quartz tube that was assumed to be approximately equivalent to the diameter of the preform,  $P$  is the mean pressure in kPa, across the thickness of the sample. The medium was considered to be constituted of a single monosized straight pore and hence, the pore gas velocity,  $v_p$ , was defined as

$$v_p = \frac{v}{\varepsilon_p} \quad (3-6)$$

where  $\varepsilon_p$  is the porosity volume fraction.

The residence time  $\tau$  in s, was defined as the time taken for the gas molecule to cross the preform thickness  $l$  in m:

$$\tau = \frac{L}{v_p} \xi \quad (3-7)$$

where  $\xi$  is an adimensional factor called tortuosity, defined as the ratio of the length of the curve running through the axis of the pore to the distance between the ends of it.

#### 3.2.2.4 Cooling at the end of the run

The MTS-H<sub>2</sub> flow was stopped and hydrogen flow was increased to 2.0 l min<sup>-1</sup> to aid the removal of reactants and by-products left over in the bell jar environment. The microwave generator was still operational and for this reason this stage of the process was called “hot purging”. After 10 minutes, the microwave generator

was shut down and the hydrogen flow was substituted by argon with a flow rate of  $2.0 \text{ l min}^{-1}$ . The reactor was pumped down to the minimum pressure achievable ( $700 \text{ Pa}$  if  $2.0 \text{ l min}^{-1}$  of gas was flushed through the reactor). The sample was allowed to cool down to room temperature, an operation that took approximately 30 minutes. Finally, the cavity was brought to atmospheric pressure, the bell jar removed and the sample removed.

### 3.2.2.5 Experimental problems encountered during MECVI experiments

The highly corrosive chemicals involved in the CVI process deteriorated a number of the parts constituting the vacuum system, including the rotating pumps, throttle valve and pressure transducer. The latter, for example, has been replaced by a model that is heated at  $45^\circ\text{C}$ ; in this way the condensation of MTS on it is reduced. The rotating mechanism of the turntable, including the seals between the shaft and the vane, was attacked by the acid by-products. Continuous care, cleaning, removal of the rust which is microwave-absorptive and the use of special seals made of Kalrez™ (perfluoroelastomer) were required. Limiting, as much as possible, the contact of the internal parts of the equipment with air and moisture was found to be beneficial. Moreover, un-reacted MTS and by-products blocked the pipelines of the scrubber system and periodic cleaning was required.

The decomposition of MTS also led to the formation of a white film on the wall of the bell jar. This film was not transparent in the IR wavelength range of the 2-colour pyrometer and affected the reading of the temperature. For this reason the pyrometer was moved from the top of the cavity to the bottom, centred on the axis of the turntable. The plot in Figure 3-13 reports the difference in temperature

detected by the 2-colour pyrometers placed at the top and at the bottom of the cavity.

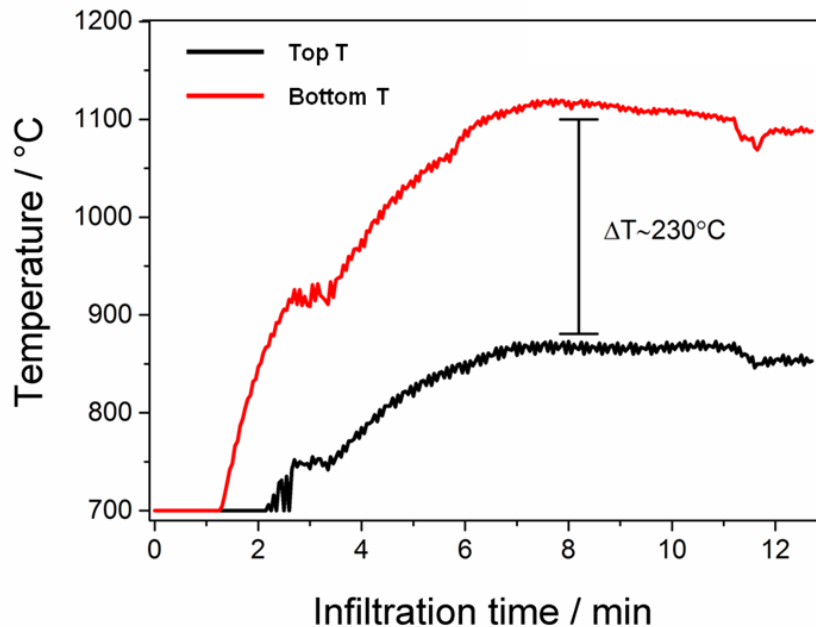


Figure 3-13. Temperature difference of the reading of the 2-colour pyrometers at the top (black solid line) and at the bottom of the cavity (red solid line).

The pyrometer at top of the cavity erroneously detected the temperature of the sample to be ca. 850°C. Relocating the control pyrometer, the actual temperature of the sample was above 1100°C.

A hindrance experienced during the entire research activity was the presence of residual oxygen in the cavity; in particular, the oxygen entrapped within the preform and/or absorbed on the fibre surface:

- I. SiO<sub>2</sub> could form on the fibres and although it is microwave transparent at high temperature [303], it contaminated the deposited matrix. The purge procedure was improved by carrying out an evacuation with an external pump able to achieve an initial vacuum of below 100 Pa whilst with the two original pumps the level was only 700 Pa. Also, the number of purges with Ar and H<sub>2</sub>

was increased to six in total to further dilute the 20 Pa of residual oxygen. Some basic thermodynamics of the MTS-H<sub>2</sub>-O<sub>2</sub> system was investigated.

- II. SiO<sub>2</sub> formation from MTS is an endothermic reaction [317]. A drop of temperature in the first few minutes of the infiltration was often observed and required a power increase as shown in Figure 3-14.

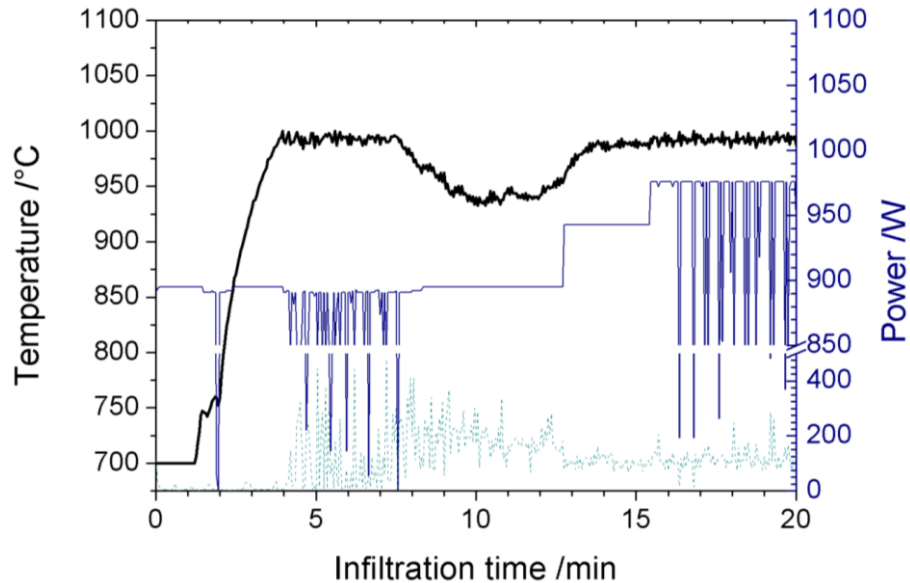


Figure 3-14. Temperature (black solid line) drop due to the formation of silica in the first stage of MECVI. Power (blue solid line) was increased from 890 to 970 W. Blue dotted line represents the reflected power.

Additional and substantial issues were related to the heating behaviour of the samples:

- I. The high aspect ratio of the fibres developed arcing between the layers of fabric. This effect was more accentuated with increasing the power and hence higher temperatures were more complicated to achieve. A relationship with the pressure was also found; in particular, unacceptable arcing occurred when the pressure was set below 16-20 kPa. This phenomenon was explained by Paschen's law [318] that correlates the breakdown voltage, the voltage necessary to initiate an electric arc (or discharge), between two

electrodes in a gas as a function of partial pressure of the gas and gap length. From the graph in Figure 3-15 it was found that the typical distance between two layers of fabric corresponds to a minimum in the Paschen's curve when the partial pressure of hydrogen is below 20 kPa. This is consistent with the phenomenon observed in this research project. Coating the side of the preform with aqueous silicon carbide slurry was found to be beneficial to not leave sharp points exposed and, hence reduce the arcing.

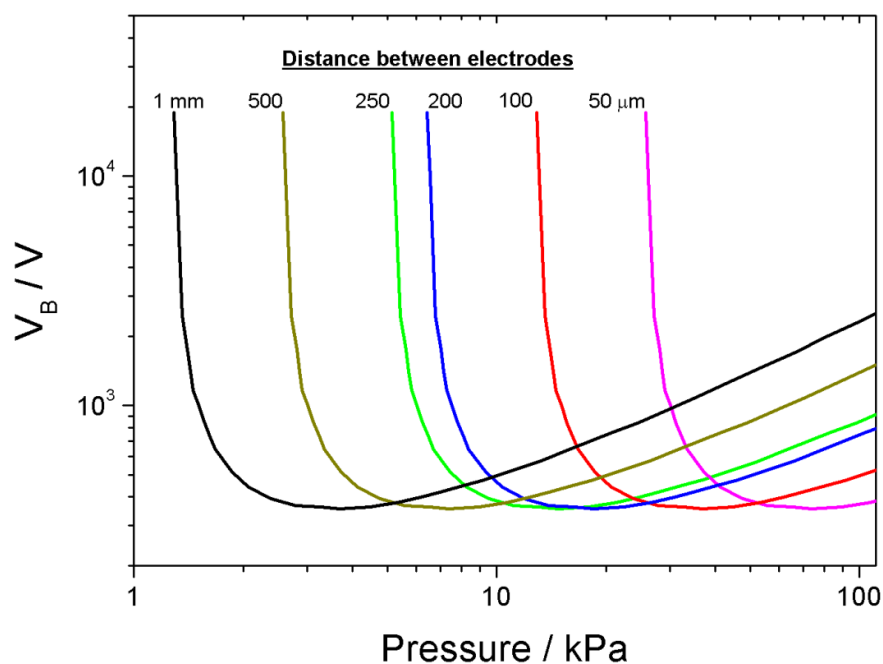


Figure 3-15. Breakdown voltage as function of partial pressure of hydrogen at different distance between two electrodes.

- II. A change in the electromagnetic properties of the preform occurred with the increase in the amount of SiC matrix deposited. It must be borne in mind that SiC is a semiconductor, hence, when an infiltrated sample was reheated with microwave radiation, the heating became more difficult and the system struggled to reach the setpoint temperature. Moreover, it cannot be assumed that the heating pattern remain unchanged, and hence temperature distribution as well.

Finally, the bell jar, likely due to the thermal fatigue, imploded during a heating test in hydrogen causing the loss of several samples and the suspension of the research activities.

### 3.3 Characterisation

The main objective of the analysis was to determine the physical and chemical properties of the deposit and how the deposition pattern was affected by parameters such as temperature, pressure and gas flow. Regular characterisation techniques such as optical and electron microscopy, X-ray diffraction and Raman spectroscopy were employed. Dielectric permittivity measurements were carried out to understand the interaction of the preform with the microwave field.

#### 3.3.1 Microscopy

The deposition pattern was studied by optical microscopy whilst the thickness of the deposit, morphology, stoichiometry and remaining porosity were investigated by electron microscopy analysis.

##### 3.3.1.1 Optical microscopy

The preforms were embedded in epoxy resin (EpoFix Resin, Struers Ltd, Catcliffe Rotherham, UK). Then, cross-section surfaces were obtained by cutting out cross-sections with a resin-bonded diamond wheel (Metprep Ltd, Coventry, UK with a thickness of 0.6 mm) and the cut samples polished to a 1  $\mu\text{m}$  mirror-finish (1 $\mu\text{m}$  diamond suspension, DiaDuo-2, Struers Ltd, Catcliffe Rotherham, UK). In a typical polishing cycle, the mounted samples were initially plane-ground using a grinding disc with grit size 220 (MD-Piano200, Struers Ltd. Catcliffe

Rotherham), followed by fine grinding using MD-Piano 600 (grit size 600) and MD-Piano 1200 (grit size 1200), followed by polishing using a diamond paste containing 3 and 1 µm size particles. Between each polishing step, the samples were removed from the specimen holder and cleaned with deionised water in an ultrasound bath. After the final polishing stage, the sample was subjected to ultrasound for 10 minutes in soapy water and then 10 minutes in ethanol to get a surface free from contamination and remains of the polishing media. An optical microscope (Axio Scope A1, Carl Zeiss Microscopy GmbH, Jena, Germany), capable of scanning automatically the entire cross-sectional surface of a preform (51 mm) diameter was then used to analyse the deposition pattern.

### 3.3.1.2 Scanning electron microscopy

Specimens were prepared with the same procedure outlined in the previous section but, in addition, the surface to be analysed was coated with a 5 nm-layer of chromium deposited with a rotary-pumped sputter coater (Q150R ES, Quorum Technologies Ltd., Lewes, UK). Chromium was used in place of the gold because of the finer grain size of the deposited layer. Analysis of the cross-sectioned samples and layers of fabric was then carried out using a SEM-FEG (JSM 7000F, JEOL USA Inc., Peabody, Massachusetts) equipped with an energy-dispersive X-Ray spectrometer (EDS Oxford, Oxford Instruments Ltd., High Wycombe, UK).

Secondary electrons (SE) with an acceleration voltage in the range 8-10 kV and work distance of 7 mm were used for higher magnification-analysis of the deposit morphology whilst back-scattered electrons (BSE) imaging, 20 kV voltage and larger spot size, was necessary to clearly differentiate the matrix from the fibres.

### 3.3.1.3 Energy-dispersive X-ray analysis (EDS)

EDS provided an elemental map of the cross-sections and, in particular, a map of the stoichiometry of the samples. Also, the oxygen content was investigated.

The spatial resolution  $R_s$  ( $\mu\text{m}$ ) in an EDS analysis varies according to a number of parameters as defined by Anderson and Hasler [319]:

$$R_s = \frac{0.064(E_0^{1.68} - E_c^{1.68})}{\rho_s} \quad (3-8)$$

where  $E_0$  and  $E_c$  are, respectively, the accelerating voltage (keV) and critical excitation energy (keV) and  $\rho_s$  is the mean sample density ( $\text{g cm}^{-3}$ ).

The penetration depth,  $X$ , can be calculated using the equation of Thomas and Widdington [320]:

$$X = \frac{E_0^2}{B\rho_s} \quad (3-9)$$

where  $B$  is a constant equivalent to  $6.2 \times 10^{11} \text{ eV g}^{-1}\text{m}^2$ . Due to the small thickness of the deposit, especially within the bundle of the fibres, a low accelerating voltage was used to minimise the interaction volume. At 10 kV, the interaction volume for SiC corresponds to a hemisphere with a diameter of  $\sim 1 \mu\text{m}$  and a penetration depth of  $\sim 0.5 \mu\text{m}$ . For these reasons, the measurements were generally carried out at least  $1 \mu\text{m}$  away from the fibres. As reference, a slab of high-purity SiC (semiconductor grade, Air Force Research Laboratory, Wright-Patterson Air Force Base, OH, USA) was considered as stoichiometric silicon carbide.

### 3.3.1.4 Wavelength-dispersive X-ray analysis (WDS)

Unlike EDS, Wavelength-Dispersive X-ray Spectroscopy (WDS) detects only the X-rays of a single wavelength at a time, without generating a broad spectrum of wavelengths or energies simultaneously. The X-rays emitted by the sample are collimated into a single crystal at a precise angle and then are dispersed by it so that the crystal passes X-rays of only one wavelength to the detector. This inherently allows a precise identification of the elements constituting the sample and also a precise quantification of light elements such as boron, carbon and oxygen. Different crystals were used, with automated changing of the crystal depending on the energy being analysed: pentaerythritol (PET) for silicon, thallium acid phthalate (TAP) for oxygen and layered synthetic W-Si crystal (known as LSM-060) for carbon. In WDS, standardization is required every time the SEM is used. A crystal of wollastonite for Si, graphite for C and alumina for O were used.

WDS has a higher spectral resolution and lower detection limit than EDS. It is more accurate for the elemental quantification, especially for light elements. The error on the Si/C ratio was found to be 0.01. However, it takes longer to acquire the necessary counts (computational times are 10 times greater than for EDS) and the interaction volume has a diameter of 3-4  $\mu\text{m}$ .

### 3.3.1.5 Transmission electron microscopy

A more detailed analysis of the grains and crystallographic orientation was carried out by transmission electron microscopy. A JEOL JEM 2000FX (JEOL Ltd. Tokyo, Japan) transmission electron microscope was used for the study. The TEM in bright-field mode provided an indication of the shape and size of the growing

matrix, whilst the dark-field imaging from the encircled reflections in the selected area electron diffraction (SAED) served to light up only that subset of crystals that were Bragg-reflecting at a given orientation and also any possible texturing of the deposit. Samples for TEM were prepared at Air Force Research Laboratory, Wright-Patterson Air Force Base, OH, USA.

### 3.3.2 Raman Spectroscopy

The micro-Raman study was performed using a Raman microscope (InVia confocal Raman microscope, Renishaw Plc, Wotton-under-Edge, UK). It was equipped with two objective lenses; x40 and x50 magnification. The optical microscope of the micro-Raman device was connected to a video monitor that allowed selection of specific areas on the sample surface to record the Raman spectrum. The spectroscopy was equipped with argon (wavelength 514 nm) and helium-neon (wavelength 632.8 nm) lasers; the He-Ne laser was used in the present study to excite the sample with the laser power being 20 mW. When micro-Raman spectra were recorded the samples were excited with the laser for 60 seconds and the average of two spectra were taken every time; spectra were collected from  $100\text{ cm}^{-1}$  to  $2000\text{ cm}^{-1}$ .

### 3.3.3 Dielectric permittivity measurements

#### 3.3.3.1 Introduction

The complex permittivity as function of the temperature was measured by the cavity perturbation method (CPM), which has been of increasing interest and is nowadays one of the most popular techniques for determining the dielectric properties of materials [321]. CPM is based on the changes in the resonance of

a cavity due to the insertion of a dielectric sample [322]. There are some stringent conditions for the applicability of this technique; the sample has to be very small compared with the cavity so that the frequency shift is within the range 0.01-0.5 Hz and the change of the inverse of the Q-factor is less than the relative shift of frequency when a sample is inserted in the cavity [323].

### 3.3.3.2 Equipment

The dielectric properties of SiC fabric and powders were measured at ITACA Research Institute of Valencia, Spain. The equipment, shown in Figure 3-16 [324], was a dual-mode microwave cavity, where heating and measuring were performed simultaneously.



Figure 3-16. Dual mode microwave cavity at ITACA, Spain.

The schematic of the experimental setup used for the heating and dielectric measurements is shown in Figure 3-17.

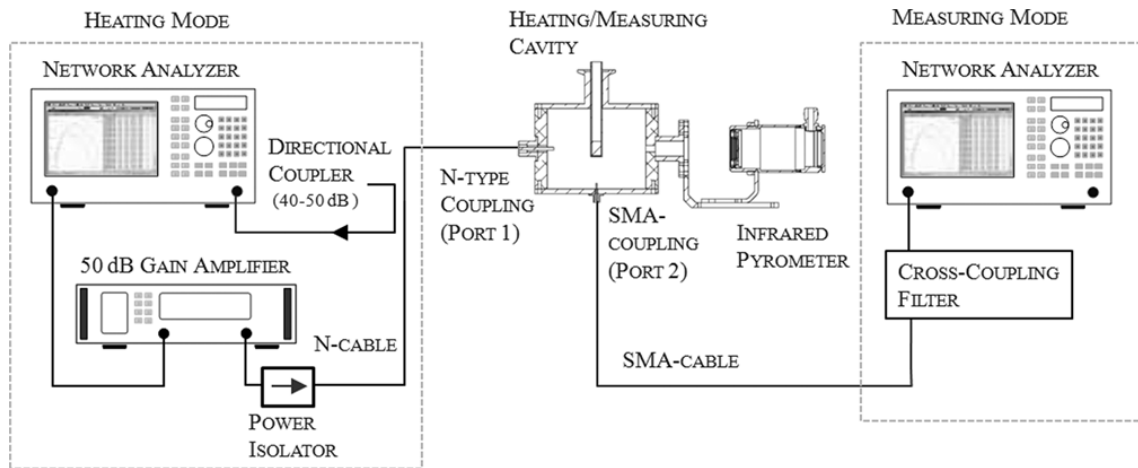


Figure 3-17. Schematic of the dual mode cavity for the measurements of the dielectric properties at high temperature. Adapted from [324].

The use of a dual-mode cavity allows short and fast heating cycles and at the same time in-situ [324] dynamic sample measurements during sample heating [321]. The cavity has been designed to heat in the cylindrical  $TE_{111}$  mode (theoretical resonance frequency 2.432 GHz) and to measure in the  $TM_{010}$  mode (2.187 GHz). To avoid any conflict between the heating and testing modes, a cross-coupling filter was used. A PID controller provided the required power for a desirable heating rate. The sample holder was a quartz vial with an inner diameter of  $\sim 9$  mm, which was inserted within the cavity through a hole located at the central plane of the top wall. The advantage of the dual-mode cavity system is that the sample has not to be inserted and removed every time that the permittivity measurements are taken [325]. The small shift of each mode when the empty quartz vial was inserted in the cavity was taken into account. The temperature of the sample (through the quartz holder) was detected using an IR pyrometer with an accuracy of  $0.1^\circ\text{C}$ . The walls of the cavity were water-cooled to minimise thermal expansion. To avoid the effect of oxidation of the SiC fabric on the dielectric properties, the cavity was evacuated and the experiments were carried out in flowing nitrogen.

### 3.3.3.3 Calculations

According to CPM and making use of the quasi-static approximation (the sample introduced in the cavity is small compared to the spatial variation of the field so that the electric field can be nearly homogeneous in the sample) [326], the dielectric permittivity  $\varepsilon'$  and the dielectric loss factor  $\varepsilon''$  can be related to the shift of the resonant frequency and the change of Q-factor  $\Delta(1/2Q)$  by [327]:

$$\varepsilon' = 1 + \frac{-\frac{\Delta f}{f} \left( \eta_g + N \frac{\Delta f}{f} \right) - N \left[ \Delta \left( \frac{1}{2Q} \right) \right]^2}{\left( \eta_g + N \frac{\Delta f}{f} \right)^2 + N^2 \left[ \Delta \left( \frac{1}{2Q} \right) \right]^2} \quad (3-10)$$

$$\varepsilon'' = \frac{\eta_g \Delta \left( \frac{1}{2Q} \right)}{\left( \eta_g + N \frac{\Delta f}{f} \right)^2 + N^2 \left[ \Delta \left( \frac{1}{2Q} \right) \right]^2} \quad (3-11)$$

where  $N$  is the sample depolarisation factor in the direction of the electric field polarisation; it measures how much the internal field within the sample is weakened by the polarisation [328].  $\eta_g$  indicates the relative volume sample/cavity weighted with the squared magnitude of the field in the empty cavity resonant mode [327].  $N$  and  $\eta_g$  were determined by calibration with reference materials whose permittivity is known [324] and they were respectively 0.102 and 0.00238. They are related to the geometry of the cavity and material sample.

Under these assumptions, and for a thin and very-low loss sample holder, the relative frequency and Q-factor shifts can be expressed, respectively as:

$$\frac{\Delta f}{f} = \frac{f_{uts} - f_{ut}}{f_{uts}} \quad (3-12)$$

$$\Delta\left(\frac{1}{2Q}\right) = \frac{f_{ut}}{2f_{uts}} \left( \frac{1}{Q_{uts}} - \frac{1}{Q_{ut}} - \frac{1}{Q_0} \frac{f_{uts}^2 - f_{ut}^2}{f_{u0}^2} \right) \quad (3-13)$$

where the subscripts  $u_0$ ,  $ut$  and  $uts$  refer respectively to the empty cavity, the empty sample holder and the sample holder containing the specimen. Combining (13) with (15) and (16), (14) with (15) and (16) the permittivity can be found. Consequently, the loss factor is:

$$\tan\delta = \frac{\varepsilon''}{\varepsilon'} \quad (3-14)$$

and the skin depth can be estimated as:

$$d = \frac{c}{\omega} \sqrt{\frac{2 \left[ 1 + \sqrt{1 + (\tan \delta)^2} \right]}{\varepsilon' (\tan \delta)^2}} \quad (3-15)$$

## 4 Results and discussion

This chapter is divided into four sections. The first section presents some preliminary results concerning a thermodynamic study of the composition of the gas phase and the deposit. The role of the residual oxygen in the reactor was also investigated. The second section is dedicated to the kinetics of the reaction occurring during the MECVI of SiC preforms with respect to the infiltration parameters such as temperature and pressure. The third section focuses on the physiochemical properties of the deposit and establishes the processing-microstructure relationship. The following section presents the deposition pattern within the preforms for different conditions of temperature and pressure. In the last section the results of the dielectric properties of the silicon carbide cloth and the microwave heating of the SiC preform are reported.

### 4.1 Preliminary results

In this section the results of the thermodynamics of the decomposition of MTS, the composition of the gas phase at equilibrium with the substrate and the composition of the solid are reported. The aim of this section is to show the chemical species involved in the deposition of silicon carbide and the influence of residual oxygen on the composition of the deposit

#### 4.1.1 Thermodynamics of the Si-C-H-Cl system

The software used for the calculations was HSC Chemistry 7.0 (Outotec, Espoo, Finland). It must be noted that the following results are thermodynamic predictions based on the assumption that the system was at equilibrium [329] and the kinetics was not taken into account. CVD and CVI are processes far from

equilibrium, which implies the potential for a disagreement between predictions and actual experimental results [237, 330].

The CVD/CVI of SiC with MTS as precursor can be divided in four parts i) initial decomposition of MTS, ii) silicon pathway, iii) carbon pathway and iv) surface reaction. The carbon pathway vs. temperature is shown in Figure 4-1. Methane was the major carbon source. However, it is reported to have a low sticking coefficient<sup>§</sup> and a low reactivity [332]. For this reason, it is believed that the dominant reactive intermediates bearing carbon were C<sub>2</sub>H<sub>x</sub> species [235, 333]. The reduced generation of hydrocarbons and low reactivity of CH<sub>4</sub> at low temperature is the reason why formation of silicon was particularly expected at low temperature as confirmed also from experimental works [227, 231, 233-236, 333-337].

SiCl<sub>4</sub> and SiHCl<sub>3</sub> were the main species bearing silicon as seen in Figure 4-2. However, their reactivity is expected to be lower than radical species such as SiCl<sub>2</sub>, which have unpaired valence electrons [333]. The concentration of SiCl<sub>2</sub> increased with temperature, whilst SiCl<sub>4</sub> decreased indicating a temperature-assisted cleavage of the Si-Cl bond. C and Si species generation are also a function of the pressure as shown in Figure 4-3 and Figure 4-4 respectively. For carbon there was a competitive effect between temperature and pressure in terms of the relative abundance of C<sub>2</sub>H<sub>2</sub> and C<sub>2</sub>H<sub>4</sub>. For the other hydrocarbons, a general increase was found. Except for SiCl<sub>2</sub> and SiCl<sub>3</sub>, the amount of silicon bearing species increased with the pressure. In terms of the composition of the matrix, the SiC content was almost stable above 1050°C, Figure 4-5. It has been

---

<sup>§</sup> The ratio of the rate of adsorption to the rate at which the adsorptive strikes the total surface, i.e. covered and uncovered [331]. It is usually a function of surface coverage, of temperature and of the details of the surface structure of the adsorbent.

reported in experimental works that at 1050°C the SiC generated from thermolysis of MTS is free from Si and C [232, 236]. However, from Figure 4-5, it can be noted that there was no agreement with the literature with respect to the carbon codeposition. In fact, carbon has been found experimentally only at very high temperatures [335] or for low values of  $\alpha$  [338]. Also, the prediction of the increase of silicon above 1100°C is not confirmed in the literature [236]. As shown in Figure 4-6, pressure had a significant effect on carbon and silicon codeposition, particularly in the low pressure range (i.e. up to 10 kPa). An increase of Si codeposition with pressure has been found in experiments [332].

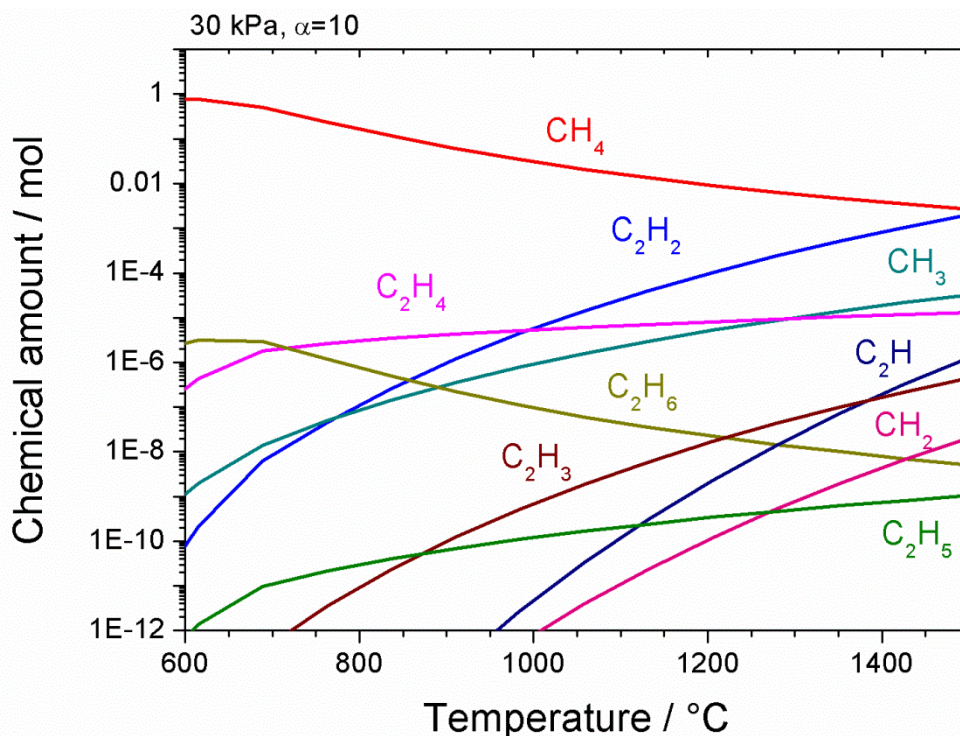


Figure 4-1. Variation of the carbon species generated by the decomposition of MTS as function of the temperature. The plot was generated by the software HSC Chemistry 7.0.

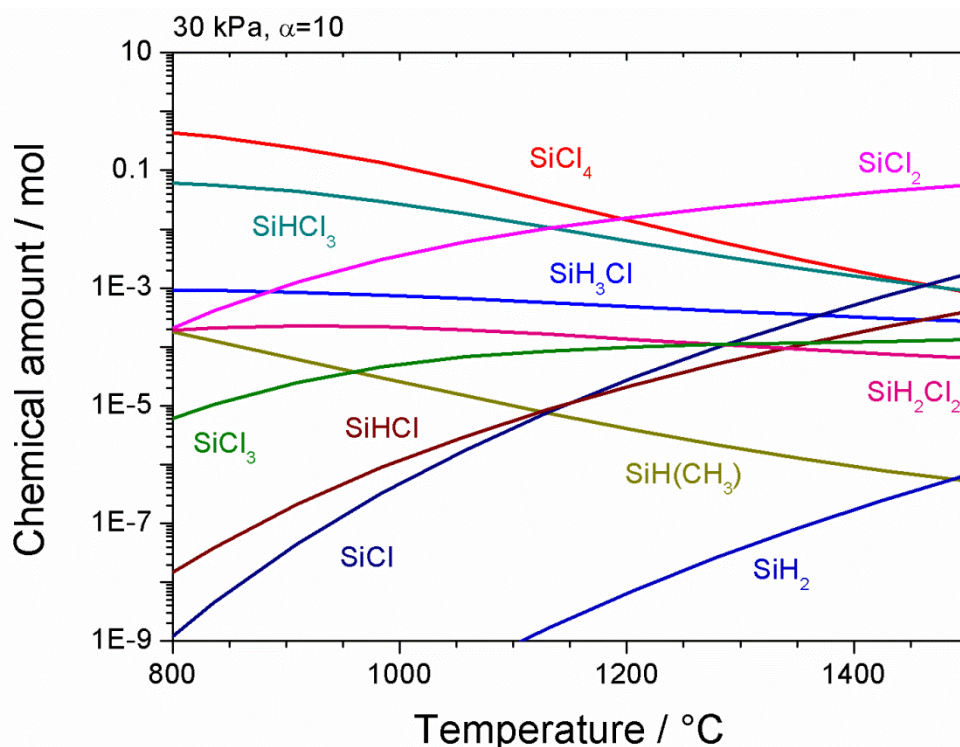


Figure 4-2. Variation of the silicon species generated by the decomposition of MTS as function of the temperature. The plot was generated by the software HSC Chemistry 7.0.

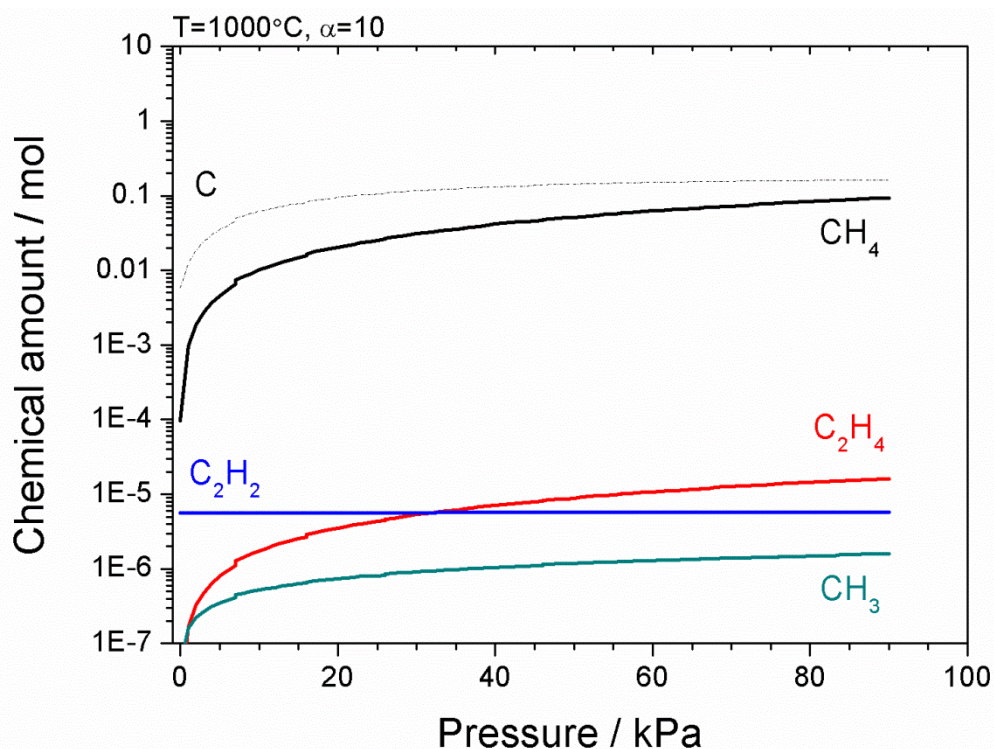


Figure 4-3. Variation of the carbon species generated by the decomposition of MTS as function of the pressure. The plot was generated by the software HSC Chemistry 7.0.

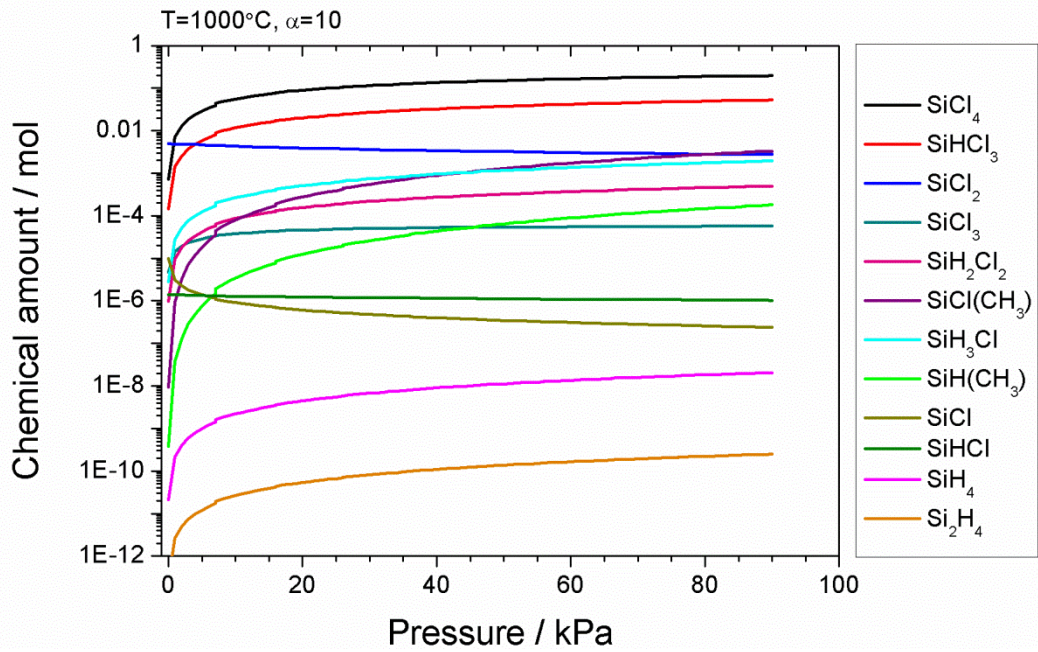


Figure 4-4. Variation of the silicon species generated by the decomposition of MTS as function of the pressure. The plot was generated by the software HSC Chemistry 7.0.

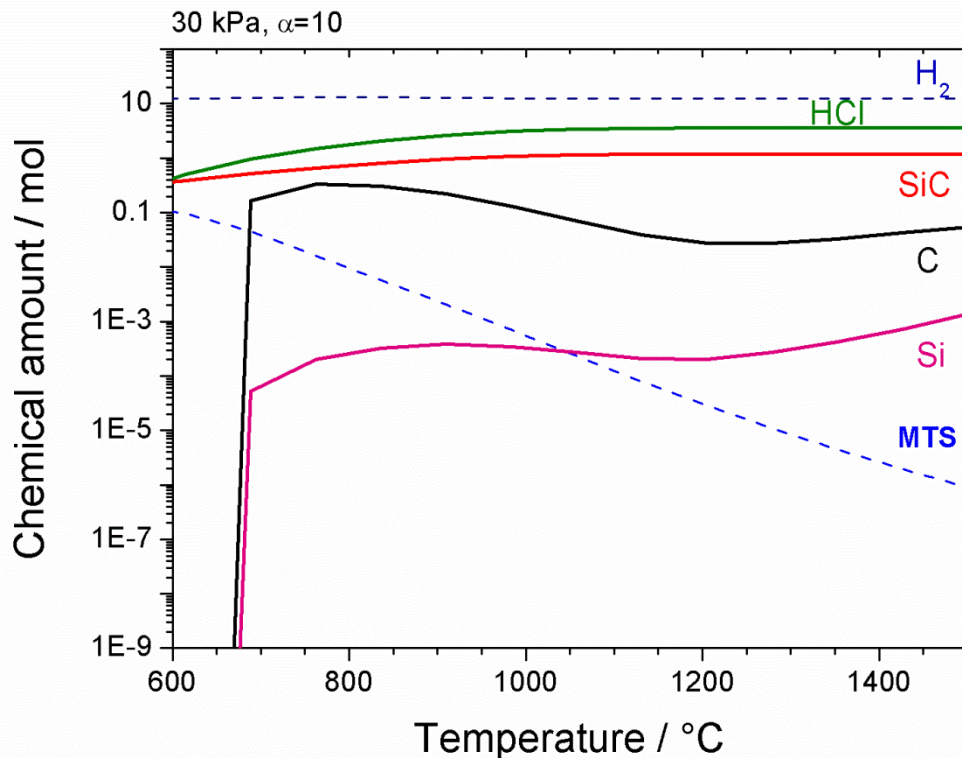


Figure 4-5. Composition of the solid deposit generated from the decomposition of MTS as function of the temperature. The plot was generated by the software HSC Chemistry 7.0.

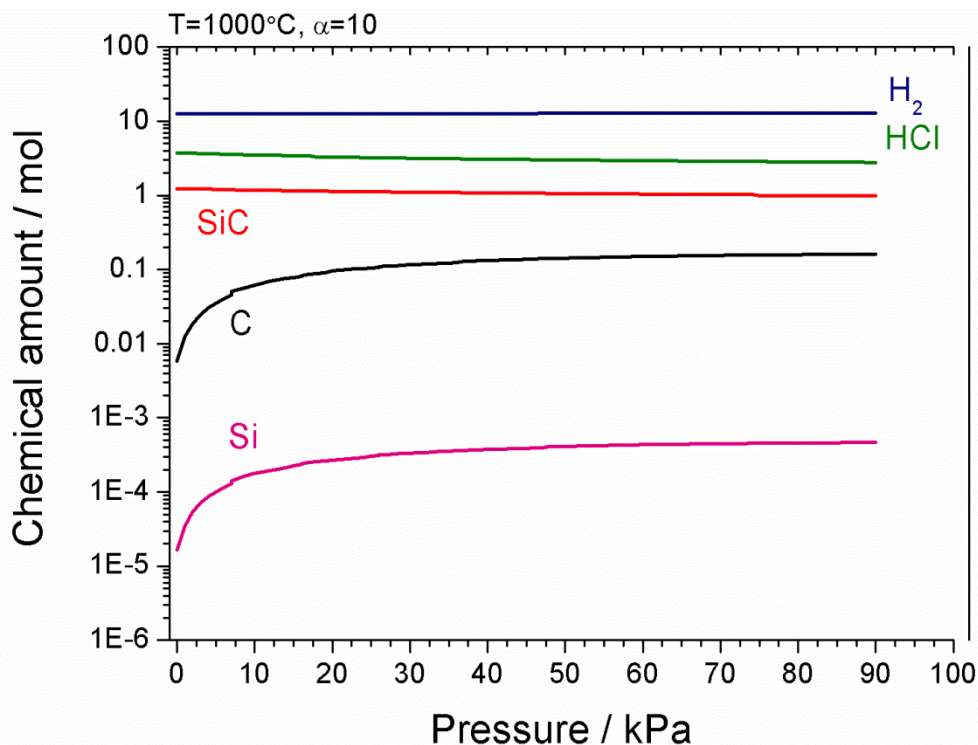


Figure 4-6. Composition of the solid deposit generated from the decomposition of MTS as function of the pressure. The plot was generated by the software HSC Chemistry 7.0.

#### 4.1.2 The presence of oxygen in the Si-C-H-Cl system

The chemical relevance of the residual oxygen and the leak rate in the reactor were investigated thermodynamically to understand the effect on the composition of the deposit. As concluded in the previous section, these thermodynamic calculations do not take into account the kinetics and they are based on the hypothesis of chemical equilibrium. Figure 4-7 shows the effect of the oxygen content on the deposition of silicon species. The calculations were based on an MTS feed of 1 mole. Over the whole range of temperature, the formation of silica was predicted and when the mole fraction of oxygen was 0.3, the deposition of silica was higher than that of the silicon carbide. When the oxygen fraction was close to 0.5, the deposition of SiC was totally suppressed at 900 and 950°C. In

the same range of oxygen content, at 1000°C, there was no suppression of SiC growth, but the deposit was made of 99 mol% of silica.

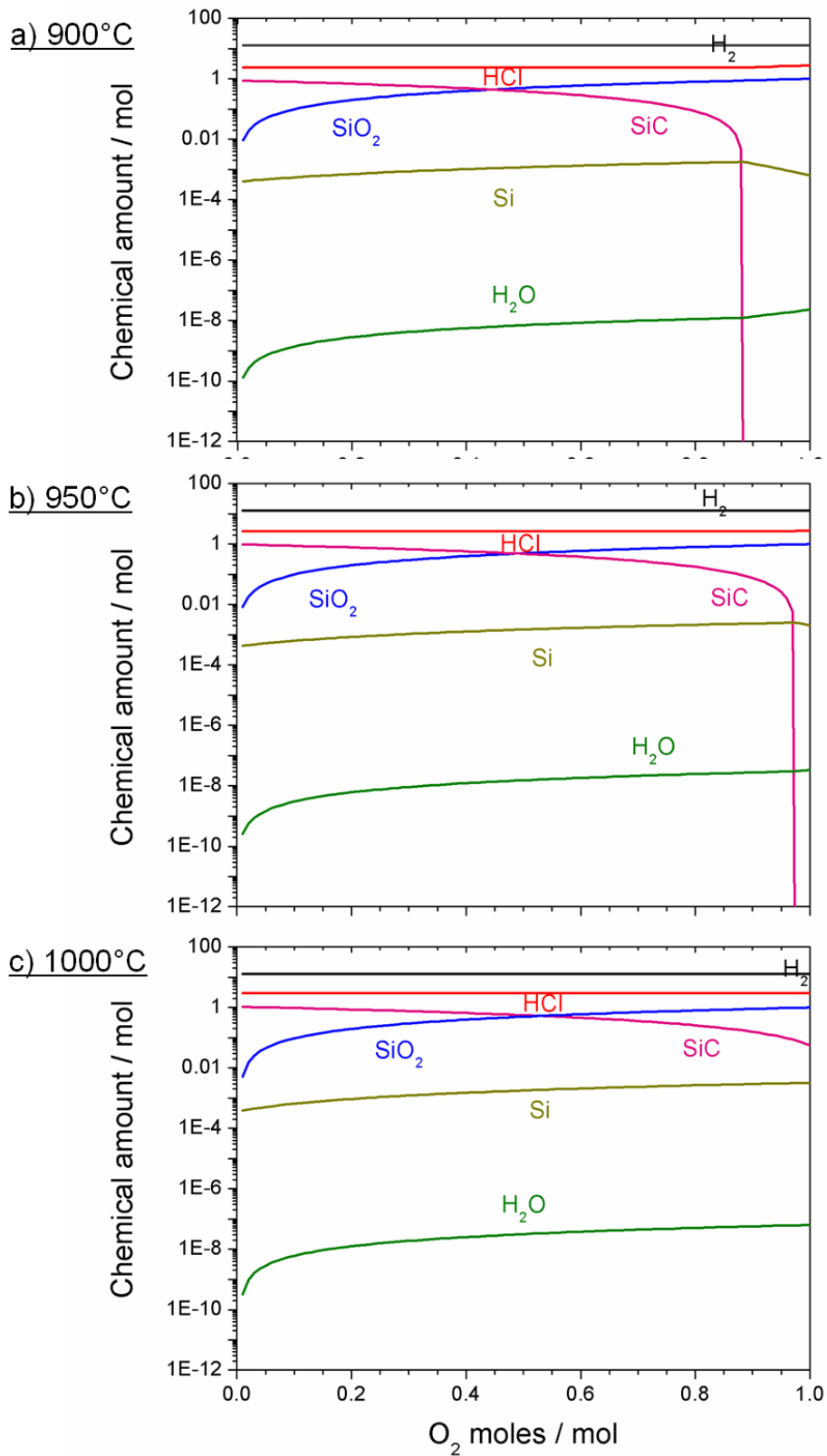


Figure 4-7. Variation of the composition of the deposit and species containing oxygen as a function of increasing oxygen content during the decomposition of

MTS at a) 900°C, b) 950°C and c) 1000°C. The plot was generated by the software HSC Chemistry 7.0.

On the basis of the data available from the pressure transducer and of the leak rate, the amount of residual oxygen during the first stage of the MECVI was estimated. The minimum vacuum achieved was 0.5 kPa and it was assumed that the composition of the residual gas was N<sub>2</sub> and O<sub>2</sub> in the molecular ratio 4:1. From the ideal gas law, the residual amount of oxygen after evacuating the reactor was thus  $n_{O_2}^{res} = 1.5 \cdot 10^{-3} \text{ mol}$ . Prior to the MTS infiltration, the reactor was filled with hydrogen to the set pressure in a time  $t_0$  and considering the leak rate  $L_{O_2}$ , the initial amount of oxygen in the reactor was estimated as

$$n_{O_2}^i = n_{O_2}^{res} + t_0 \times L_{O_2} \quad (4-1)$$

This backfill of the reactor took approximately  $t_0 = 10$  minutes and with a leak rate of  $L_{O_2} = 1.5 \times 10^{-4} \text{ mol min}^{-1}$ , the initial amount of oxygen in the reactor will have been approximately  $3.0 \times 10^{-3} \text{ mol}$ .

As will be discussed later in the chapter, during the first stage of the MECVI there was the formation of a silica layer. The MTS reacted initially with the oxygen and only after the latter's consumption did SiC deposition begin. This transitional time,  $T$ , was estimated as the ratio of the total content in moles of the oxygen in the reactor,  $n_{O_2}^i$ , and the number of moles MTS per minute,  $n_{MTS}$ , entering the reactor:

$$T = \frac{n_{O_2}^i}{n_{MTS}} \approx 2.5 \text{ mins} \quad (4-2)$$

However, the decomposition of the MTS will not have been over the range of temperatures investigated but the degree of decomposition undergone will have

depended on the temperature and residence time. It must be also considered that not all the species bearing silicon, generated by the splitting of the MTS molecules, actively participate in the formation of the solid deposit. A factor  $\Psi$ , varying between 0 and 1, was used to take into account the effective percentage of active species and the transitional time,  $T$ , was estimated as follows

$$T = \frac{n_{O_2}^i}{\Psi(T, \tau) \times n_{MTS}} \quad (4-3)$$

When the 70% of the MTS leads effectively to the deposition of silica, the transient time increases to 3.8 mins and it further increases to 5.8 mins when  $\Psi$  is 0.5. This transient time of 5 mins was approximately the period of time in which a temperature drop was observed at beginning of each MECVI run during this research project, Figure 3-14.

## 4.2 Kinetics

The aim of this section was to determine the kinetics laws that regulate the thermal decomposition of MTS and hence the deposition of silicon carbide. Moreover, the dependence of the SiC deposition on temperature and pressure was also studied to predict a set of experimental conditions that would be adequate to achieve the full densification of the SiC preforms.

### 4.2.1 Matrix growth rate

#### 4.2.1.1 Influence of temperature

The Arrhenius plot in Figure 4-8 presents the natural logarithm of the matrix growth rate ( $G_{SiC}$ ) against the reciprocal temperature.

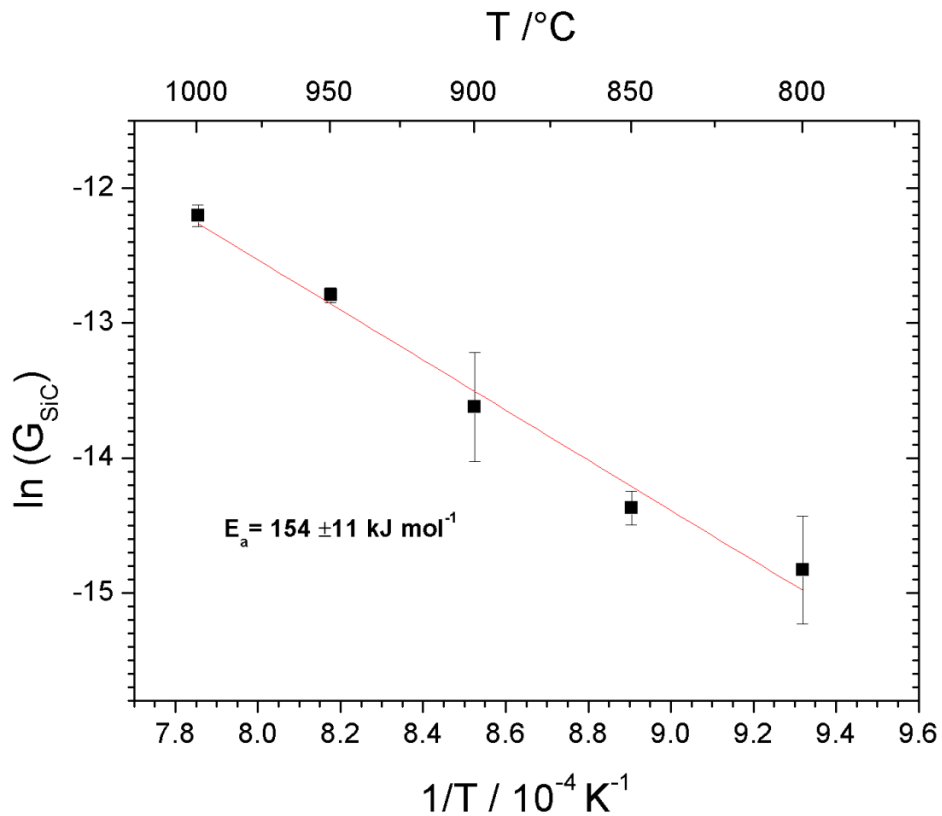


Figure 4-8. Natural logarithm of the matrix growth rate  $G_{SiC}$  against the reciprocal temperature at  $P = 30$  kPa,  $Q_{H_2} = 300$  ml min<sup>-1</sup>.

The matrix growth rate increases with the temperature as higher temperature promotes faster decomposition of MTS to silicon and carbon-bearing species [227, 231, 233-236, 333-337]. The SiC deposition shows an Arrhenius behaviour in the range 800 - 1000°C, consistently with the literature [333]. The linear dependence is typical of the growth mechanism being limited by chemical reaction, which is favourable for CVI [193]. The values of the activation energy  $E_a$  were determined by linear fitting and it was  $154 \pm 11$  kJ mol<sup>-1</sup> and the magnitude of the calculated activation energy is discussed in more detail in section 4.2.2.

### 4.2.1.2 Influence of pressure

Figure 4-9 shows the infiltration rate and matrix growth rate as function of pressure and temperature. The yield was calculated from the infiltration rate, equation (3-1), and varied from ~ 5 to 25%. The minimum infiltration pressure was 20 kPa since below ~ 7.5 kPa plasma formed, whilst between 10 - 20 kPa the process was negatively affected by the occurrence of arcing, see section 3.2.2.5. The growth rate was studied for  $Q_{H_2} = 300 \text{ ml min}^{-1}$  and  $\alpha = 10$ . The deposition rate increased at 900 and 950°C over the entire pressure range (20 - 70 kPa), which is characteristic of a kinetic limited process. At the highest temperature investigated of 1000°C, the growth rate did not depend on the total gas pressure, in agreement with a mass-transfer regime. Similar results were reported from Loumagne et al. [233].

In terms of matrix growth rate, the linear increase with pressure at 900 and 950°C is related to the increased residence time of the gas, which in turn, increases linearly with the pressure [242]. Similar results were reported from Loumagne et al. [233]. At lower pressure the residence time was so short that the critical reaction rate could become larger than the gas residence time. Therefore, the MTS had insufficient time to react, leading to less deposition. At 1000°C the infiltration rate did not depend on pressure.

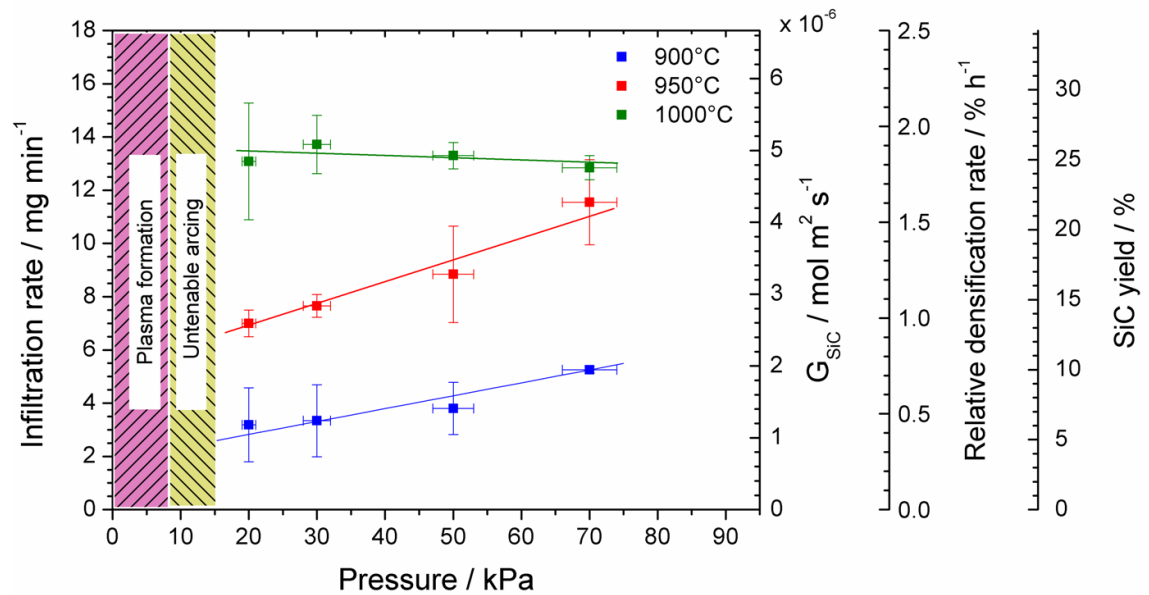


Figure 4-9. SiC matrix growth rate, relative densification rate and yield of the decomposition of MTS as function of the pressure for infiltration temperature of 900, 950 and 1000°C,  $Q_{H_2} = 300 \text{ ml min}^{-1}$ .

Calculations using equation ( 3-7 ) yielded Figure 4-10, Figure 4-11 and Figure 4-12, which illustrates the pore gas residence time variations, respectively, as a function of the temperature, pressure and gas flow rate. The porosity of the preforms used was 70% and the tortuosity was estimated as 1.4 [339]. A 7 mm-thick fibre preform was considered. The residence time at 1000°C and 30 kPa was 0.15 seconds whilst at 900°C it was 0.16 s. The dependence on the pressure at different flow rates was much stronger, Figure 4-11. With a flow rate of 300 ml  $\text{min}^{-1}$  and at 1000°C the residence time varied linearly from 0.1 to 0.34 s in the range 20-70 kPa. The strongest dependence was on the flow rate as, close to atmospheric pressure, the residence time at 70 kPa and 100 ml  $\text{min}^{-1}$  was above 1 second, Figure 4-12.

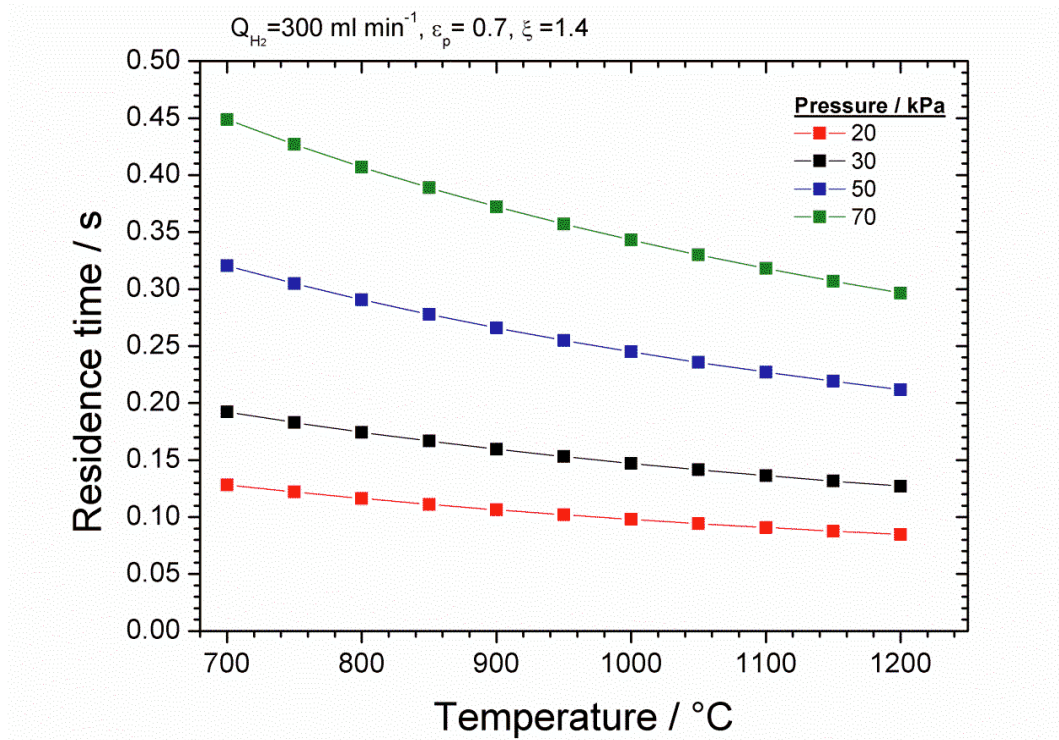


Figure 4-10. Average pore residence time as a function of the infiltration temperature ranging from 700 to 1200°C.

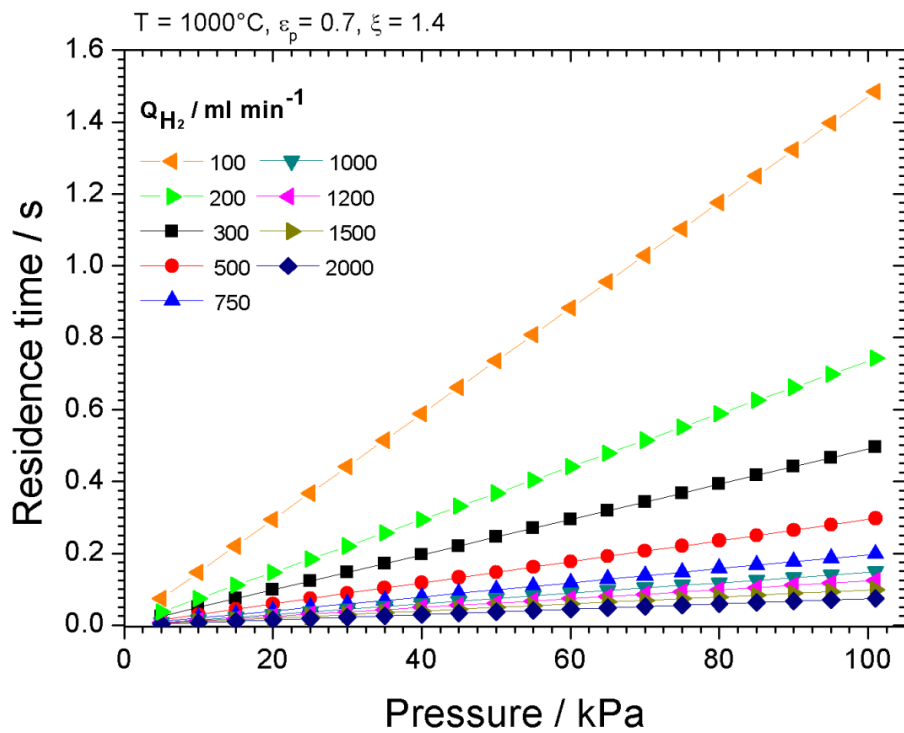


Figure 4-11. Average pore residence time as a function of the total pressure for various hydrogen flow rates.

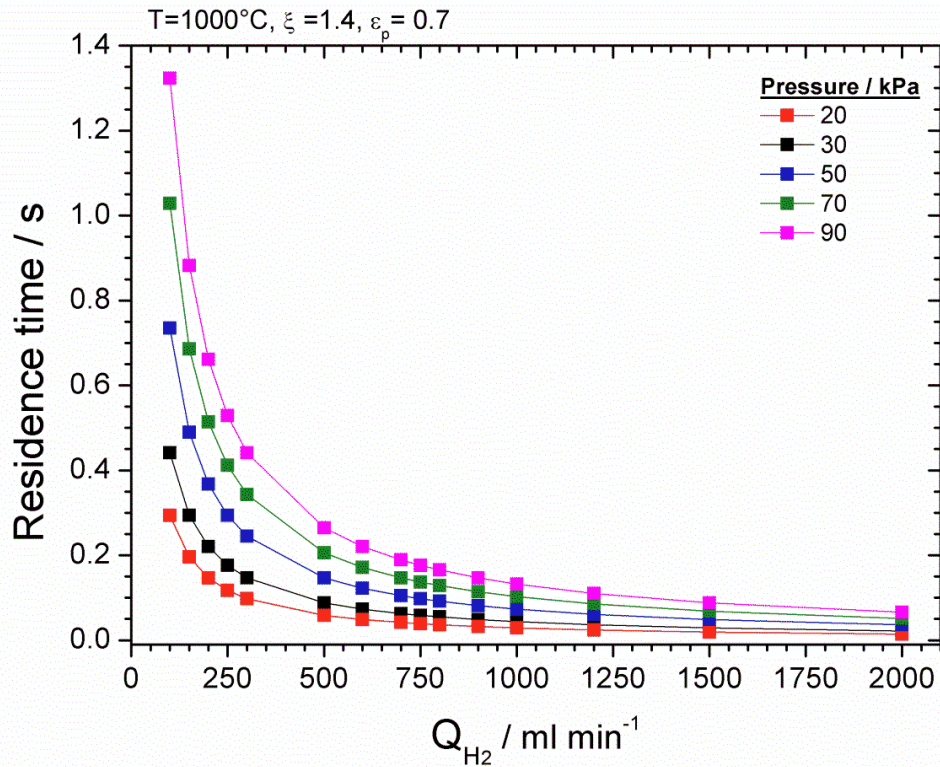


Figure 4-12. Average pore residence time as a function of the flow rate for various total gas pressures.

#### 4.2.2 Activation energy

Calculations of the activation energy to the matrix growth resulted in values with a dependence on the pressure, Figure 4-13. As mentioned in section 4.2.1.1, the value of the activation energy  $E_a$  was determined by linear fitting of the Arrhenius plot of the matrix growth rate. At the lowest pressure of 20 kPa, the activation energy corresponded to its highest value of  $176 \pm 7 \text{ kJ mol}^{-1}$ , which was close to the value reported under similar pressure conditions,  $\sim 190 \text{ kJ mol}^{-1}$ , from different authors [233-235, 240, 336, 340]. At 30 kPa, the value of the activation energy was  $154 \pm 11 \text{ kJ mol}^{-1}$ , Figure 4-8. A decrease in activation energy with pressure has been reported by several authors [333, 337, 341]. At 50 kPa the activation energy was effectively unchanged at  $146 \pm 17 \text{ kJ mol}^{-1}$ , whilst at 70 kPa it decreased to  $112 \pm 47 \text{ kJ mol}^{-1}$ , as shown in Figure 4-13. However, in the latter

case, the linear fitting generated an uncertainty too large to be considered representative. The dependence ceased to be linear at the high partial pressure of 70 kPa and above 950°C. The data suggest that above this temperature the growth rate was almost independent of temperature, which is a typical behaviour for crystal growth in a mass-transport limited regime [193].

Generally, the activation energy of the deposition of SiC from MTS/H<sub>2</sub> lies in the range 130-300 kJ mol<sup>-1</sup> [227, 235, 340, 342], which is almost in agreement with the values reported in the present work. Higher value have been reported only at < 850°C [233, 235]. Since the deposition of pyrocarbon has an activation energy ranging from 138 to 272 kJ mol<sup>-1</sup> (depending on the hydrocarbon source) [343], the energy barrier is represented by the low extent of carbon species participating in the deposition [240].

Interestingly, the activation energies of the SiC deposition reported in this work are lower than those calculated by other authors [233-235, 240, 336, 340]. The interaction of the microwaves with the substrate and the reactants can change the kinetics with the following additional mechanisms [315]:

- Additional active sites can be available on the surface of the fibres because of the electric field applied. In fact, microwave field can induce charges on the surface of the fibres and/or interact with impurities and the zirconium naturally contained in the ZMI SiC fibres
- The electric field is applied on free radicals and unsaturated hydrocarbon species (see section 4.1.1) [315] resulting in an increased collision probability both in the gas phase and on the surface of the fibres. Thus, the deposition rate is accelerated.

All these phenomena can be considered examples of the so-called “microwave field non-thermal effect” [261].

However, it should be carefully taken into account that all the results were obtained under conditions of inhomogeneous temperature distribution across the sample.

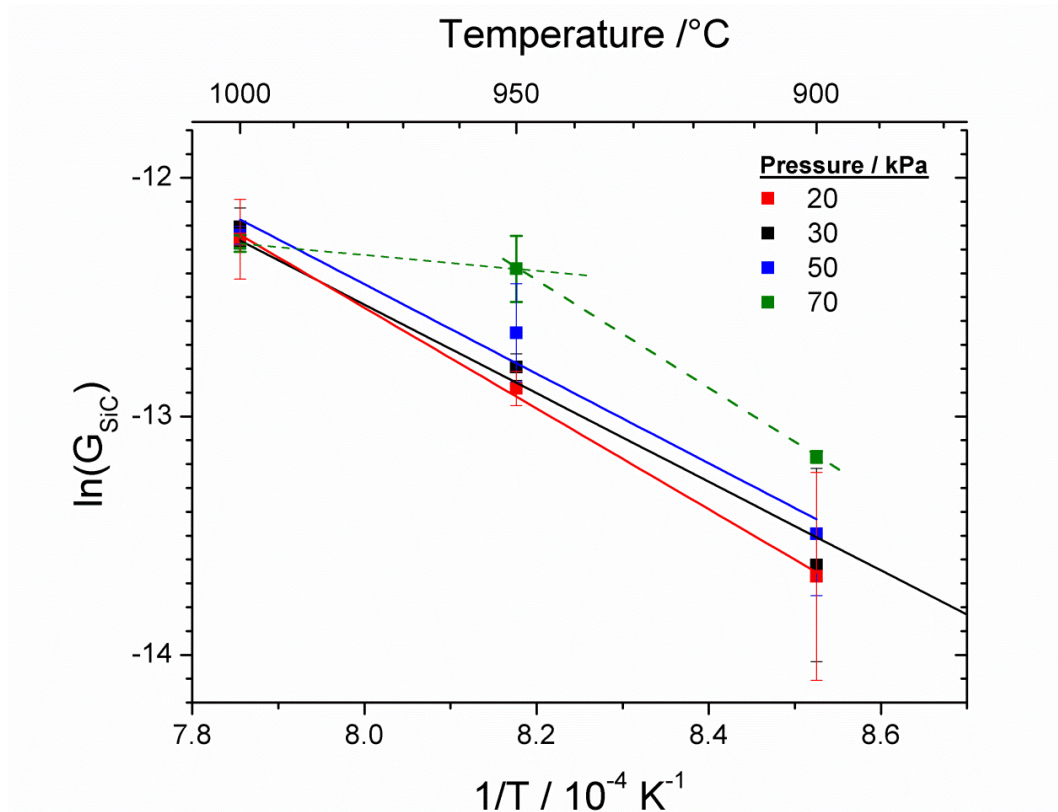


Figure 4-13. Matrix growth rate against the reciprocal of the temperature at different pressures.  $Q_{H_2} = 300 \text{ ml min}^{-1}$  and  $\alpha = 10$

### 4.2.3 Mass transport and chemical reactivity

To assess the transport phenomena and the kinetic mechanisms taking place during the MECVI process, some dimensionless numbers were calculated to describe the competition between chemical reaction rate and the mass transport of the gaseous mixture into the pores. In Table 14 the meaning and definitions of

the transport parameters and transition values between each regime are reported [193, 203, 344].

Table 14. Parameters and dimensionless numbers describing transport phenomena in CVD/CVI.

Transport parameter	CVD	CVI	Transition value for CVI
Characteristic dimension of mass transport $d$	$d$	$4r_H = \frac{d_p \varepsilon_p}{(1 - \varepsilon_p)}$	--
**Diffusivity $D$	$\left(\frac{1}{D_m} + \frac{1}{D_K}\right)^{-1}$	$\frac{\varepsilon_p D_{eff}}{\xi}$	--
†† Gas velocity $v$	$v$	$\frac{v\xi}{\varepsilon_p}$	--
Reynolds number $Re$  <i>inertia forces</i> <i>viscous forces</i>	$\frac{vd\rho_s}{\mu_v}$	$\frac{v_p d_p \rho_s}{\mu_v} \frac{\varepsilon_p}{(1 - \varepsilon_p)}$	1
Peclet number $Pe$  <i>advective transport</i> <i>diffusive transport</i>	$\frac{vd}{D_{eff}}$	$\frac{v_p d_p}{D_{eff}} \frac{\xi}{(1 - \varepsilon_p)}$	$10^{-2}$ - $10^{-3}$
Damkohler number (I) $Da_I$  <i>reaction rate</i> <i>convective mass transport rate</i>	$\frac{4k_r}{v}$	$\frac{4k_r}{v_p}$	$6 \times 10^{-2}$
Damkohler number (II) $Da_{II}$  <i>reaction rate</i> <i>diffusive mass transport rate</i>	$\frac{4dk_r}{D_{eff}}$	$\frac{4d_p k_r}{D_{eff}} \frac{\xi}{(1 - \varepsilon_p)}$	$10^{-4}$ - $10^{-5}$

where  $r_H$  is the hydraulic radius (m),  $d_p$  is the average pore diameter (m),  $D_{eff}$  is the effective gas diffusion coefficient ( $m^2 s^{-1}$ ),  $\rho_s$  and  $\mu_v$  are respectively the density ( $kg m^{-3}$ ) and the viscosity (Pa s) of the gaseous mixture MTS/H<sub>2</sub> and  $k_r$  is the first order reaction rate coefficient ( $m s^{-1}$ ).

\*\* Defined as  $D_{eff}$ , in Appendix I it is reported how to calculate  $D_{eff}$  for MTS/H<sub>2</sub> mixture

†† Defined as  $v_p$  in Chapter

## Chapter 4. Results and discussion

As pore size, the fibre diameter ( $\sim 10 \mu\text{m}$ ) was chosen as representative for the intratow porosity and an average pore diameter of  $250 \mu\text{m}$  for the intertow porosity.  $v_p$  has been calculated according to equations ( 3-5 ) and ( 3-6 ). At low Peclet numbers, diffusion will control the transport mechanism, whereas convection will be predominant at high  $Pe$ . As shown in Table 15, advection is the predominant mass transport in the largest pores, whilst mass transport of the gaseous species into the tows is in the transition region from diffusive to advective transport. Although diffusion depends on the reciprocal of the pressure, the residence time ( $v_p \propto \frac{1}{\tau}$ ) decreases with pressure much faster.

Table 15. Estimation of the Peclet number for intratow and intertow porosities in different conditions of temperature and pressure ( $Q_{\text{H}_2} = 300 \text{ ml min}^{-1}$ ).

$P / \text{kPa}$	$T / ^\circ\text{C}$	$v_p / \text{m s}^{-1}$	$D_{\text{eff}} / \text{m}^2 \text{ s}^{-1}$	$Pe$	
				Intratow $d_p = 10 \mu\text{m}$	Intertow $d_p = 250 \mu\text{m}$
20	900	$9.7 \times 10^{-2}$	$1.1 \times 10^{-4}$	$1.2 \times 10^{-2}$	$5.1 \times 10^{-1}$
20	950	$1.0 \times 10^{-1}$	$1.1 \times 10^{-4}$	$1.2 \times 10^{-2}$	$5.2 \times 10^{-1}$
20	1000	$1.1 \times 10^{-1}$	$1.2 \times 10^{-4}$	$1.3 \times 10^{-2}$	$5.2 \times 10^{-1}$
30	900	$6.5 \times 10^{-2}$	$9.9 \times 10^{-5}$	$9.2 \times 10^{-3}$	$3.8 \times 10^{-1}$
30	950	$6.8 \times 10^{-2}$	$1.0 \times 10^{-4}$	$9.3 \times 10^{-3}$	$3.9 \times 10^{-1}$
30	1000	$7.0 \times 10^{-2}$	$1.1 \times 10^{-4}$	$9.3 \times 10^{-3}$	$3.9 \times 10^{-1}$
50	900	$3.9 \times 10^{-2}$	$8.2 \times 10^{-5}$	$6.7 \times 10^{-3}$	$2.8 \times 10^{-1}$
50	950	$4.1 \times 10^{-2}$	$8.5 \times 10^{-5}$	$6.7 \times 10^{-3}$	$2.8 \times 10^{-1}$
50	1000	$4.2 \times 10^{-2}$	$8.8 \times 10^{-5}$	$6.7 \times 10^{-3}$	$2.8 \times 10^{-1}$
70	900	$2.8 \times 10^{-2}$	$6.9 \times 10^{-5}$	$5.6 \times 10^{-3}$	$2.4 \times 10^{-1}$
70	950	$2.9 \times 10^{-2}$	$7.2 \times 10^{-5}$	$5.6 \times 10^{-3}$	$2.3 \times 10^{-1}$
70	1000	$3.0 \times 10^{-2}$	$7.5 \times 10^{-5}$	$5.6 \times 10^{-3}$	$2.3 \times 10^{-1}$

Damkohler numbers, defined in Table 15, can be used to relate the chemical reaction timescale to transport phenomena rate occurring in the system.

At low Damkohler numbers, the surface reaction is step-limiting and it controls the deposition mechanism, whereas mass transport/diffusion will be predominant at high  $Da_{I-II}$ .

The reaction rate  $k_r$  can be obtained from  $G_{SiC}$  considering a first order reaction rate with respect to the MTS concentration:

$$G_{SiC} = k_r \times C_{MTS} \quad (4-4)$$

Where  $C_{MTS}$  is the MTS concentration in mol m<sup>-3</sup>.

Results of the calculation for  $Da_I$  and  $Da_{II}$  for intertow and intratow pores, listed in Table 16, show the matrix deposition in the intertow is limited by surface kinetics. This agrees with observations that the coatings deposited on the fibres had cylindrical symmetry and hence there was no obvious difference coating thickness on the upstream and downstream surfaces of the fibres. However at 1000°C,  $Da_I$  was around the transition value and similarly at 950 and 1000°C for  $Da_{II}$ . It must be noted that this model does not take into account that the surface available for the matrix growth changed with the infiltration time. In fact, once the tow was sealed the available surface for the deposition drastically decreased affecting  $G_{SiC}$  and hence  $k_r$ .

Table 16. Estimation of Damkohler numbers under different conditions of temperature and pressure.

<b><i>P</i></b> / kPa	<b><i>T</i></b> / °C	<b><i>K<sub>r</sub></i></b> / ms <sup>-1</sup>	<b><i>Da<sub>I</sub></i></b>	<b><i>Da<sub>II</sub></i></b>
20	900	6.27 x10 <sup>-6</sup>	1.5 x10 <sup>-2</sup>	6.5 x10 <sup>-5</sup>
20	950	1.44 x10 <sup>-5</sup>	3.2 x10 <sup>-2</sup>	1.4 x10 <sup>-4</sup>
20	1000	2.79 x10 <sup>-5</sup>	6.1 x10 <sup>-2</sup>	2.7 x10 <sup>-4</sup>
30	900	4.38 x10 <sup>-6</sup>	1.5 x10 <sup>-2</sup>	5.1 x10 <sup>-5</sup>
30	950	1.05 x10 <sup>-5</sup>	3.5 x10 <sup>-2</sup>	1.2 x10 <sup>-4</sup>
30	1000	1.95 x10 <sup>-5</sup>	6.4 x10 <sup>-2</sup>	2.1 x10 <sup>-4</sup>
50	900	2.99 x10 <sup>-6</sup>	1.8 x10 <sup>-2</sup>	4.2 x10 <sup>-5</sup>
50	950	7.25 x10 <sup>-6</sup>	4.1 x10 <sup>-2</sup>	9.8 x10 <sup>-5</sup>
50	1000	1.14 x10 <sup>-5</sup>	6.2 x10 <sup>-2</sup>	1.5 x10 <sup>-4</sup>
70	900	2.95 x10 <sup>-6</sup>	2.4 x10 <sup>-2</sup>	4.9 x10 <sup>-5</sup>
70	950	6.77 x10 <sup>-6</sup>	5.4 x10 <sup>-2</sup>	1.1 x10 <sup>-4</sup>
70	1000	7.84 x10 <sup>-6</sup>	6.0 x10 <sup>-2</sup>	1.2 x10 <sup>-4</sup>

### **4.3 Morphology and stoichiometry**

In this sections the morphology and physiochemical properties of the matrix were investigated and, particularly, the effect of the pressure and temperature on the crystal growth. Dispersive and Raman spectroscopy were used to analyse the composition of the matrix. Finally, a crystal growth model was proposed and a qualitative phase diagram drawn.

#### **4.3.1 Morphology of the deposit**

##### **4.3.1.1 Influence of the temperature**

Figure 4-14 shows the different SiC coating morphologies on the fibres, located in the interior of the tow, at different temperatures of 900, 950 and 1000°C. At

900°C, Figure 4-14(a) and (b), the matrix growth produced a “cauliflower-like” aspect with rounded particles on the surface with diameter in the range of 20-50 nm. The aspect became rougher when the temperature was increased to 950, Figure 4-14(c) and (d), and 1000°C, Figure 4-14(e) and (f). The fracture surface of the deposit in Figure 4-15 shows columnar growth of the matrix with an angular surface.

High temperature increases the surface mobility and the crystals can achieve stable growth and hence affect the morphology of the matrix. The deposit is nanocrystalline, globular and overall smooth at low temperature (nucleation is favoured and density nuclei is high), whilst deposits assume a rough and columnar aspect with arrow-head surface morphology at higher temperatures. This is in agreement with Loumagne et al. [332] and with the results of the CVD experiments in Figure 4-23.

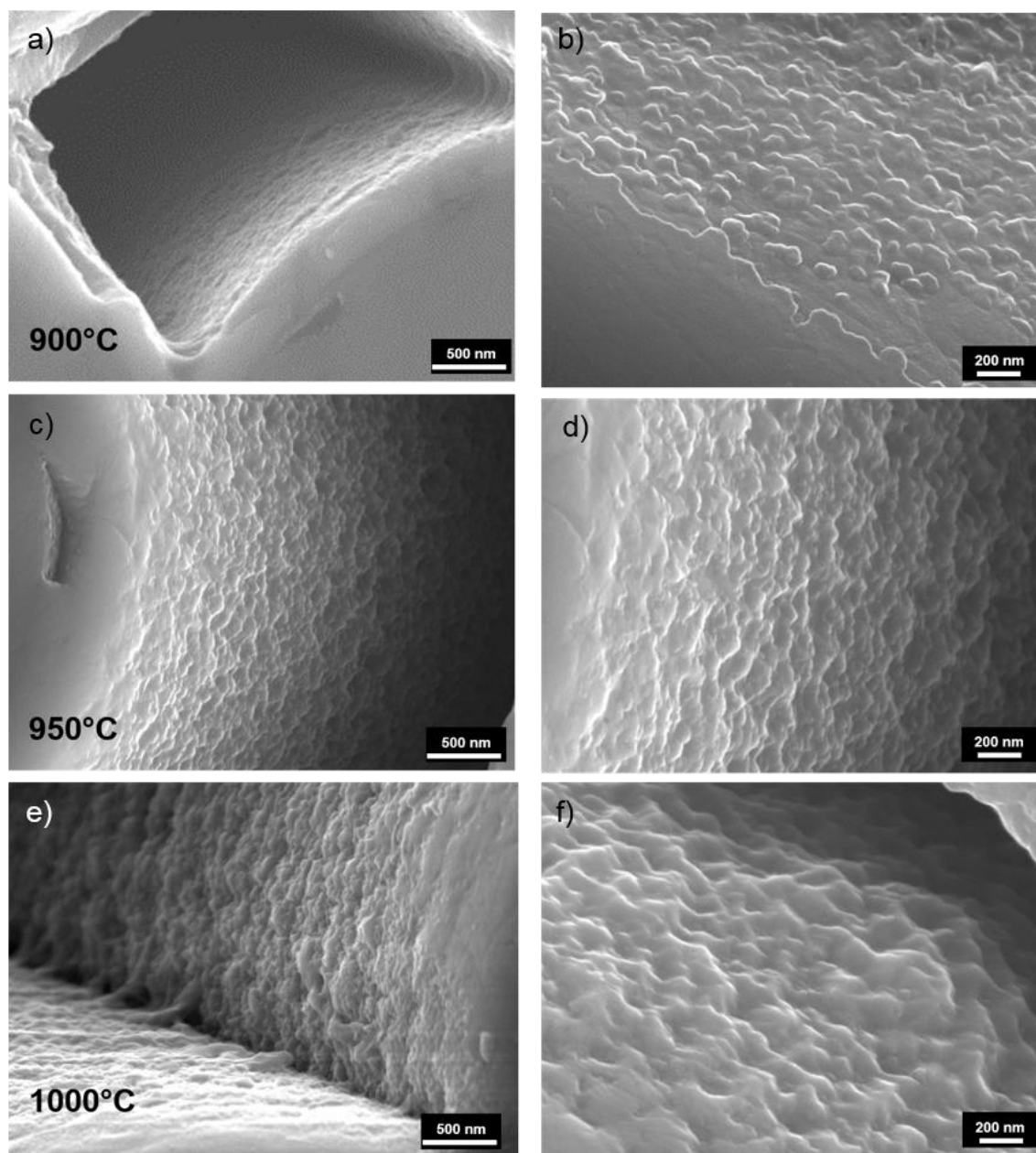


Figure 4-14. SEM-SEI images of the morphology of the deposit at: (a) and (b) 900°C, (c) and (d) 950°C and (e) and (f) 1000°C. Total pressure was 30 kPa, total flow rate 300 cm<sup>3</sup> min<sup>-1</sup> and gas ratio ~10.

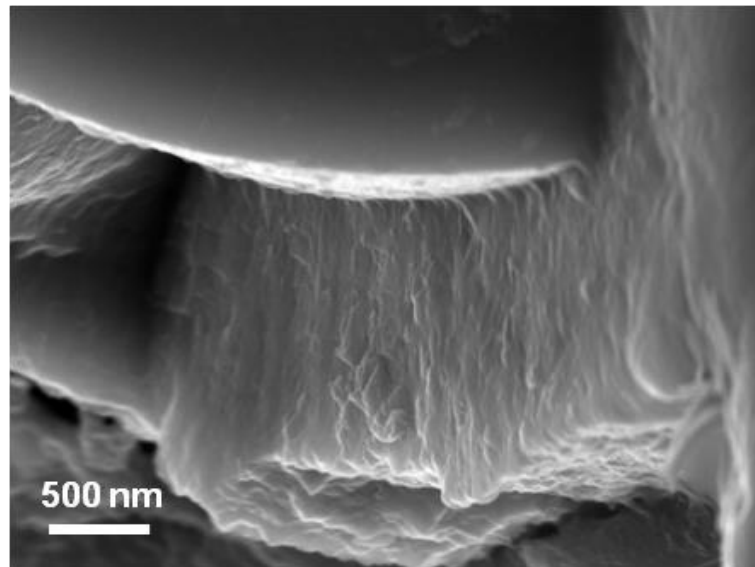


Figure 4-15. SEM-SEI image of the fracture surface showing columnar growth

For the preform infiltrated at 900°C and 30 kPa a change of morphology was observed at different locations as shown in Figure 4-16. The cauliflower-like structure of the matrix observed in the centre, Figure 4-16(a) and (b), changed to a highly angular morphology at 10 mm from the centre, Figure 4-16(e) and (f). In the region containing this deposit morphology it was observed that more SiC was deposited. Since MECVI promotes a temperature profile across the samples, the deposit undergoes to morphology changes. In fact, in the region containing more deposit the morphology was similar to that of the samples infiltrated at 950 and 1000°C and, therefore, suggests that the local temperature was higher than 900°C.

For infiltrations at 1000°C, the morphology varied across the diameter of the preform, Figure 4-17. The roughness of the deposit decreased from the centre, Figure 4-17(a) and (b), toward the periphery of the sample, Figure 4-17(c) to (f). At 20 mm from the centre, the deposit presented a well-developed globular morphology, Figure 4-17(e) and (f), typical of low temperature.

Figure 4-18 illustrates the variation in deposit morphology that could be observed between the interior and the exterior of a typical tow infiltrated at 950°C. Inside the tow the deposit can be observed to be smoother, Figure 4-18(a), whilst on the exterior the growth front is clearly not linear, Figure 4-18(b). This may be due to the different mechanism of transport of the reactant species existing for the inter- and intratow porosity. Higher concentration of by-product such HCl in the intratow pores could also lead to smoother surface [330].

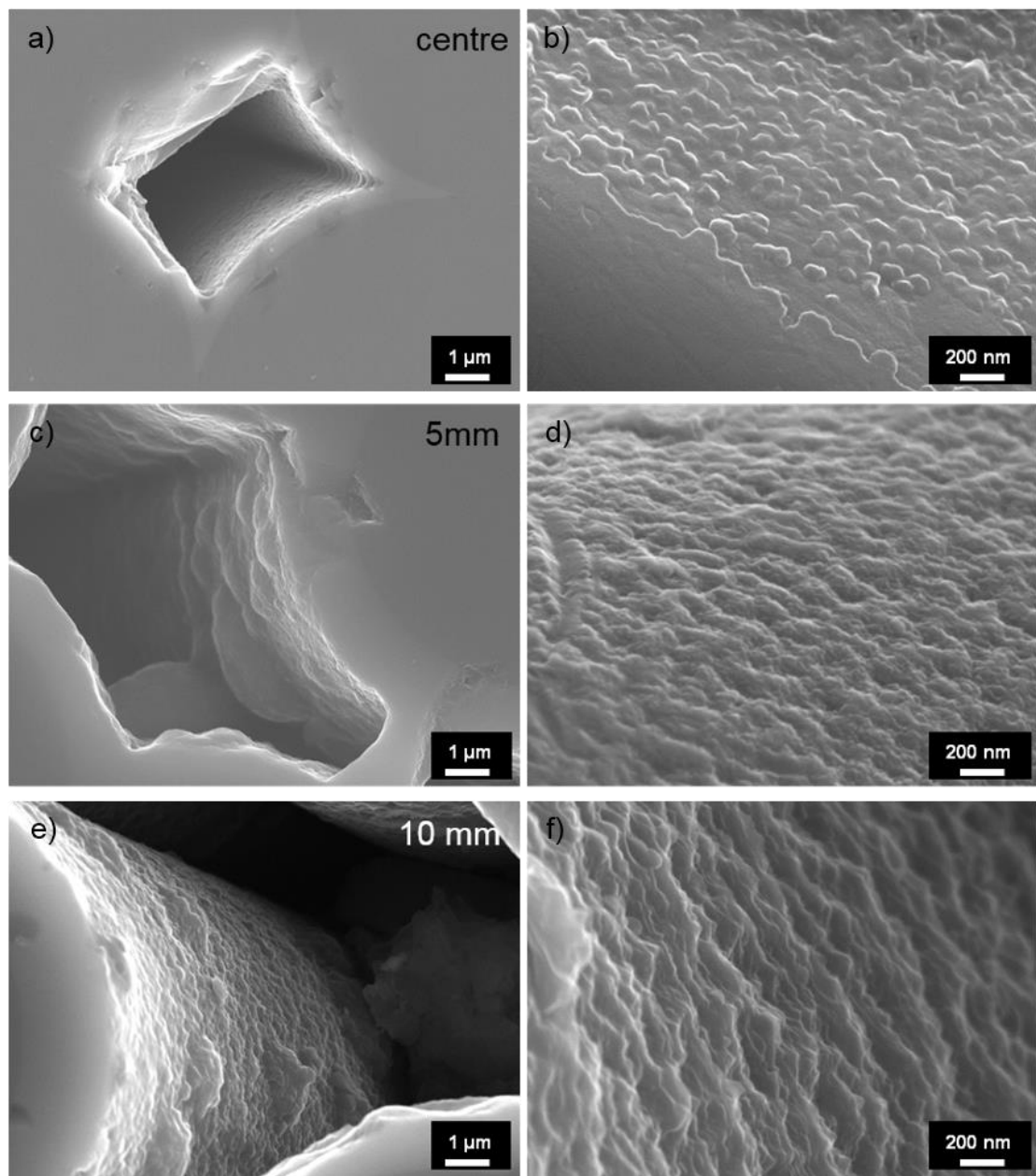


Figure 4-16. SEM-SEI images of the morphology of the SiC deposited at 900°C in different location within the preform: (a) and (b) centre, (c) and (d) 5 mm and (e) and (f) 10 mm from the centre. Total pressure was 30 kPa, total flow rate 300 cm<sup>3</sup> min<sup>-1</sup> and gas ratio ~10.

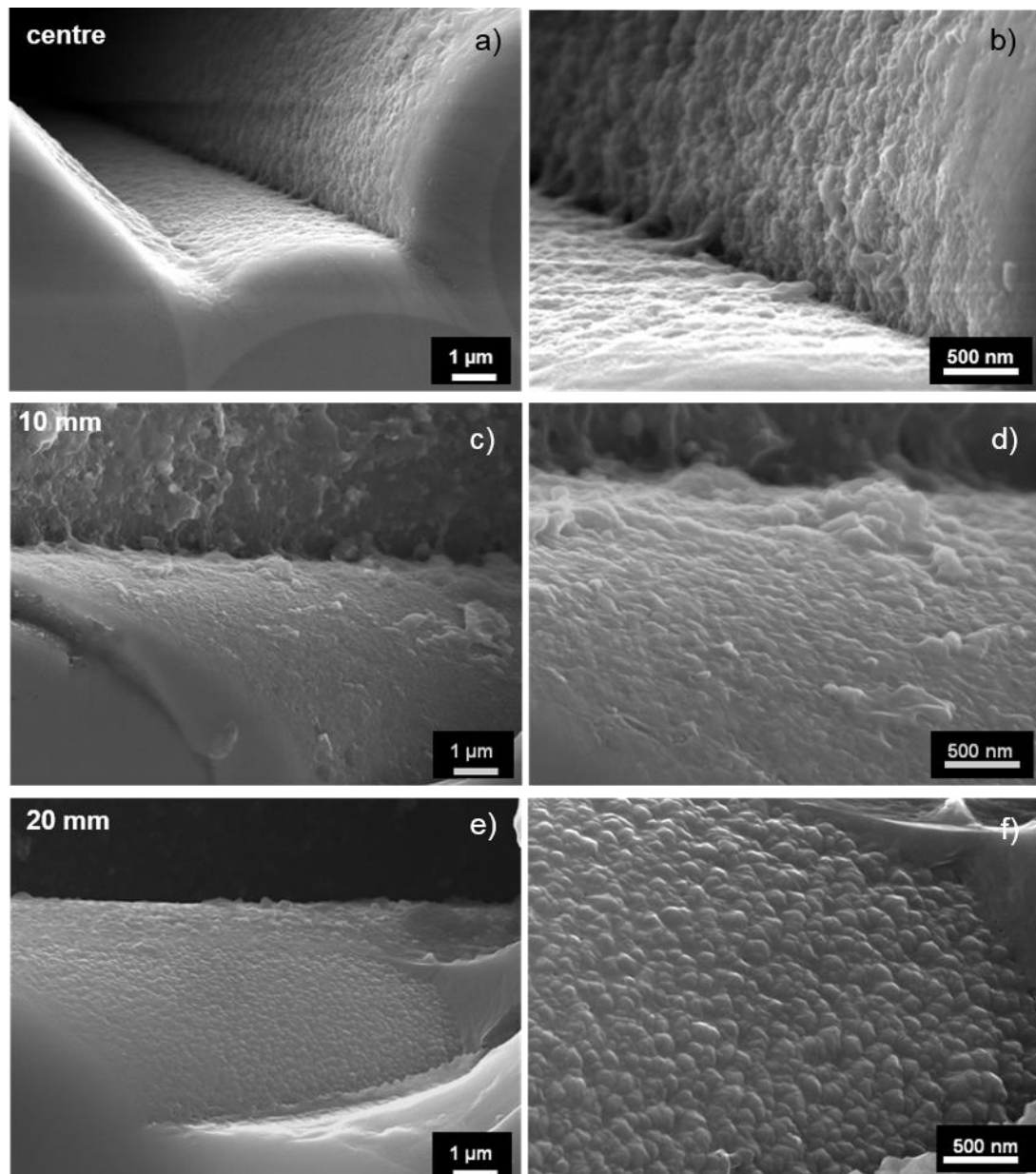


Figure 4-17. SEM-SEI images of the morphology of the SiC deposited at 1000°C in different location within the preform: (a) and (b) centre, (c) and (d) 10 mm and (e) and (f) 20 mm from the centre. Total pressure was 30 kPa, total flow rate 300 cm<sup>3</sup> min<sup>-1</sup> and gas ratio ~10.

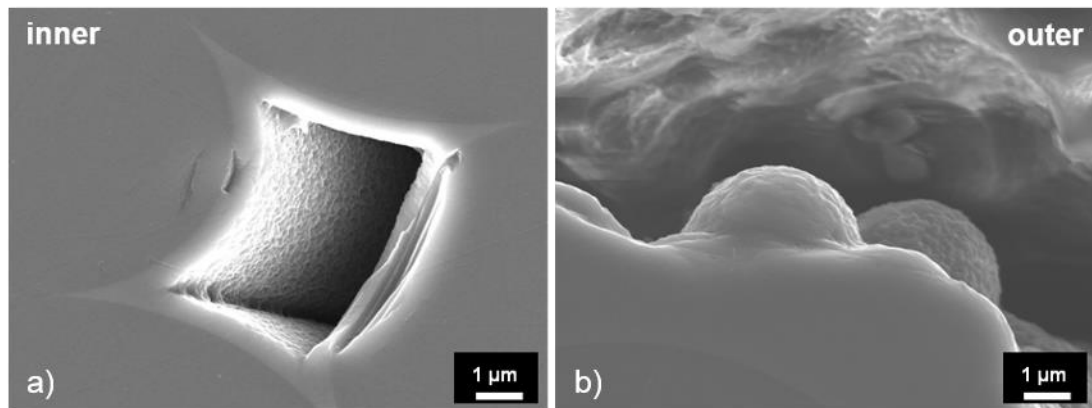


Figure 4-18. SEM-SEI images of the difference between the deposit morphology in the inner (a) and on the outer (b) part of the tow. Sample infiltrated at 950°C, 30 kPa, total flow rate of 300 ml min<sup>-1</sup> and gas ratio ~10.

### 4.3.1.2 Influence of the pressure

Figure 4-19 shows the effect of the pressure on the morphology of the SiC matrix growth at different pressures. The location for all the images was from the sample centres. At 30 kPa, Figure 4-19(a) and (b), the deposit was relatively smooth and homogeneously surrounded the fibre. At higher pressure, the matrix evolved to highly rough morphologies, Figure 4-19(c) and (d) and at 70 kPa the deposit took on the appearance of “scales”, Figure 4-19(e) and (f). This deposit also showed a higher tendency to flake apart. Experiments performed using the highest value of temperature and pressure (1000°C and 70 kPa) yielded the formation of elongated and branched SiC structures, Figure 4-20(a) and (b).

The deposit morphology alterations at different pressure cannot be explained with the type of mass transport as the Peclet number is independent of the pressure [156]. For a given substrate/gas phase system, the morphology of the deposit is determined by the competitive processes of nucleation and growth. The overall process is governed by surface kinetics provided the surface is not saturated with reactive species. In addition, the residence time of the gas is short. Under these

conditions, the nucleation regime appears predominant and the resulting deposit is smooth, with rounded and nanosized crystallites. Similar results are reported in literature [232, 332, 345]. Conversely, when the pressure increases, the concentration of reactant is higher within the area of infiltration resulting in a stable growth of crystallites with a columnar, rough or angular morphology. A further demonstration is represented by the excrescences and elongated structures, Figure 4-20, deposited at 1000°C and 70 kPa. It should be noted that the range of pressure examined in this research project is usually considered for CVD process rather than CVI.

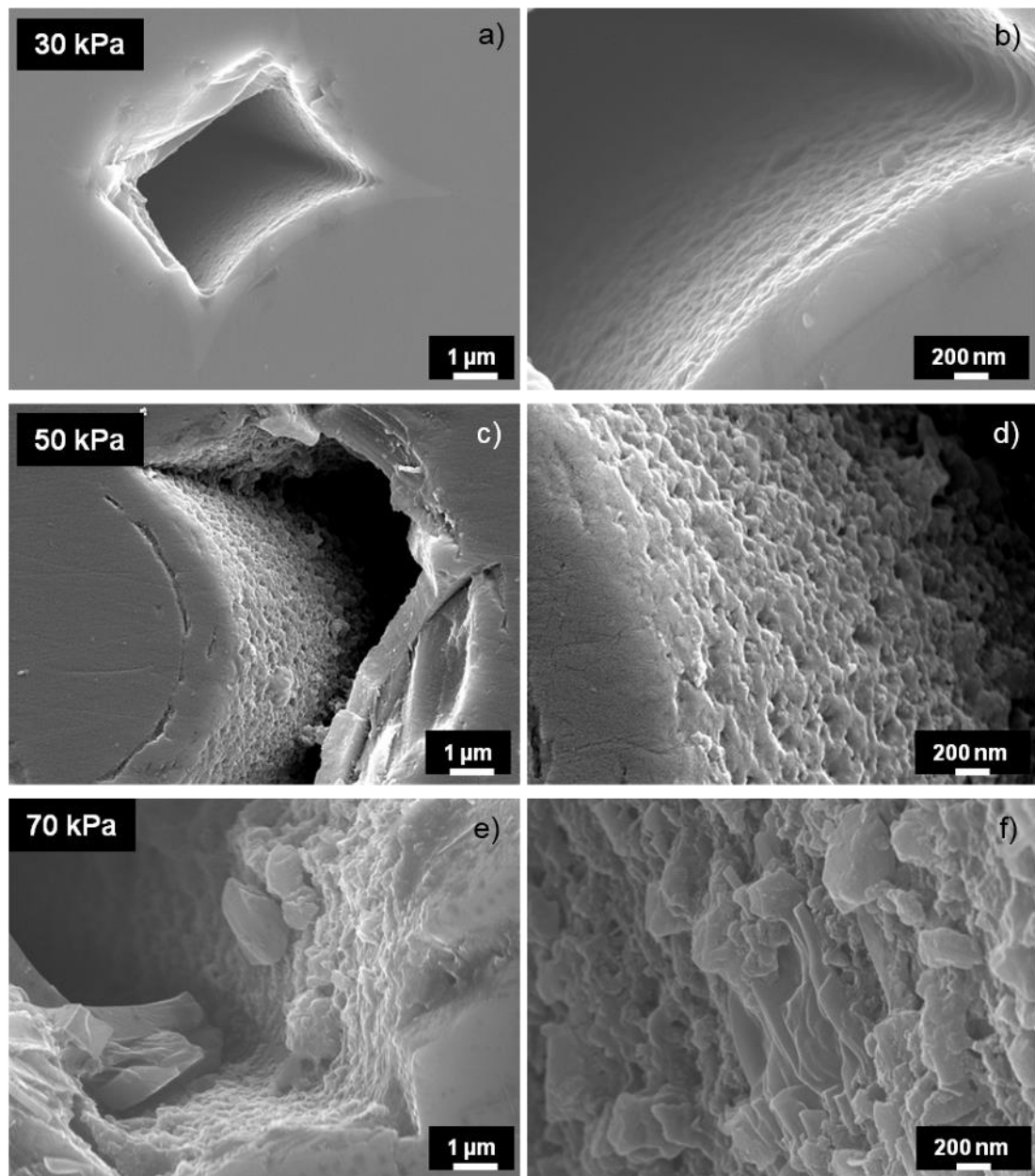


Figure 4-19. SEM-SEI images of the morphology of the SiC deposited at 900°C at different pressure: (a) and (b) 30 kPa, (c) and (d) 50 kPa and (e) and (f) 70 kPa. Total flow rate 300 cm<sup>3</sup> min<sup>-1</sup> and gas ratio ~10.

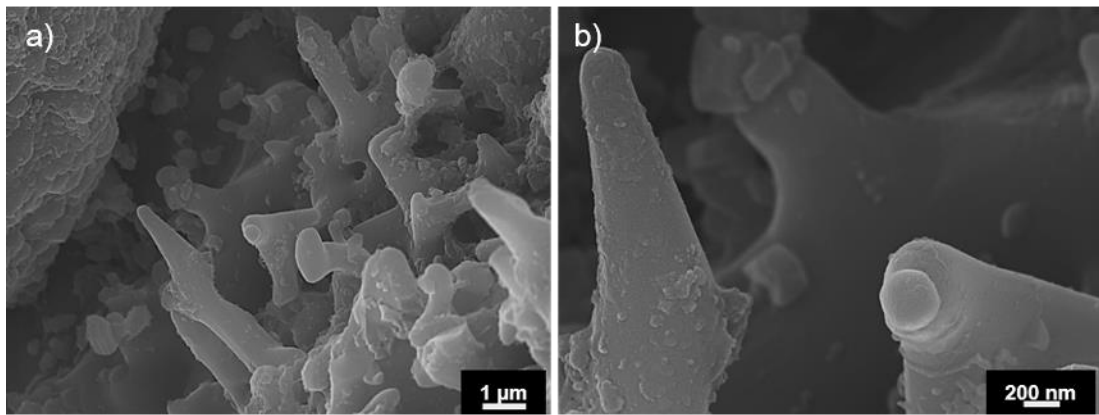


Figure 4-20. SEM-SEI images at different magnification of the formation of SiC deposit with elongated structure at 1000°C, 70 kPa, flow rate 300 cm<sup>3</sup> min<sup>-1</sup> and gas ratio ~10.

### 4.3.1.3 Influence of arcing on the morphology of the matrix

An arc is an electrical breakdown of a gas that produces an electrical discharge. Arcing in the microwave cavity was experienced during this research project, as discussed in the previous chapter, when the partial pressure of the gas was particularly low, the temperature of the preform was above 1000°C, the arrangement of the preform and whether the sharp ends of the fibre were coated with SiC slurry. The locally very high temperatures resulting from the arcs led to an interaction with the alumina insulation and also affected the deposition of the SiC matrix since the CVI process consists of the thermal decomposition of a gaseous mixture. The presence of arcs led to the formation of filamentary SiC, Figure 4-21(a) and (b); the length of the filaments formed was up to 200 μm. The filamentary SiC could have formed from the gaseous phase along the arc pathways and, hence, it is a consequence of the homogeneous decomposition of MTS at high temperatures.

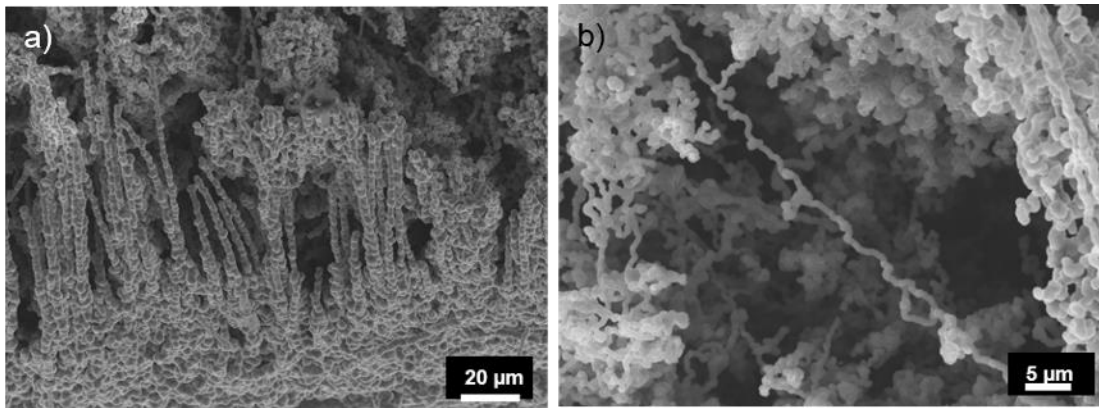


Figure 4-21. SEM-SEI images at different magnification of the formation of SiC filaments following arcing events; infiltration conditions were 1000°C, 20 kPa,  $\alpha \sim 10$ .

At lower pressures (15 kPa), the SiC filaments had a reduced diameter and agglomerated in a spherical formation, as shown in Figure 4-22. These formations were found also on the insulation foam, indicating that the nucleation may have happened in the gas phase as suggested by Schlitchting [342]. A high content of oxygen was measured, 5 - 6 at%, suggesting an interaction of the deposit with the adjacent Al<sub>2</sub>O<sub>3</sub> foam.

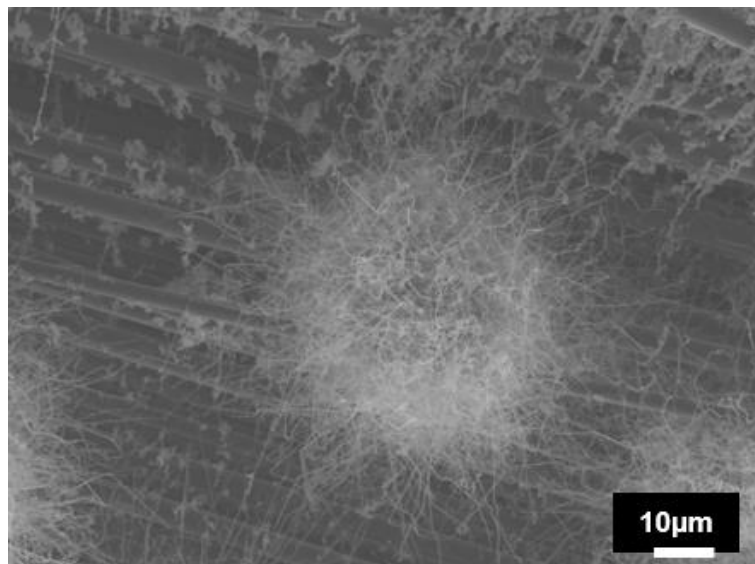


Figure 4-22. SEM-SEI images of the formation of spherical agglomerate of SiC whiskers due to the arcing; infiltration conditions were 1000°C, 15 kPa,  $\alpha \sim 10$ .

### 4.3.1.4 CVD experiments

Figure 4-23 illustrates the results from chemical vapour deposition experiments carried out on a single disc of SiC fibres. The electron microscope characterisation was conducted on the area of the disc where the temperature was directly observed by the pyrometer and hence known precisely. At 900°C, Figure 4-23(e) and (f), the matrix had a globular aspect with primary particles of ~50 nm. It must be noted that the coverage of the fibre was incomplete and that the formation and then merger of islands was the favoured growth mechanism. At 1000°C, Figure 4-23(c) and (d), the coverage of the fibre was homogeneous with an apparent particle size ranging from 200 nm to 1 µm. At 1100°C, Figure 4-23(a) and (b), the coverage of the fibres was complete with the formation of some semi-spherical protuberances. CVD experiments further support the change of morphology with the temperature with a transition from rounded to angular aspect of the SiC when temperature increases. Another consideration from these experiments concerns the dependence of growth mechanism on temperature. According to surface chemistry and thin film growth [346, 347], the formation three-dimensional adatom<sup>‡‡</sup> clusters or islands, Volmer-Weber growth mode in Figure 4-24(a), is typical of systems where the cohesion between two adatoms is stronger than that of the adatom with the surface, Figure 4-23(a) and (b). It must be always kept in mind that the substrate, the ZMI fibres, is not SiC but an amorphous solid mixture of Si, C, O and Zr. With the increase of temperature, 1000°C in Figure 4-23(c) and (d), these interactions may change and the surface-adatom adhesion is stronger than adatom-adatom forces, called

---

<sup>‡‡</sup> An atom adsorbed on a crystal surface. A molecule or a cluster of molecules may all be referred to by the general term "adparticle".

Frank–van der Merwe growth mode, as shown in Figure 4-24(b). This results in a homogeneous coverage of the substrate. At even higher temperatures, the growth is characterised by both 2D layer and 3D island growth known as Stranski–Krastanov growth mode, Figure 4-24(c). In the latter growth mode, the transition from the layer-by-layer to island-based growth typically occurs at a critical layer thickness [348] and the temperature may not be the only factor responsible of the change for crystal growth mode. This model could also explain the variation in deposition morphology that could be observed between the interior and the exterior of a typical tow, Figure 4-18. In the interior of the tow, the deposit around the fibre cannot grow indefinitely because of the other adjacent growths, whereas on the exterior the growth front was not linear because the deposit could grow without any constraints, reach the critical thickness and growing according to the Stranski–Krastanov growth mode.

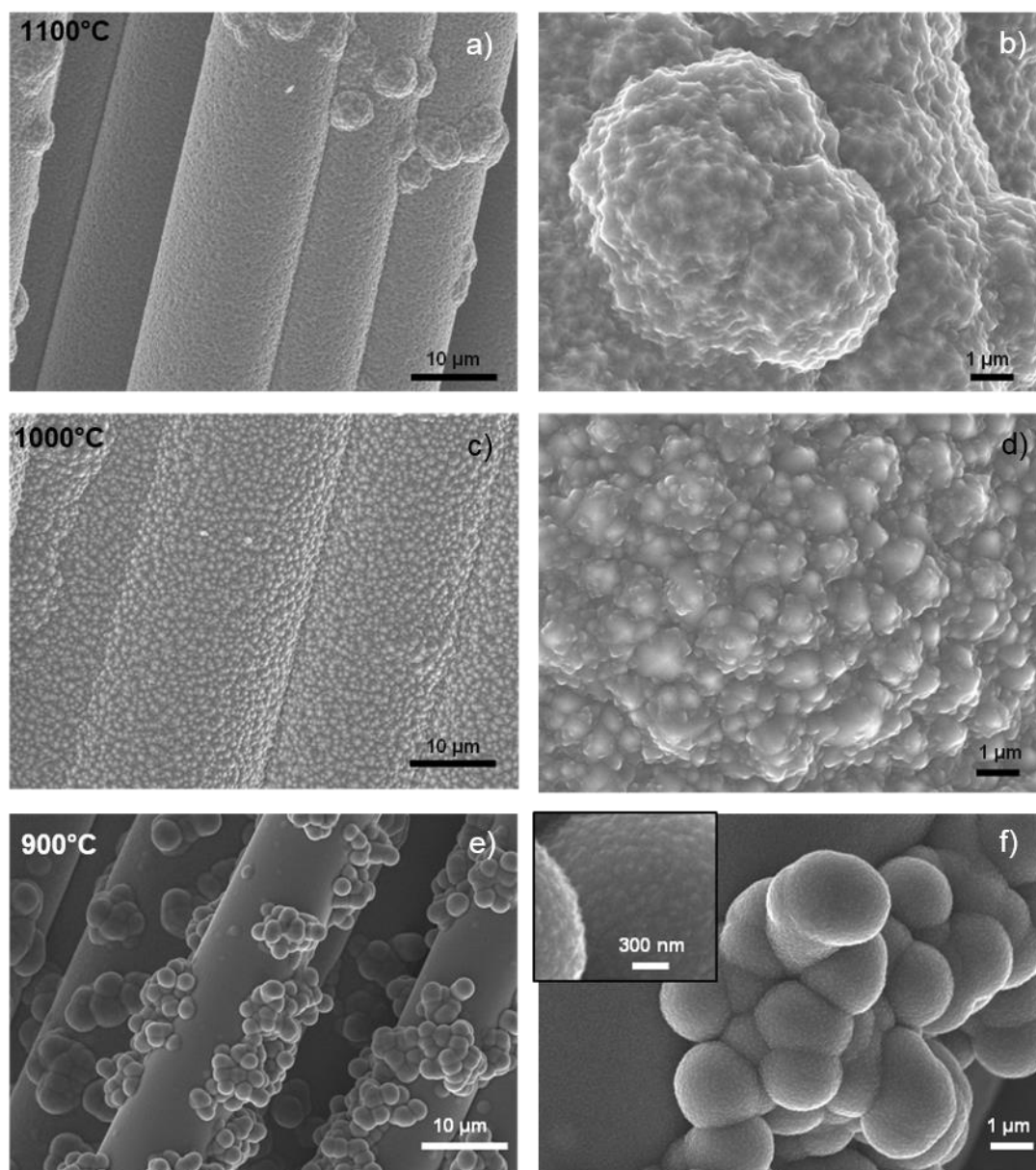


Figure 4-23. SEM-SEI images of the deposit grown on a single layer of fabric made of Tyranno- ZMI silicon carbide fibre at: (a) and (b) 1100°C, (c) and (d) 1000°C, (e) and (f) 900°C. Hydrogen flow rate was 300 ml min<sup>-1</sup> and gas ratio ~10.

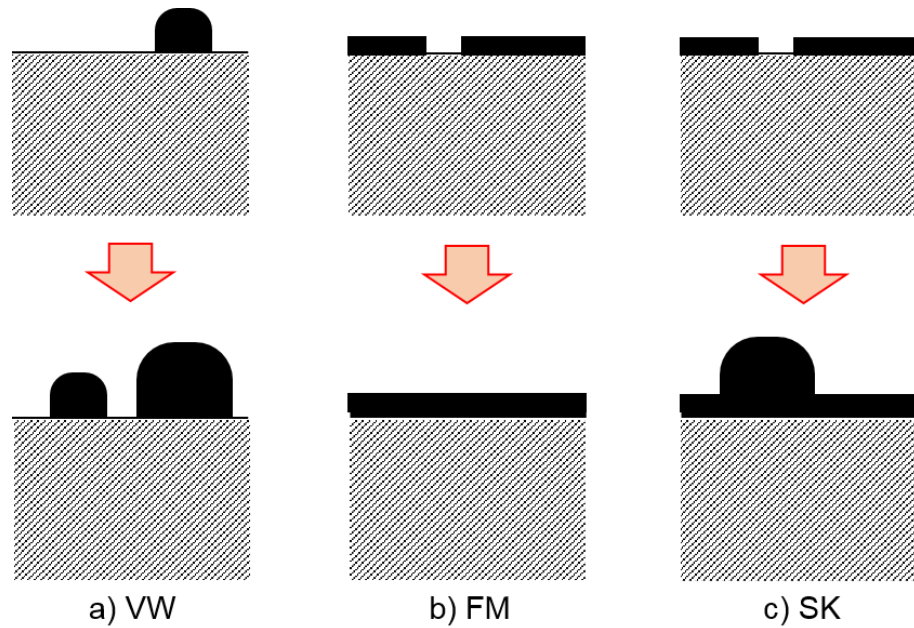


Figure 4-24. Schematic of the deposit growth modes (a) Volmer-Weber (or island formation), (b) Frank-van der Mer (layer-by-layer) and (c) Stranski-Krastanov (layer-plus-island)

### 4.3.2 Composition of the deposit

#### 4.3.2.1 Dispersive X-ray spectroscopy

Figure 4-25 shows colour maps of the spatial composition of the SiC deposits at different temperatures. White areas correspond to regions where the deposit was too thin for the composition to be measured and there would have been a volume interaction with the fibres. The compositions are expressed as deviation of the Si/C ratio from stoichiometric. The range varied from a silicon excess of up to ~2.6% to a carbon excess of up to ~0.8%. A similar range has been observed at 1000°C,  $\alpha=10$ , and  $Q_{H_2} = 200 \text{ ml min}^{-1}$  at atmospheric pressure [333]. In all cases, the SiC deposited near the centre line was the closest being stoichiometric. At 900°C, the deposit become steadily more Si-rich the further from the centre line, though note that only the top half of the sample had a deposit thick enough to be analysed. At 950°C the deposit at the top half of the sample became steadily

more Si-rich, whilst that in the bottom half was C-rich. At 1000°C the deposit was very symmetrical around the centre-line, becoming steadily more Si-rich the farther from the initial deposit.

Higher temperatures, across the range examined, allow faster decomposition of MTS to silicon and carbon bearing species resulting in a higher matrix growth rate. According to the work of Papasouliotis et al. [333] SiC forms by separate silicon and carbon pathways, where the carbon reaction is rate limiting. The current belief is that CVI and CVD at low temperature promote the codeposition of silicon. It must be noted that there is not univocal agreement on the temperature threshold for the Si deposition because reactor geometry, pressure, flow rate, gas ratio and substrate have all an influence on the deposition mechanism. However, Si from MTS has been found up to 1400°C [233-236, 332, 333, 338, 349, 350]. A further support to the temperature selectivity of the codeposition is the composition of the sample infiltrated at 900°C that displays an excess of silicon in the entire region analysed. Figure 4-26(c) shows a comparison of the spectra of the SiC matrix, carried out by EDS, and the free silicon. Interestingly, free silicon is always located within the tow rather than between the tows. A possible explanation is the different free volume,  $V_r$ , and surface available,  $A_s$ , for the decomposition of MTS and deposition of SiC. In fact, as discussed by Zhang et al. [236], the ratio  $A_s/V_r$  affects the amount of silicon deposited.

Silicon was found in all the preforms infiltrated in this work and its distribution in the sample infiltrated at 1000°C, Figure 4-29, is consistent with the silicon-rich areas of the stoichiometry map in Figure 4-25. The Si excess is more localised at low temperatures, but the concentration is larger than at higher temperature.

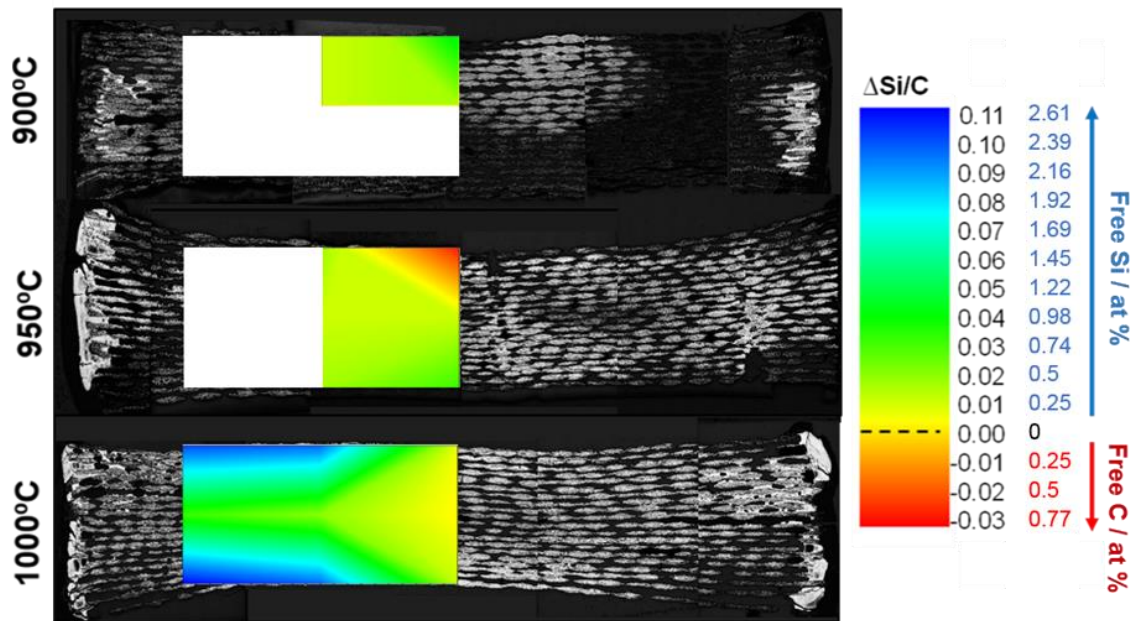


Figure 4-25. Contour map of the composition of the deposit growth at different temperatures.  $\Delta\text{Si/C}$  indicates the deviation of the Si/C ratio from stoichiometric silicon carbide. Negative values represent regions with carbon excess whilst positive values indicate excess of silicon.

Silicon inclusions were therefore counted and mapped and the samples infiltrated at 1000°C, Figure 4-29, showed a more homogenous distribution of Si across the entire preform especially far from the centre. This is consistent with the composition map shown in Figure 4-25. At lower temperatures, Figure 4-27 and Figure 4-28, the silicon was widely less distributed but the number of the detected locations was higher.

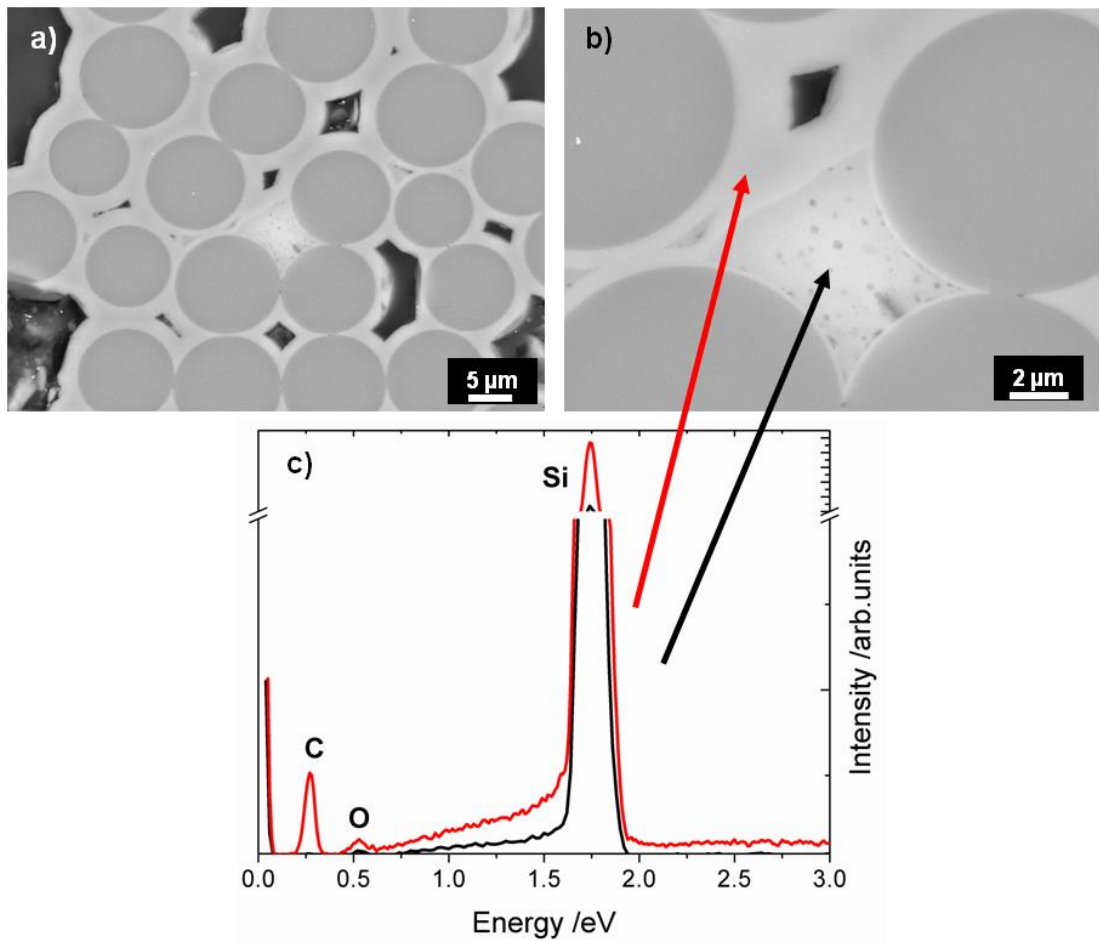


Figure 4-26. SEM-BSE images of the co-deposition of silicon within the fibre tow at different magnification (a) and (b); (c) comparison of the EDS spectra in two different locations within the tow.

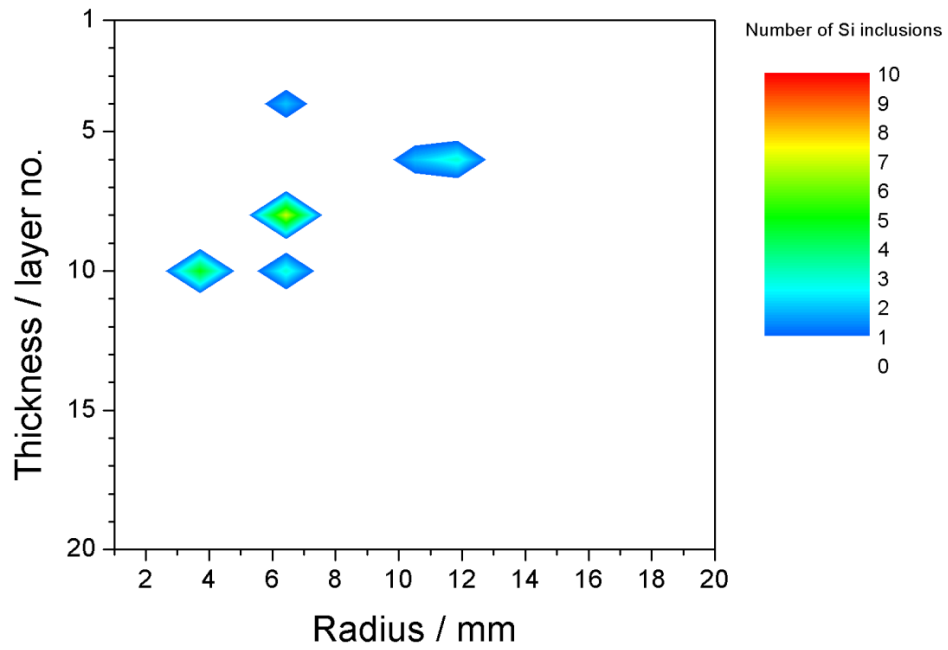


Figure 4-27. Silicon inclusions counted in the SiC matrix grown at 900°C, 30 kPa,  $\alpha \sim 10$  and  $Q_{H_2} = 300 \text{ ml min}^{-1}$ .

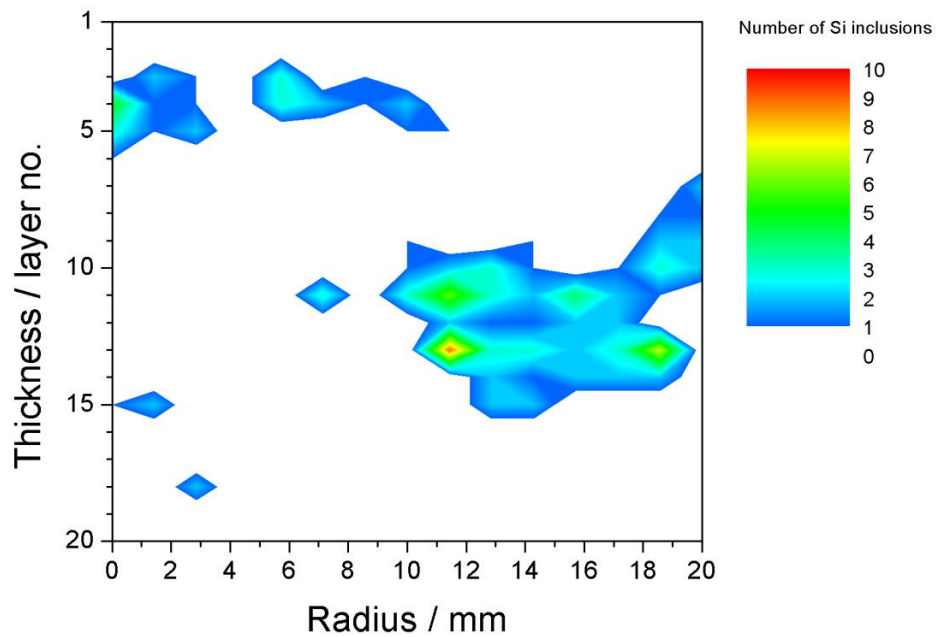


Figure 4-28. Contour map of the silicon inclusions counted in the SiC matrix grown at 950°C, 30 kPa,  $\alpha \sim 10$  and  $Q_{H_2} = 300 \text{ ml min}^{-1}$ .

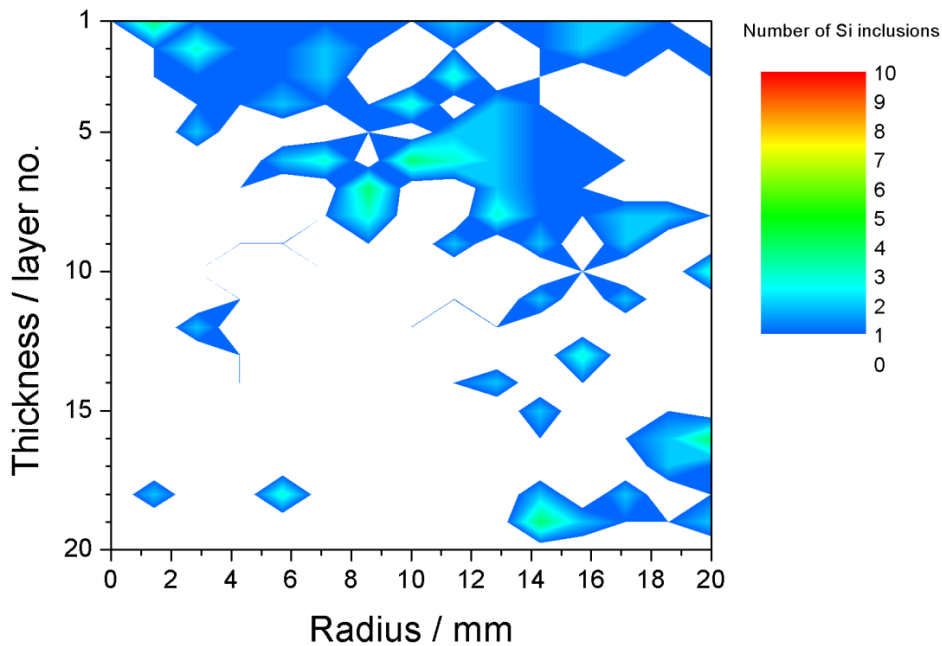


Figure 4-29. Silicon inclusions counted in the matrix growth at 1000°C, 30 kPa,  $\alpha \sim 10$  and  $Q_{H_2} = 300 \text{ ml min}^{-1}$ .

Oxygen content in the SiC deposit was determined in atomic percent and is illustrated in Figure 4-30 to Figure 4-32 for 900, 950 and 1000°C respectively. The increase in the temperature of infiltration yielded a higher oxygen content (up to 3 at%). A comparison with the colour maps of Figure 4-25 showed that the oxygen content was higher where the excess of free Si was more significant. This suggests that some silica and/or silicon oxycarbide phase was co-deposited. As discussed earlier,  $\text{SiO}_2$  and/or Si-C-O were generated mainly from the residual oxygen in the reactor in the first stage of MECVI (Figure 4-45 and Figure 4-46). Therefore, the actual surface for the deposition is a thin layer of silica and not the SiC fibre. The substrate is a major factor in determining nucleation and growth kinetics and hence the physical and chemical properties of the matrix [351]. For instance, Lespiaux et al. [231] reported that the coverage of a wafer of silica with silicon and carbon-bearing species is lower than a substrate of 3C-SiC. The

current belief is that high coverage and formation of the strong bond O-H inhibits the chemisorption of Si and C atoms.

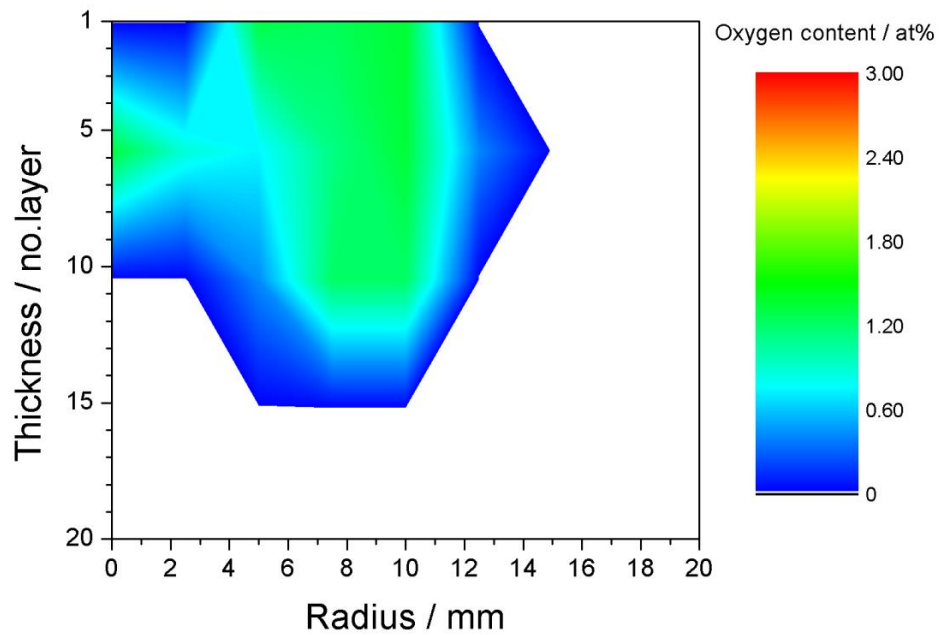


Figure 4-30. Oxygen content (atomic percentage) in the matrix growth at 900°C, 30 kPa,  $\alpha \sim 10$  and  $Q_{H_2} = 300 \text{ ml min}^{-1}$ .

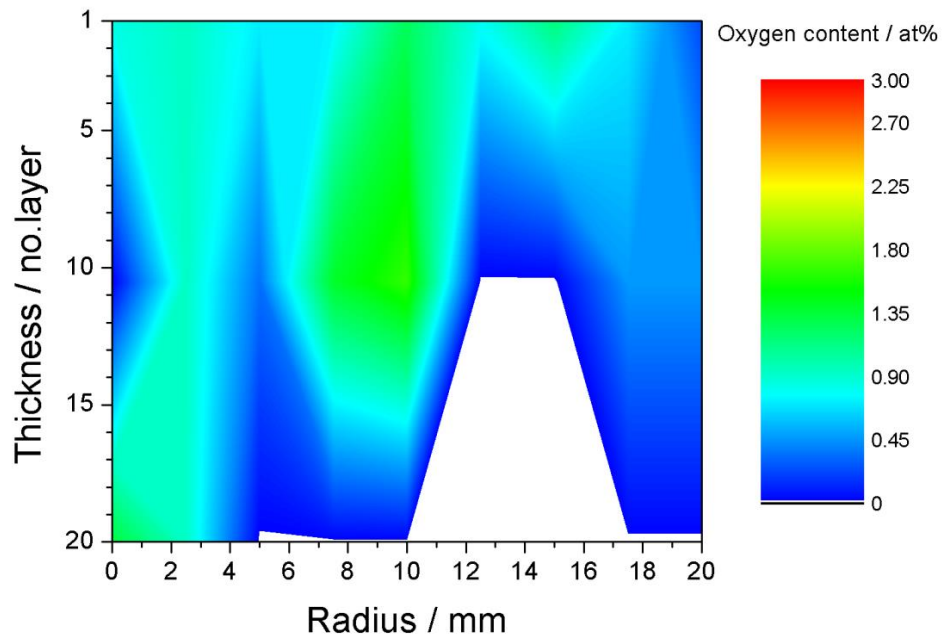


Figure 4-31. Oxygen content (atomic percentage) in the matrix growth at 950°C, 30 kPa,  $\alpha \sim 10$  and  $Q_{H_2} = 300 \text{ ml min}^{-1}$ .

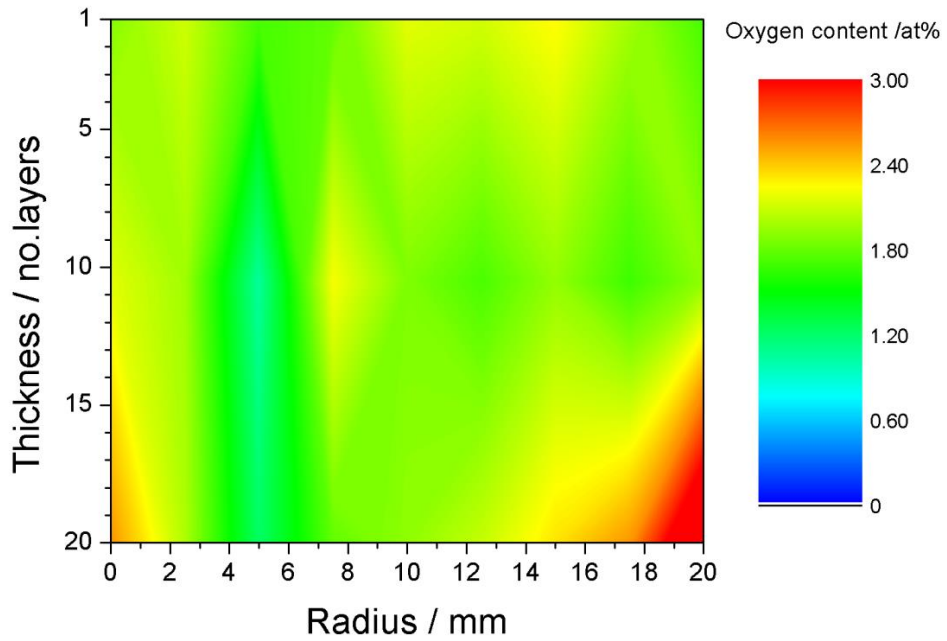


Figure 4-32. Oxygen content (atomic percentage) in the matrix growth at 1000°C, 30 kPa,  $\alpha \sim 10$  and  $Q_{H_2} = 300 \text{ ml min}^{-1}$ .

#### 4.3.2.2 Raman spectroscopy

Figure 4-33 shows a comparison of the Raman spectra of  $\alpha$ -SiC (courtesy of the Air Force Research Laboratory, USA) and  $\beta$ -SiC (courtesy of Dr S. Grasso, Queen Mary College, London, UK). Table 17 reports the peak frequencies of the Raman spectra of the different polytypes of silicon carbide

Table 17. Raman frequencies of the principal cubic and hexagonal polytypes of silicon carbide. Adapted from [352] and [353].

Polytype	Frequency / cm <sup>-1</sup>			
	Transverse acoustic (TA)	Transverse optic (TO)	Longitudinal Acoustic (LA)	Longitudinal optic (LO)
3C	--	796	--	972
2H	264	799 764	--	968
4H	196, 204 266	796 776	610	964 838
6H	145, 150 236, 241 266	797 789 767	504, 514	965 889
15R	167, 173 255, 256	797 785 769	331, 337 569, 577	965 932, 938 860

Cubic silicon carbide presented two intense peaks at 797 and 972 cm<sup>-1</sup>, respectively, due to the transverse (TO) and longitudinal (LO) optical phonons. For hexagonal SiC two additional peaks at lower frequency were detected and a red shift of the LO was observed. These results were consistent with the literature [352-357] and the hexagonal peaks corresponded mainly to the 6H polytype [352, 353, 357, 358]. Second order scattering was the cause of the two peaks above 1500 cm<sup>-1</sup> [359].

The SiC fibres used in this research project were characterised by a noticeable excess of carbon, as shown by the intense peaks corresponding to the D and G bands of the Raman spectrum of carbon, Figure 4-34. The 2D and D+G bands were detectable at high shifts [360].

The spectrum of the SiC matrix deposited at 900°C, Figure 4-35, showed the sharp peak of silicon at 520 cm<sup>-1</sup> [361, 362]. The peaks of cubic silicon carbide

were not sharp but broad which implied the presence of numerous defects in the microstructure [352]. Some weak peaks of hexagonal SiC were also detected, Figure 4-35 inset. With an increase in temperature, 950°C in Figure 4-36 and 1000°C in Figure 4-37, the intensity of the Si peak decreased and the TO peaks of cubic silicon carbide were significantly more intense. In the infiltration at 950°C, both stacking faults (highlighted in Figure 4-36 inset) [363] and the presence of hexagonal polytypes became clearer, although the predominant SiC polytype was cubic. Second order scattering peaks were identified and for the matrix growth at 1000°C, Figure 4-37, there was probably some carbon co-deposition because of the presence of the carbon D band. This trend of increasing content of carbon with the increasing temperature of deposition has been confirmed also from Chin et al. [338] although shifted to higher temperature. The spectra are compared in Figure 4-38, where four main features may be identified:

- The intensity of the Si peak at  $520\text{ cm}^{-1}$  decreased with increasing temperature;
- The deposit was mainly cubic SiC across the temperature range investigated;
- Stacking faults, defects and a small quantity of hexagonal polytypes were identified ;
- Some carbon may have co-deposited at the higher temperatures.

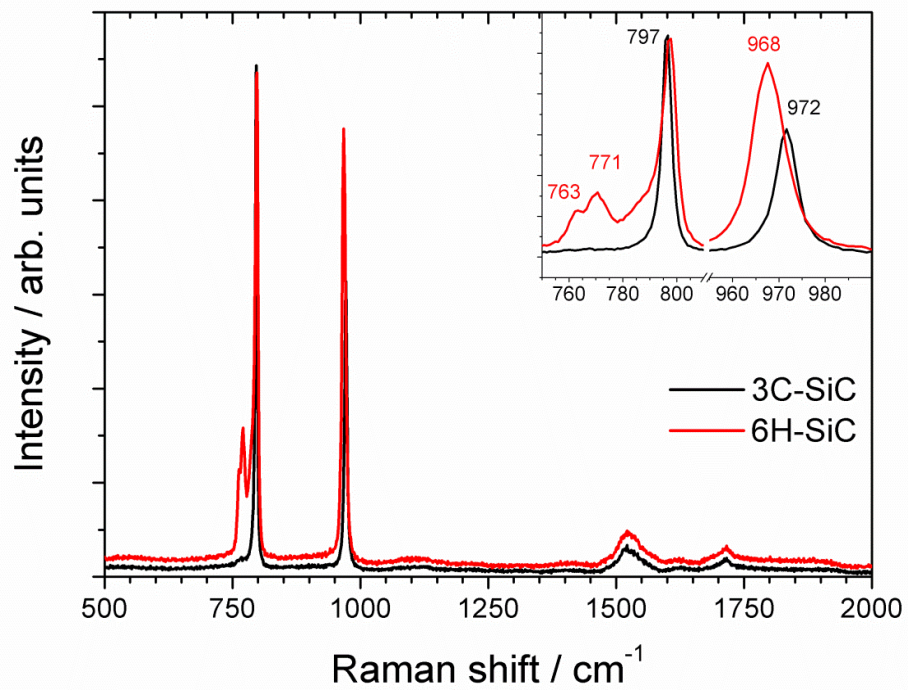


Figure 4-33. Raman spectra of high purity SiC (in red) and cubic silicon carbide (in black) grown by CVD. The inset shows in detail the range of shift in which the LO and TO bands of SiC are typically located.

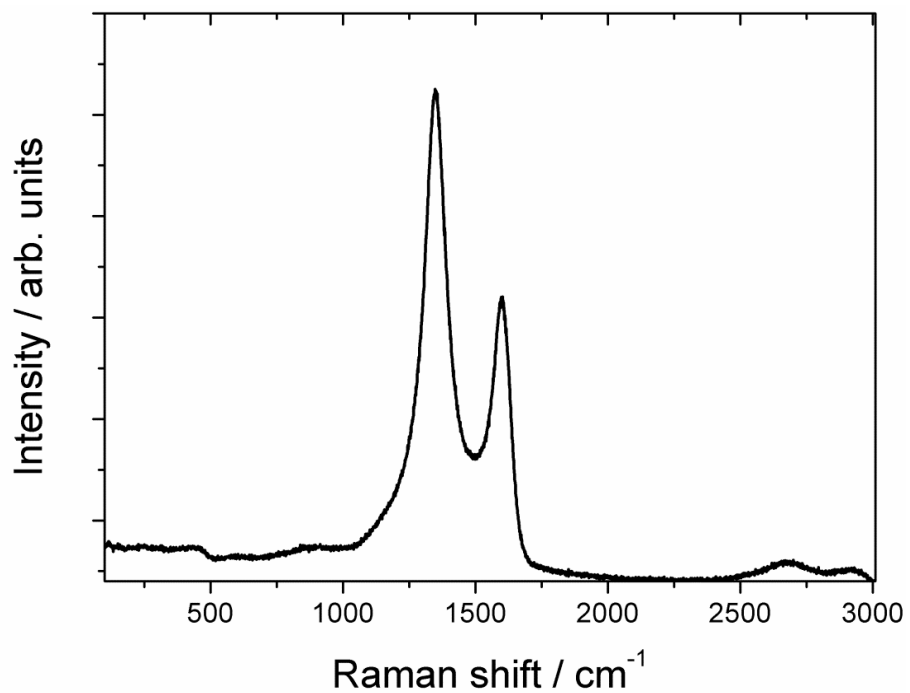


Figure 4-34. Raman spectra of Tyranno ZMI SiC fibres.

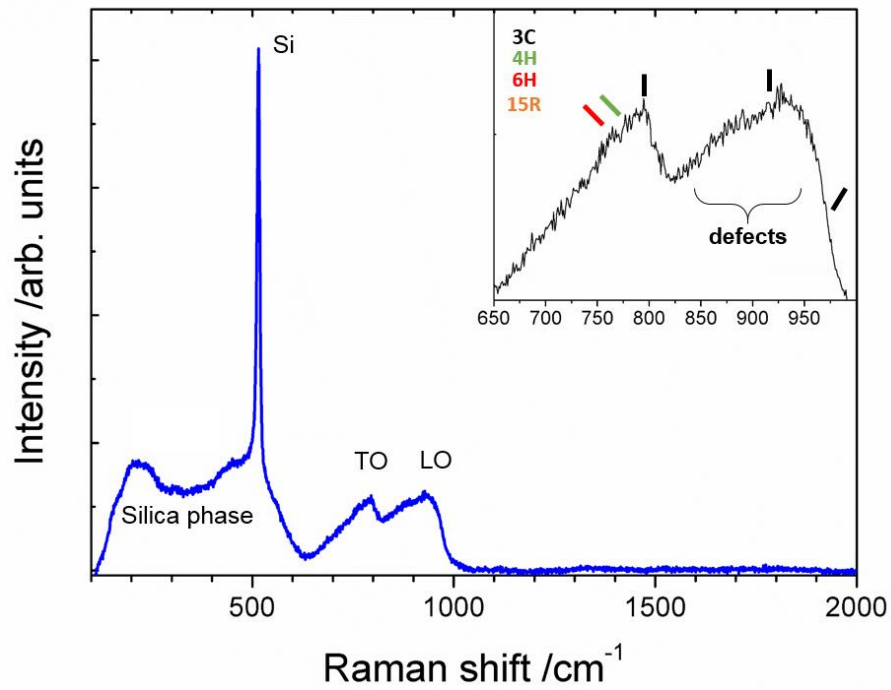


Figure 4-35. Raman spectra of the SiC matrix growth at 900°C, 30 kPa and  $\alpha$  ratio  $\sim 10$ . The inset shows the shift range 650-1000  $\text{cm}^{-1}$  in which the TO and LO bands of SiC are typically located.

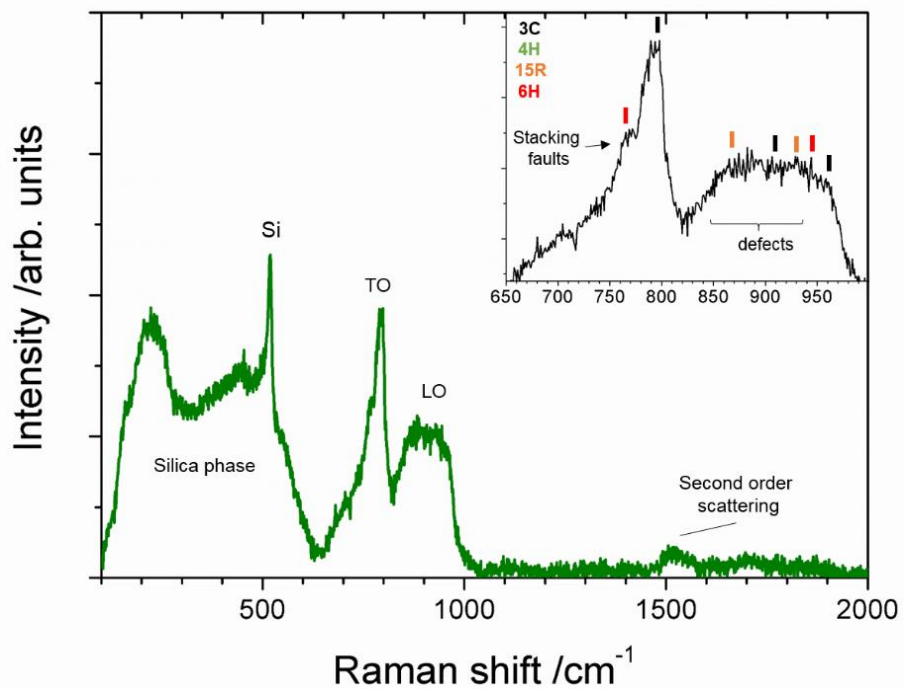


Figure 4-36. Raman spectra of the SiC matrix growth at 950°C, 30 kPa and  $\alpha$  ratio  $\sim 10$ . The inset shows the shift range 650-1000  $\text{cm}^{-1}$  in which the TO and LO bands of SiC are typically located

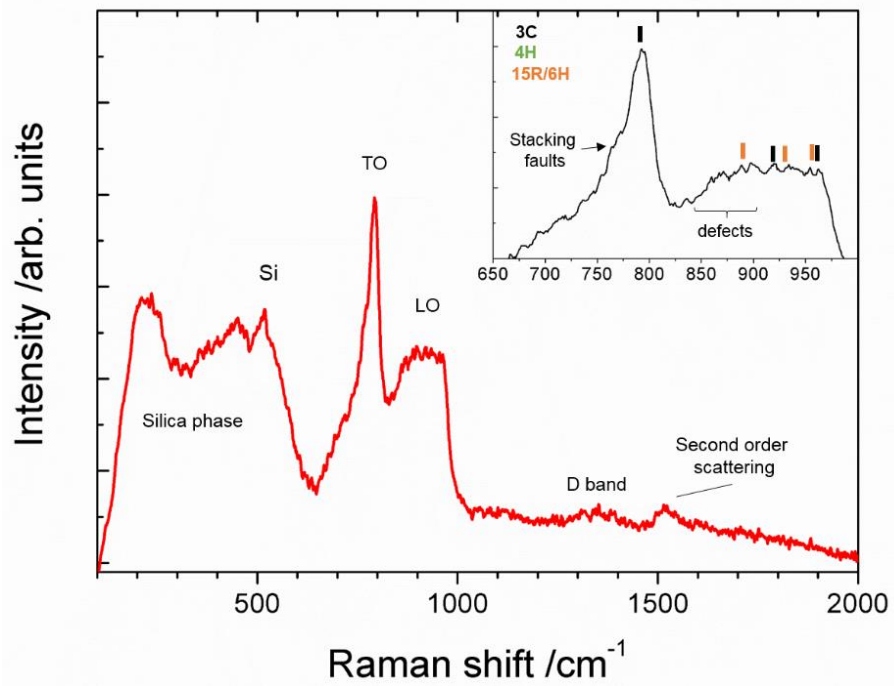


Figure 4-37. Raman spectra of the SiC matrix growth at 1000°C, 30 kPa and  $\alpha$  ratio  $\sim 10$ . The inset shows the shift range 650-1000 cm<sup>-1</sup> in which the TO and LO bands of SiC are typically located

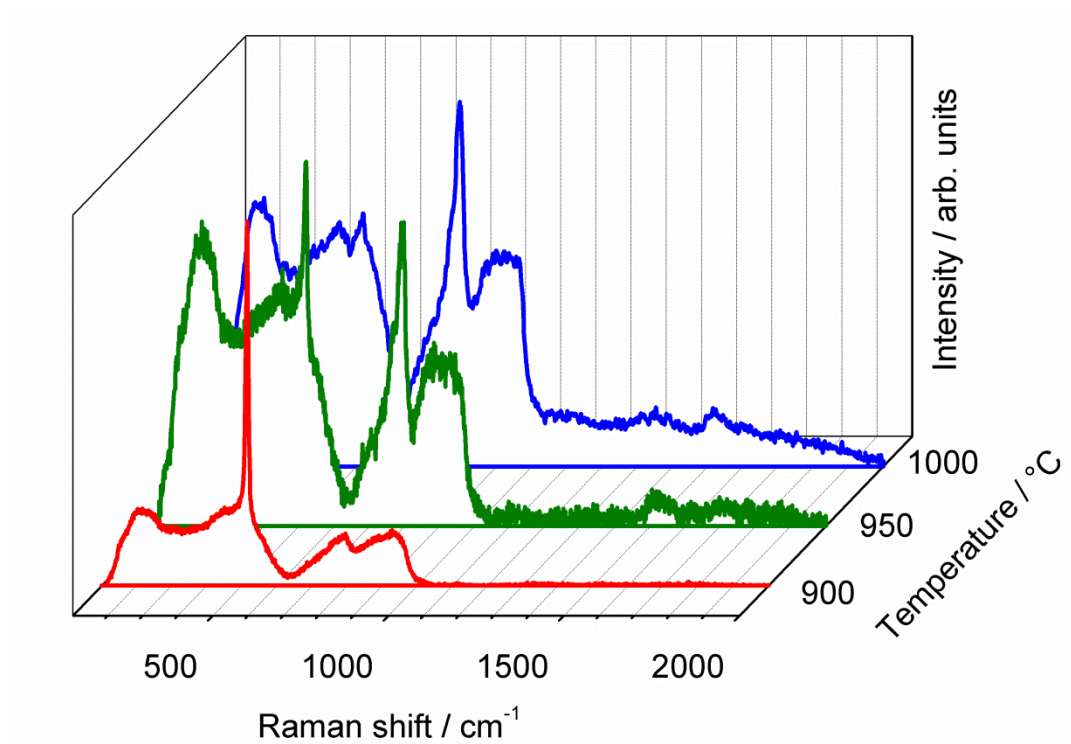


Figure 4-38. Comparison of the Raman spectra of the SiC matrix growth at different temperatures, 30 kPa and  $\alpha$  ratio  $\sim 10$ .

### 4.3.3 TEM analysis

Figure 4-39 and Figure 4-40 (bright and dark field respectively) show the microstructure and the crystalline orientation of the matrix growth at 900°C. The fibres were confirmed to be amorphous and the SiC deposit had a cubic habit. This is the polytype of the SiC grown by CVI/CVD below 2000°C [341, 364].

[111] is the predominant direction because it is the surface with lower energy [231]. A mixture of elongated grains of up to 1 µm in length grown perpendicular to the fibre (along the crystallographic direction [111]) and some equiaxed grains were also found in the matrix. Some circular inclusions were observed, Figure 4-41, that acted as seed for columnar grains with [002] orientation. Although, the nature of these inclusions has not been identified with certainty because of the limits of the equipment, a similar microstructure has been reported to correspond to silicon inclusions [234]. They initiated the formation of dendritic blocks and deteriorate the homogeneous crystallisation favouring the deposition of silicon and vice versa [365]. The streaking of the diffraction patterns was distinctive of a high concentration of stacking faults.

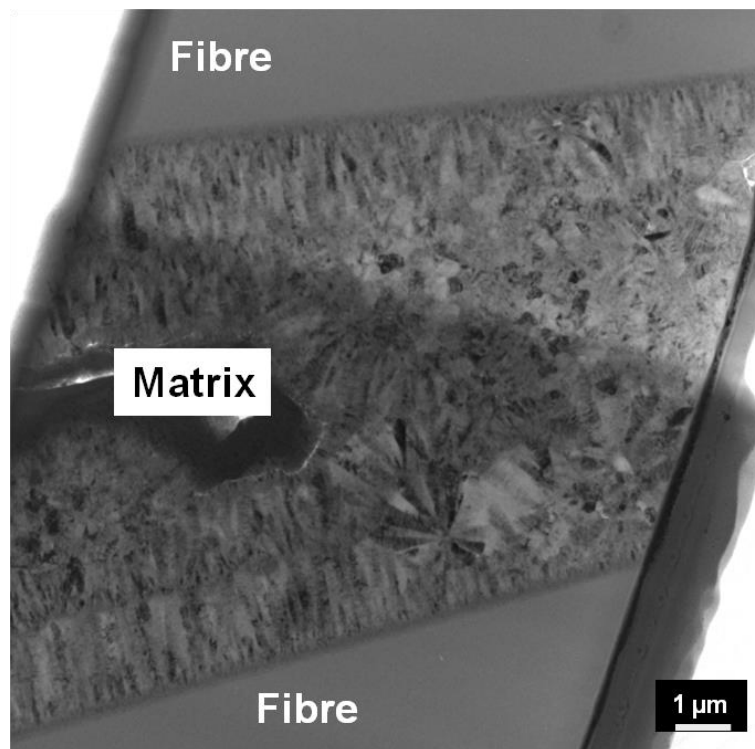


Figure 4-39. Bright field of the matrix growth between two SiC fibres at 900°C, 30 kPa,  $\alpha \sim 10$  and  $Q_{\text{H}_2} = 300 \text{ ml min}^{-1}$ .

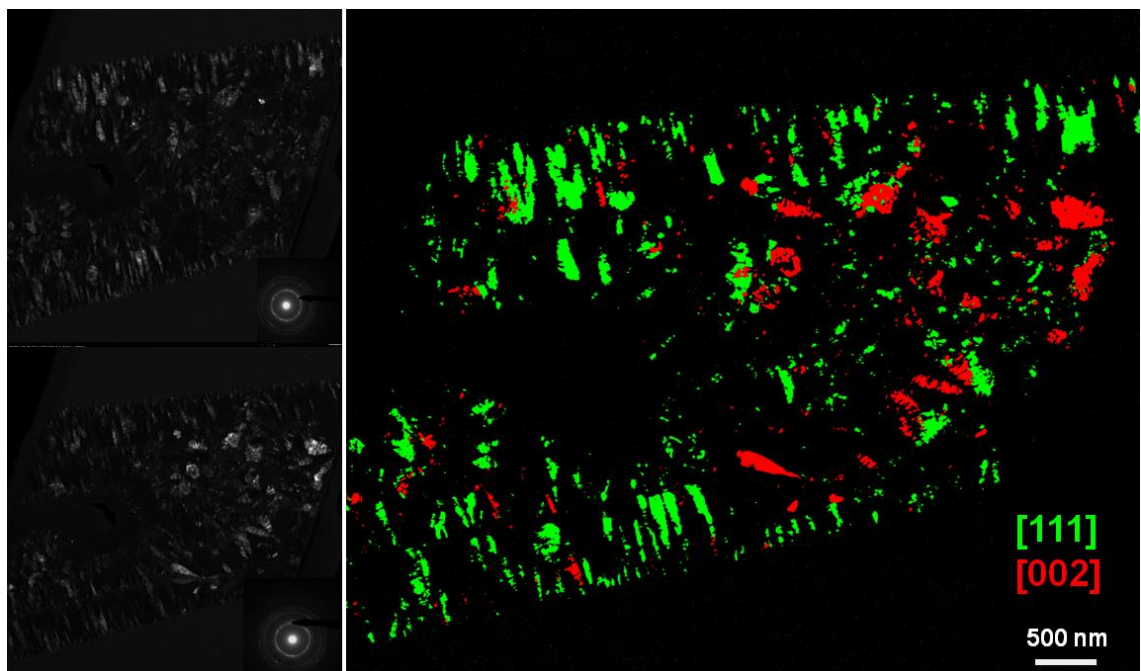


Figure 4-40. Dark field of the matrix growth between two SiC fibres at 900°C, 30 kPa,  $\alpha \sim 10$  and  $Q_{\text{H}_2} = 300 \text{ ml min}^{-1}$ .

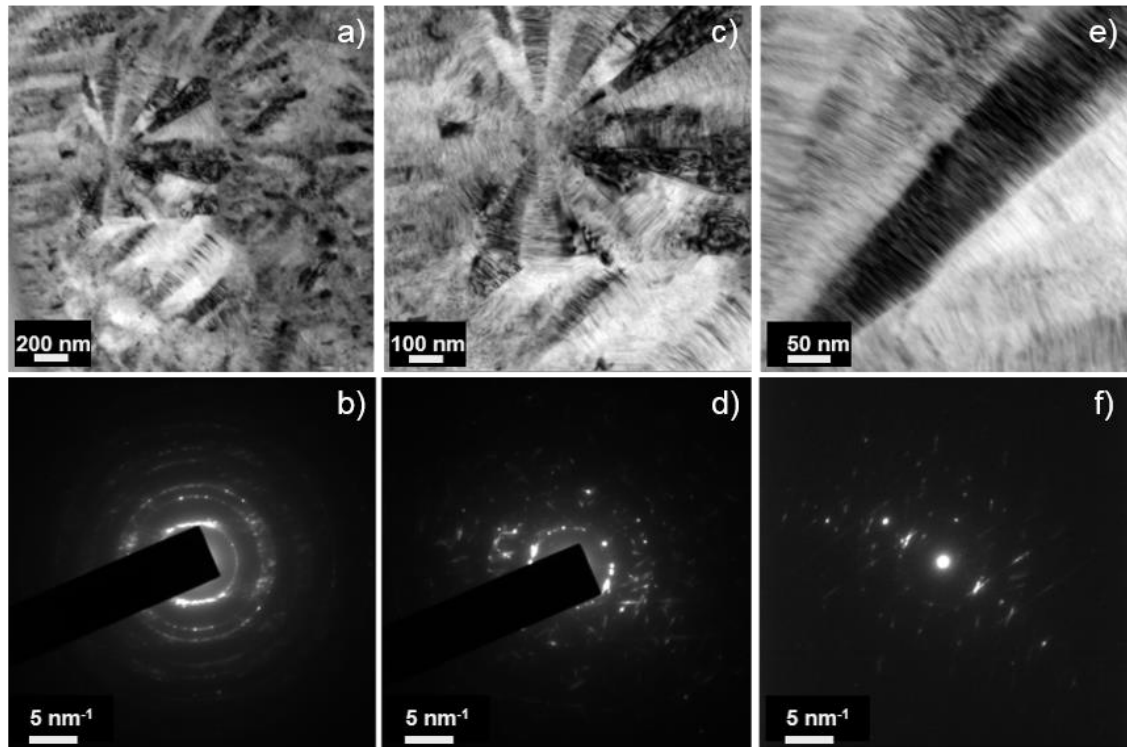


Figure 4-41. Details of the inclusions within the matrix at different magnification, (a), (c) and (e). Striations perpendicular to the growth directions indicated the presence of stacking faults which produced the streaking of the diffraction pattern (b), (d) and (f).

Increasing the temperature of infiltration to 950°C, Figure 4-42, the discontinuity introduced by the circular inclusions disappeared and the degree of texturing and anisotropic morphology increased. In fact the growth direction [111] was predominant. After an initial growth of nanometric crystallites on the fibre, the size of the SiC crystals gradually increased and, at 4-5  $\mu\text{m}$  far from the fibre, they reached a length of up to 2  $\mu\text{m}$ . At this location the aspect ratio approached 10.

As shown in Figure 4-43, at 1000°C highly anisotropic SiC crystal growth occurred extensively, even at 200 nm from the fibres crystals as long as 2  $\mu\text{m}$  were observed. After a competitive initial growth of 100 nm long crystallites, the microstructure developed into coarse grains that were mainly oriented along the [111] direction, as shown by Figure 4-43.

As the temperature increased, the formation of crystals with different orientation was observed, particularly [002] and [220]. Similar results have been reported in the literature [242, 338, 342, 366]. Even if [111] is the preferential growth direction for thermodynamic reasons [231], at higher temperatures the intermediate species of the reaction were different. The different stereochemical arrangement of the intermediate molecule could lead to a different adsorption mechanism and hence different direction growth [236, 338, 367].

As a general trend, with an increase in processing temperature the deposit evolved from a smooth, nanocrystalline and equiaxed morphology into a rougher, more textured microstructure and eventually to angular and large columnar crystallites.

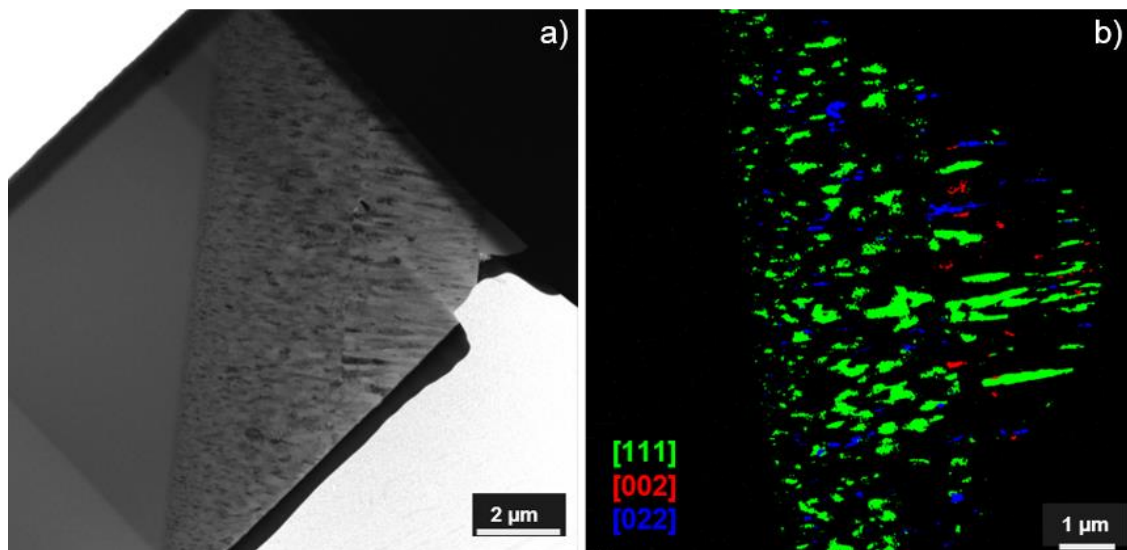


Figure 4-42. (a) Bright field of the matrix growth between two SiC fibres at 950°C, 30 kPa,  $\alpha \sim 10$  and  $Q_{H_2} = 300 \text{ ml min}^{-1}$ ; (b) colour map reconstruction of the crystalline orientation; the main direction of growth is [111].

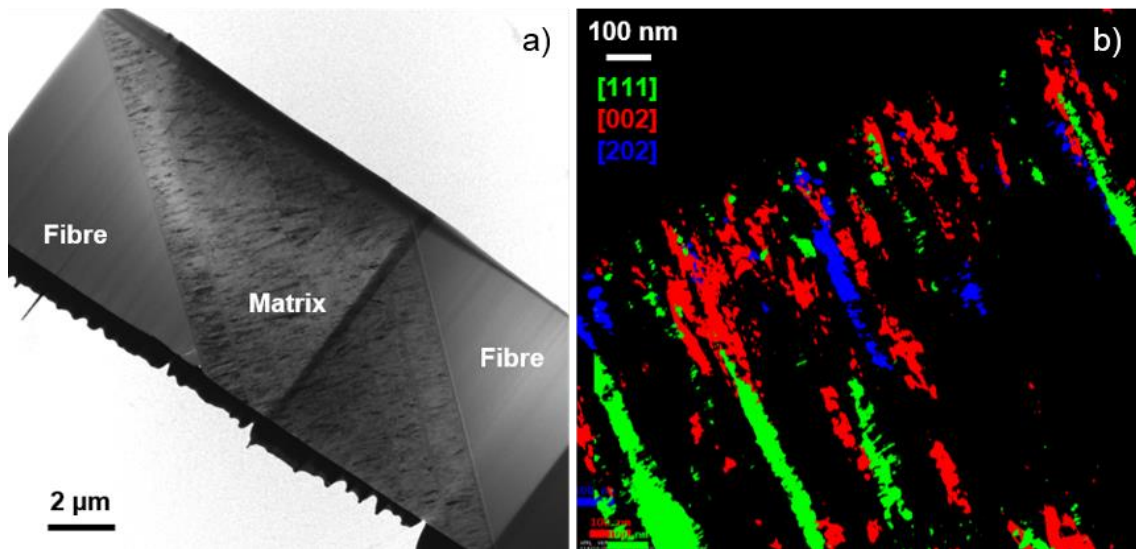


Figure 4-43. (a) Bright field of the matrix growth between two SiC fibres at 1000°C, 30 kPa,  $\alpha \sim 10$  and  $Q_{H_2} = 300 \text{ ml min}^{-1}$ ; (b) colour map reconstruction of the crystalline orientation.

In addition, distinctive interfaces were observed in the matrix microstructure between each pair of fibres, Figure 4-44. In the latter, four interfaces may be observed, which are highlighted by arrows of different colours. The interface between the fibre and the deposit (yellow arrow) is shown in greater detail in Figure 4-45; it was oxygen-rich. This was presumably the result of the formation of a silica layer due to either the oxidation of the fibre when heated by microwaves, as a result of the presence of residual oxygen in the reactor adsorbed on the fibre surface, or to the reaction of MTS with the residual oxygen. The latter is also consistent with the drop of temperature observed in the first stage of MCVI because of the endothermicity of  $\text{SiO}_2$  formation from MTS [317].

Once the oxygen rich layer was formed, 30 nm long acicular crystallites grew, though they were increasingly replaced by larger and longer SiC crystals. Moving further inwards, a second silica layer was observed in the matrix, green arrow in Figure 4-46. Presumably its formation was due to an analogous mechanism of the previous layer when infiltration restarted after the mass gain check. Three

silica layers were noted in total, the third is highlighted by the blue arrow. This corresponds to the number of times the CVI process was started. The zig-zag profile of the oxides in Figure 4-46 derived from the angular termination of the SiC crystals.

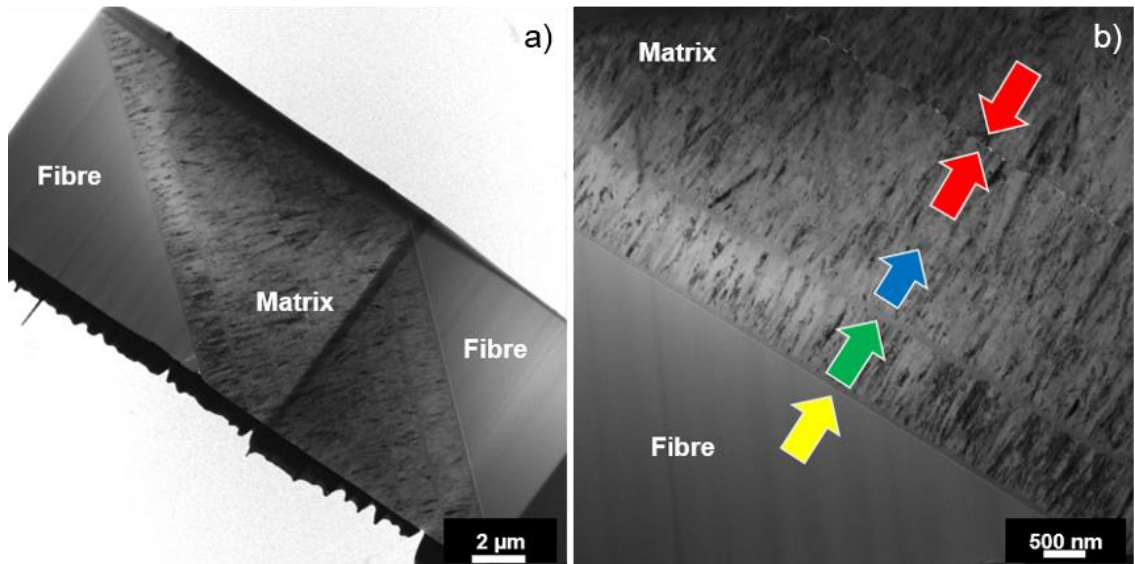


Figure 4-44. (a) Bright field image of the matrix growth between two fibres; (b) the different coloured arrows indicate typical discontinuities observed in the SiC deposit; 1000°C, 30 kPa,  $\alpha \sim 10$  and  $Q_{H_2} = 300 \text{ ml min}^{-1}$ .

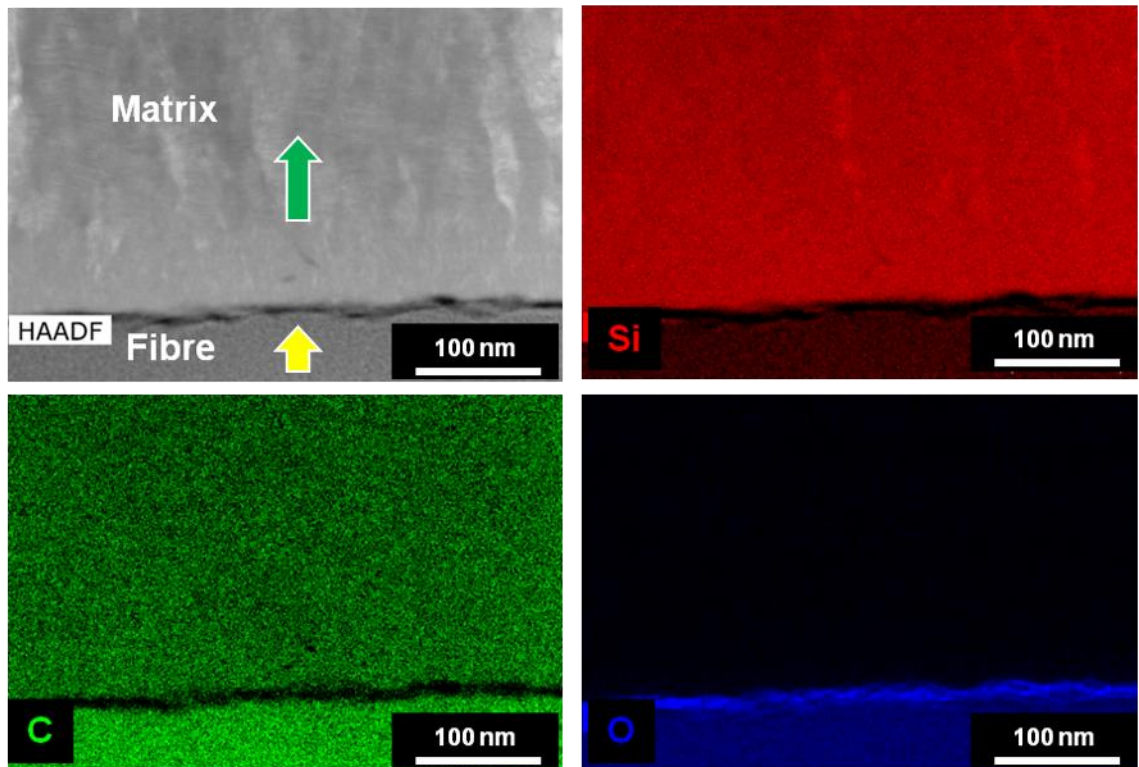


Figure 4-45. Layer of Si-O was formed between the fibre and the matrix. Very fine and acicular crystallites growth was observed on the Si-O layer during the first stage of the CVI.

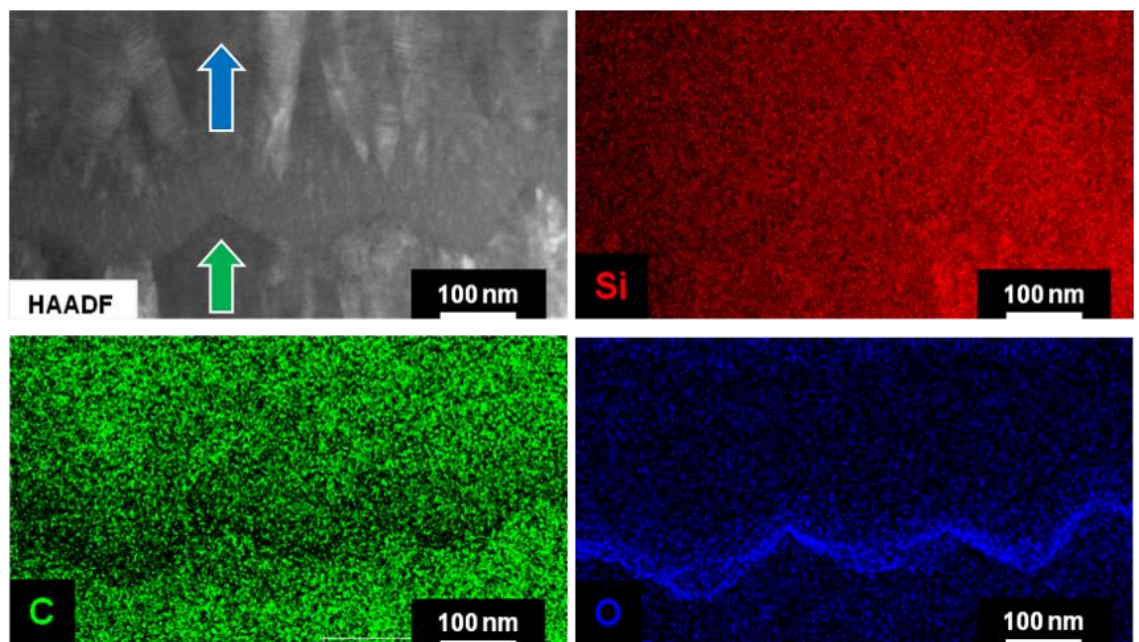


Figure 4-46. Layers of Si-O were formed on the growing SiC matrix each time the CVI process was stopped to allow the mass gain to be measured. The zig-zag morphology observed was due the angular termination of SiC crystallites.

Finally, an entire line of 70 nm nanopores was observed between the red arrows in Figure 4-44. It is shown magnified in Figure 4-47. It represents the line where the two deposition on the adjacent fibres met and is equidistant between the two fibres. Clearly, the pores were formed by the imperfect joint of the angular-terminated matrices growing in opposite directions from the adjacent fibres. It should be mentioned that the nanoporosity could have a beneficial effect on the fracture toughness [368]

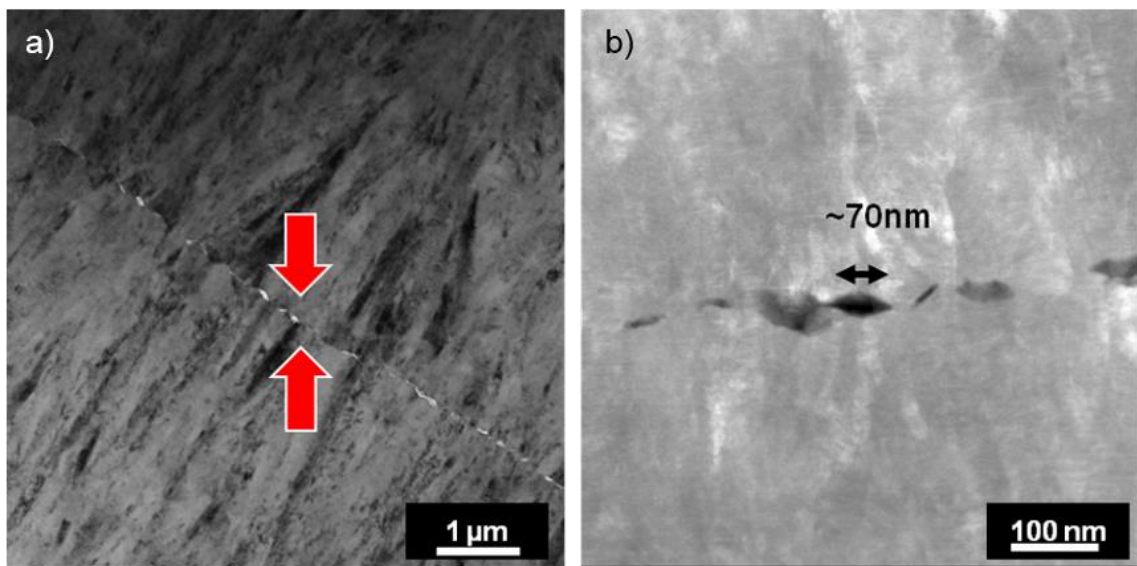


Figure 4-47. (a) Residual nanoporosity due to the imperfect merging of the matrix growing in opposite directions from two adjacent fibres; (b) the nanoporosity has a typical size of ~70 nm.

On the basis of these observations, a crystal growth model is proposed in Figure 4-48 and a schematic summarising the morphology and physiochemical properties of the SiC deposit is depicted in Figure 4-49.

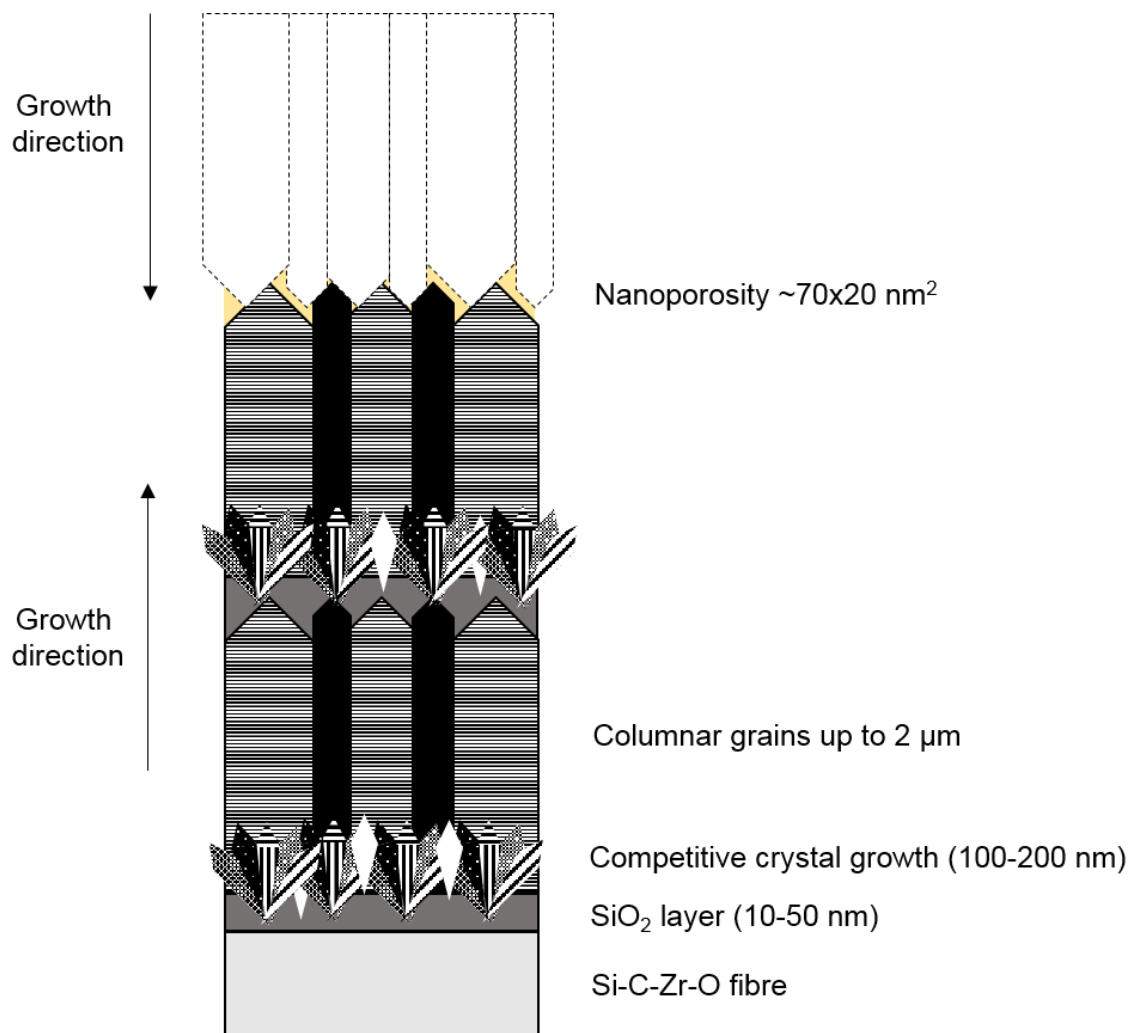


Figure 4-48. Growth model of the SiC matrix on ZMI Tyranno SiC fibres.

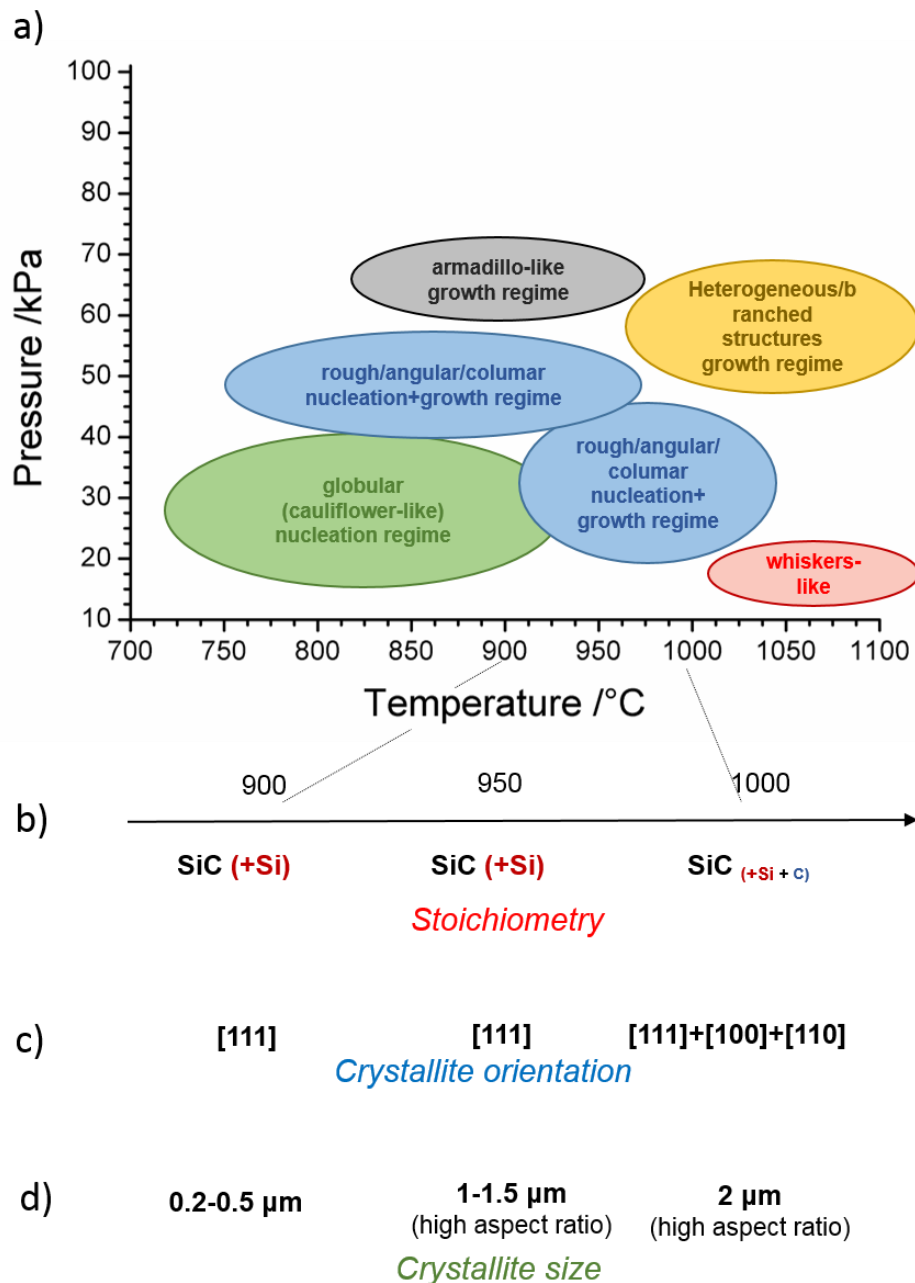


Figure 4-49. Schematic of the (a) different morphology as function of temperature and pressure, (b) stoichiometry, (c) crystallite orientation and (d) size in the temperature interval 900-1000°C

## 4.4 Deposition pattern

### 4.4.1 Influence of temperature

Figure 4-50 shows the deposition pattern of the SiC deposit at different temperatures after 8 hours of infiltration. The amount of deposit is larger in the

brighter areas of the micrographs. At 900°C, Figure 4-50(a), the matrix grew in a specific region located at the top of the preform and 10 mm off the centre.

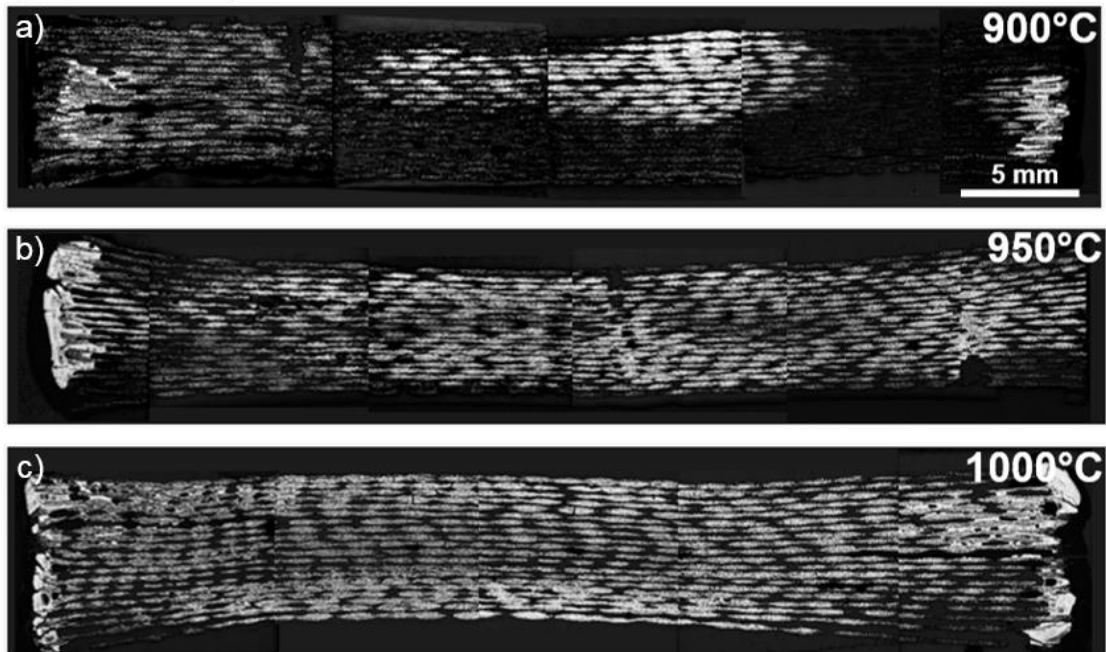


Figure 4-50. Optical microscopy images of the deposition pattern of SiC preforms infiltrated for 8 hours (stopped at interval of 2, 4 and 8 hours) at different temperatures, (a) 900°C, (b) 950°C and (c) 1000°C; 30 kPa,  $\alpha \sim 10$  and  $Q_{H_2} = 300 \text{ ml min}^{-1}$ .

Back-scattered electron micrographs, Figure 4-51, revealed some details of the intratow infiltration at different locations of the preform. At the geometrical centre of the preform, Figure 4-51(g), the porosity of the tow was generally still open, though almost closed in the fifth layer from the top, Figure 4-51(d). Most of the deposit was located in the range 5-10 mm from the centre, where the tow was completely sealed by the growing matrix. At location “c” the deposit had a thickness of almost 50  $\mu\text{m}$ , Figure 4-51(c). It should be noted that layer facing the gas inlet were not infiltrated at all leaving the gas mixture free to flow within the preform.

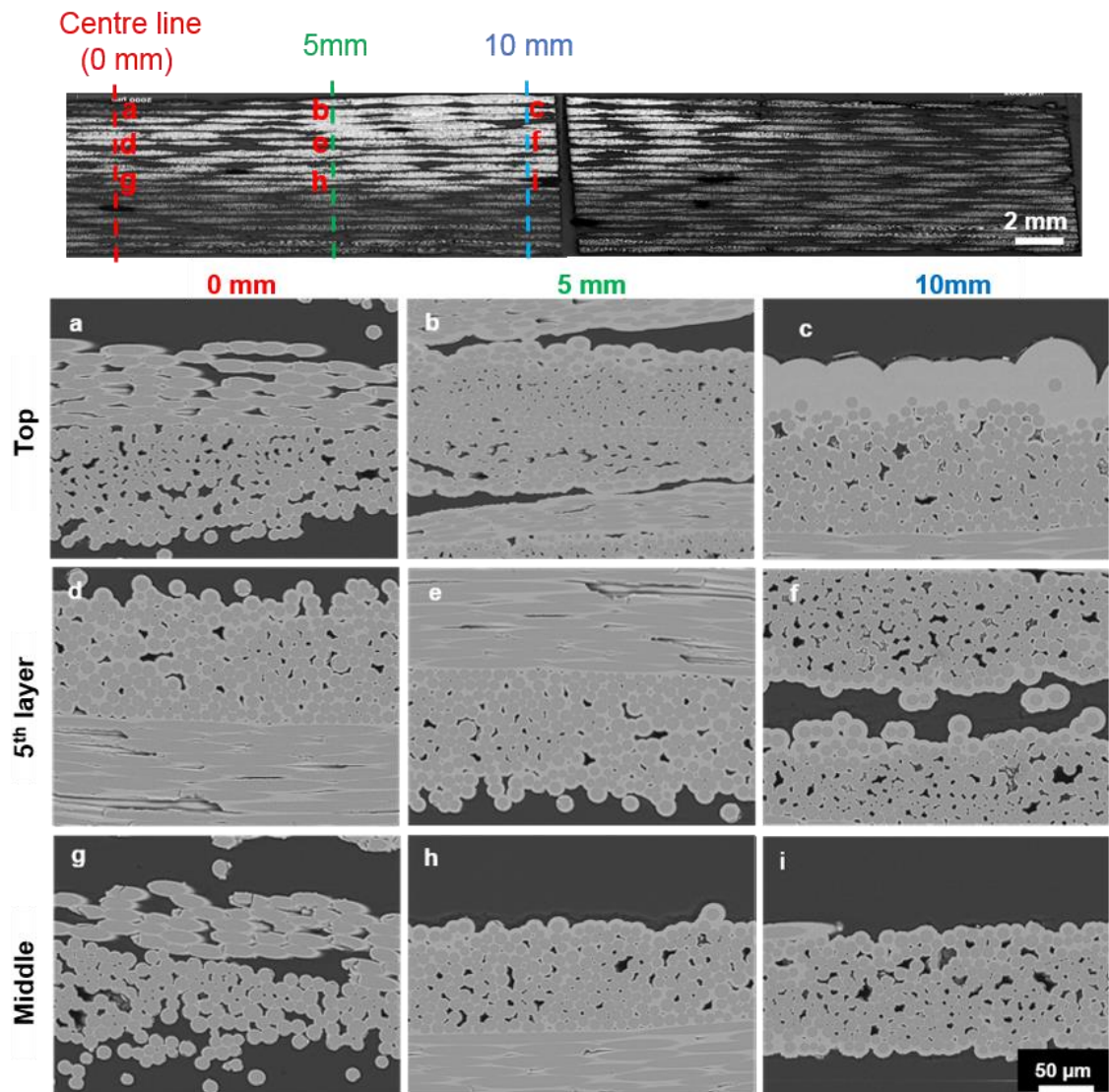


Figure 4-51. SEM-BSE images of the state of the intratow infiltration at different location in preform infiltrated for 8 hours at 900°C, 30 kPa,  $\alpha \sim 10$  and  $Q_{H_2} = 300 \text{ ml min}^{-1}$ .

The preforms infiltrated at 950°C, Figure 4-50(b) and Figure 4-52 showed a deposition distributed over the diameter of the preform. This would be expected as at higher temperature the decomposition of MTS is larger and hence the deposition proceeds further and in a wider area than at 900°C, for instance. However, a noticeable lack of infiltration was observable in the middle layer, Figure 4-52(d), (e) and (f). After 8 hours of infiltration the tows were not sealed. As shown by Figure 4-53(a) and (b), it must be noted that the top and bottom layer were completely non-infiltrated and that the formation of the deposit started

from the third layers from the top and the bottom, Figure 4-53(c) and (d), presumably due to the outer layers being colder.

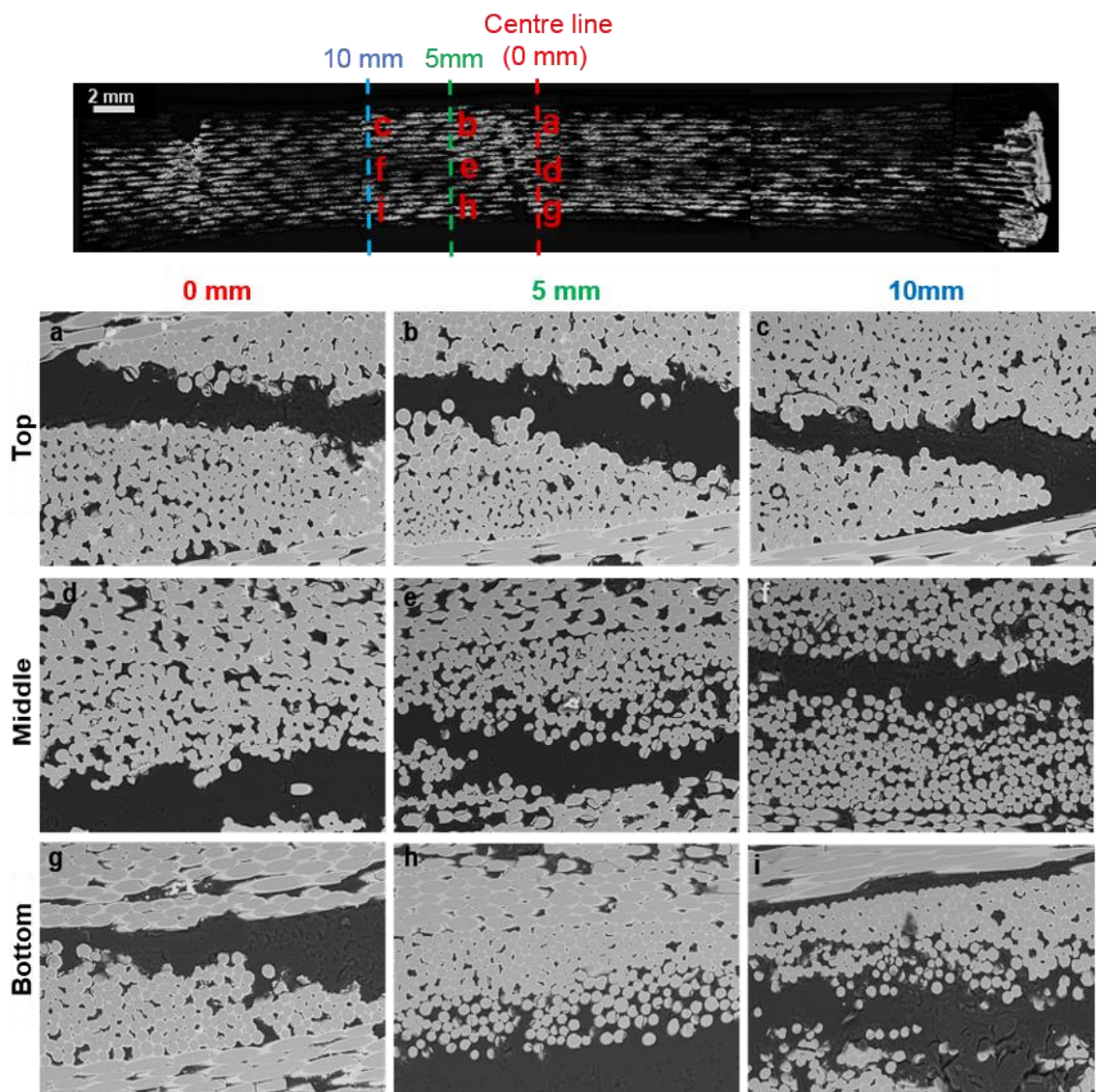


Figure 4-52. SEM-BSE images of the state of the intratow infiltration at different location in preform infiltrated for 8 hours at 950°C, 30 kPa,  $\alpha \sim 10$  and  $Q_{H_2} = 300 \text{ ml min}^{-1}$ .

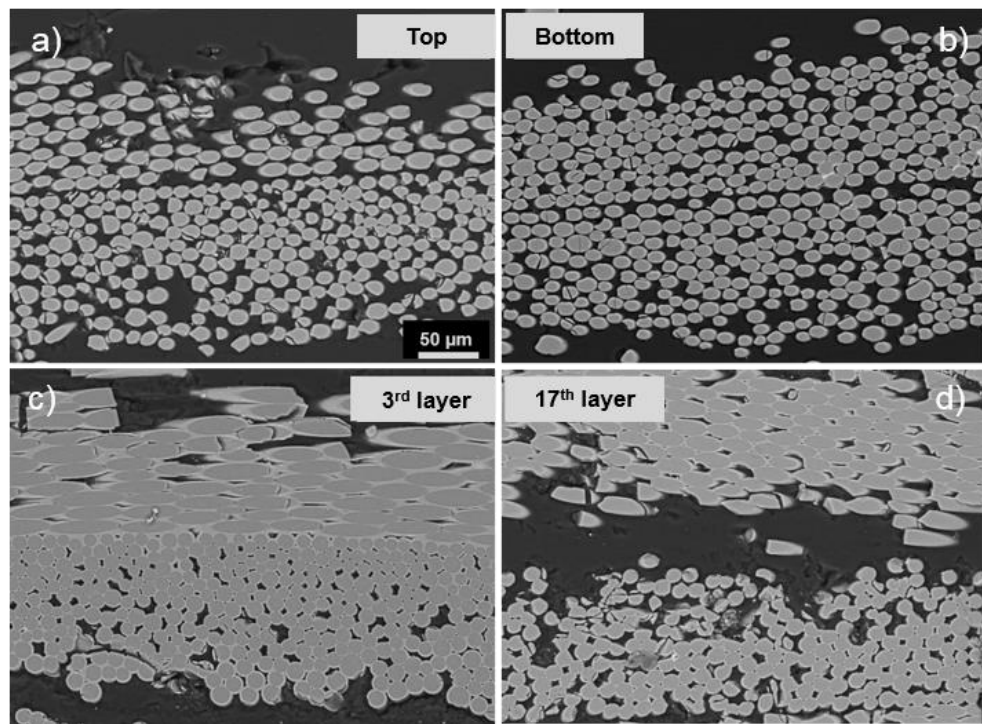


Figure 4-53. SEM-BSE images of the state of the intratow over the thickness at 0 mm from the centre in preform infiltrated for 8 hours at 950°C, 30 kPa,  $\alpha \sim 10$  and  $Q_{H_2} = 300 \text{ ml min}^{-1}$ .

At 1000°C, Figure 4-50(c) and Figure 4-54, the deposit had a deposition pattern that can be broadly described as the extension of the infiltration at 950°C. In fact, at higher temperatures also the bottom and the top layers were coated with SiC deposit, Figure 4-54(a), (b), (c), (g), (h) and (i). This was not observed for preforms infiltrated at lower temperatures, where the bottom and top layers were substantially free from deposit after 8 hours, Figure 4-53(a) and (b). The thickness of the deposit on the fibre of the middle layer was lower than that of the top and bottom layers, Figure 4-54(d), (e) and (f). In addition, at 20 mm from the centre, some SiC deposit was observed on the filaments of the top and middle layer, Figure 4-55(b), (d) and (f); this was not observed at lower temperatures, Figure 4-55(a), (c) and (e). These results suggest that i) within a radius of 20 mm from the centre there were the suitable conditions for the deposition of SiC and ii) there

is a gradient of temperature across the thickness; in particular, the bottom layer was colder than the middle and top layer, presumably due to the gas flow.

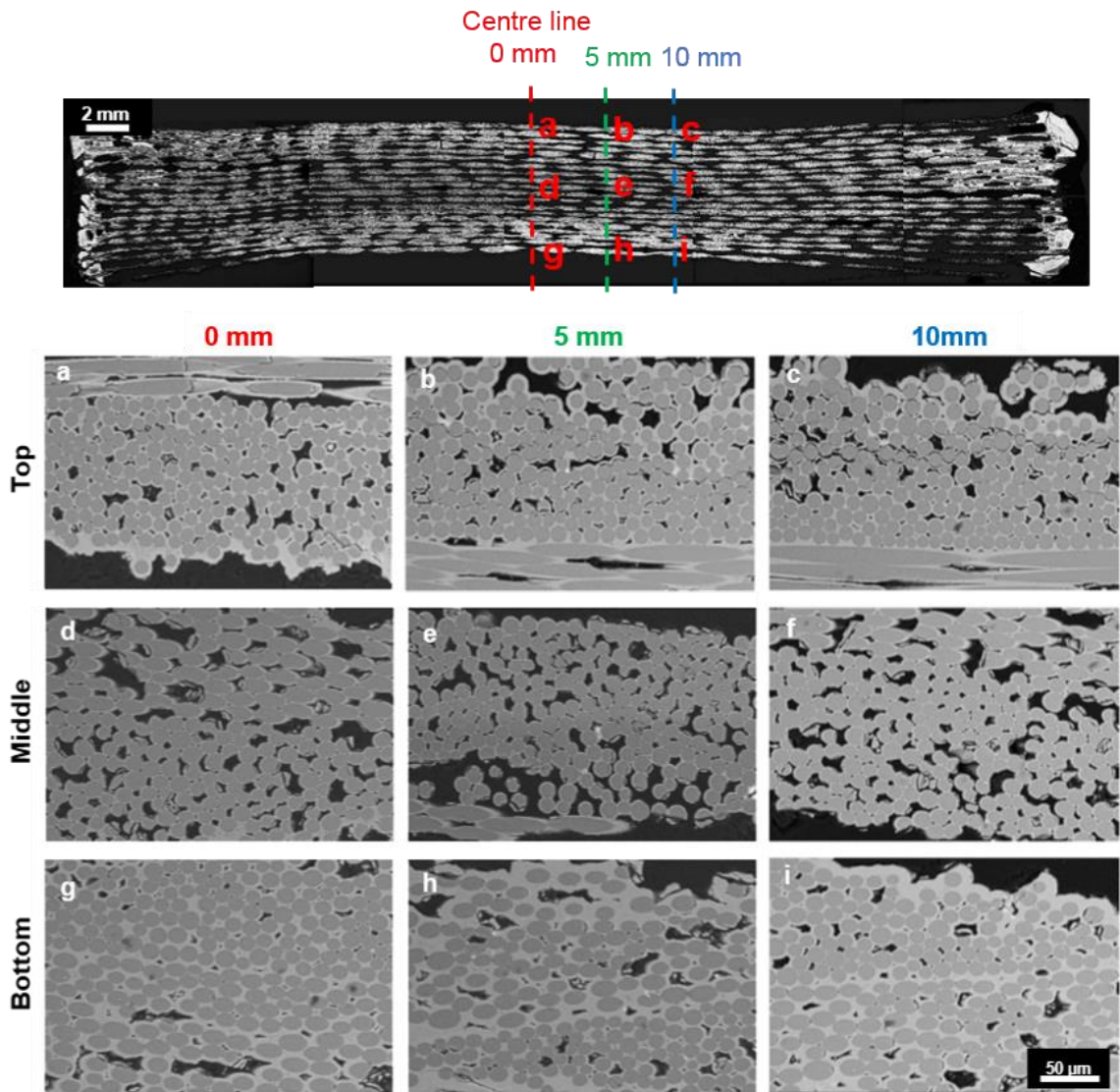


Figure 4-54. SEM-BSE images of the state of the intratow infiltration at different location in preform infiltrated for 8 hours at 1000°C, 30 kPa,  $\alpha \sim 10$  and  $Q_{H_2} = 300 \text{ ml min}^{-1}$ .

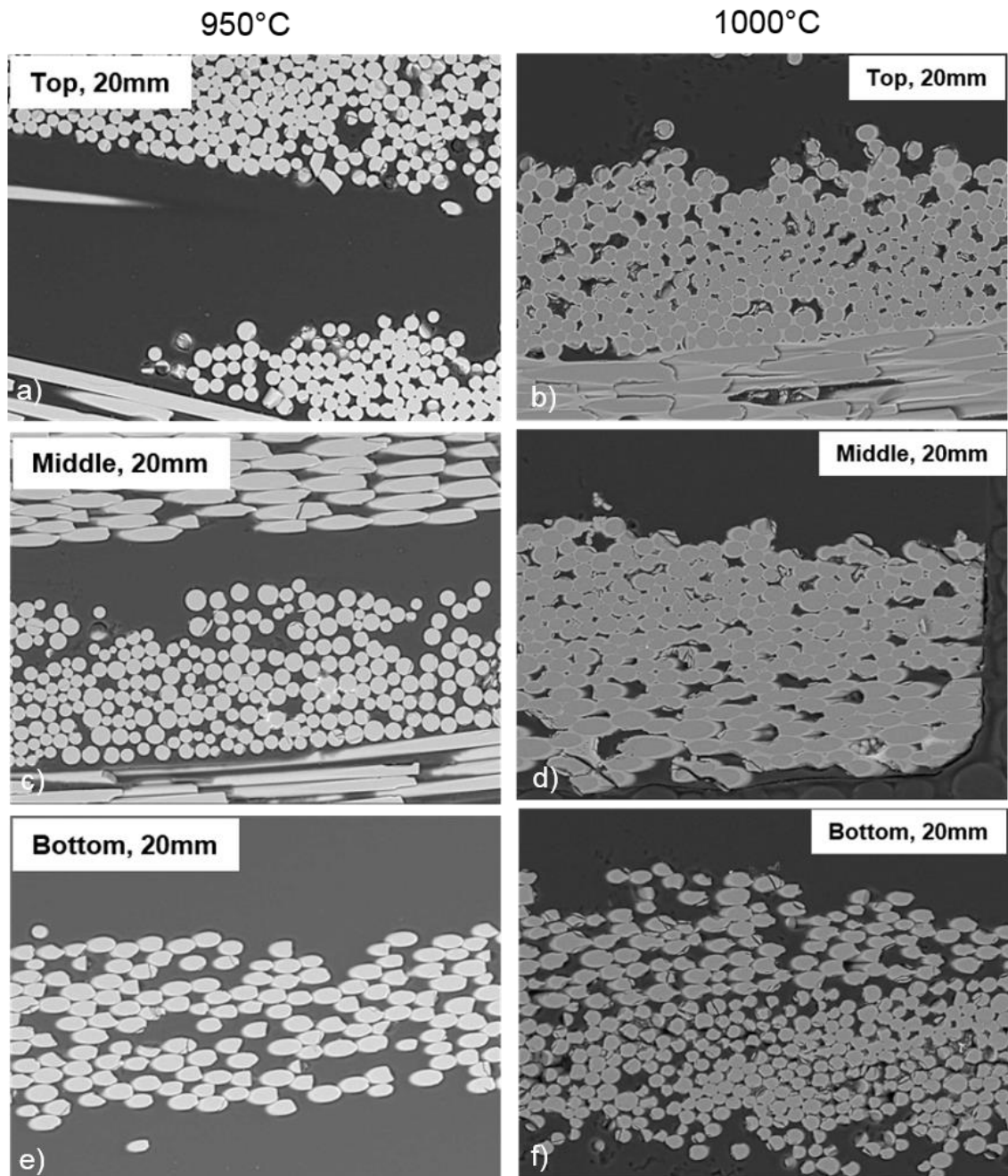


Figure 4-55. SEM-BSE images of the state of the infiltration in the preforms infiltrated at 950 and 1000°C at 20 mm from the centre and at different locations over the thickness.

As indicated previously, the sides of the preforms were coated by the SiC slurry. As shown by Figure 4-56(a) and (b), the layer of powder (up to 1 mm thick) was partially infiltrated. In particular, the powder closer to the fibres showed an advanced degree of infiltration, Figure 4-56(c), whilst the powder at the edge of the preform was not infiltrated. This difference in infiltration suggests that there

was a gradient of temperature across the layer of powder and in particular the inner part closer to the sharp ends of the fibres was hotter; the sharp ends are hot enough to noticeably heat the powder in their proximity and promote the deposition of SiC. Conversely the powder at the edge was relatively cold, confirmed by the pyrometer measuring the temperature to be as low as 800°C,

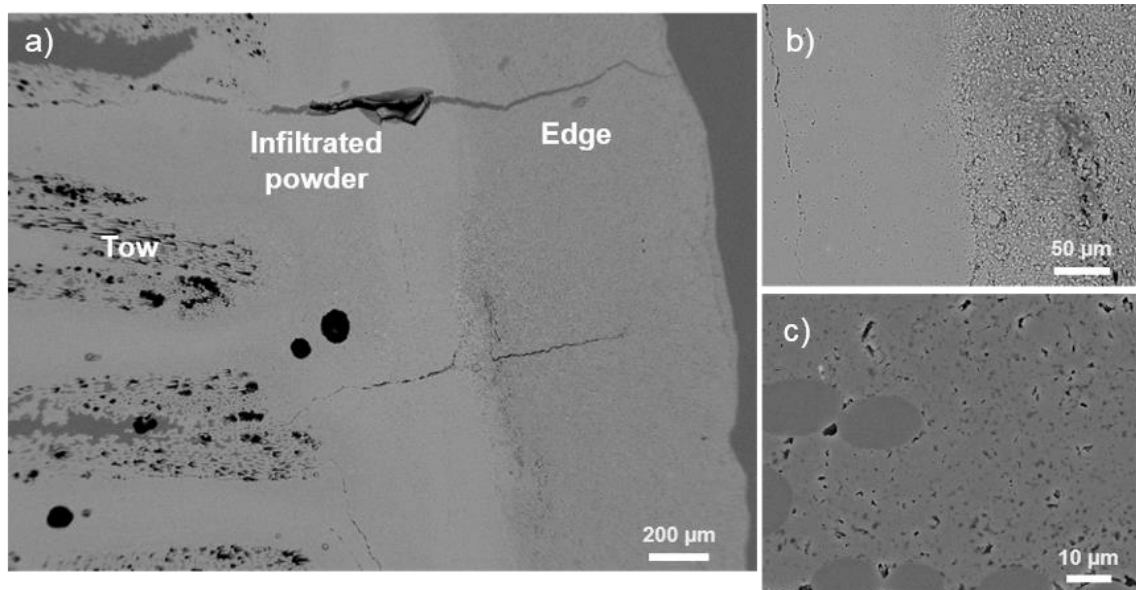


Figure 4-56. SEM-BSE images of the side of the preform showing an infiltrated layer of powder adjacent to the SiC fibres.

Another characteristic of the preform infiltrated at 1000°C is that some layers of fabric started being connected by the matrix as shown in Figure 4-57.

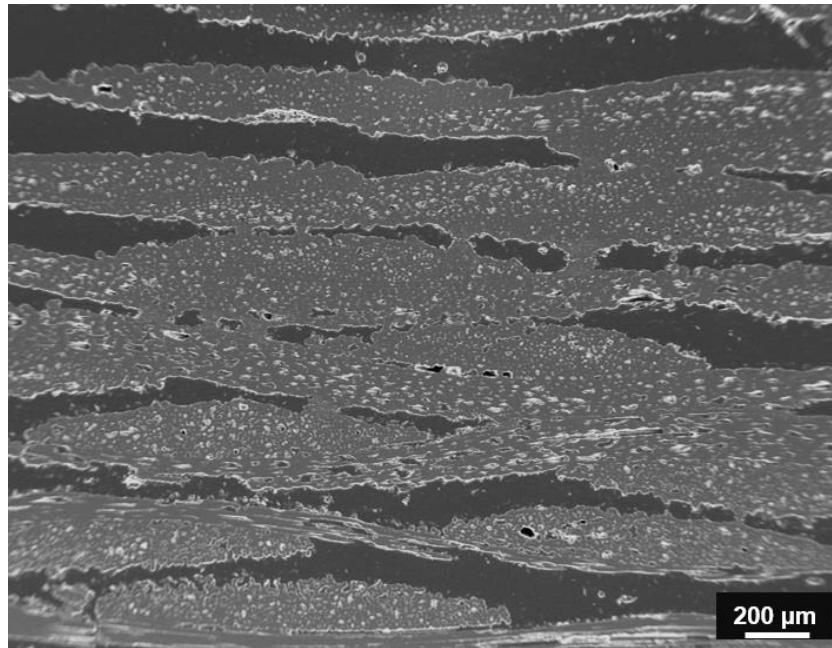


Figure 4-57. SEM-SEI image showing the initiation of the tows merging in a preform infiltrated for 8 hours at 1000°C, 30 kPa,  $\alpha \sim 10$  and  $Q_{H_2} = 300 \text{ ml min}^{-1}$ .

### 4.4.2 Influence of the pressure

The effect of the pressure on the deposition pattern was investigated by fixing the conditions at 900°C,  $\alpha \sim 10$  and  $Q_{H_2} = 300 \text{ ml min}^{-1}$ . The deposition pattern of the preform infiltrated at 30 kPa has been commented in the previous section and in Figure 4-51. At 50 kPa, Figure 4-58(b), the increase of residence time (Figure 4-10) moves the infiltration front toward the centre of the preform, whilst at 70 kPa the residence time was too high and the deposit was located mainly at the surface facing the inlet. The preform infiltrated at 50 kPa was investigated further since it was considered a good example of inside-out densification. The deposition pattern was consistent with the formation of an inverse temperature profile, although slightly shifted to the gas inlet and 5 mm off from the centre as shown in more detail in Figure 4-59.

In fact, the top and bottom surfaces remained open to the gas flow since the deposition was concentrated in the middle of the preform in terms of the

thickness. In the central layer, and within 10 mm from the centre, the intratow infiltration was in an advanced state with the tows completely sealed by the deposit. At 15 mm, only the middle and five adjacent layers were marginally infiltrated and they remained open to the gas flow. At 20 mm, only the central and two adjacent layers showed the presence of a submicron thin coating. At 25 mm, very close to the edge of the preform, the deposition zone was actually larger than that at 20 mm though this effect may be related to the increase of temperature near the sharp ends of the fibres. In Figure 4-61, the infiltrated region was delimited by the red dotted lines. This infiltrated region decreased moving to the edge, which indicates the potential for inside-out densification.

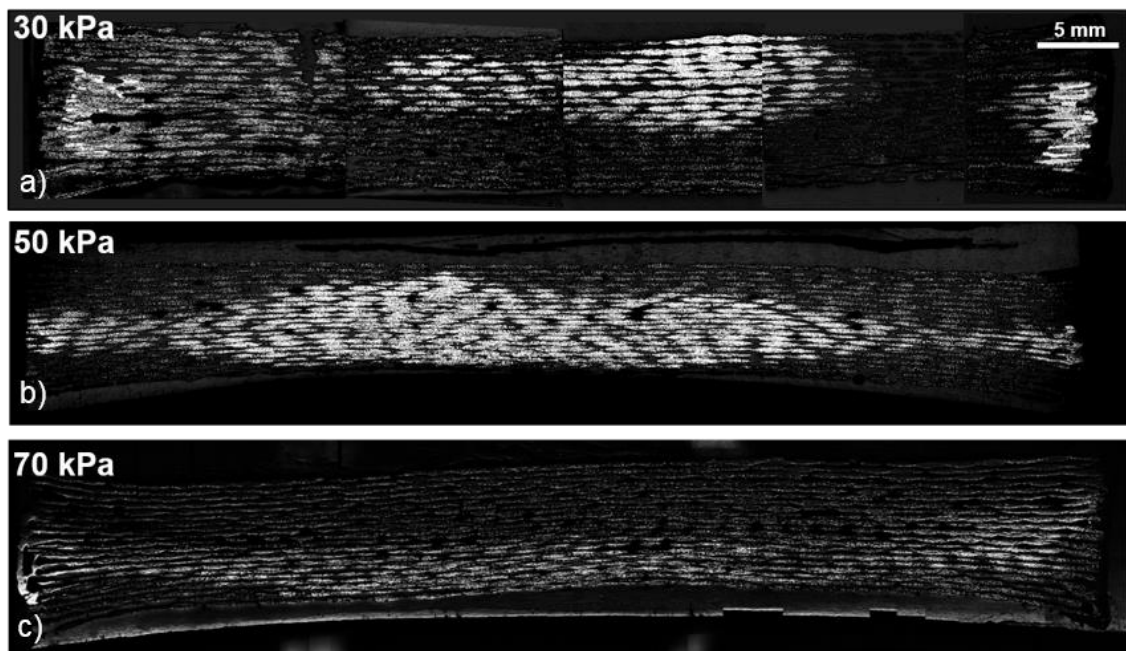


Figure 4-58. Optical microscopy imaged of the deposition pattern of SiC preforms infiltrated for 8 hours (stopped at intervals of 2, 2 and 4 hours) at different pressure; 900°C,  $\alpha \sim 10$  and  $Q_{H_2} = 300 \text{ ml min}^{-1}$ .

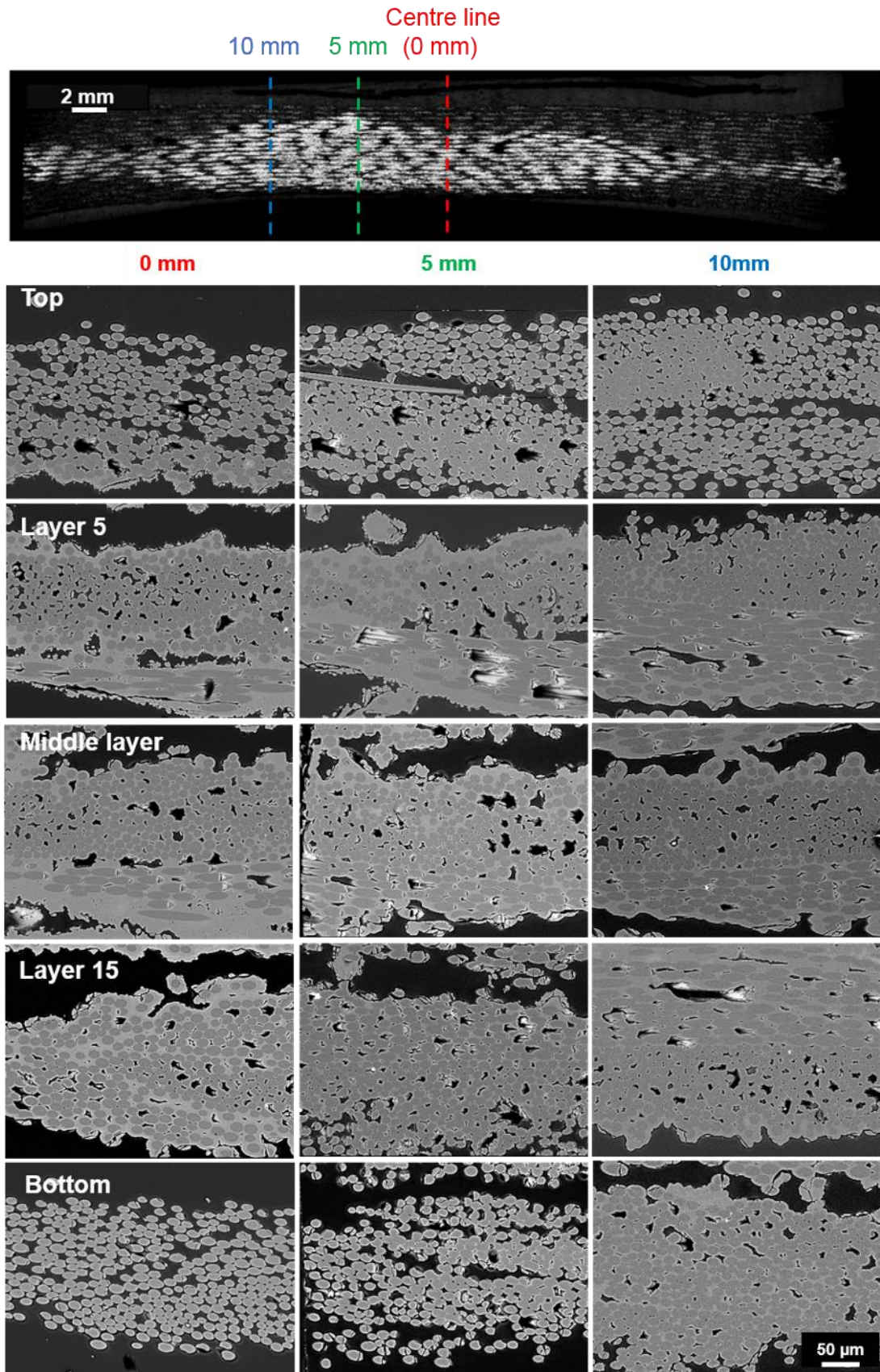


Figure 4-59. SEM-BSE images showing the details of the state of the intratow infiltration at different locations in the range 0-10 mm from the centre; preform infiltrated for 8 hours at 900°C, 50 kPa,  $\alpha \sim 10$  and  $Q_{H_2} = 300 \text{ ml min}^{-1}$ .

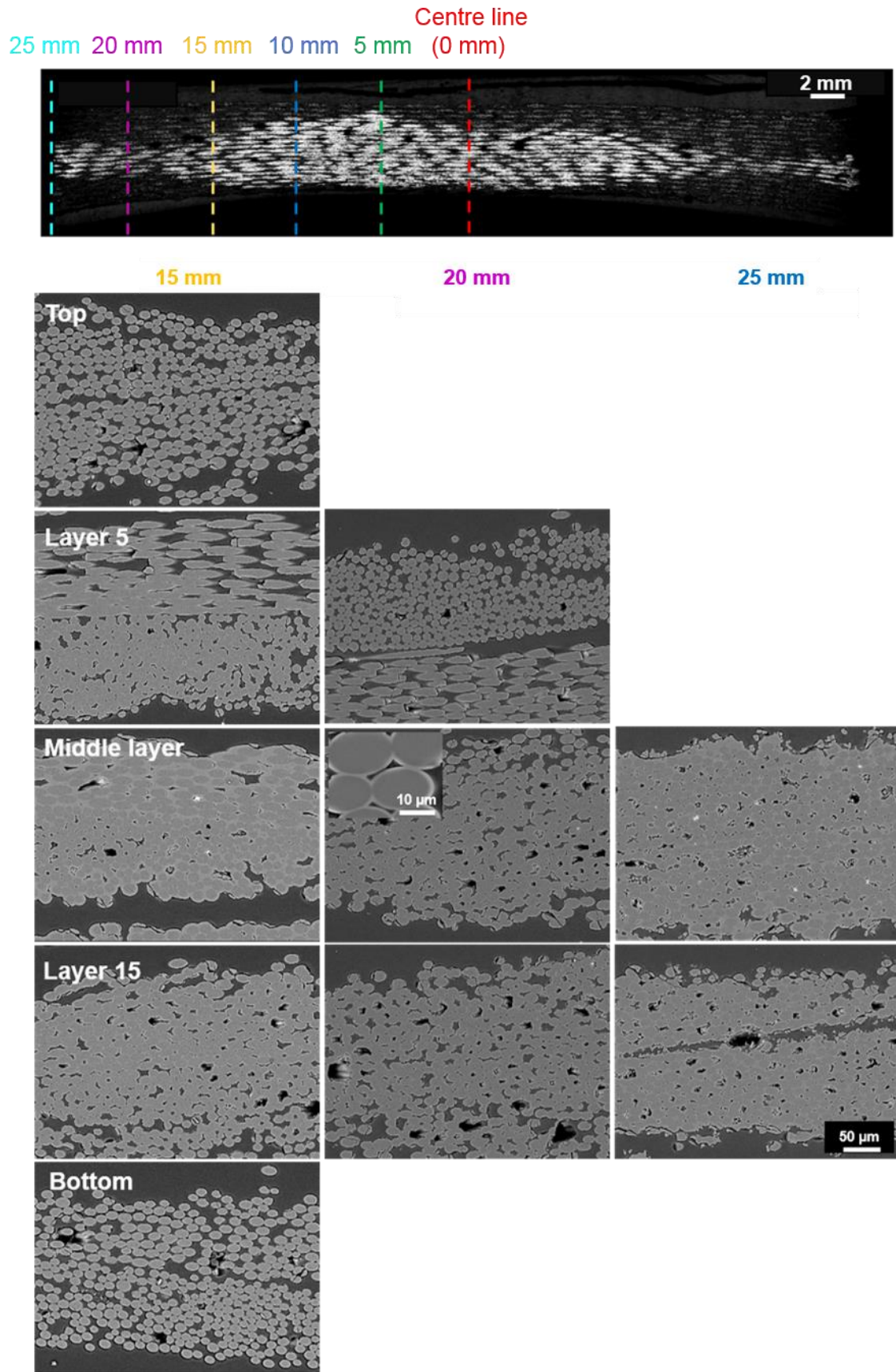


Figure 4-60. SEM-BSE images showing the details of the state of the intratow infiltration at different locations in the range 15-25 mm from the centre; preform infiltrated for 8 hours at 900°C, 50 kPa,  $\alpha \sim 10$  and  $Q_{H_2} = 300 \text{ ml min}^{-1}$ .

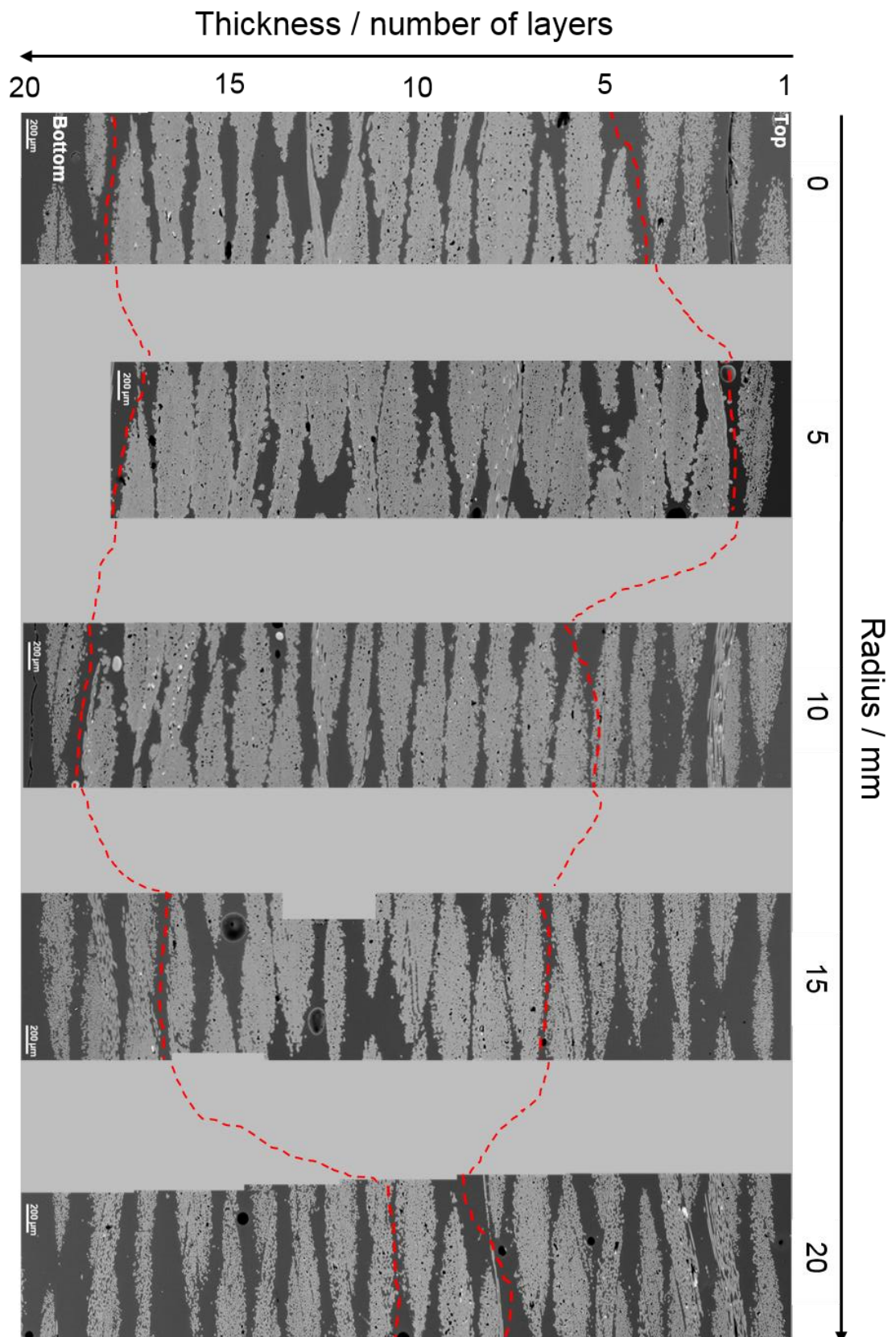


Figure 4-61. Reconstruction of different locations from the centre of the entire

thickness of the preform infiltrated for 8 hours at 900°C, 50 kPa,  $\alpha \sim 10$  and  $Q_{H_2} = 300 \text{ ml min}^{-1}$ .

In order to investigate if an increase in temperature to 950°C at 50 kPa leads to a simple extension of the nature of the deposition for the preform infiltrated at 900°C and the same pressure, an infiltration of 4 hours was carried out. Figure 4-62. Under these conditions an inside-out deposition pattern appeared though, based on optical microscopy, the middle layer seemed to be scarcely infiltrated. Infiltrations were also performed at 950°C and 70 kPa, Figure 4-63. It is unclear if there is an actual inside-out deposition.

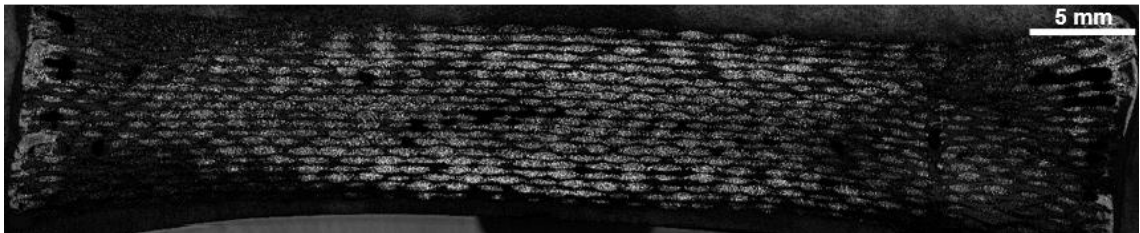


Figure 4-62. Optical microscopy image of the SiC preform infiltrated for 4 hours at 950°C and 50 kPa.

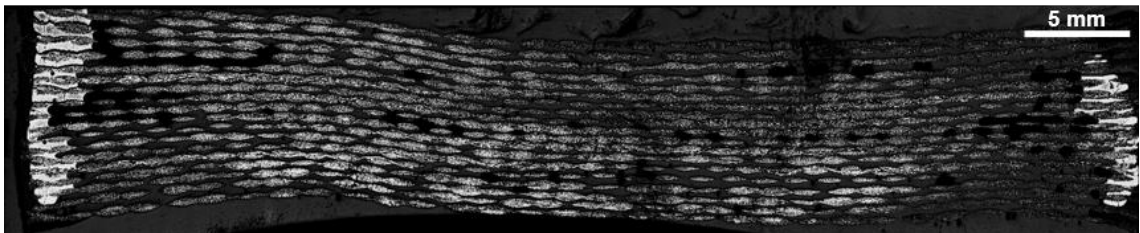


Figure 4-63. Optical microscopy image of the SiC preform infiltrated for 4 hours at 950°C and 70 kPa.

Since the yield of the MECVI at these temperature and pressure was above 20% (only 8% at 900°C) and since the deposit contained less free silicon, these conditions are particularly tempting for the overall densification of SiC preform. In fact, infiltrations at higher temperature correspond to an extension of the infiltration at lower temperatures. However, this is not true when the temperature

and pressure are simultaneously too high. For instance, as shown in Figure 4-64, the thickest deposit, which was hundreds of micrometres thick, was mainly located on the layer facing the inlet, which caused the sealing of the preform. The deposit is not homogeneous and depletion of the reagent with consequent formation of powder in the gas phase cannot be excluded. The results indicate that at high pressures and high temperatures the chemical vapour infiltration was turned into more of a chemical vapour deposition process with only the surface layers being infiltrated. In this case, too long a residence time permits the homogeneous decomposition of MTS in the proximity of the hot substrate represented by the fibres.

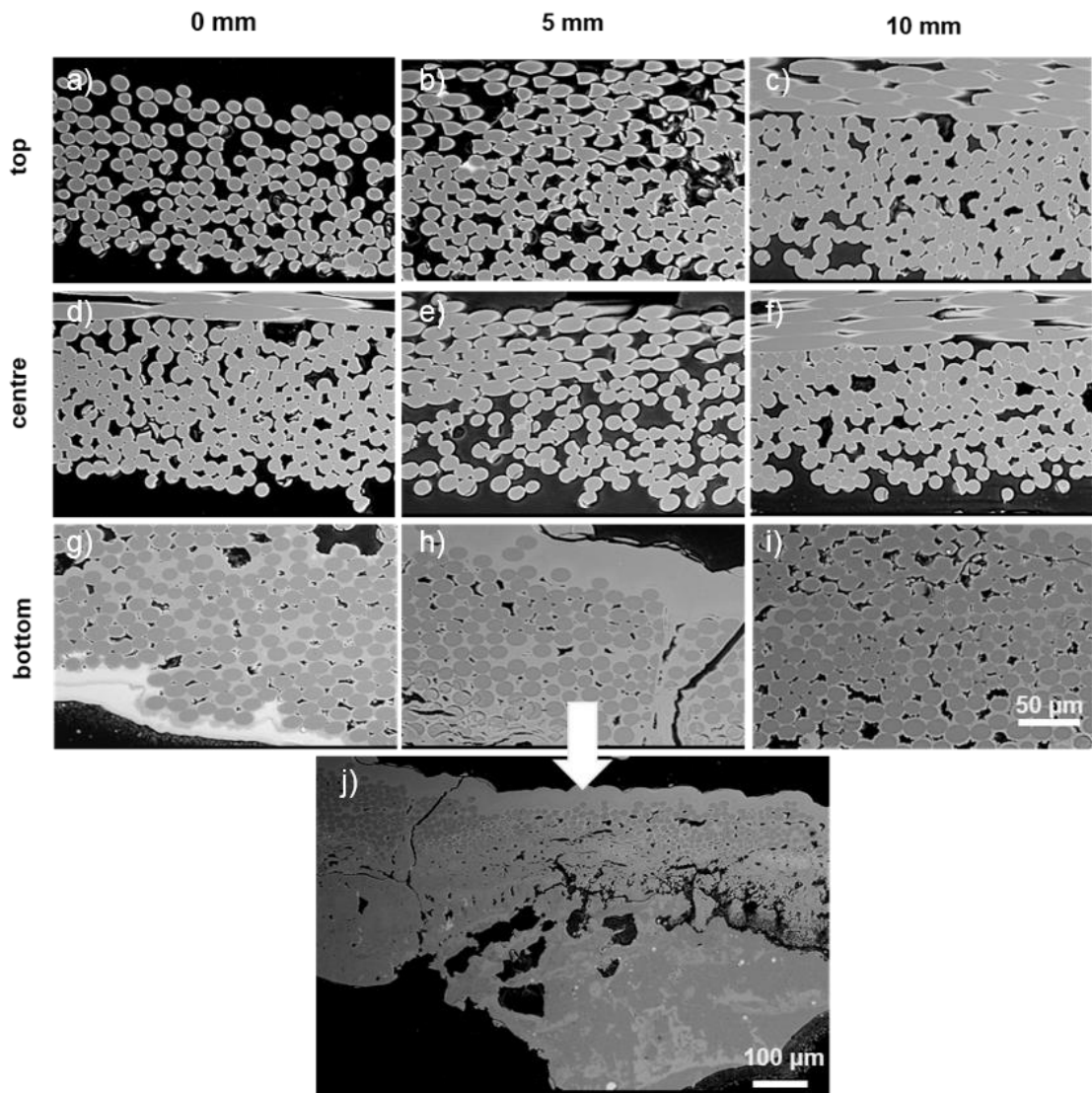


Figure 4-64. SEM-BSE images showing the details of the state of the infiltration at different location of a preform infiltrated for 8 hours at 1000°C, 70 kPa,  $\alpha \sim 10$  and  $Q_{H_2} = 300 \text{ ml min}^{-1}$ .

#### 4.4.3 Thermal conductivity influence

Heat transfer in composite materials is governed by the thermal conductivities of the individual constituents, the relative volume fractions, and the architecture of the fibrous reinforcement including porosity, which is a thermal insulator. Density variation, due to the deposition of the matrix material within the porous preform, increases the thermal conductivity.

Tyranno ZMI fibres have low thermal conductivity [85, 369] and constitute 30-35 vol% of the preforms. A preform of SiC with the architecture examined in this work has approximately the same conductivity both in-plane and perpendicular to the layers. The heat conduction is mainly influenced by the SiC matrix, which has a conductivity of two orders of magnitude higher than the fibres [23]. It can be expected that as the infiltration proceeds and matrix is deposited on the fibres, the porosity decreases and, in turn, the thermal conductivity increases and the temperature profile flattens. According to Carrier et al. [312] the solid phase percolation threshold can be reached when the relative porosity is 30%. This means that when the density is 70% in the centre, the thermal conductivity will be close to the value of SiC and possibly flatten out the gradient over the diameter but especially over the thickness. After 8 hours of infiltration the difference of temperature between the centre of the top surface and side of the preform decrease from 270 to 180°C (Figure 4-74) and from the mass gain the densification rate is 2.4% h<sup>-1</sup>. This means that with additional hours of infiltration, presumably ~16-20 hours, the temperature profile could be almost flattened out. Hence, the entire central region has to be densified after ~24-30 hours for the MECVI process to offer a real improvement compared to the other CVI variations available. However, from the present work is not possible to precisely estimate the time before the gradient of temperature flattens out because the CVI was performed for only 8 hours. It is known that after a certain number of hours the densification rate in CVI processes ceases to be linear and slows down [11].

### 4.4.4 The role of the powder

As discussed earlier, the SiC powder applied to the sides of the preform was primarily to reduce the occurrence of arcing. However, the results suggest that

the temperature of the fibre at the edge of the preform could be very high; the matrix was capable of growing on the SiC particles and eventually joining them. Occasionally, SiC slurry from the side penetrated deeper into the preform where it could be found located between the tows or even, within the tow. When the matrix formed on the powder between the tows it was porous because of the imperfect merger of the deposits growing on the particles from numerous different directions, Figure 4-65(a), (b) and (c). When the matrix was formed on the particles within the tows, it deposited in a similar manner to when it coated the fibres, Figure 4-65(d) and (e). However, if the path was blocked before all the voids were filled, some particles remained uncoated, and hence loose, within the tow as shown in Figure 4-65(f). This is likely to reduce the overall strength of the composite.

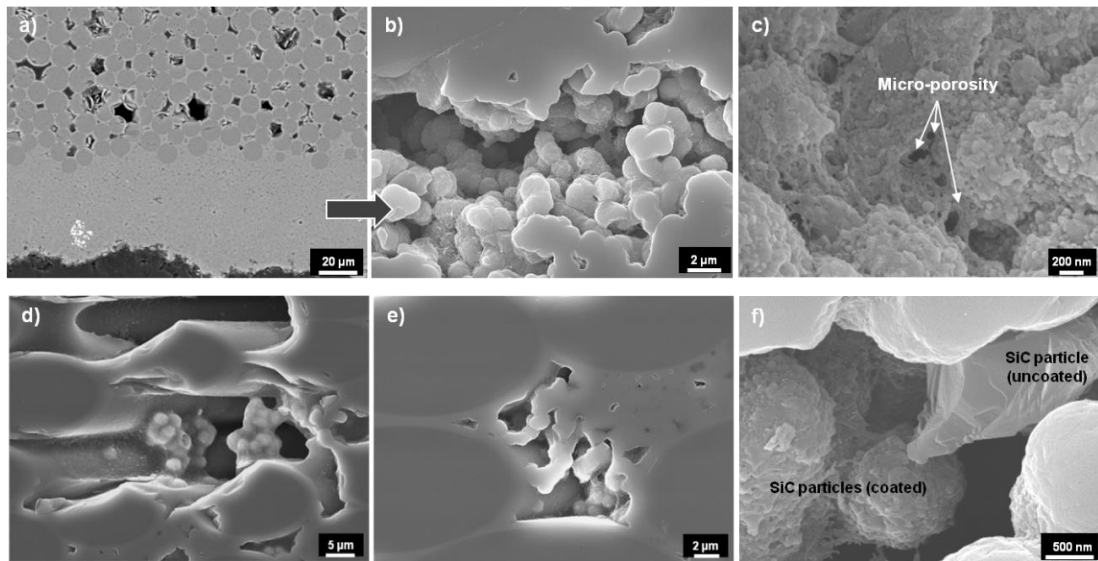


Figure 4-65. SEM images of the infiltration of a powder layer between the tow (a) and (b); (c) microporosity due to the incomplete merging of the matrix growth on the SiC powder; (d) and (e) penetration of the powder within the tow and incomplete infiltration; (f) some SiC particles were not coated by CVI. Micrograph (a) was obtained in backscattered electron mode whilst micrographs from (b) to (f) in secondary electron mode

Powder certainly represented a substrate for the growth of matrix growth and if a layer of powder was too thick and well-compacted, there may have been a lack of intratow densification. However the use of powder represents an opportunity [154, 155]; as shown in Figure 4-66 where there was powder the intertow gap reduced from 70 to 30  $\mu\text{m}$  and there is still some intratow infiltration, Figure 4-65.

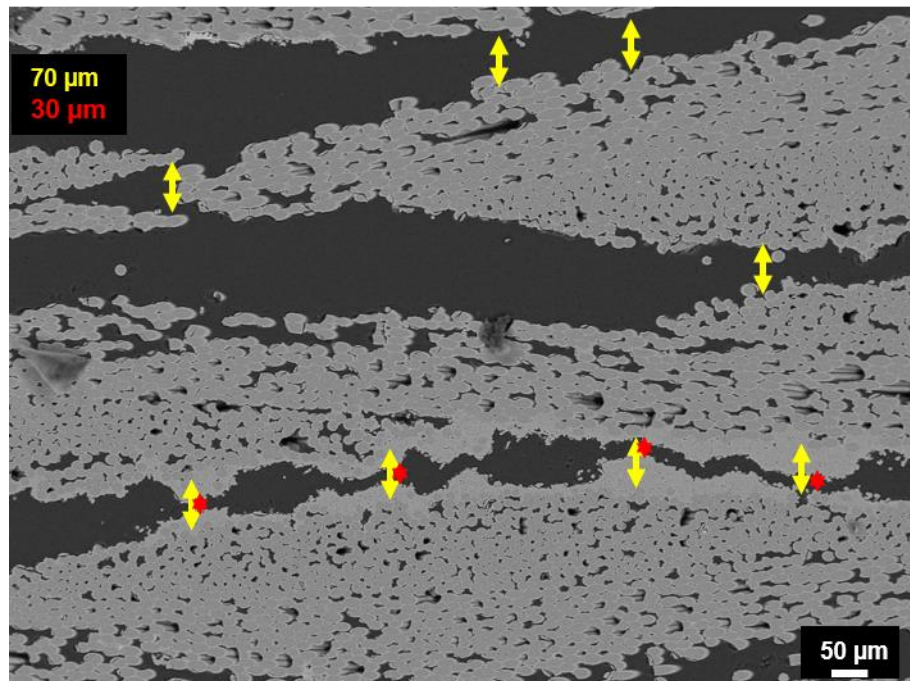


Figure 4-66. SEM-BSE imaged showing the reduction of intertow spacing because of the powder layer.

### 4.5 Dielectric properties

Figure 4-67a and b show the variation of the dielectric permittivity with temperature for Tyranno-ZMI SiC fabric and four commercially available silicon carbide powders with different particle size. With regard to the SiC fibres, the dielectric permittivity was monitored during both heating and cooling. For the range of temperatures investigated, it can be seen that  $\epsilon'$  lay approximately between 6 and 9. After a marginal increase from room temperature to 800°C, there was a drop with the minimum value reached at 1100°C. On the other hand,

$\epsilon''$  was found to have an exponential increase over the range of temperature investigated. As observed by Mo et al. [194] Tyranno ZMI fibre are favourable microwave absorber. The dielectric behaviour of the powder was less predictable, the powders with a particle size above one micrometre showed metallic behaviour above 800°C, Figure 4-68(a). The same powders were found to have a steeper exponential growth with temperature than the submicron powder;  $\epsilon''$  peaked at a value of 70, Figure 4-68(b), whilst Tyranno ZMI SiC fibres had a peak at a value of ~15. Figure 4-69 shows the comparison of the 300nm SiC powder with the fibres; the permittivity of the powder was different during heating and cooling. The powder could have absorbed moisture before heating. At the temperatures of interest for the MECVI process, Figure 4-69(a);  $\epsilon'$  of the powder was higher than the real permittivity than the fibres.  $\epsilon''$  of the powder was lower than the fibres in the entire range of temperature considered, Figure 4-69b.

From equation ( 3-15 ), the values of penetration depth were calculated and are presented in Figure 4-70. The penetration depth decreased with increasing temperature for both the powder and the fibres: in the range 900-1000°C the penetration depth of the fibres was approximately 15 mm, whilst that for the powder remained above 20 mm. The effect of the penetration depth on the deposition pattern will be discussed in the section 4.5.1.

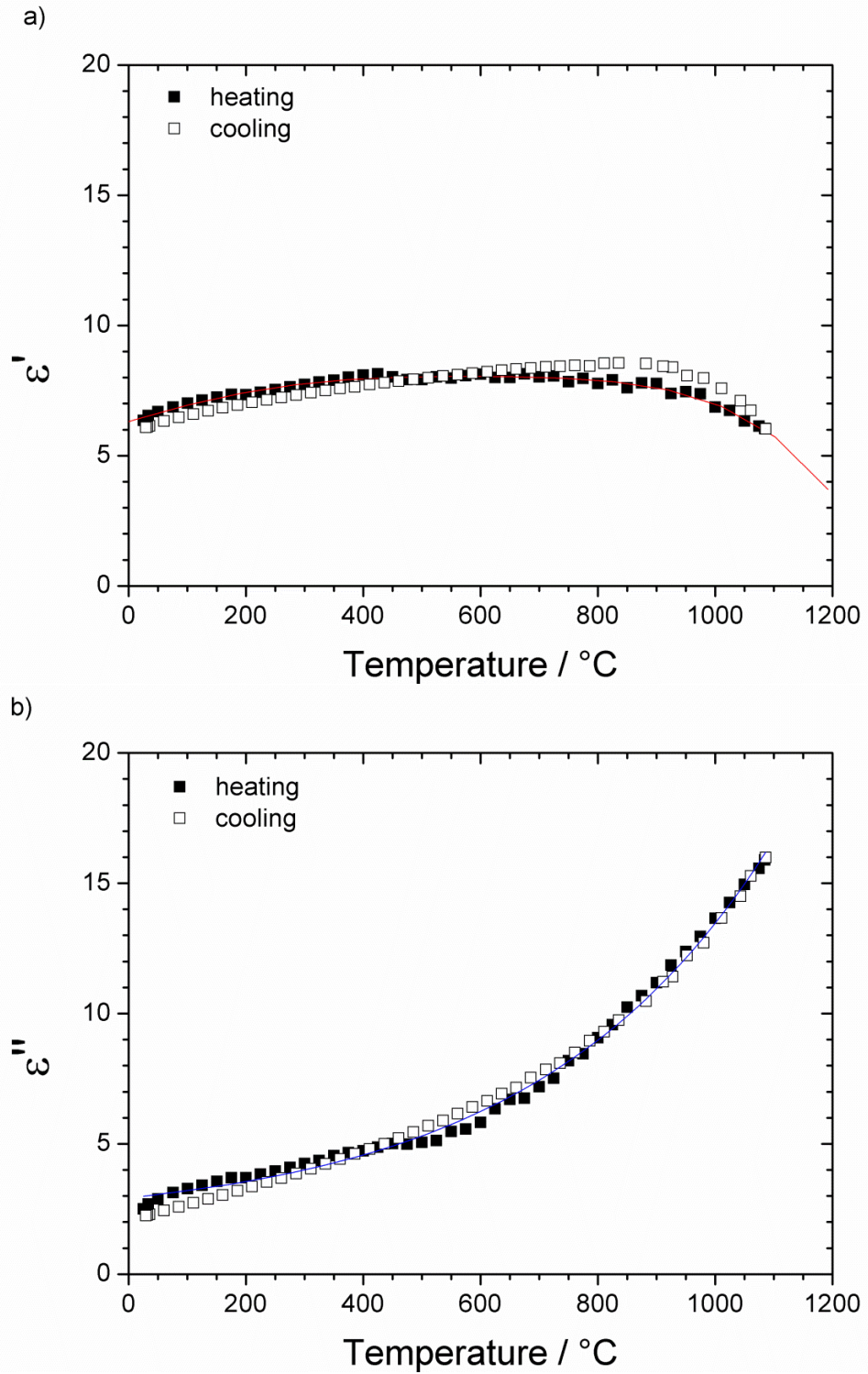


Figure 4-67. Dielectric permittivity of silicon carbide fibres Tyranno ZMI as function of the temperature; (a) is the real part and (b) the imaginary part.

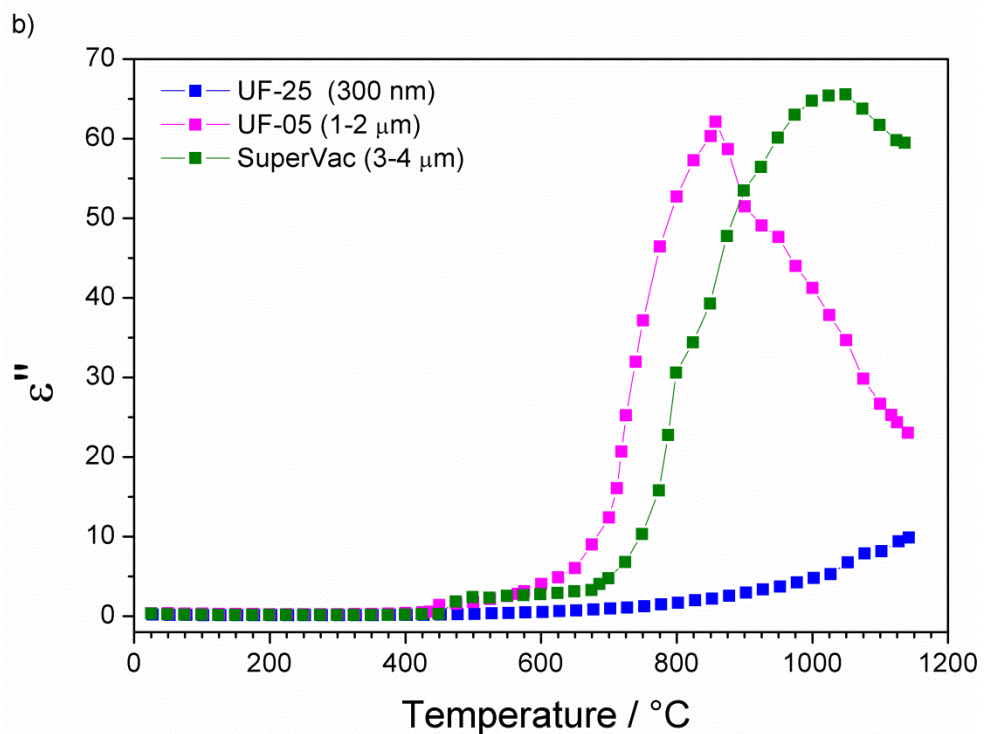
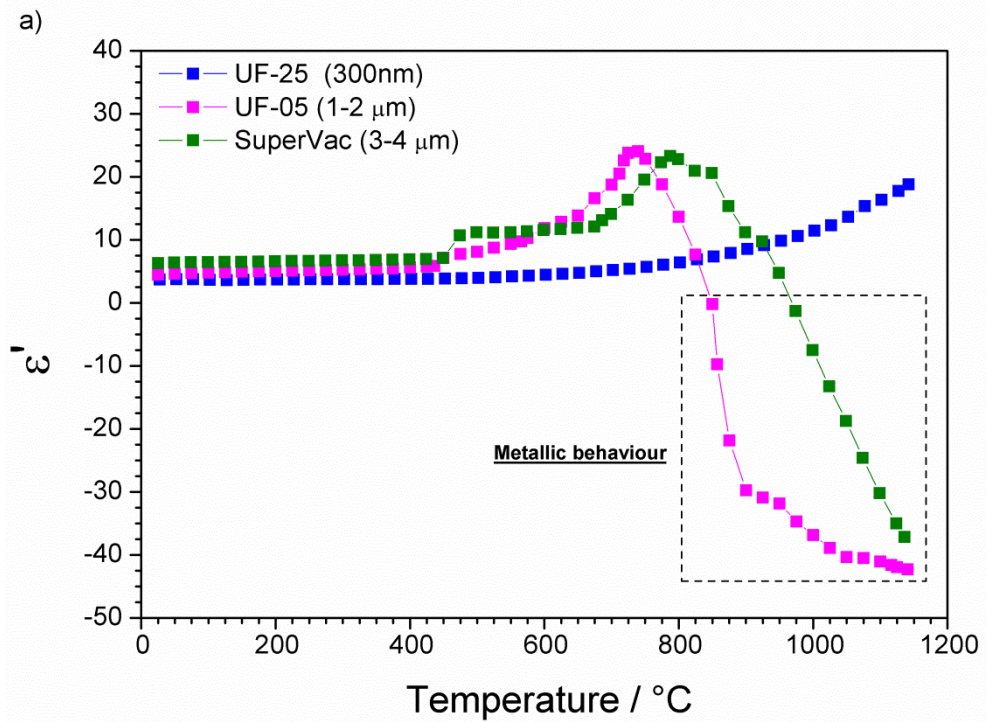


Figure 4-68. Dielectric permittivity of three commercial available silicon carbide powders with different particle size (D50); (a) is the real part and (b) is the imaginary part.

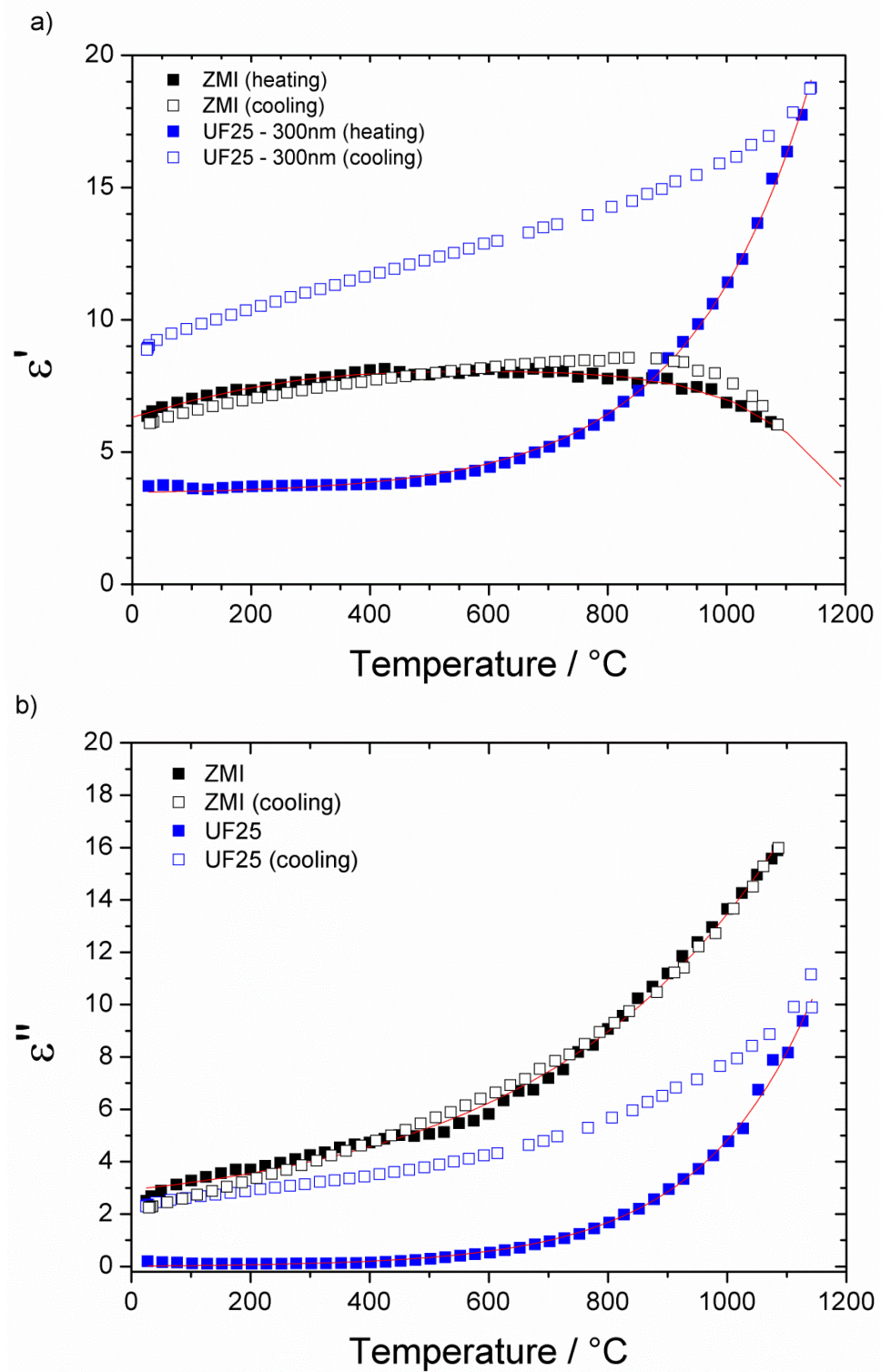


Figure 4-69. Comparison of the dielectric permittivity of the single constituents of a SiCf/SiC preform; (a) and (b) the real and imaginary parts.

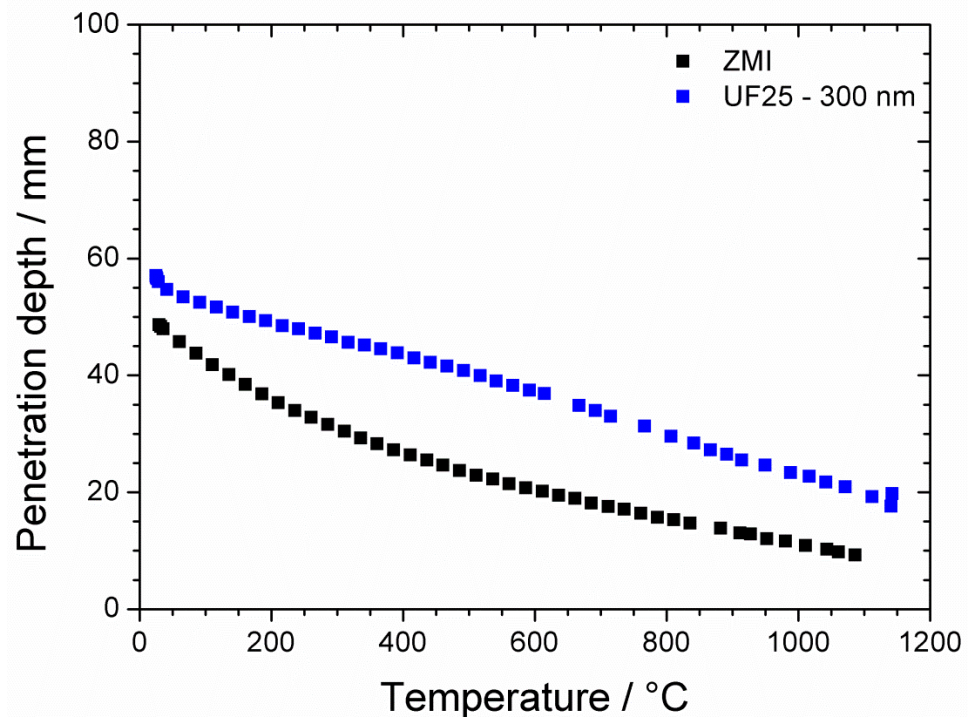


Figure 4-70. Variations of the half-power penetration depth as a function of the temperature for the single constituents of a SiCf/SiC preform.

Figure 4-71 shows the power required to heat a 50.8 mm diameter / 20 layer-SiC<sub>f</sub> preform to different temperatures. Almost twice the power is required to reach 1100°C compared to that required to reach 800°C. It should be noted that no attempts were made to heat preforms to higher than 1100°C because of the likely occurrence of arcing.

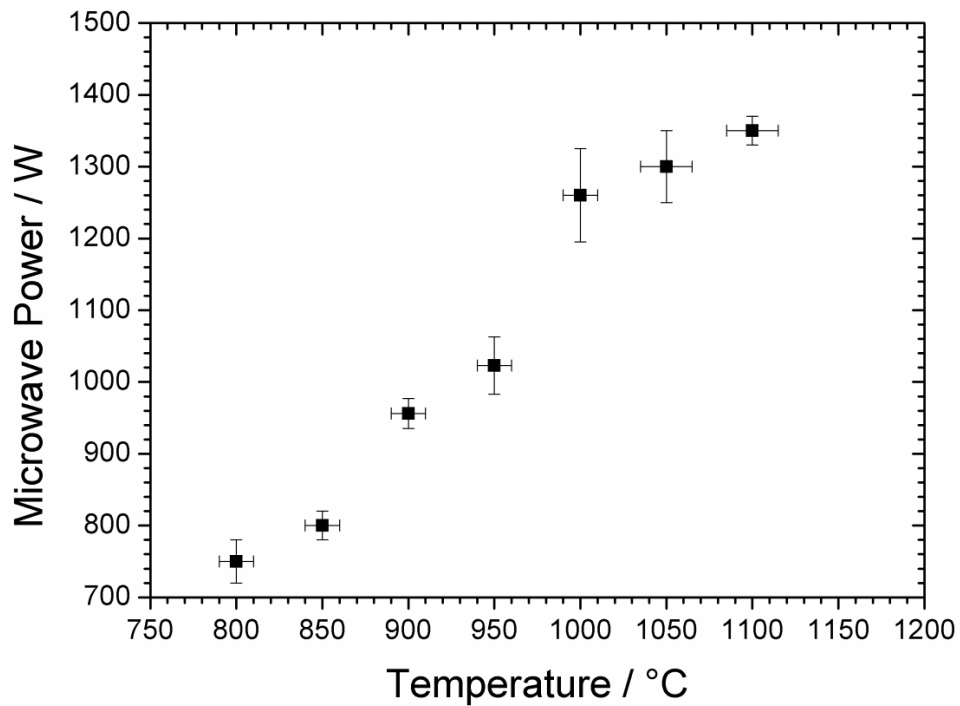


Figure 4-71. Microwave power required to heat a SiCf/SiC preform up to the setpoint temperature. Preform consisted of a stack of twenty 51 mm-diameter discs; the hydrogen flow rate was 300 ml min<sup>-1</sup>.

Figure 4-72(a) and (b) show the variation of the side temperature of the preform over the course of a typical infiltration and the microwave power needed to control the setpoint temperature (controlled via the temperature measurement on the top surface). After 2 hours the side temperature was approximately 25-30°C higher than the value prior to initiation of the MTS infiltration and an increase of 100 W was required to maintain the setpoint temperature. As anticipated in the experimental procedure, Figure 3-14, the power required in the first 5-10 minutes was higher because of the endothermic reaction of the silica formation from MTS. The forward power spikes visible in Figure 4-72(b) were due to the microwave controller unit, which cut the forward power when the temperature was  $\geq 3^{\circ}\text{C}$  above the setpoint.

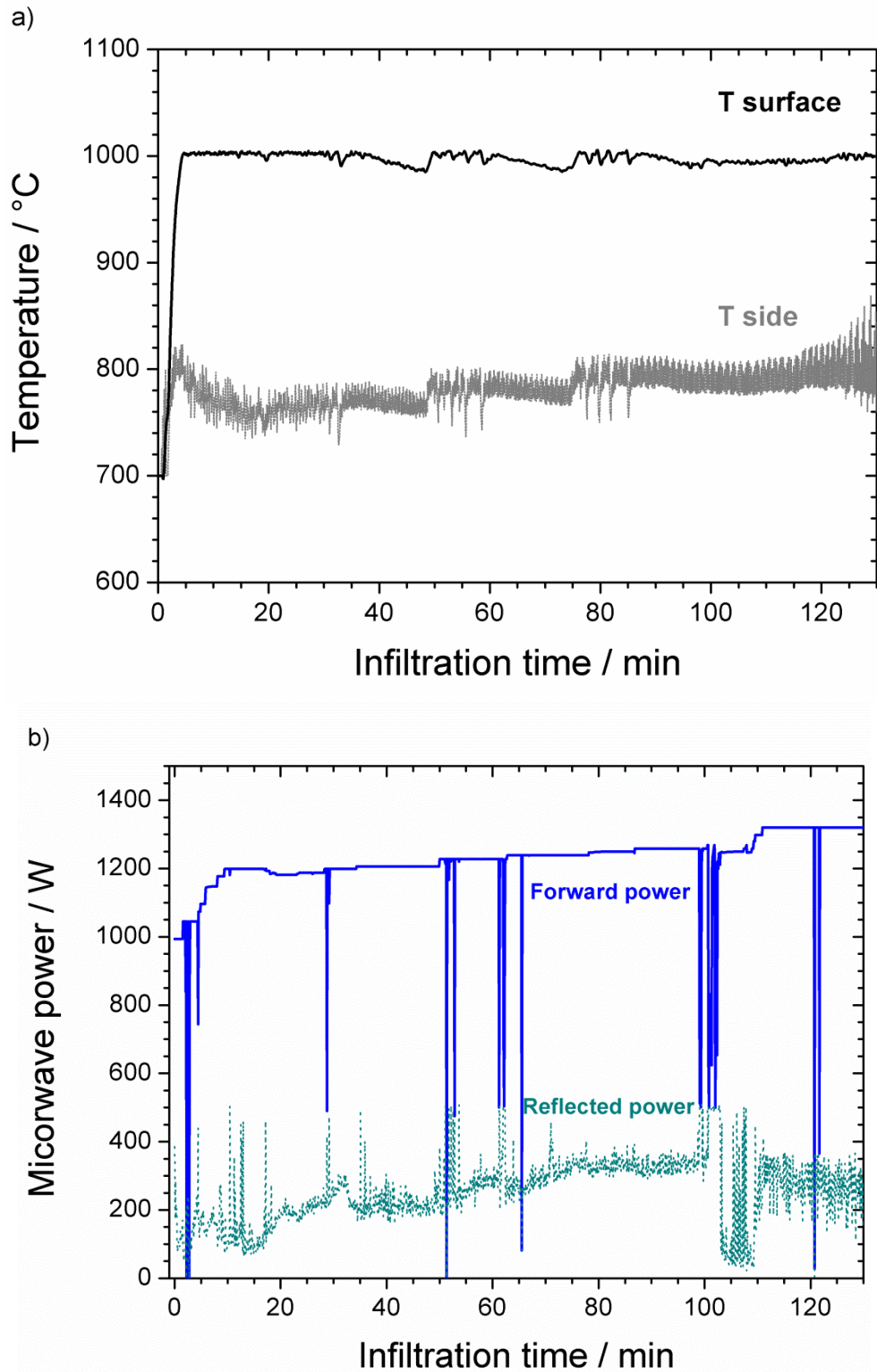


Figure 4-72. (a) Heating behaviour and (b) microwave power variation for a standard 20-layer sample during a MECVI process. The fluctuations of forward power are due to the control unit when the setpoint temperature was reached.

Figure 4-73 shows the variation of power required to maintain the setpoint temperature as a function of the infiltration intervals of 2, 4 and 8 hours. For the infiltration at 900°C (black solid squares) no significant power adjustments were required for the first 4 hours. In the following 4 hours an increase of 50 W was necessary. The power was linearly increased during the infiltration at 950°C (red solid circles); the power required after 8 hours of infiltration was nearly 25% higher than the initial value. The sample infiltrated at 1000°C (blue solid triangles) demanded a power of 1200 W, which was the same power required from the sample infiltrated at 950°C after 8 hours. Practically, no further power adjustment was required after 4 hours of infiltration.

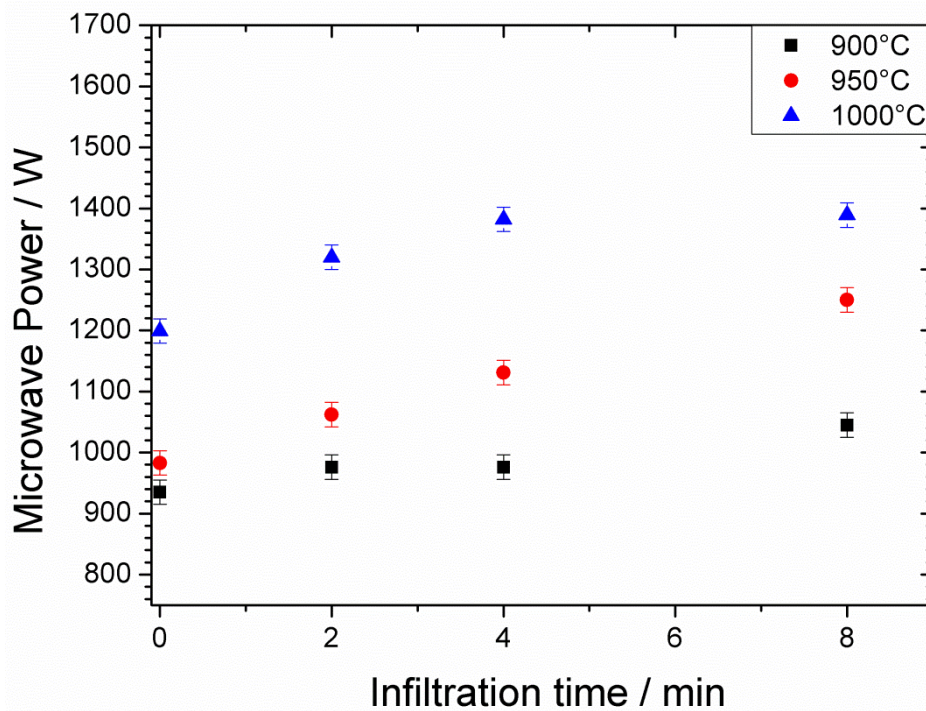


Figure 4-73. Microwave power increase as the infiltration process proceeds for 8 hours.

Figure 4-74 shows the variation in the temperature difference between the centre of the top surface side during a typical CVI run lasting of 8 hours. The average temperature difference decreased as the infiltration proceeded. In fact,  $\Delta T_{CE}$  was

280°C prior to the infiltration, remained almost unchanged after 2 hours and then reduced to 180°C after 8 hours suggesting that the radius of the hot spot increased with the processing time.

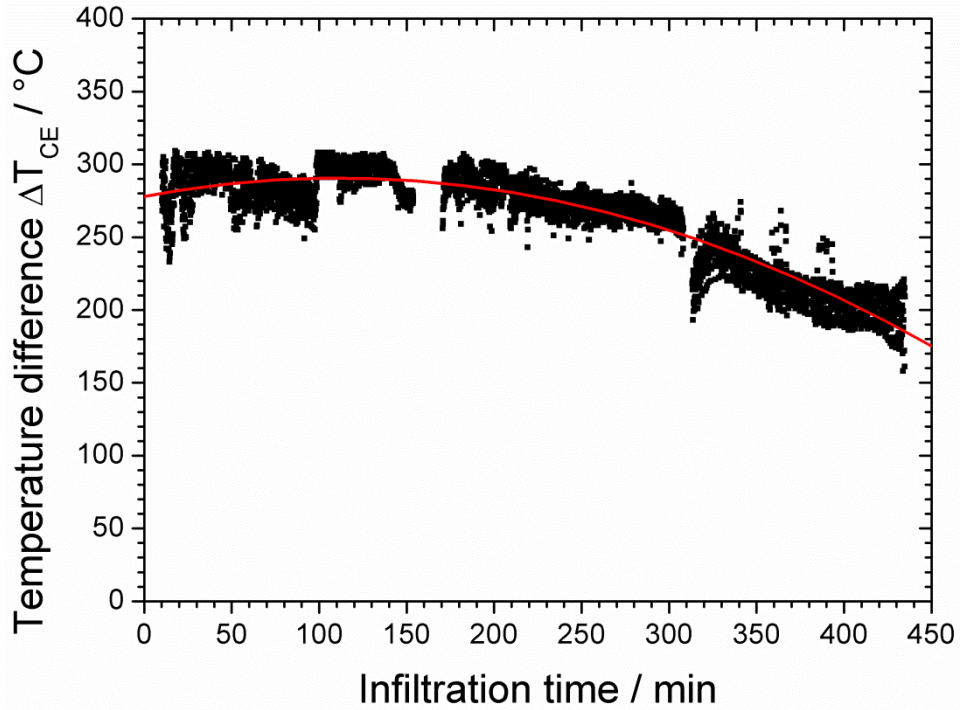


Figure 4-74. Variation of the temperature difference  $\Delta T_{CE}$  between the centre of the surface of the preform and the side surface distant 25 mm from the centre.

### 4.5.1 Permittivity effect

The properties of deposited matrix may perturb the absorption of microwave energy. For instance, the deposition of  $\beta$ -SiC on the fibres [370] can provoke a decrease in temperature as the microwave absorption is less efficient than the fibres. The penetration depth  $D_p$  is larger than the radius up to  $\sim 600^\circ\text{C}$  but then it decreases down to  $\sim 10$  mm at  $\sim 1000^\circ\text{C}$ , as shown in Figure 4-70. This means that the volumetric nature of the heating may not be retained through all the duration of the process unless  $D_p$  increases with the density (equivalently the deposition of  $\beta$ -SiC) of the preform as shown by Jaglin [156]. Although in the present work the variation of the dielectric permittivity with the densification of the

preform has not been analysed, the formation of the inside-out deposition pattern in Figure 4-59, and Figure 4-61 can influence the dielectric characteristics of the preform as the infiltration proceeds.

High values of  $\epsilon''$  for Tyranno ZMI fibres, Figure 4-67b, implies that the absorbed microwave radiation was readily dissipated in the form of heat and volumetric heating was generated. However, the preferential deposition of  $\beta$ -SiC in the hottest area, located in the centre of the preform, may have reduced the dielectric factors locally. As a consequence, more power was required to maintain the setpoint temperature, Figure 4-73. This, sequentially, resulted in the temperature increasing where the SiC deposition had not taken place extensively. Therefore, the less densified region benefits from the extra microwave power, leading to a progressive flattening of the temperature gradient, Figure 4-74. It is fundamental that the core of the preform is nearly-full infiltrated before this takes place.

Another effect influencing the microwave absorption is the stoichiometry variation [370]. In fact, matrix consisted of a silicon-rich SiC can dissipate microwave energy efficiently because silicon increases the electrical resistivity of the matrix [371]. As shown in Figure 4-25 and in Raman spectroscopy analysis in section 4.3.2.2, in all the preforms analysed in the present work silicon-rich areas have been observed, especially away from the centre of the preforms. Silicon enhances the heat dissipation in these Si-rich areas and additionally contributes to the flattening of the temperature gradient across the diameter, Figure 4-74. On the other hand, codeposition of carbon may be deleterious as, because of its elevated electrical conductivity, it can trigger arcing.

Finally, electrical resistivity is also influenced by the crystallite size of  $\beta$ -SiC [17]. It was observed that Si-C-O Nicalon fibre increased its electrical resistivity by one order of magnitude when the  $\beta$ -SiC crystallite size increased from 1.8 to 2.0 nm following annealing in inert atmosphere at 1200-1300°C. The process temperatures of the present work have been limited to ~1000°C and hence the crystallites of ZMI Tyranno may have not undergone any transformation. However, different temperatures have produced SiC deposit with different crystal size, as shown in Figure 4-40, Figure 4-42 and Figure 4-43, and, possibly, different electrical resistance.

## 5 Conclusions and future work

### 5.1 Conclusions

#### 5.1.1 Thermodynamics study

The thermodynamics of the decomposition of MTS and formation of the SiC deposit were investigated. Gas phase composition, including the carbon and silicon-bearing species, was studied and the role of oxygen in the formation of silica was investigated.

- The amount of silicon species is more abundant than carbon species and for this reason carbon formation and adsorption is believed to be the limiting step in formation of SiC from MTS decomposition in CVI processes. The lower activity of carbon species explained also the tendency of silicon formation at low temperature.
- Methane and silicon tetrachloride are the most abundant intermediate species in the gas phase, but their content decreased with increasing temperature.  $C_2H_4$ ,  $C_2H_2$  and  $SiCl_2$  formation was prompted with temperature increase and they are believed to be the actual precursor of SiC.
- Residual oxygen in the reactor determined the formation of  $SiO_2$ , which can suppress the formation of SiC.
- The transient time for the formation of silica from MTS and residual oxygen is comparable with the duration of the temperature drop experienced in the first stage of all the MECVI runs carried out in this research project.

### 5.1.2 Kinetics study

A kinetics study of the decomposition of MTS in Tyranno ZMI-based fibre preform in a MECVI process was performed.

- This study showed that the SiC deposition at 30 kPa displayed an Arrhenius behaviour in the range 850-1050°C and that the growth of the deposit was surface-limited.
- At 1000°C the matrix growth rate did not depend on the temperature, which is typical behaviour for a mass transfer regime. This behaviour is particularly accentuated at higher pressures.
- Pressure increase determined a decrease of the activation energy, from  $176 \pm 7$  at 20 kPa to  $146 \pm 17$  kJ mol<sup>-1</sup> at 50 kPa. All these values were in agreement with literature. At 70 kPa the matrix growth rate ceased to have a linear relationship with the reciprocal of the temperature.
- The mass transport of the gaseous mixture was predominantly convective in the intertow pores, whilst diffusion-driven in the intratow pores. In both cases the deposition of the matrix was rate-limiting, which is preferable in the CVI processes.

### 5.1.3 Physiochemical properties of the SiC deposit

The morphology and the chemical composition of the deposit were investigated by using electron microscopy and spectroscopic techniques such as WDS and Raman spectroscopy.

- Pressure and temperature were the influential parameters studied in the deposition of the SiC matrix
- High temperature and pressure promoted the formation of angular morphology and acicular crystals, whilst low temperatures and pressure led to the formation of smooth, fine-grained and globular morphology.
- The competitive effect of nucleation and growth determined the morphology of the deposit. Fine-grained and globular deposits were observed in the nucleation regime (low pressures and temperatures) whilst SiC grains up to 2  $\mu\text{m}$  in length were observed in the growth regime (high pressures and temperatures).
- The morphology of the deposit varied across the diameter of the preform and this is a direct consequence of the temperature profile induced by microwave heating
- The matrix, made of cubic  $\beta$ -SiC, grew anisotropically perpendicular to the fibre surface. The growth followed the crystallographic direction  $[111]$  which is the surface with the lowest energy. At higher temperatures, the grains were coarser and the formation of crystallites oriented along the  $[110]$  and  $[001]$  directions were clearly observed, in agreement with the literature.
- Silica layers were formed because of the presence of residual oxygen in the reactor. The number of layers corresponded to the number of times the CVI process was re-started. A line of nanopores was formed where the depositions on adjacent fibres met.

- In terms of chemical composition, the co-deposition of silicon was observed in all the preforms infiltrated with a maximum of 2.6 at%. In all cases, the SiC deposited near the centre line was the closest being stoichiometric.

### 5.1.4 Deposition pattern

An analysis of the spatial distribution of the deposit within the preforms was conducted and the influence of the pressures and temperatures on the deposition pattern was investigated.

An inverse temperature profile was produced at 900°C and 50 kPa. Potential improvement in terms of reaction yield and reduced total infiltration time can be done at 950°C, 50 and 70 kPa, although a more detailed analysis is needed to check if there is a lack of infiltration in the middle layer at higher pressures.

At 30 kPa, the increase of temperatures induced an extension of the infiltrated area. After 8 hours, the intratow infiltration at 1000°C extended to 20 mm in radius and also the tows of the top layer and the one facing the gas inlet were sealed by the SiC deposit. However, the inside-out densification front was not clearly observed. At very high temperatures and pressures (1000°C, 70 kPa), the CVI turned into a CVD and the side of the preform facing the gas inlet was totally sealed.

A partial infiltration of the side of the preform was observed. The micrometric gap between the powder particles at the side of the preform was filled by the SiC deposit. This suggested that the temperature of the sharp ends of the fibres was elevated enough to heat the surrounding SiC powder which became a substrate for the SiC deposition.

### 5.1.5 Dielectric permittivity

Measurements of the dielectric properties ( $\epsilon'$ ,  $\epsilon''$  and  $D_p$ ) against the temperature of the SiC fibres and commercial available SiC powders were carried out.

The dielectric loss factor of the Tyranno ZMI fibres increased exponentially with the temperature. Similar behaviour but with lower magnitude was observed for the powder with a mean particle size of 300 nm, which was used to paint the edge of the preform. SiC powders, with a particle size above 1  $\mu\text{m}$ , showed metallic behaviour above 800°C.

The penetration depth of the SiC fibres was ~50 mm at room temperature and decreased to ~15 mm at 1000°C. This implies some restrictions on the maximum dimensions of the preforms that can be densified by MECVI.

The deposition of silicon carbide affected the dielectric properties of the preform. In fact, more microwave power was necessary to keep the setpoint temperature during the 8 hour infiltration. A gradual flattening of the temperature gradient (difference of temperature between the centre of the bottom surface and the temperature at the side of the preform) was observed. Effects of the thermal conductivity and the composition of the matrix are expected to play a role in the development of the temperature profile and hence of the densification front.

## 5.2 Future Work

Future work on microwave-enhanced chemical vapour infiltration should be mainly oriented to confirm the proper condition of temperature, pressure, gas ratio and total flow rate for an efficient infiltration. From the present work, it has been

found that very high temperatures and pressures can lead to a premature sealing of the preform and that the ideal conditions of infiltration are in the range 900-950°C. However, the silicon codeposition at these temperatures suggests that infiltrations with lower gas flow ratios should be carried out and the compositions assessed by WDS, Raman spectroscopy and TEM. Gas flow rate will have presumably an effect on the efficiency but too high gas flow rates could induce the transition from surface-reaction limited regime to mass-transfer regime. Once the right conditions are achieved, full densification by MECVI of a standard preform (20 layers) should be performed to prove the effectiveness of the microwave heating in CVI processes, in particular, to assess the intertow infiltration time [200].

In terms of characterisation, Micro-computed tomography (Micro-CT) can be applied to evaluate the evolution of the densification pattern with the infiltration time [369]. Micro-CT is a non-destructive technique with a resolution of 1-5 micrometres. Quantification of the porosity and pore size distribution are also possible [372].

Preferential deposition of carbon at high temperatures and silicon at low temperature could lead to a two-phase matrix with inhomogeneous thermal and mechanical properties. Only mechanical testing, thermal conductivity and local permittivity measurements of the sample can shed the light on this effect. For mechanical characterisation, SiC fibres require interfacial coating (BN or pyrolytic carbon) to avoid strong interfacial bonding with resultant brittle fracture. The effect of this interfacial coating on the dielectric permittivity of the preform has to be evaluated. Generally, boron nitride is considered microwave-transparent and previous works have shown that the coating does not deleteriously affect the

microwave absorption [373]. Carbon may change the absorption of the electromagnetic energy [17] and affect the electrical resistivity of the composite [374, 375]. Heat transfer is governed by thermal conductivity, which should be measured to verify the effect of the densification with the deposit material on the temperature profile evolution.

To further speed up the CVI of SiC fibre preform, a multistep approach could be adopted. For instance, pre-impregnation of the preform with ceramic slurries using vacuum bagging (VB) could reduce the intertow porosity and speed up the densification process. On the other hand, VB would be an additional step in the manufacturing process and particle size and viscosity of the slurry, dielectric and thermal properties of the powders would be certainly parameters to take into account. The accessibility for the gas within the tows should not be limited by the powder and hence the right balance between amount of powder and remaining porosity would be crucial.

An additional technique to further improve the efficiency of the MECVI is the use of a pulsed-power source of microwaves [300, 376]. Microwave CVI with pulsed-power has the potential to reduce the process time without compromising density uniformity. In fact, the source power is modulated in time with a specific period and duty cycle. When the temperature of the preform decreases, the reaction rate is lower allowing the reactants to diffuse into the preform. This mitigates limitations of uniform deposition pattern due to the diffusion phenomena within the composite. The high-power part of the cycle leads to rapid reaction rates, thereby minimizing the processing time.

Microwave-heated chemical vapour infiltration presents undoubtedly some advantages as shown throughout this research work. Overall, future work should be focused on addressing the issues arising from the electromagnetic nature of the heating source.

A major concern is that not all the CMC systems can be densified by MECVI. C<sub>f</sub>/C and C<sub>f</sub>/SiC cover a considerable share of the CMC market, but they are not suitable for MECVI because of the enhanced conductivity of the carbon fibres. Reinforcements with a high aspect ratio such as fibres are in principle difficult to process because the concentration of the electromagnetic field at the ends of the fibre could trigger arcing.

Scale-up of the process and the densification of complex-shaped preforms are other notable issues. In fact, the reduced penetration depth of the microwaves at the typical temperatures of the CVI process (900-1100°C) sets a limitation on the preform size. The use of lower frequency (e.g. 915 MHz) can increase the penetration depth, but the dielectric loss could be affected. Additional limitations on the preform size are due to the reactor size and shape because of the microwave cavity dimensions. Only one preform per run can be densified with MECVI as arcing between two preforms and reciprocal interference of the local electromagnetic fields may occur. Complex-shaped preforms are unsuitable for MECVI because of a potential inhomogeneous temperature distribution. Experiments using MECVI on asymmetrical preforms with corners have not been carried out yet and the current belief is that the electric field and the temperature profile developed in a shape such as a squared panel could be unsuitable for an inside-out densification.

A spatially non-uniform density profile, as well as compositionally and microstructurally non-uniform deposits can compromise the thermal and mechanical performance of the composites. For example, silicon limits the creep resistance and carbon is deleterious for the oxidation resistance. A possible approach is the use of hybrid heating which combines the volumetric heating of microwaves with radiation heating [15, 377]. A susceptor absorbs some of the microwave power in the cavity and increases the temperature around the preform [15].

## 6 Appendix I

The effective diffusivity in a porous body is described by [212]:

$$D_{eff} = \frac{\rho_r}{\xi} \left[ \frac{1}{D_m} + \frac{1}{D_K} \right]^{-1}$$

where  $D_m$  is the molecular diffusivity and  $D_K$  is the Knudsen diffusivity.

Using the Chapman-Enskog relationship for MTS [203]  $D_m$  depends on temperature and pressure by:

$$D_m = 1.858 \times 10^{-3} \frac{1}{\Omega_D \sigma_{MTS/H_2}^2} \times \sqrt{\frac{M_{MTS} + M_{H_2}}{M_{MTS} M_{H_2}}} \frac{T^{1.5}}{P}$$

:

Where  $\sigma_{MTS/H_2}$  is the average shell diameter between  $H_2$  ( $2.827 \times 10^{-10}$  m) and MTS ( $5.114 \times 10^{-10}$  m) and  $\Omega_D$  is the integral collision for diffusion, i.e. 0.8099 [212]. The Knudsen diffusion  $D_K$  has been estimated assuming that the diffusion occurs in cylindrical pores [378].

$$D_K = \frac{d_p}{3} \sqrt{\frac{2RT}{\pi M_{MTS}}}$$

$D_K$  is independent from the pressure and it is proportional to  $T^{0.5}$ . It has a contribution only into the diffusion in small pores and hence during the intratow infiltration.

Table 18. Molecular diffusivity  $D_m$  and  $D_{eff}$  of the mixture MTS/ $H_2$  as function of pressure and temperature

$P$ / kPa	$T$ / °C	$D_m$ / cm <sup>2</sup> s <sup>-1</sup>	$D_{eff}$ / cm <sup>2</sup> s <sup>-1</sup>
-----------	----------	---	---

**Chapter 6. Appendix I**

20	900	21.50	2.21
20	950	22.88	2.28
20	1000	24.30	2.35
30	900	14.33	1.98
30	950	15.25	2.04
30	1000	16.20	2.11
50	900	8.60	1.63
50	950	9.15	1.69
50	1000	9.72	1.76
70	900	6.14	1.38
70	950	6.54	1.44
70	1000	6.94	1.50

## 7 Appendix II

The findings of this research work have been disseminated in international scientific conferences:

- Material Science and Technology 2014 Pittsburgh, USA
- ECerS 2015 Conference, Toledo, Spain
- 6<sup>th</sup> International Congress on Ceramics, Dresden, Germany
- CARAT meeting, Westinghouse Electric Company, Hopkins, SC, USA

During the PhD, a 3-month research exchange program has been carried out at Missouri University of Science and Technology under the supervision of Prof. W.E. Fahrenholtz and Prof. G. Hilmas. This work was supported by Aerospace Materials for Extreme Environments program of the Air Force Office of Scientific Research (Grant number FA9550-14-1-0385) and the JECS Trust Foundation (Contract No. 201363-01)

The research was part of the activity focused on the microstructure-properties relationship of ZrB<sub>2</sub>-based ceramic and the outcome was the journal article:

D'Angio, A., Zou, J., Binner, J., Ma, H. B., Hilmas, G. E., and Fahrenholtz, W. G., *Mechanical properties and grain orientation evolution of zirconium diboride-zirconium carbide ceramics*. Journal of the European Ceramic Society, 2018. **38**(2), 391-402.

## 8 References

1. Wachtman, J., *Mechanical properties of ceramics*. Vol. 69. 1996, New York: New York: John Wiley & Sons, Inc. 265-267.
2. Lehman, R.L., S.K. El-Rahaiby, and J.B. Wachtman, *Handbook on continuous fiber-reinforced ceramic matrix composites*. 1995, West Lafayette, Ind.: Ceramics Information Analysis Center, Center for Information and Numerical Data Analysis and Synthesis, Purdue University ; Westerville, OH : American Ceramic Society.
3. Chawla, K., *Ceramic Matrix Composites*, in *Composite Materials*. 1998, Springer New York. p. 212-251.
4. Marshall, D.B. and A.G. Evans, *Failure Mechanisms in Ceramic-Fiber/Ceramic-Matrix Composites*. *Journal of the American Ceramic Society*, 1985. **68**(5): p. 225-231.
5. Campbell, F.C., *Chapter 10 - Ceramic Matrix Composites*, in *Manufacturing Technology for Aerospace Structural Materials*, F.C. Campbell, Editor. 2006, Elsevier Science: Oxford. p. 459-493.
6. Zok, F.W., *Ceramic-matrix composites enable revolutionary gains in turbine engine efficiency*. *American Ceramic Society Bulletin*, 2016. **95**: p. 22-28.
7. Naslain, R., *Design, preparation and properties of non-oxide CMCs for application in engines and nuclear reactors: an overview*. *Composites Science and Technology*, 2004. **64**(2): p. 155-170.
8. Leuchs, M., *Chemical Vapor Infiltration Processes for Ceramic Matrix Composites: Manufacturing, Properties, Applications*. *Ceramic Matrix Composites: Fiber Reinforced Ceramics and their Applications*, 2008: p. 141-164.
9. Lackey, W.J. and T.L. Starr, *Fabrication of fiber-reinforced ceramic composites by chemical vapour infiltration: Processing, structure and properties*. *Fiber Reinforced Ceramic Composites*. 1990, Park Ridge, NJ: Noyes Publications. 49.
10. Katoh, Y., K. Ozawa, C. Shih, T. Nozawa, R.J. Shnavski, A. Hasegawa, and L.L. Snead, *Continuous SiC fiber, CVI SiC matrix composites for nuclear applications: Properties and irradiation effects*. *Journal of Nuclear Materials*, 2014. **448**(1): p. 448-476.
11. Golecki, I., *Rapid vapor-phase densification of refractory composites*. *Materials Science & Engineering R-Reports*, 1997. **20**(2): p. 37-124.
12. Lazzeri, A., *CVI Processing of Ceramic Matrix Composites*, in *Ceramics and composites processing methods*. 2012, John Wiley & Sons, Inc. p. 313-349.
13. Besmann, T.M., B.W. Sheldon, R.A. Lowden, and D.P. Stinton, *Vapor-Phase Fabrication and Properties of Continuous-Filament Ceramic Composites*. *Science*, 1991. **253**(5024): p. 1104-1109.
14. Probst, K.J., T.M. Besmann, D.P. Stinton, R.A. Lowden, T.J. Anderson, and T.L. Starr, *Recent advances in forced-flow, thermal-gradient CVI for refractory composites*. *Surface & Coatings Technology*, 1999. **120**: p. 250-258.
15. Skamsner, D.J., P.S. Day, H.M. Jennings, and D.L. Johnson. *Hybrid Microwave-Assisted Chemical Vapor Infiltration of alumina fiber composites*. in *18th Annual Conference on Composites and Advanced Ceramic Materials-B: Ceramic Engineering and Science Proceedings, Volume 15*. 2009. John Wiley & Sons.
16. Jaglin, D., J. Binner, B. Vaidyanathan, C. Prentice, B. Shatwell, and D. Grant, *Microwave Heated Chemical Vapor Infiltration: Densification Mechanism of SiCf/SiC Composites*. *Journal of the American Ceramic Society*, 2006. **89**(9): p. 2710-2717.
17. Devlin, D., R. Currier, R. Barbero, and B. Espinoza. *Chemical vapor infiltration with microwave heating*. in *Proceedings of the 17th Annual Conference on Composites and Advanced Ceramic Materials, Part 2 of 2: Ceramic Engineering and Science Proceedings, Volume 14, Issue 9/10*. 1993. Wiley Online Library.

18. Deepak and J.W. Evans, *Mathematical-Model for Chemical-Vapor Infiltration in a Microwave-Heated Preform*. Journal of the American Ceramic Society, 1993. **76**(8): p. 1924-1929.
19. Yin, Y., J.G.P. Binner, and T.E. Cross, *Microwave assisted chemical vapour infiltration for ceramic matrix composites*. Ceramics Transactions, 1997(80): p. 349-356.
20. Cioni, B. and A. Lazzeri, *Modeling and development of a microwave heated pilot plant for the production of SiC-based ceramic matrix composites*. International Journal of Chemical Reactor Engineering, 2008. **6**.
21. Day, P.S., M.S. Spatz, D.J. Skamser, H.M. Jennings, and D. Johnson, *Microwave-assisted Chemical Vapour Infiltration*. Ceram. Trans., 1993. **42**: p. 95-102.
22. Upadhya, K., J.M. Yang, and W.P. Hoffman, *Materials for ultrahigh temperature structural applications*. American Ceramic Society Bulletin, 1997. **76**(12): p. 51-56.
23. Pierson, H.O., *Handbook of Refractory Carbides & Nitrides: Properties, Characteristics, Processing and Apps*. 1996: William Andrew.
24. Opeka, M.M., I.G. Talmy, E.J. Wuchina, J.A. Zaykoski, and S.J. Causey, *Mechanical, thermal, and oxidation properties of refractory hafnium and zirconium compounds*. Journal of the European Ceramic Society, 1999. **19**(13-14): p. 2405-2414.
25. Harris, G.L., *Properties of silicon carbide*. 1995: Int.
26. Gupta, T.K., F. Lange, and J. Bechtold, *Effect of stress-induced phase transformation on the properties of polycrystalline zirconia containing metastable tetragonal phase*. Journal of Materials Science, 1978. **13**(7): p. 1464-1470.
27. Barsoum, M. and M. Barsoum, *Fundamentals of ceramics*. 2002: CRC press.
28. Fahrenholtz, W.G., E.J. Wuchina, W.E. Lee, and Y. Zhou, *Ultra-high temperature ceramics: materials for extreme environment applications*. 2014: John Wiley & Sons.
29. Kandola, B. and E. Kandare, *Composites having improved fire resistance*, in *Advances in fire retardant materials*. 2008, Elsevier. p. 398-442.
30. Dion, C., A. Dufresne, M. Jacob, and G. Perrault, *Assessment of exposure to quartz, cristobalite and silicon carbide fibres (whiskers) in a silicon carbide plant*. Annals of Occupational Hygiene, 2005. **49**(4): p. 335-343.
31. Green, D.J., *Fracture Toughness Predictions for Crack Bowing in Brittle Particulate Composites*. Journal of the American Ceramic Society, 1983. **66**(1): p. C4-C5.
32. Erdogan, F. and P.F. Joseph, *Toughening of ceramics through crack bridging by ductile particles*. Journal of the American Ceramic Society, 1989. **72**(2): p. 262-270.
33. Nemat-Nasser, S. and M. Hori, *Toughening by partial or full bridging of cracks in ceramics and fiber reinforced composites*. Mechanics of Materials, 1987. **6**(3): p. 245-269.
34. Wei, G.C. and P.F. Becher, *Improvements in Mechanical-Properties in SiC by the Addition of TiC Particles*. Journal of the American Ceramic Society, 1984. **67**(8): p. 571-574.
35. Zhang, S.C., G.E. Hilmas, and W.G. Fahrenholtz, *Mechanical properties of sintered ZrB<sub>2</sub>-SiC ceramics*. Journal of the European Ceramic Society, 2011. **31**(5): p. 893-901.
36. Watts, J., G. Hilmas, W.G. Fahrenholtz, D. Brown, and B. Clausen, *Stress measurements in ZrB<sub>2</sub>-SiC composites using Raman spectroscopy and neutron diffraction*. Journal of the European Ceramic Society, 2010. **30**(11): p. 2165-2171.
37. Zhu, S., W.G. Fahrenholtz, and G.E. Hilmas, *Influence of silicon carbide particle size on the microstructure and mechanical properties of zirconium diboride-*

- silicon carbide ceramics*. Journal of the European Ceramic Society, 2007. **27**(4): p. 2077-2083.
38. Porter, D.L. and A.H. Heuer, *Mechanisms of Toughening Partially Stabilized Zirconia (PSZ)*. Journal of the American Ceramic Society, 1977. **60**(3-4): p. 183-184.
  39. Clarke, I.C., M. Manaka, D.D. Green, P. Williams, G. Pezzotti, Y.-H. Kim, M. Ries, N. Sugano, L. Sedel, C. Delauney, B.B. Nissan, T. Donaldson, and G.A. Gustafson, *Current Status of Zirconia Used in Total Hip Implants*. Vol. 85. 2003. 73-84.
  40. Chiang, Y.C., *On fiber debonding and matrix cracking in fiber-reinforced ceramics*. Composites Science and Technology, 2001. **61**(12): p. 1743-1756.
  41. Homeny, J., W.L. Vaughn, and M.K. Ferber, *Silicon-Carbide Whisker Alumina Matrix Composites - Effect of Whisker Surface-Treatment on Fracture-Toughness*. Journal of the American Ceramic Society, 1990. **73**(2): p. 394-402.
  42. Kerans, R.J., R.S. Hay, T.A. Parthasarathy, and M.K. Cinibulk, *Interface Design for Oxidation-Resistant Ceramic Composites*. Journal of the American Ceramic Society, 2002. **85**(11): p. 2599-2632.
  43. Tressler, R.E., *Recent developments in fibers and interphases for high temperature ceramic matrix composites*. Composites Part A: Applied Science and Manufacturing, 1999. **30**(4): p. 429-437.
  44. Yang, B., X. Zhou, and Y. Chai, *Mechanical properties of SiCf/SiC composites with PyC and the BN interface*. Ceramics International, 2015. **41**(5): p. 7185-7190.
  45. Chai, Y., H. Zhang, and X. Zhou, *Mechanical properties of SiCf/SiC composites with alternating PyC/BN multilayer interfaces*. Advances in Applied Ceramics, 2017. **116**(7): p. 392-399.
  46. DiCarlo, J.A., H.-M. Yun, G.N. Morscher, and R.T. Bhatt, *SiC/SiC Composites for 1200°C and Above*, O. NASA Glenn Research Center; Cleveland, United States, Report NASA/TM-2004-213048, 2004.
  47. Dong, S., Y. Katoh, and A. Kohyama, *Processing optimization and mechanical evaluation of hot pressed 2D Tyranno-SA/SiC composites*. Journal of the European Ceramic Society, 2003. **23**(8): p. 1223-1231.
  48. Katoh, Y., L.L. Snead, T. Nozawa, S. Kondo, and J.T. Busby, *Thermophysical and mechanical properties of near-stoichiometric fiber CVI SiC/SiC composites after neutron irradiation at elevated temperatures*. Journal of Nuclear Materials, 2010. **403**(1): p. 48-61.
  49. Xu, Y., L. Cheng, L. Zhang, X. Yin, and H. Yin, *High performance 3D textile Hi-Nicalon SiC/SiC composites by chemical vapor infiltration*. Ceramics International, 2001. **27**(5): p. 565-570.
  50. Yang, W., T. Noda, H. Araki, J. Yu, and A. Kohyama, *Mechanical properties of several advanced Tyranno-SA fiber-reinforced CVI-SiC matrix composites*. Materials Science and Engineering: A, 2003. **345**(1): p. 28-35.
  51. Yu, H., X. Zhou, W. Zhang, H. Peng, C. Zhang, and Z. Huang, *Mechanical properties of 3D KD-I SiCf/SiC composites with engineered fibre-matrix interfaces*. Composites Science and Technology, 2011. **71**(5): p. 699-704.
  52. Buckley, J.D., *Carbon-Carbon, an Overview*. American Ceramic Society Bulletin, 1988. **67**(2): p. 364-368.
  53. Riccardi, B., L. Giancarli, A. Hasegawa, Y. Katoh, A. Kohyama, R.H. Jones, and L.L. Snead, *Issues and advances in SiCf/SiC composites development for fusion reactors*. Journal of Nuclear Materials, 2004. **329**: p. 56-65.
  54. Miriyala, N., J. Kimmel, J. Price, H. Eaton, G. Linsey, and S. E. *The evaluation of CFCC Liners After Field Testing in a Gas Turbine – III*. in *ASME TURBO EXPO 2002*. 2002. Amsterdam, The Netherlands.
  55. Gardiner, G., *Aeroengine composites, Part 1: the CMC invasion*. Composites World, 2015. **31**.

56. Levy, D. *Ceramic matrix composites take flight in LEAP jet engine*. 2017; Available from: <https://www.ornl.gov/news/ceramic-matrix-composites-take-flight-leap-jet-engine>.
57. *Ceramic Matrix Composites Market by Matrix Type (Oxide/Oxide, SiC/SiC, Carbon/Carbon), Application (Aerospace & Defense, Automotive, Energy & Power, Electrical & Electronics), and Region - Global Forecast to 2026*. Markets and Markets, Press release; Available from: [www.marketsandmarkets.com/Market-Reports/ceramic-matrix-composites-market-60146548.html](http://www.marketsandmarkets.com/Market-Reports/ceramic-matrix-composites-market-60146548.html).
58. Krenkel, W., *Carbon Fibre Reinforced Silicon Carbide Composites (C/SiC, C/C-SiC)*, in *Handbook of Ceramic Composites*, N. Bansal, Editor. 2005, Springer US. p. 117-148.
59. Savage, G., *Carbon-carbon composites*. 1993: Chapman & Hall.
60. Lamouroux, F., S. Bertrand, R. Pailler, R. Naslain, and M. Cataldi, *Oxidation-resistant carbon-fiber-reinforced ceramic-matrix composites*. *Composites Science and Technology*, 1999. **59**(7): p. 1073-1085.
61. Gulbransen, E.A. and S.A. Jansson, *The high-temperature oxidation, reduction, and volatilization reactions of silicon and silicon carbide*. *Oxidation of metals*, 1972. **4**(3): p. 181-201.
62. Mühlratzer, A. and M. Leuchs, *Applications of Non-Oxide CMCs*. *High temperature ceramic matrix composites*, 2001: p. 288-298.
63. Mühlratzer, A. and H. Pfeiffer. *CMC Body Flaps for the X-38 Experimental Space Vehicle*. in *26th Annual Conference on Composites, Advanced Ceramics, Materials, and Structures: A: Ceramic Engineering and Science Proceedings, Volume 23, Issue 3*. 2002. Wiley Online Library.
64. Meschter, P.J., E.J. Opila, and N.S. Jacobson, *Water vapor-mediated volatilization of high-temperature materials*. *Annual Review of Materials Research*, 2013. **43**: p. 559-588.
65. DiCarlo, J.A., *Advances in SiC/SiC Composites for Aero-Propulsion*, in *Ceramic Matrix Composites*. 2014, John Wiley & Sons, Inc. p. 217-235.
66. Berdoyes I., T.J. *Thermostructural composite materials: from space to advanced fission applications*. in *European Congress on Advanced Materials and Processes EUROMAT*. 2005. Prague, Czech Republic.
67. Lamicq, P.J., G. Bernhart, M. Dauchier, and J. Mace, *SiC/SiC composite ceramics*. *American Ceramic Society Bulletin*, 1986. **65**(2): p. 336-338.
68. Jamet, J. and P. Lamicq. *Composite thermostructures: an overview of the French experience*. in *High Temperature Ceramic Matrix Composites. Proc. 6th European Conf. on Composite Materials. Bordeaux*. 1993.
69. *The Leap Engine*. CFM International; Available from: <https://www.cfmaeroengines.com/engines/leap/>.
70. Kellner, T. *Space Age Ceramics Are Aviation's New Cup Of Tea*. GE Reports 2016; Available from: <https://www.ge.com/reports/space-age-cmcs-aviations-new-cup-of-tea/>.
71. European Commission. *Reducing emissions from transport*. EU Action 2017; Available from: [http://ec.europa.eu/clima/policies/transport\\_en](http://ec.europa.eu/clima/policies/transport_en).
72. Ramdane, C.B., A. Julian-Jankowiak, R. Valle, Y. Renollet, M. Parlier, E. Martin, and P. Diss, *Microstructure and mechanical behaviour of a Nextel™ 610/alumina weak matrix composite subjected to tensile and compressive loadings*. *Journal of the European Ceramic Society*, 2017. **37**(8): p. 2919-2932.
73. Flores, O., R.K. Bordia, D. Nestler, W. Krenkel, and G. Motz, *Ceramic Fibers Based on SiC and SiCN Systems: Current Research, Development, and Commercial Status*. *Advanced Engineering Materials*, 2014. **16**(6): p. 621-636.
74. Wilson, D.M., *Statistical tensile strength of Nextel(TM) 610 and Nextel(TM) 720 fibres*. *Journal of Materials Science*, 1997. **32**(10): p. 2535-2542.
75. *COI Ceramics Inc.*; Available from: <http://www.coiceramics.com/>.

76. *Axiom Materials Inc.*; Available from: <http://www.axiommaterials.com/>.
77. Weimer, A.W., *Carbide, Nitride and Boride Materials Synthesis and Processing*. 1997: Chapman & Hall.
78. Tairov, Y.M. and V. Tsvetkov, *Investigation of growth processes of ingots of silicon carbide single crystals*. *Journal of Crystal Growth*, 1978. **43**(2): p. 209-212.
79. Byrappa, K. and T. Ohachi, *Crystal Growth Technology*. 2003: Springer.
80. Dhanaraj, G., K. Byrappa, V. Prasad, and M. Dudley, *Springer handbook of crystal growth*. 2010: Springer Science & Business Media.
81. Laine, R.M. and F. Babonneau, *Preceramic polymer routes to silicon carbide*. *Chemistry of Materials*, 1993. **5**(3): p. 260-279.
82. Cheung, R., *Silicon carbide microelectromechanical systems for harsh environments*. 2006: World Scientific.
83. Yajima, S., Y. Hasegawa, K. Okamura, and T. Matsuzawa, *Development of High-Tensile Strength Silicon-Carbide Fiber Using an Organosilicon Polymer Precursor*. *Nature*, 1978. **273**(5663): p. 525-527.
84. Caputo, A.J. and W.J. Lackey, *Continued Development of the Fabrication of Ceramic Fiber-Reinforced Ceramic Composites*. *American Ceramic Society Bulletin*, 1984. **63**(12): p. 1477-1477.
85. Bunsell, A.R. and A. Piant, *A review of the development of three generations of small diameter silicon carbide fibres*. *Journal of Materials Science*, 2006. **41**(3): p. 823-839.
86. DiCarlo, J. and H.-M. Yun, *Non-oxide (Silicon Carbide) Fibers*, in *Handbook of Ceramic Composites*, N. Bansal, Editor. 2005, Springer US. p. 33-52.
87. Flores, O., T. Schmalz, W. Krenkel, L. Heymann, and G. Motz, *Selective cross-linking of oligosilazanes to tailored meltable polysilazanes for the processing of ceramic SiCN fibres*. *Journal of Materials Chemistry A*, 2013. **1**(48): p. 15406-15415.
88. Schawaller, D., B. Clauß, and M.R. Buchmeiser, *Ceramic filament fibers—A review*. *Macromolecular Materials and Engineering*, 2012. **297**(6): p. 502-522.
89. Green, D.J., *An introduction to the mechanical properties of ceramics*. 1998: Cambridge University Press.
90. Hynes, A. and R. Doremus, *Theories of creep in ceramics*. *Critical Reviews in Solid State and Material Sciences*, 1996. **21**(2): p. 129-187.
91. DiCarlo, J.A. and H.-M. Yun, *Non-oxide (silicon carbide) fibers*, in *Handbook of ceramic composites*. 2005, Springer. p. 33-52.
92. Ionescu, E., C. Balan, H.J. Kleebe, M.M. Müller, O. Guillon, D. Schliephake, M. Heilmaier, and R. Riedel, *High-Temperature Creep Behavior of SiOC Glass-Ceramics: Influence of Network Carbon Versus Segregated Carbon*. *Journal of the American Ceramic Society*, 2014. **97**(12): p. 3935-3942.
93. Ishikawa, T., Y. Kohtoku, K. Kumagawa, T. Yamamura, and T. Nagasawa, *High-strength alkali-resistant sintered SiC fibre stable to 2,200 C*. *Nature*, 1998. **391**(6669): p. 773-775.
94. Le Coustumer, P., M. Monthieux, and A. Oberlin, *Understanding Nicalon® fibre*. *Journal of the European Ceramic Society*, 1993. **11**(2): p. 95-103.
95. Ning, X., P. Pirouz, K. Lagerlof, and J. DiCarlo, *The structure of carbon in chemically vapor deposited SiC monofilaments*. *Journal of Materials Research*, 1990. **5**(12): p. 2865-2876.
96. *TISICS fibres*. TISICS Ltd; Available from: [www.tisics.co.uk](http://www.tisics.co.uk).
97. Leucht, R. and H.J. Dudek, *Properties of SiC-fibre reinforced titanium alloys processed by fibre coating and hot isostatic pressing*. *Materials Science and Engineering: A*, 1994. **188**(1): p. 201-210.
98. *Specialty Materials Inc.*; Available from: <http://www.specmaterials.com>
99. Chollon, G., R. Naslain, C. Prentice, R. Shatwell, and P. May, *High temperature properties of SiC and diamond CVD-monofilaments*. *Journal of the European Ceramic Society*, 2005. **25**(11): p. 1929-1942.

100. DiCarlo, J. and H. Yun. *Factors controlling stress-rupture of fiber-reinforced ceramic composites*. in *Proceedings of ICCM-12 Congress*. 1999.
101. Kumagawa, K., H. Yamaoka, M. Shibuya, and T. Yamamura, *Fabrication and Mechanical Properties of New Improved Si-M-C(O) Tyranno Fiber*, in *22nd Annual Conference on Composites, Advanced Ceramics, Materials, and Structures: A: Ceramic Engineering and Science Proceedings*. 2008, John Wiley & Sons, Inc. p. 65-72.
102. Ichikawa, H., K. Okamura, and T. Sequchi, Oxygen-free ceramic fibers from organosilicon precursors and e-beam curing, Report 1995.
103. Sha, J., T. Hinoki, and A. Kohyama, *Thermal and mechanical stabilities of Hi-Nicalon SiC fiber under annealing and creep in various oxygen partial pressures*. *Corrosion Science*, 2008. **50**(11): p. 3132-3138.
104. Berger, M., N. Hochet, and A. Bunsell, *Microstructure and thermo-mechanical stability of a low-oxygen Nicalon fibre*. *Journal of microscopy*, 1995. **177**(3): p. 230-241.
105. Sha, J., T. Hinoki, and A. Kohyama, *Microstructure and mechanical properties of Hi-Nicalon™ Type S fibers annealed and crept in various oxygen partial pressures*. *Materials Characterization*, 2009. **60**(8): p. 796-802.
106. Lipowitz, J., J. Rabe, A. Zangvil, and Y. Xu. *Structure and Properties of Sylramic™ Silicon Carbide Fiber—A Polycrystalline, Stoichiometric  $\beta$ -SiC Composition*. in *Proceedings of the 21st Annual Conference on Composites, Advanced Ceramics, Materials, and Structures: A: Ceramic Engineering and Science Proceedings, Volume 18, Issue 3*. 1997. Wiley Online Library.
107. Porte, L. and A. Sartre, *Evidence for a Silicon Oxycarbide Phase in the Nicalon Silicon-Carbide Fiber*. *Journal of Materials Science*, 1989. **24**(1): p. 271-275.
108. Dong, S.M., G. Chollon, C. Labrugère, M. Lahaye, A. Guette, J.L. Bruneel, M. Couzi, R. Naslain, and D.L. Jiang, *Characterization of nearly stoichiometric SiC ceramic fibres*. *Journal of Materials Science*. **36**(10): p. 2371-2381.
109. Yajima, S., K. Okamura, T. Matsuzawa, Y. Hasegawa, and T. Shishido, *Anomalous characteristics of the microcrystalline state of SiC fibres*. *Nature*, 1979. **279**(5715): p. 706-707.
110. Takeda, M., Y. Imai, H. Ichikawa, T. Ishikawa, T. Seguchi, and K. Okamura. *Properties of the low oxygen content SiC fiber on high temperature heat treatment*. in *Proceedings of the 15th Annual Conference on Composites and Advanced Ceramic Materials, Part 1 of 2: Ceramic Engineering and Science Proceedings, Volume 12, Issue 7/8*. 1991. Wiley Online Library.
111. Yamamura, T., T. Ishikawa, M. Shibuya, T. Hisayuki, and K. Okamura, *Development of a new continuous Si-Ti-CO fibre using an organometallic polymer precursor*. *Journal of Materials Science*, 1988. **23**(7): p. 2589-2594.
112. Yamaoka, H., T. Ishikawa, and K. Kumagawa, *Excellent heat resistance of Si-Zr-CO fibre*. *Journal of Materials Science*, 1999. **34**(6): p. 1333-1339.
113. Prochazka, S. and R.M. Scanlan, *Effect of boron and carbon on sintering of SiC*. *Journal of the American Ceramic Society*, 1975. **58**(1-2): p. 72-72.
114. Deleeuw, D.C., J. Lipowitz, and P.P.Y. Lu, Preparation of substantially crystalline silicon carbide fibers from polycarbosilane, 1991,
115. Freiman, S. and R.D. Cook, *Global Roadmap for Ceramic and Glass Technology*. 2007: John Wiley & Sons.
116. Dever, J.A., M.V. Nathal, and J.A. DiCarlo, *Research on high-temperature aerospace materials at NASA glenn research center*. *Journal of Aerospace Engineering*, 2013. **26**(2): p. 500-514.
117. Yun, H., D. Wheeler, Y. Chen, and J. DiCarlo. *Thermo-mechanical properties of super sylramic SiC fibers*. in *Mechanical Properties and Performance of Engineering Ceramics and Composites: A Collection of Papers Presented at the 29th International Conference on Advanced Ceramics and Composites, Jan 23-*

- 28, 2005, *Cocoa Beach, FL, Ceramic Engineering and Science Proceedings, Vol 26*. 2009. John Wiley & Sons.
118. Birot, M., J.-P. Pillot, and J. Dunogues, *Comprehensive chemistry of polycarbosilanes, polysilazanes, and polycarbosilazanes as precursors of ceramics*. Chemical reviews, 1995. **95**(5): p. 1443-1477.
119. Mocaer, D., R. Pailler, R. Naslain, C. Richard, J. Pillot, J. Dunogues, C. Gerardin, and F. Taulelle, *Si-CN ceramics with a high microstructural stability elaborated from the pyrolysis of new polycarbosilazane precursors*. Journal of Materials Science, 1993. **28**(10): p. 2615-2631.
120. Ziegler, G., H.-J. Kleebe, G. Motz, H. Müller, S. Traßl, and W. Weibelzahl, *Synthesis, microstructure and properties of SiCN ceramics prepared from tailored polymers*. Materials chemistry and physics, 1999. **61**(1): p. 55-63.
121. Delverdier, O., M. Monthieux, D. Mocaer, and R. Pailler, *Thermal behavior of polymer-derived ceramics. IV. Si · C · N · O fibers from an oxygen-cured polycarbosilazane*. Journal of the European Ceramic Society, 1994. **14**(4): p. 313-325.
122. *MATECH, Military Advanced Technology*. Available from: <https://www.matech.net/>.
123. Bernard, S., M. Weinmann, P. Gerstel, P. Miele, and F. Aldinger, *Boron-modified polysilazane as a novel single-source precursor for SiBCN ceramic fibers: synthesis, melt-spinning, curing and ceramic conversion*. Journal of Materials Chemistry, 2005. **15**(2): p. 289-299.
124. Baldus, H.-P., G. Passing, H. Scholz, D. Sporn, M. Jansen, and J. Göring. *Properties of amorphous SiBNC-ceramic fibres*. in *Key Engineering Materials*. 1996. Trans Tech Publ.
125. Lasday, S.B., *Production of ceramic matrix composites by CVI and DMO for industrial heating industry*. Industrial Heating, 1993. **60**(4): p. 31-35.
126. Newsome, G., L.L. Snead, T. Hinoki, Y. Katoh, and D. Peters, *Evaluation of neutron irradiated silicon carbide and silicon carbide composites*. Journal of Nuclear Materials, 2007. **371**(1): p. 76-89.
127. Hasegawa, A., A. Kohyama, R. Jones, L. Snead, B. Riccardi, and P. Fenici, *Critical issues and current status of SiC/SiC composites for fusion*. Journal of Nuclear Materials, 2000. **283**: p. 128-137.
128. Iveković, A., S. Novak, G. Dražić, D. Blagoeva, and S.G. de Vicente, *Current status and prospects of SiC f/SiC for fusion structural applications*. Journal of the European Ceramic Society, 2013. **33**(10): p. 1577-1589.
129. Blagoeva, D., J. Hegeman, M. Jong, M. Heijna, S.G. de Vicente, T. Bakker, P. ten Pierick, and H. Nolles, *Characterisation of 2D and 3D Tyranno SA 3 CVI SiC f/SiC composites*. Materials Science and Engineering: A, 2015. **638**: p. 305-313.
130. *MSC Software*. Available from: <http://www.mscsoftware.com/>.
131. *Fibre Glast Development Corporation*. Available from: <http://www.fibreglast.com>.
132. Mouritz, A.P., *Review of applications for advanced three-dimensional fibre textile composites*. 1999.
133. *Fiber Materials Inc.*; Available from: <http://www.fibermaterialsinc.com>.
134. Evans, A.G., *Perspective on the development of high-toughness ceramics*. Journal of the American Ceramic Society, 1990. **73**(2): p. 187-206.
135. Naslain, R., O. Dugne, A. Guette, J. Sevely, C.R. Brosse, J.P. Rocher, and J. Cotteret, *Boron Nitride Interphase in Ceramic-Matrix Composites*. Journal of the American Ceramic Society, 1991. **74**(10): p. 2482-2488.
136. Rebillat, F., J. Lamon, and A. Guette, *The concept of a strong interface applied to SiC/SiC composites with a BN interphase*. Acta Materialia, 2000. **48**(18): p. 4609-4618.
137. Coons, T.P., J.W. Reutenauer, B. Flandermeyer, M.A. Kmetz, E. Prevost, and S.L. Suib, *An investigation into a multilayered BN/Si<sub>3</sub>N<sub>4</sub>/BN interfacial coating*. Journal of Materials Science, 2013. **48**(18): p. 6194-6202.

138. Chawla, K., Z. Xu, J.-S. Ha, M. Schmücker, and H. Schneider, *Effect of BN coating on the strength of a mullite type fiber*. Applied Composite Materials, 1997. **4**(5): p. 263-272.
139. Yano, T., K. Budiyo, K. Yoshida, and T. Iseki, *Fabrication of silicon carbide fiber-reinforced silicon carbide composite by hot-pressing*. Fusion Engineering and Design, 1998. **41**: p. 157-163.
140. Riccitiello, S.R., W.L. Love, and W.C. Pitts, *A Ceramic-Matrix Composite Thermal Protection System for Hypersonic Vehicles*. Sampe Quarterly-Society for the Advancement of Material and Process Engineering, 1993. **24**(4): p. 10-17.
141. Naslain, R., *Materials for aeronautic craft: towards more and more structural and thermostructural composites*. Actualite Chimique, 1999(11): p. 72-75.
142. Kaya, H., *The application of ceramic-matrix composites to the automotive ceramic gas turbine*. Composites Science and Technology, 1999. **59**(6): p. 861-872.
143. Izumi, T. and H. Kaya, *Ceramic matrix composites application in automotive gas turbines*. Journal of Engineering for Gas Turbines and Power-Transactions of the Asme, 1997. **119**(4): p. 790-798.
144. Brewer, D., *HSR/EPM combustor materials development program*. Materials Science and Engineering a-Structural Materials Properties Microstructure and Processing, 1999. **261**(1-2): p. 284-291.
145. Campbell Jr, F.C., *Manufacturing technology for aerospace structural materials*. 2011: Elsevier.
146. Dong, S., Y. Katoh, and A. Kohyama, *Preparation of SiC/SiC Composites by Hot Pressing, Using Tyranno-SA Fiber as Reinforcement*. Journal of the American Ceramic Society, 2003. **86**(1): p. 26-32.
147. Sciti, D., L. Pienti, D.D. Fabbriche, S. Guicciardi, and L. Silvestroni, *Combined effect of SiC chopped fibers and SiC whiskers on the toughening of ZrB<sub>2</sub>*. Ceramics International, 2014. **40**(3): p. 4819-4826.
148. Tiegs, T.N. and P.F. Becher, *SiC Whisker Reinforced Alumina*. American Ceramic Society Bulletin, 1984. **63**(8): p. 1013-1013.
149. Yonathan, P., J. Lee, H. Kim, and D. Yoon, *Properties of SiCf/SiC composites fabricated by slurry infiltration and hot pressing*. Materials Science and Technology, 2011. **27**(1): p. 257-263.
150. Nannetti, C.A., A. Ortona, D.A. Pinto, and B. Riccardi, *Manufacturing SiC fiber-reinforced SiC matrix composites by improved CVI/slurry infiltration/polymer impregnation and pyrolysis*. Journal of the American Ceramic Society, 2004. **87**(7): p. 1205-1209.
151. Shimoda, K., J. Park, T. Hinoki, and A. Kohyama, *Microstructural optimization of high-temperature SiC/SiC composites by NITE process*. Journal of Nuclear Materials, 2009. **386**: p. 634-638.
152. Boccaccini, A.R., I. MacLaren, M.H. Lewis, and C.B. Ponton, *Electrophoretic deposition infiltration of 2-D woven SiC fibre mats with mixed sols of mullite composition*. Journal of the European Ceramic Society, 1997. **17**(13): p. 1545-1550.
153. Raju, K., H.-W. Yu, J.-Y. Park, and D.-H. Yoon, *Fabrication of SiC f/SiC composites by alternating current electrophoretic deposition (AC-EPD) and hot pressing*. Journal of the European Ceramic Society, 2015. **35**(2): p. 503-511.
154. Timms, L., W. Westby, C. Prentice, D. Jaglin, R. Shatwell, and J. Binner, *Reducing chemical vapour infiltration time for ceramic matrix composites*. Journal of microscopy, 2001. **201**(2): p. 316-323.
155. Binner, J., B. Vaidyanathan, D. Jaglin, and S. Needham, *Use of Electrophoretic Impregnation and Vacuum Bagging to Impregnate SiC Powder into SiC Fiber Preforms*. International Journal of Applied Ceramic Technology, 2015. **12**(1): p. 212-222.

156. Jaglin, D., *Densification of SiC<sub>f</sub>/SiC composites via microwave enhanced chemical vapour infiltration*. 2002, University of Nottingham.
157. Ortona, A., T. Fend, H.-W. Yu, K. Raju, and D.-H. Yoon, *Fabrication of cylindrical SiC<sub>f</sub>/Si/SiC-based composite by electrophoretic deposition and liquid silicon infiltration*. *Journal of the European Ceramic Society*, 2014. **34**(5): p. 1131-1138.
158. Krenkel, W. *Cost effective processing of CMC composites by melt infiltration (LSI-process)*. in *Ceramic Engineering and Science Proceedings*. 2009.
159. Shin, D.-W., S.S. Park, Y.-H. Choa, and K. Niihara, *Silicon/Silicon Carbide Composites Fabricated by Infiltration of a Silicon Melt into Charcoal*. *Journal of the American Ceramic Society*, 1999. **82**(11): p. 3251-3253.
160. Gern, F.H. and R. Kochendorfer, *Liquid silicon infiltration: Description of infiltration dynamics and silicon carbide formation*. *Composites Part a-Applied Science and Manufacturing*, 1997. **28**(4): p. 355-364.
161. Margiotta, J.C., D. Zhang, D.C. Nagle, and C.E. Feeser, *Formation of dense silicon carbide by liquid silicon infiltration of carbon with engineered structure*. *Journal of Materials Research*, 2008. **23**(05): p. 1237-1248.
162. Hillig, W.B., *Making Ceramic Composites by Melt Infiltration*. *American Ceramic Society Bulletin*, 1994. **73**(4): p. 56-62.
163. Lau, S.-K., S.J. Calandra, and R.W. Ohnsorg, *Process for making silicon carbide reinforced silicon carbide composite*. 1998, Google Patents.
164. Brennan, J.J., *Interfacial characterization of a slurry-cast melt-infiltrated SiC/SiC ceramic-matrix composite*. *Acta Materialia*, 2000. **48**(18-19): p. 4619-4628.
165. Corman, G. and K. Luthra, *Silicon melt infiltrated ceramic composites (HiPerComp™)*, in *Handbook of ceramic composites*. 2005, Springer. p. 99-115.
166. Kopeliovich, D. *Fabrication of Ceramic Matrix Composites by Chemical Vapor Infiltration (CVI)*. Available from: <http://www.substech.com>.
167. Berbon, M.Z., D.R. Dietrich, D.B. Marshall, and D.P.H. Hasselman, *Transverse thermal conductivity of thin C/SiC composites fabricated by slurry infiltration and pyrolysis*. *Journal of the American Ceramic Society*, 2001. **84**(10): p. 2229-2234.
168. Ortona, A., A. Donato, G. Filacchioni, U. De Angelis, A. La Barbera, C.A. Nannetti, B. Riccardi, and J. Yeatman, *SiC-SiC<sub>f</sub>CMC manufacturing by hybrid CVI-PIP techniques: process optimisation*. *Fusion Engineering and Design*, 2000. **51-52**: p. 159-163.
169. Kim, Y.W., J.S. Song, S.W. Park, and J.G. Lee, *Nicalon-Fiber-Reinforced Silicon-Carbide Composites Via Polymer-Solution Infiltration and Chemical-Vapor Infiltration*. *Journal of Materials Science*, 1993. **28**(14): p. 3866-3868.
170. Dong, S.M., Y. Katoh, A. Kohyama, S.T. Schwab, and L.L. Snead, *Microstructural evolution and mechanical performances of SiC/SiC composites by polymer impregnation/microwave pyrolysis (PIMP) process*. *Ceramics International*, 2002. **28**(8): p. 899-905.
171. Takeda, M., Y. Kagawa, S. Mitsuno, Y. Imai, and H. Ichikawa, *Strength of a Hi-Nicalon™/Silicon-Carbide-Matrix Composite Fabricated by the Multiple Polymer Infiltration-Pyrolysis Process*. *Journal of the American Ceramic Society*, 1999. **82**(6): p. 1579-1581.
172. Interrante, L.V., C. Whitmarsh, W. Sherwood, H.-J. Wu, R. Lewis, and G. Maciel. *High yield polycarbosilane precursors to stoichiometric SiC. Synthesis, pyrolysis and application*. in *MRS Proceedings*. 1994. Cambridge Univ Press.
173. Kotani, M., Y. Katoh, A. Kohyama, and M. Narisawa, *Fabrication and oxidation-resistance property of allylhydridopolycarbosilane-derived SiC/SiC composites*. *Journal of Ceramic Society Japan*, 2003. **111**(5): p. 300-307.
174. Greil, P., *Polymer derived engineering ceramics*. *Advanced Engineering Materials*, 2000. **2**(6): p. 339-348.
175. Zhao, S., X. Zhou, J. Yu, and P. Mummery, *Effect of heat treatment on microstructure and mechanical properties of PIP-SiC/SiC composites*. *Materials Science and Engineering: A*, 2013. **559**: p. 808-811.

176. Riccitiello, S. and M.K. Marshall, *3-D Ceramic-Matrix Composite Development*. Journal of Advanced Materials, 1994. **25**(2): p. 22-28.
177. Takeda, M., Y. Imai, H. Ichikawa, Y. Kagawa, H. Iba, and H. Kakisawa, *Some Mechanical Properties of SiC(Hinicalon™) Fiber-Reinforced Sic Matrix Nicaloceram™ Composites*, in *Proceedings of the 21st Annual Conference on Composites, Advanced Ceramics, Materials, and Structures—A: Ceramic Engineering and Science Proceedings*. 2008, John Wiley & Sons, Inc. p. 779-784.
178. Somiya, S., *Handbook of Advanced Ceramics: Materials, Applications, Processing, and Properties*. 2013: Academic Press.
179. Gonon, M.F. and S. Hampshire, *Comparison of two processes for manufacturing ceramic matrix composites from organometallic precursors*. Journal of the European Ceramic Society, 1999. **19**(3): p. 285-291.
180. Naslain, R., H. Hannache, L. Heraud, F. Christin, J.Y. Rossignol, and R. Colmet, *Advanced Ceramic-Ceramic Composite-Materials from the CVI Process*. American Ceramic Society Bulletin, 1983. **62**(11).
181. Gupte, S.M. and J.A. Tsamopoulos, *An Effective Medium Approach for Modeling Chemical Vapor Infiltration of Porous Ceramic Materials*. Journal of the Electrochemical Society, 1990. **137**(5): p. 1626-1638.
182. Naslain, R., F. Langlais, R. Paillet, and G. Vignoles, *Processing of SiC/SiC fibrous composites according to CVI-techniques*. Advanced Sic/Sic Ceramic Composites: Developments and Applications in Energy Systems, 2002. **144**: p. 19-37.
183. Naslain, R., *2-Dimensional SiC/SiC Composites Processed According to the Isobaric Isothermal Chemical Vapor Infiltration Gas-Phase Route*. Journal of Alloys and Compounds, 1992. **188**(1-2): p. 42-48.
184. Delhaes, P., *Chemical vapor deposition and infiltration processes of carbon materials*. Carbon, 2002. **40**(5): p. 641-657.
185. Araki, H., T. Noda, F. Abe, and H. Suzuki, *Interfacial Structural of Chemical Vapor Infiltration Carbon Fibre/SiC Composite*. Journal of Materials Science Letters, 1992. **11**(23): p. 1582-1584.
186. Fitzer, E. and R. Gadow, *Fiber-Reinforced Silicon-Carbide*. American Ceramic Society Bulletin, 1986. **65**(2): p. 326-335.
187. Bryant, W.a., *The fundamentals of chemical vapour deposition*. Journal of Materials Science, 1977. **12**(7): p. 1285-1306.
188. Sherman, A., *Chemical vapor deposition for microelectronics: principles, technology, and applications*. Materials science and process technology series. 1987, Park Ridge, N.J.: Noyes Publications.
189. Ofori, J.Y. and S.V. Sotirchos, *Optimal pressures and temperatures for isobaric, isothermal chemical vapor infiltration*. Aiche Journal, 1996. **42**(10): p. 2828-2840.
190. Oh, B.J., Y.J. Lee, D.J. Choi, G.W. Hong, J.Y. Park, and W.J. Kim, *Fabrication of Carbon/Silicon Carbide Composites by Isothermal Chemical Vapor Infiltration, Using the In Situ Whisker-Growing and Matrix-Filling Process*. Journal of the American Ceramic Society, 2001. **84**(1): p. 245-247.
191. Wei, X., L. Cheng, L. Zhang, Y. Xu, and Q. Zeng, *Numerical Simulation of Effect of Methyltrichlorosilane Flux on Isothermal Chemical Vapor Infiltration Process of C/SiC Composites*. Journal of the American Ceramic Society, 2006. **0**(0): p. 2762-2768.
192. Pierson, H.O., *Handbook of chemical vapor deposition (CVD) : principles, technology and applications*. 1992, Park Ridge, N.J.: Noyes.
193. Naslain, R., F. Langlais, and R. Fedou, *The CVI-Processing of Ceramic Matrix Composites*. Journal De Physique, 1989. **50**(C-5): p. 191-207.
194. Ma, X., X. Yin, X. Cao, L. Chen, L. Cheng, and L. Zhang, *Effect of heat treatment on the mechanical properties of SiCf/BN/SiC fabricated by CVI*. Ceramics International, 2016. **42**(2): p. 3652-3658.

195. Golecki, I., R.C. Morris, D. Narasimhan, and N. Clements, *Rapid densification of porous carbon-carbon composites by thermal-gradient chemical vapor infiltration*. Applied Physics Letters, 1995. **66**(18): p. 2334-2336.
196. Kotlensky, W., *Deposition of pyrolytic carbon in porous solids*. Chemistry and physics of carbon, 1973. **9**: p. 173-262.
197. Kotlensky, W. and J. Pappis, *Properties of CVD Infiltrated Composites*. Carbon, 1969. **7**(6): p. 729-730.
198. Roman, Y.G., D.P. Stinton, and T.M. Besmann, *Development of High-Density Fiber Reinforced Silicon-Carbide Fcvi Composites*. Journal De Physique Ii, 1991. **1**(C2): p. 689-695.
199. Roman, Y.G., M.H.J.M. Decroon, and R. Metselaar, *Analysis of the Isothermal Forced Flow Chemical-Vapor Infiltration Process .2. Experimental-Study*. Journal of the European Ceramic Society, 1995. **15**(9): p. 887-898.
200. Bertrand, S., J.F. Lavaud, R. El Hadi, G. Vignoles, and R. Pailler, *The thermal gradient-pulse flow CVI process: A new chemical vapor infiltration technique for the densification of fibre preforms*. Journal of the European Ceramic Society, 1998. **18**(7): p. 857-870.
201. Matlin, W.M., D. Stinton, and T. Besmann, *Development of a two-step, forced chemical vapor infiltration process*. Ceramic Transactions, 1995. **58**: p. 119-23.
202. Stinton, D.P., A.J. Caputo, and R.A. Lowden, *Synthesis of Fiber-Reinforced Sic Composites by Chemical Vapor Infiltration*. American Ceramic Society Bulletin, 1986. **65**(2): p. 347-350.
203. Roman, Y.G., *Forced flow chemical vapour infiltration*. 1994: Technische Universiteit Eindhoven.
204. Besmann, T.M., J. McLaughlin, and H.-T. Lin, *Fabrication of ceramic composites: forced CVI*. Journal of Nuclear Materials, 1995. **219**: p. 31-35.
205. Gupte, S. and J. Tsamopoulos, *Forced-Flow Chemical Vapor Infiltration of Porous Ceramic Materials*. Journal of the Electrochemical Society, 1990. **137**(11): p. 3675-3682.
206. Naslain, R., J. Lamon, and D. Doumeingts, *High temperature ceramic matrix composites*. 1993: Woodhead Publishing.
207. Dupel, P., X. Bourrat, and R. Pailler, *Structure of pyrocarbon infiltrated by pulse-CVI*. Carbon, 1995. **33**(9): p. 1193-1204.
208. Naslain, R., *Ceramic Matrix Composites - 5th Conference of the European Ceramic Society - 22-26 June 1997 - Versailles, France - Foreword*. Journal of the European Ceramic Society, 1998. **18**(13): p. 1795-1795.
209. Golecki, I., R.C. Morris, and D. Narasimhan, *Method of rapidly densifying a porous structure*. 1994, Google Patents.
210. Golecki, I., R. Morris, D. Narasimhan, and N. Clements, *Rapid densification of porous carbon-carbon composites by thermal-gradient chemical vapor infiltration*. Applied Physics Letters, 1995. **66**(18): p. 2334-2336.
211. Midha, V. and D.J. Economou, *A two-dimensional model of chemical vapor infiltration with radio-frequency heating - II. Strategies to achieve complete densification*. Journal of the Electrochemical Society, 1998. **145**(10): p. 3569-3580.
212. Sheldon, B.W. and T.M. Besmann, *Reaction and Diffusion Kinetics during the Initial-Stages of Isothermal Chemical Vapor Infiltration*. Journal of the American Ceramic Society, 1991. **74**(12): p. 3046-3053.
213. Igawa, N., T. Taguchi, T. Nozawa, L.L. Snead, T. Hinoki, J.C. McLaughlin, Y. Katoh, S. Jitsukawa, and A. Kohyama, *Fabrication of SiC fiber reinforced SiC composite by chemical vapor infiltration for excellent mechanical properties*. Journal of Physics and Chemistry of Solids, 2005. **66**(2-4): p. 551-554.
214. Igawa, N., T. Taguchi, L.L. Snead, Y. Katoh, S. Jitsukawa, A. Kohyama, and J.C. McLaughlin, *Optimizing the fabrication process for superior mechanical*

- properties in the FCVI SiC matrix/stoichiometric SiC fiber composite system.* Journal of Nuclear Materials, 2002. **307–311**, Part 2(0): p. 1205-1209.
215. Katoh, Y., T. Nozawa, and L.L. Snead, *Mechanical Properties of Thin Pyrolytic Carbon Interphase SiC–Matrix Composites Reinforced with Near-Stoichiometric SiC Fibers.* Journal of the American Ceramic Society, 2005. **88**(11): p. 3088-3095.
  216. Sugiyama, K. and T. Kishida, *Pressure-pulsed chemical vapour infiltration of SiC to porous carbon from a gas system SiCl<sub>4</sub>-CH<sub>4</sub>-H<sub>2</sub>.* Journal of Materials Science, 1996. **31**(14): p. 3661-3665.
  217. Moralesrodriguez, A., P. Reynaud, G. Fantozzi, J. Adrien, and E. Maire, *Porosity analysis of long-fiber-reinforced ceramic matrix composites using X-ray tomography.* Scripta Materialia, 2009. **60**(6): p. 388-390.
  218. Guan, K., L. Cheng, Q. Zeng, L. Zhang, J. Deng, K. Li, H. Li, and R. Naslain, *Modeling of Pore Structure Evolution Between Bundles of Plain Woven Fabrics During Chemical Vapor Infiltration Process: The Influence of Preform Geometry.* Journal of the American Ceramic Society, 2013. **96**(1): p. 51-61.
  219. Guillaumat, L. and J. Lamon, *Probabilistic-statistical simulation of the non-linear mechanical behavior of a woven SiCSiC composite.* Composites Science and Technology, 1996. **56**(7): p. 803-808.
  220. Binner, J., B. Vaidyanathan, D. Jaglin, and S. Needham, *Use of Electrophoretic Impregnation and Vacuum Bagging to Impregnate SiC powder into SiC Fiber Preforms.* International Journal of Applied Ceramic Technology, 2013: p. 212-222.
  221. Sugiyama, K. and K. Norizuki, *Preparation of low density free-standing shape of SiC by pressure-pulsed chemical vapour infiltration.* Journal of Materials Science Letters, 1995. **14**(23): p. 1720-1722.
  222. Lackey, W.J., S. Vaidyaraman, G.B. Freeman, and P.K. Agrawal, *Technique for Monitoring Densification during Chemical-Vapor Infiltration.* Journal of the American Ceramic Society, 1995. **78**(4): p. 1131-1133.
  223. Honglei, W., Z. Xingui, Y. Jinshan, C. Yingbin, and L. Rongjun, *Microstructure, mechanical properties and reaction mechanism of KD-1 SiCf/SiC composites fabricated by chemical vapor infiltration and vapor silicon infiltration.* Materials Science and Engineering: A, 2011. **528**(6): p. 2441-2445.
  224. Licciulli, A., F. DeRiccardis, A. Quirini, C.A. Nannetti, G. Filacchioni, L. Pilloni, S. Botti, A. Ortona, and A. Cammarota, *Preparation and characterization of SiC/C/SiC composites by hybrid wet/vapour processing.* Cmmc 96 - Proceedings of the First International Conference on Ceramic and Metal Matrix Composites, Pts 1 and 2, 1997. **127-3**: p. 279-285.
  225. Nannetti, C., B. Riccardi, A. Ortona, A. La Barbera, E. Scafè, and G. Vekinis, *Development of 2D and 3D Hi-Nicalon fibres/SiC matrix composites manufactured by a combined CVI–PIP route.* Journal of Nuclear Materials, 2002. **307**: p. 1196-1199.
  226. Stinton, D.P., D.M. Hembree, K.L. More, B.W. Sheldon, T.M. Besmann, M.H. Headinger, and R.F. Davis, *Matrix Characterization of Fiber-Reinforced SiC Matrix Composites Fabricated by Chemical Vapor Infiltration.* Journal of Materials Science, 1995. **30**(17): p. 4279-4285.
  227. Fitzer, E. and D. Hegen, *Chemical Vapor Deposition of Silicon Carbide and Silicon Nitride—Chemistry's Contribution to Modern Silicon Ceramics.* Angewandte Chemie International Edition, 1979. **18**(4): p. 295-304.
  228. Papisoulitiotis, G.D. and S.V. Sotirchos, *Heterogeneous Kinetics of the Chemical-Vapor-Deposition of Silicon-Carbide from Methyltrichlorosilane.* Gas-Phase and Surface Chemistry in Electronic Materials Processing, 1994. **334**: p. 111-116.
  229. Lee, Y.-J., D.-J. Choi, J.-Y. Park, and G.-W. Hong, *The effect of diluent gases on the growth behavior of CVD SiC films with temperature.* Journal of Materials Science, 2000. **35**(18): p. 4519-4526.

230. Kim, H.S. and D.J. Choi, *Effect of diluent gases on growth behavior and characteristics of chemically vapor deposited silicon carbide films*. Journal of the American Ceramic Society, 1999. **82**(2): p. 331-337.
231. Lespiaux, D. and F. Langlais, *Chemisorption on  $\beta$ -SiC and amorphous SiO<sub>2</sub> during CVD of silicon carbide from the Si-CH-Cl system. Correlations with the nucleation process*. Thin Solid Films, 1995. **265**(1-2): p. 40-51.
232. Lespiaux, D., F. Langlais, R. Naslain, S. Schamm, and J. Sevely, *Correlations between gas phase supersaturation, nucleation process and physico-chemical characteristics of silicon carbide deposited from Si-CH-Cl system on silica substrates*. Journal of Materials Science, 1995. **30**(6): p. 1500-1510.
233. Loumagne, F., F. Langlais, and R. Naslain, *Experimental kinetic study of the chemical vapour deposition of SiC-based ceramics from CH<sub>3</sub>SiCl<sub>3</sub>H<sub>2</sub> gas precursor*. Journal of Crystal Growth, 1995. **155**(3-4): p. 198-204.
234. Loumagne, F., F. Langlais, and R. Naslain, *Reactional mechanisms of the chemical vapour deposition of SiC-based ceramics from CH<sub>3</sub>SiCl<sub>3</sub>H<sub>2</sub> gas precursor*. Journal of Crystal Growth, 1995. **155**(3-4): p. 205-213.
235. Josiek, A. and F. Langlais, *Residence-time dependent kinetics of CVD growth of SiC in the MTSH<sub>2</sub> system*. Journal of Crystal Growth, 1996. **160**(3-4): p. 253-260.
236. Zhang, W.G. and K.J. Hüttinger, *CVD of SiC from methyltrichlorosilane. Part II: Composition of the gas phase and the deposit*. Chemical Vapor Deposition, 2001. **7**(4): p. 173-181.
237. Hopfe, V., H. Mosebach, M. Erhard, and M. Meyer, *In-situ FTIR emission spectroscopy in a technological environment: chemical vapour infiltration (CVI) of SiC composites*. Journal of molecular structure, 1995. **347**: p. 331-342.
238. Allendorf, M.D. and C.F. Melius, *Theoretical-Study of the Thermochemistry of Molecules in the Si-C-Cl-H System*. Journal of Physical Chemistry, 1993. **97**(3): p. 720-728.
239. Langlais, F. and C. Prebende. *On the chemical process of CVD of SiC-based ceramics from the Si-C-H-Cl system*. in Proc. 11th Int. Conf. on CVD (Electrochem. Soc. Inc., Pennington, NJ). 1990.
240. Lu, C., L. Cheng, C. Zhao, L. Zhang, and Y. Xu, *Kinetics of chemical vapor deposition of SiC from methyltrichlorosilane and hydrogen*. Applied Surface Science, 2009. **255**(17): p. 7495-7499.
241. Schlichting, J., *Chemical Vapor-Deposition of Silicon-Carbide*. Powder Metallurgy International, 1980. **12**(3): p. 141-147.
242. Chiu, C.C., S.B. Desu, and C.Y. Tsai, *Low pressure chemical vapor deposition (LPCVD) of  $\beta$ -SiC on Si (100) using MTS in a hot wall reactor*. Journal of Materials Research, 1993. **8**(10): p. 2617-2626.
243. Van der Putte, P., L. Giling, and J. Bloem, *Surface morphology of HCl etched silicon wafers: I. Gas phase composition in the silicon HCl system and surface reactions during etching*. Journal of Crystal Growth, 1977. **41**(1): p. 133-145.
244. Fischman, G.S. and W.T. Petuskey, *Thermodynamic Analysis and Kinetic Implications of Chemical Vapor-Deposition of Sic from Si-C-Cl-H Gas Systems*. Journal of the American Ceramic Society, 1985. **68**(4): p. 185-190.
245. Decroon, M.H.J.M. and L.J. Giling, *Chemical-Boundary Layers in CVD .1. Irreversible Reactions*. Journal of the Electrochemical Society, 1990. **137**(9): p. 2867-2876.
246. Decroon, M.H.J.M. and L.J. Giling, *Chemical-Boundary Layers in CVD .2. Reversible-Reactions*. Journal of the Electrochemical Society, 1990. **137**(11): p. 3606-3612.
247. Cholet, V. and L. Vandenbulcke, *Chemical Vapor Infiltration of Boron Nitride Interphase in Ceramic Fiber Preforms: Discussion of Some Aspects of the Fundamentals of the Isothermal Chemical Vapor Infiltration Process*. Journal of the American Ceramic Society, 1993. **76**(11): p. 2846-2858.

## Chapter 8. References

---

248. Gupte, S. and J. Tsamopoulos, *Densification of porous materials by chemical vapor infiltration*. Journal of the Electrochemical Society, 1989. **136**(2): p. 555-561.
249. Thiele, E.W., *Relation between catalytic activity and size of particle*. Industrial and Engineering Chemistry, 1939. **31**: p. 916-920.
250. Sorrentino, R. and G. Bianchi, *Microwave and RF engineering*. Vol. 1. 2010: John Wiley & Sons. 4.
251. University, S.o.C.o.D.C., *Summary of electromagnetic spectrum*.
252. Sutton, W.H., *Microwave Processing of Ceramic Materials*. American Ceramic Society Bulletin, 1989. **68**(2): p. 376-386.
253. Thuery, J., *Microwaves: industrial, scientific, and medical applications*. 1992: Artech House on Demand. 84-97.
254. Sorrentino, R. and G. Bianchi, *Microwave and RF engineering*. Vol. 1. 2010: John Wiley & Sons.
255. Pozar, D.M., *Microwave engineering*. 4th ed. ed. 2012, Hoboken, NJ: Wiley.
256. Thuery, J., *Microwaves: industrial, scientific, and medical applications*. 1992: Artech House on Demand. 33-47.
257. Thostenson, E. and T.-W. Chou, *Microwave processing: fundamentals and applications*. Composites Part A: Applied Science and Manufacturing, 1999. **30**(9): p. 1055-1071.
258. Metaxas, A. and J. Binner, *Microwave processing of ceramics*. Noyes Publications, Advanced Ceramic Processing and Technology., 1990. **1**: p. 285-367.
259. Rybakov, K.I., E.A. Olevsky, E.V. Krikun, and D.J. Green, *Microwave Sintering: Fundamentals and Modeling*. Journal of the American Ceramic Society, 2013. **96**(4): p. 1003-1020.
260. Ramesh, P.D., D. Brandon, and L. Schachter, *Use of partially oxidized SiC particle bed for microwave sintering of low loss ceramics*. Materials Science and Engineering a-Structural Materials Properties Microstructure and Processing, 1999. **266**(1-2): p. 211-220.
261. Bykov, Y.V., K.I. Rybakov, and V.E. Semenov, *High-temperature microwave processing of materials*. Journal of Physics D-Applied Physics, 2001. **34**(13): p. R55-R75.
262. Venkatesh, M. and G. Raghavan, *An overview of microwave processing and dielectric properties of agri-food materials*. Biosystems Engineering, 2004. **88**(1): p. 1-18.
263. Zong, L., S. Zhou, N. Sgriccia, M. Hawley, and L. Kempel, *A review of microwave-assisted polymer chemistry (MAPC)*. The Journal of microwave power and electromagnetic energy: a publication of the International Microwave Power Institute, 2002. **38**(1): p. 49-74.
264. Fletcher, R., E. University of Nottingham. Theses. Materials, and D. Materials, *Investigation into microwave heating of uranium dioxide*. 1995. viii, 176 p.
265. Devlin, D.J., R.P. Currier, R.S. Barbero, B.F. Espinoza, and N. Elliott, *Microwave Assisted Chemical Vapor Infiltration*. Chemical Vapor Deposition of Refractory Metals and Ceramics li, 1992. **250**: p. 245-250.
266. Thomas, J.J., D.J. Skamser, and D.L. Johnson, *Microwave Processing of a Compositionally Changing System*. 29th Microwave Power Symposium - Proceedings, 1994: p. 140-143.
267. Wroe, R., *Microwave-assisted firing of ceramics*. Power Engineering Journal, 1996. **10**(4): p. 181-183.
268. Ramesh, P.D. and K.J. Rao, *Microwave-Assisted Synthesis of Aluminum Nitride*. Advanced Materials, 1995. **7**(2): p. 177-179.
269. Pozar, D.M., *A Modern Course in Microwave Engineering*. Ieee Transactions on Education, 1990. **33**(1): p. 129-134.

270. Clark, D.E., D.C. Folz, R.L. Schulz, Z. Fathi, and A.D. Cozzi, *Recent Developments in the Microwave Processing of Ceramics*. Mrs Bulletin, 1993. **18**(11): p. 41-46.
271. Clark, D.E., J. Binner, and D.A. Lewis, *Microwaves : theory and application in materials processing V : "Bridging science, technology, and applications" : proceedings of the Second World Congress on Microwave and Radio Frequency Processing : April, 2000, in Orlando, Florida*. Ceramic Transactions. 2001, Westerville, Ohio: American Ceramic Society. 588.
272. Peng, J., J. Binner, and S. Bradshaw, *Microwave initiated self-propagating high-temperature synthesis of SiC*. Journal of Materials Synthesis and Processing, 2001. **9**(6): p. 363-368.
273. Vaidhyanathan, B., K. Annapoorani, J. Binner, and R. Raghavendra, *Microwave sintering of multilayer integrated passive devices*. Journal of the American Ceramic Society, 2010. **93**(8): p. 2274-2280.
274. Olevsky, E.A., S. Kandukuri, and L. Froyen, *Consolidation enhancement in spark-plasma sintering: impact of high heating rates*. Journal of Applied Physics, 2007. **102**(11): p. 114913.
275. *Cavity magnetron oscillator*. 2004, Encyclopædia Britannica.
276. Palaith, D., R. Silbergliitt, C. Wu, R. Kleiner, and E.L. Libeld. *Microwave joining of ceramics*. in *MRS Proceedings*. 1988. Cambridge Univ Press.
277. Tinga, W., J. Xu, and F. Vermeulen, *Open coaxial microwave spot joining applicator*. Ceramic Transactions, 1995. **59**: p. 347-356.
278. Wei, J., M.C. Hawley, J.D. Delong, and M. Demeuse, *Comparison of microwave and thermal cure of epoxy resins*. Polymer Engineering & Science, 1993. **33**(17): p. 1132-1140.
279. Grellinger, D. and M. Janney, *Temperature measurement in a 2.45 GHz Microwave furnace*. Ceram. Trans., 1993. **36**: p. 529-538.
280. Pert, E., Y. Carmel, A. Birnboim, T. Olorunyolemi, D. Gershon, J. Calame, I.K. Lloyd, and O.C. Wilson, *Temperature measurements during microwave processing: the significance of thermocouple effects*. Journal of the American Ceramic Society, 2001. **84**(9): p. 1981-1986.
281. Michalski, L., K. Eckersdorf, and J. McGhee, *Temperature measurement*. 1991: Wiley.
282. Howell, J.R., M.P. Menguc, and R. Siegel, *Thermal radiation heat transfer*. 2010: CRC press.
283. Omega. *Emissivity common materials*. Omega; Available from: [www.omega.com](http://www.omega.com).
284. Mercer, C., *Optical metrology for fluids, combustion and solids*. 2013: Springer Science & Business Media.
285. Obermayer, D., B. Gutmann, and C.O. Kappe, *Microwave chemistry in silicon carbide reaction vials: separating thermal from nonthermal effects*. Angewandte Chemie, 2009. **121**(44): p. 8471-8474.
286. Kremsner, J.M. and C.O. Kappe, *Silicon carbide passive heating elements in microwave-assisted organic synthesis*. The Journal of organic chemistry, 2006. **71**(12): p. 4651-4658.
287. Clark, D.E., D.C. Folz, and J.K. West, *Processing materials with microwave energy*. Materials Science and Engineering: A, 2000. **287**(2): p. 153-158.
288. Zhang, H., Y. Xu, J. Zhou, J. Jiao, Y. Chen, H. Wang, C. Liu, Z. Jiang, and Z. Wang, *Stacking fault and unoccupied densities of state dependence of electromagnetic wave absorption in SiC nanowires*. Journal of Materials Chemistry C, 2015. **3**(17): p. 4416-4423.
289. Yao, Y., A. Jänis, and U. Klement, *Characterization and dielectric properties of  $\beta$ -SiC nanofibres*. Journal of Materials Science, 2008. **43**(3): p. 1094-1101.

290. Sugawara, H., K. Kashimura, M. Hayashi, S. Ishihara, T. Mitani, and N. Shinohara, *Behavior of microwave-heated silicon carbide particles at frequencies of 2.0–13.5 GHz*. Applied Physics Letters, 2014. **105**(3): p. 034103.
291. Liu, C., D. Yu, D.W. Kirk, and Y. Xu, *Electromagnetic wave absorption of silicon carbide based materials*. RSC Advances, 2017. **7**(2): p. 595-605.
292. Sun, J., J. Li, G. Sun, B. Zhang, S. Zhang, and H. Zhai, *Dielectric and infrared properties of silicon carbide nanopowders*. Ceramics International, 2002. **28**(7): p. 741-745.
293. Li, Z., W. Zhou, F. Luo, Y. Huang, G. Li, and X. Su, *Improving the dielectric properties of SiC powder through nitrogen doping*. Materials Science and Engineering: B, 2011. **176**(12): p. 942-944.
294. Li, D., H.B. Jin, M.S. Cao, T. Chen, Y.K. Dou, B. Wen, and S. Agathopoulos, *Production of Ni-Doped SiC Nanopowders and their Dielectric Properties*. Journal of the American Ceramic Society, 2011. **94**(5): p. 1523-1527.
295. Kassiba, A., M. Tabellout, S. Charpentier, N. Herlin, and J. Emery, *Conduction and dielectric behaviour of SiC nano-sized materials*. Solid State Communications, 2000. **115**(7): p. 389-393.
296. Kagawa, Y., Y. Imahashi, H. Iba, T. Naganuma, and K. Matsumura, *Effect of electrical resistivity of Si-Ti-CO fiber on electromagnetic wave penetration depth of short fiber-dispersed composites*. Journal of Materials Science Letters, 2003. **22**(2): p. 159-161.
297. Mo, R., X. Yin, F. Ye, X. Liu, L. Cheng, and L. Zhang, *Mechanical and microwave absorbing properties of Tyranno® ZMI fiber annealed at elevated temperatures*. Ceramics International, 2017. **43**(12): p. 8922-8931.
298. Gupta, D. and J.W. Evans, *A Mathematical-Model for Chemical Vapor Infiltration with Microwave-Heating and External Cooling*. Journal of Materials Research, 1991. **6**(4): p. 810-818.
299. Spatz, M.S., D.J. Skamser, and D.L. Johnson, *Thermal-Stability of Ceramic Materials in Microwave-Heating*. Journal of the American Ceramic Society, 1995. **78**(4): p. 1041-1048.
300. Ahmad I., P.L., Silbergliitt R., Microwave energy-assisted chemical vapour infiltration, U.P.a.T. Office, United States, 1993, US Patent, 5,238,710
301. Devlin, D.J., R.P. Currier, J.R. Laia Jr, and R.S. Barbero, Chemical vapor infiltration using microwave energy, U.S.P.a.T. Office., US, 1993, US Patent, 5,254,374
302. Roussy, G., A. Mercier, J.-M. Thiébaud, and J.-P. Vaubourg, *Temperature runaway of microwave heated materials: Study and control*. J. Microwave Power, 1985. **20**(1): p. 47-51.
303. Ramesh, P.D., D. Brandon, and L. Schächter, *Use of partially oxidized SiC particle bed for microwave sintering of low loss ceramics*. Materials Science and Engineering: A, 1999. **266**(1): p. 211-220.
304. Reimbert, C.G., A. Minzoni, and N. Smyth, *Effect of radiation losses on hotspot formation and propagation in microwave heating*. IMA journal of applied mathematics, 1996. **57**(2): p. 165-179.
305. Jaglin, D., B. Vaidhyanathan, J. Binner, C. Prentice, and B. Shatwell, *Densification mechanisms in SiC/SiC composites by microwave enhanced chemical vapour infiltration*. Microwave and Radio Frequency Applications, 2003: p. 231-240.
306. Streckert, H.H., K.P. Norton, J.D. Katz, and J.O. Freim, *Microwave densification of electrophoretically infiltrated silicon carbide composite*. Journal of Materials Science, 1997. **32**(24): p. 6429-6433.
307. Binner, J., B. Vaidhyanathan, and D. Jaglin, *Microwave heated chemical vapour infiltration of SiC powder impregnated SiC fibre preforms*. Advances in Applied Ceramics, 2013. **112**(4): p. 235-241.

308. Tilley, B.S. and G.A. Kriegsmann, *Microwave-enhanced chemical vapor infiltration: a sharp interface model*. Journal of Engineering Mathematics, 2001. **41**(1): p. 33-54.
309. Maizza G., L.M. *Modelling of SiC Chemical Vapour Infiltration Process (CVI) Assisted by Microwave Heating*. in COMSOL Conference. 2009. Milan.
310. Spatz, M.S., D.J. Skamser, P.S. Day, H.M. Jennings, and D. Lynn. *Microwave-assisted chemical vapor infiltration*. in *17th Annual Conference on Composites and Advanced Ceramic Materials, Part 2 of 2: Ceramic Engineering and Science Proceedings, Volume 14*. 2009. Wiley-American Ceramic Society.
311. Day, P.S., D.J. Skamser, H.M. Jennings, and D.L. Johnson. *Fabrication of SiC Matrix Surface Composites by Chemical Vapor Infiltration with Microwave Heating: Temperature Effects*. in *Proceedings of the 18th Annual Conference on Composites and Advanced Ceramic Materials-B: Ceramic Engineering and Science Proceedings, Volume 15, Issue 5*. 1994. Wiley Online Library.
312. Currier, R. and D. Devlin, Ceramic matrix composites by microwave assisted CVI, Report No. LA-UR-93-1322; CONF-930438--14, 1993.
313. Currier, R. and D. Devlin, *Ceramic matrix composites by microwave assisted CVI*, in *Ceramic transactions: Microwaves. Theory and application in materials processing II. Volume 36*. 1993.
314. Yan, X.-T. and Y. Xu, *Chemical vapour deposition: an integrated engineering design for advanced materials*. 2010: Springer Science & Business Media.
315. Zeng, X.R., J.Z. Zou, H.X. Qian, X.B. Xiong, X.H. Li, and S.H. Xie, *Microwave assisted chemical vapor infiltration for the rapid fabrication of carbon/carbon composites*. New Carbon Materials, 2009. **24**(1): p. 28-32.
316. Jenkins, A.C. and G.F. Chambers, *Vapor Pressures of Silicon Compounds*. Industrial & Engineering Chemistry, 1954. **46**(11): p. 2367-2369.
317. Lide, D.R. and H.V. Kehiaian, *CRC handbook of thermophysical and thermochemical data*. Vol. 1. 1994: Crc Press.
318. Paschen, F., *Ueber die zum Funkenübergang in Luft, Wasserstoff und Kohlensäure bei verschiedenen Drucken erforderliche Potentialdifferenz*. Annalen der Physik, 1889. **273**(5): p. 69-96.
319. Anderson, C. and M. Hasler. *Extension of electron microprobe techniques to biochemistry by the use of long wavelength X-rays*. in *Proceedings of the Fourth International Conference on X-ray Optics and Microanalysis*. 1966.
320. Fitting, H.J., H. Glaefcke, and W. Wild, *Electron penetration and energy transfer in solid targets*. Physica status solidi (a), 1977. **43**(1): p. 185-190.
321. Chen, L.-F., C. Ong, C. Neo, V. Varadan, and V.K. Varadan, *Microwave electronics: measurement and materials characterization*. 2004: John Wiley & Sons.
322. Harrington, R.F. and T.-H.E. Fields, *IEEE press*. New York, 2001.
323. Bonincontro, A. and C. Cametti, *On the applicability of the cavity perturbation method to high-loss dielectrics*. Journal of Physics E: Scientific Instruments, 1977. **10**(12): p. 1232.
324. Catalá-Civera, J.M., A.J. Canós, P. Plaza-González, J.D. Gutiérrez, B. García-Baños, and F.L. Peñaranda-Foix, *Dynamic measurement of dielectric properties of materials at high temperature during microwave heating in a dual mode cylindrical cavity*. IEEE Transactions on Microwave Theory and Techniques, 2015. **63**(9): p. 2905-2914.
325. Arai, M., J. Binner, and T. Cross, *Comparison of techniques for measuring high-temperature microwave complex permittivity: Measurements on an Alumina/Zirconia system*. Journal of microwave power and electromagnetic energy, 1996. **31**(1): p. 12-18.
326. Altschuler, H., *Dielectric constant*. Handbook of microwave measurements, 1963. **2**: p. 495-548.

327. Khanna, S., E. Ehrenfreund, A. Garito, and A. Heeger, *Microwave properties of high-purity tetrathiofulvalene-tetracyanoquinodimethan (TTF-TCNQ)*. Physical Review B, 1974. **10**(6): p. 2205.
328. Landau, L.D. and E. Lifshitz, *Course of Theoretical Physics. Vol. 8: Electrodynamics of Continuous Media*. 1960: Oxford.
329. Deng, J., K. Su, X. Wang, Q. Zeng, L. Cheng, Y. Xu, and L. Zhang, *Thermodynamics of the gas-phase reactions in chemical vapor deposition of silicon carbide with methyltrichlorosilane precursor*. Theoretical Chemistry Accounts, 2008. **122**(1): p. 1.
330. Papasouliotis, G.D. and S.V. Sotirchos, *Hydrogen chloride effects on the CVD of silicon carbide from methyltrichlorosilane*. Chemical Vapor Deposition, 1998. **4**(6): p. 235-246.
331. Burwell, R.L.J., *Manual of symbols and terminology for physicochemical quantities and units, appendix II: Definitions, terminology and symbols in colloid and surface chemistry*. Pure and Applied Chemistry, 1976. **46**(1): p. 78.
332. Loumagne, F., F. Langlais, R. Naslain, S. Schamm, D. Dornignac, and J. Sevely, *Physicochemical properties of SiC-based ceramics deposited by low pressure chemical vapor deposition from CH<sub>3</sub>SiCl<sub>3</sub>H<sub>2</sub>*. Thin Solid Films, 1995. **254**(1-2): p. 75-82.
333. Papasouliotis, G.D. and S.V. Sotirchos, *Experimental study of atmospheric pressure chemical vapor deposition of silicon carbide from methyltrichlorosilane*. Journal of Materials Research, 1999. **14**(8): p. 3397-3409.
334. Golecki, I., *Rapid vapor-phase densification of refractory composites*. Materials Science and Engineering: R: Reports, 1997. **20**(2): p. 37-124.
335. Heinrich, J., S. Hemeltjen, and G. Marx, *Analytics of CVD Processes in the Deposition of SiC by Methyltrichlorosilane*. Microchimica Acta, 2000. **133**(1): p. 209-214.
336. Loumagne, F., F. Langlais, and R. Naslain, *Kinetic laws of the chemical process in the CVD of SiC ceramics from CH<sub>3</sub>SiCl<sub>3</sub>-H<sub>2</sub> precursor*. Le Journal de Physique IV, 1993. **3**(C3): p. C3-527 - C3-533.
337. Van Kemenade, A. and C. Stemfoort, *On the formation of β-SiC from pyrolysis of CH<sub>3</sub>SiCl<sub>3</sub> in hydrogen*. Journal of Crystal Growth, 1972. **12**(1): p. 13-16.
338. Chin, J., P. Gantzel, and R. Hudson, *The structure of chemical vapor deposited silicon carbide*. Thin Solid Films, 1977. **40**: p. 57-72.
339. Chung, G.Y. and B.J. McCoy, *Modeling of chemical vapor infiltration for ceramic composites reinforced with layered, woven fabrics*. Journal of the American Ceramic Society, 1991. **74**(4): p. 746-751.
340. Besmann, T., B. Sheldon, and M. Kaster, *Temperature and concentration dependence of SiC deposition on Nicalon fibers*. Surface and coatings technology, 1990. **43**: p. 167-175.
341. Cheng, D., W. Shyy, D. Kuo, and M. Hon, *Growth Characteristics of CVD Beta-Silicon Carbide*. Journal of the Electrochemical Society, 1987. **134**(12): p. 3145-3149.
342. Schlichting, J., *Chemical vapor deposition of silicon carbide*. Powder Metallurgy International, 1980. **12**(4): p. 196-200.
343. Tesner, P., T. Smegiriova, and V. Knorre, *Kinetics of dispersed carbon formation*. Combustion and Flame, 1971. **17**(2): p. 253-260.
344. Roman, Y., J. Kotte, and M. De Croon, *Analysis of the isothermal forced flow chemical vapour infiltration process. Part I: Theoretical aspects*. Journal of the European Ceramic Society, 1995. **15**(9): p. 875-886.
345. Hu, J., R. Jia, B. Xin, B. Peng, Y. Wang, and Y. Zhang, *Effect of Low Pressure on Surface Roughness and Morphological Defects of 4H-SiC Epitaxial Layers*. Materials, 2016. **9**(9): p. 743.
346. Somorjai, G.A. and Y. Li, *Introduction to surface chemistry and catalysis*. 2010: John Wiley & Sons.

347. Pimpinelli, A. and J. Villain, *Physics of crystal growth*. Vol. 53. 1998, Cambridge: Cambridge University Press.
348. Oura, K., V. Lifshits, A. Saranin, A. Zotov, and M. Katayama, *Surface science: an introduction*. 2013: Springer Science & Business Media.
349. Choi, B.J., S.H. Jeun, and D.R. Kim, *The effects of C<sub>3</sub>H<sub>8</sub> on the chemical vapor deposition of silicon carbide in the CH<sub>3</sub>SiCl<sub>3</sub> + H<sub>2</sub> system*. Journal of the European Ceramic Society, 1992. **9**(5): p. 357-363.
350. Minato, K. and K. Fukuda, *Chemical vapor deposition of silicon carbide for coated fuel particles*. Journal of Nuclear Materials, 1987. **149**(2): p. 233-246.
351. Lespiaux, D., F. Langlais, R. Naslain, S. Schamm, and J. Sevely, *Chlorine and oxygen inhibition effects in the deposition of SiC-based ceramics from the Si · C · H · Cl system*. Journal of the European Ceramic Society, 1995. **15**(1): p. 81-88.
352. Nakashima, S.-i. and H. Harima, *Raman investigation of SiC polytypes*. Physica status solidi (a), 1997. **162**(1): p. 39-64.
353. Feldman, D., J.H. Parker Jr, W. Choyke, and L. Patrick, *Phonon Dispersion Curves by Raman Scattering in SiC, Polytypes 3 C, 4 H, 6 H, 1 5 R, and 2 1 R*. Physical Review, 1968. **173**(3): p. 787.
354. Pluchery, O. and J.-M. Costantini, *Infrared spectroscopy characterization of 3C–SiC epitaxial layers on silicon*. Journal of Physics D: Applied Physics, 2012. **45**(49): p. 495101.
355. Lin, L., *Synthesis and optical property of large-scale centimetres-long silicon carbide nanowires by catalyst-free CVD route under superatmospheric pressure conditions*. Nanoscale, 2011. **3**(4): p. 1582-1591.
356. Kim, K.J., M.H. Kim, and Y.W. Kim, *Highly Conductive p-Type Zinc blende SiC Thin Films Fabricated on Silicon Substrates by Magnetron Sputtering*. Journal of the American Ceramic Society, 2015. **98**(12): p. 3663-3665.
357. Huguet-Garcia, J., A. Jankowiak, S. Miro, R. Podor, E. Meslin, L. Thomé, Y. Serruys, and J.-M. Costantini, *Characterization of the ion-amorphization process and thermal annealing effects on third generation SiC fibers and 6H-SiC*. EPJ Nuclear Sciences & Technologies, 2015. **1**: p. 8.
358. Quiñones-Galván, J., J. Arias-Cerón, F. de Moure-Flores, A. Hernández-Hernández, A. Guillén-Cervantes, J. Santoyo-Salazar, J. Mendoza-Alvarez, and M. Meléndez-Lira, *Stoichiometric 6H-SiC thin films deposited at low substrate temperature by laser ablation*. Journal of Laser Applications, 2013. **25**(5): p. 052007.
359. Feng, Z., C. Tin, R. Hu, and J. Williams, *Raman and Rutherford backscattering analyses of cubic SiC thin films grown on Si by vertical chemical vapor deposition*. Thin Solid Films, 1995. **266**(1): p. 1-7.
360. Ferrari, A.C., J. Meyer, V. Scardaci, C. Casiraghi, M. Lazzeri, F. Mauri, S. Piscanec, D. Jiang, K. Novoselov, and S. Roth, *Raman spectrum of graphene and graphene layers*. Physical review letters, 2006. **97**(18): p. 187401.
361. Campbell, I. and P.M. Fauchet, *The effects of microcrystal size and shape on the one phonon Raman spectra of crystalline semiconductors*. Solid State Communications, 1986. **58**(10): p. 739-741.
362. Parker Jr, J., D. Feldman, and M. Ashkin, *Raman scattering by silicon and germanium*. Physical Review, 1967. **155**(3): p. 712.
363. Nakashima, S., H. Ohta, M. Hangyo, and B. Palosz, *Phonon Raman scattering in disordered silicon carbides*. Philosophical Magazine B, 1994. **70**(4): p. 971-985.
364. Harris, J., H. Gatos, and A. Witt, *Growth Characteristics of Alpha-Silicon Carbide I. Chemical Vapor Deposition*. Journal of the Electrochemical Society, 1971. **118**(2): p. 335-338.

365. Josiek, A., F. Langlais, and X. Bourrat, *A study of the transition between growth of stoichiometric and silicon-excess silicon carbide by CVD in the system MTS/H<sub>2</sub>*. *Chemical Vapor Deposition*, 1996. **2**(1): p. 17-21.
366. So, M.G. and J.S. Chun, *Growth and structure of chemical vapor deposited silicon carbide from methyltrichlorosilane and hydrogen in the temperature range of 1100 to 1400°C*. *Journal of Vacuum Science & Technology A: Vacuum, Surfaces, and Films*, 1988. **6**(1): p. 5-8.
367. Pampuch, R. and L. Stobierski, *Morphology of silicon carbide formed by chemical vapour deposition*. *Ceramurgia International*, 1977. **3**(2): p. 43-52.
368. Yang, J.F., T. Ohji, S. Kanzaki, A. Díaz, and S. Hampshire, *Microstructure and mechanical properties of silicon nitride ceramics with controlled porosity*. *Journal of the American Ceramic Society*, 2002. **85**(6): p. 1512-1516.
369. Zhou, X.G., S. Zhao, P. Mummery, and J. Marrow, *Studying SiC/SiC Composites by X-Ray Tomography*. *Key Engineering Materials*, 2014. **602-603**: p. 416-421.
370. Devlin, D., R. Currier, R. Barbero, B. Espinoza, and N. Elliott, *Microwave assisted chemical vapor infiltration*. *MRS Online Proceedings Library Archive*, 1991. **250**.
371. Madelung, O., *Semiconductors: group IV elements and III-V compounds*. 2012: Springer Science & Business Media.
372. Morales-Rodriguez, A., P. Reynaud, G. Fantozzi, J. Adrien, and E. Maire, *Porosity analysis of long-fiber-reinforced ceramic matrix composites using X-ray tomography*. *Scripta Materialia*, 2009. **60**(6): p. 388-390.
373. Liu, H. and H. Tian, *Mechanical and microwave dielectric properties of SiCf/SiC composites with BN interphase prepared by dip-coating process*. *Journal of the European Ceramic Society*, 2012. **32**(10): p. 2505-2512.
374. Liu, H., H. Cheng, J. Wang, and G. Tang, *Dielectric properties of the SiC fiber-reinforced SiC matrix composites with the CVD SiC interphases*. *Journal of Alloys and Compounds*, 2010. **491**(1-2): p. 248-251.
375. Liu, H., H. Cheng, and H. Tian, *Design, preparation and microwave absorbing properties of resin matrix composites reinforced by SiC fibers with different electrical properties*. *Materials Science and Engineering: B*, 2014. **179**: p. 17-24.
376. Morell, J.I., D.J. Economou, and N.R. Amundson, *Pulsed-power volume-heating chemical vapor infiltration*. *Journal of Materials Research*, 1992. **7**(9): p. 2447-2457.
377. Binner, J., K. Annapoorani, A. Paul, I. Santacruz, and B. Vaidhyanathan, *Dense nanostructured zirconia by two stage conventional/hybrid microwave sintering*. *Journal of the European Ceramic Society*, 2008. **28**(5): p. 973-977.
378. Welty, J.R., C.E. Wicks, G. Rorrer, and R.E. Wilson, *Fundamentals of momentum, heat, and mass transfer*. 2009: John Wiley & Sons.